RADIAL BASIS FUNCTION AND DUAL RECIPROCITY BOUNDARY ELEMENT SOLUTIONS OF FLUID DYNAMICS PROBLEMS

A THESIS SUBMITTED TO
THE GRADUATE SCHOOL OF NATURAL AND APPLIED SCIENCES
OF
MIDDLE EAST TECHNICAL UNIVERSITY

BY

MERVE GÜRBÜZ

IN PARTIAL FULFILLMENT OF THE REQUIREMENTS
FOR
THE DEGREE OF DOCTOR OF PHILOSOPHY
IN
MATHEMATICS

JUNE 2017

Approval of the thesis:

RADIAL BASIS FUNCTION AND DUAL RECIPROCITY BOUNDARY ELEMENT SOLUTIONS OF FLUID DYNAMICS PROBLEMS

submitted by **MERVE GÜRBÜZ** in partial fulfillment of the requirements for the degree of **Doctor of Philosophy in Mathematics Department, Middle East Technical University** by,

Prof. Dr. Gülbin Dural Ünver _____
Dean, Graduate School of **Natural and Applied Sciences**

Prof. Dr. Mustafa Korkmaz _____
Head of Department, **Mathematics**

Prof. Dr. Münevver Tezer-Sezgin _____
Supervisor, **Mathematics Dept., METU**

Examining Committee Members:

Prof. Dr. Hakan Işık Tarman
Mechanical Engineering Dept., METU _____

Prof. Dr. Münevver Tezer-Sezgin
Mathematics Dept., METU _____

Prof. Dr. Tanıl Ergenç
Mathematics Dept., Atılım University _____

Assoc. Prof. Dr. Canan Bozkaya
Mathematics Dept., METU _____

Assoc. Prof. Dr. Niyazi Şahin
Mathematics - Computer Dept., Yıldırım Beyazıt University _____

Date: _____

I hereby declare that all information in this document has been obtained and presented in accordance with academic rules and ethical conduct. I also declare that, as required by these rules and conduct, I have fully cited and referenced all material and results that are not original to this work.

Name, Last Name: MERVE GÜRBÜZ

Signature :

ABSTRACT

RADIAL BASIS FUNCTION AND DUAL RECIPROCITY BOUNDARY ELEMENT SOLUTIONS OF FLUID DYNAMICS PROBLEMS

Gürbüz, Merve
Ph.D., Department of Mathematics
Supervisor : Prof. Dr. Münevver Tezer-Sezgin

June 2017, 173 pages

In this thesis, the two-dimensional, laminar steady or unsteady flow of a viscous, incompressible, electrically conducting fluid is considered in channels of several geometries under the impact of a uniform magnetic field with different orientations. Magnetohydrodynamic (MHD) flow governed by the hydrodynamic and electromagnetic equations is solved numerically with or without Stokes approximation and with or without magnetic induction due to the large or small values of Reynolds and magnetic Reynolds numbers, respectively. The numerical results of these MHD flow problems are obtained by using the radial basis function (RBF) approximation, the dual reciprocity boundary element method (DRBEM) and the direct interpolation boundary element method (DIBEM). The computational efficiency and easy implementation of RBF approximation is made use of to obtain the solutions of the considered MHD flow problems in terms of all the primitive variables. The MHD Stokes and the MHD incompressible flows subjected to the magnetic field in the pipe-axis direction are also studied including electric potential. The RBF approximation is also imposed to solve the MHD and the MHD Stokes convection flows in cavities. The MHD convection flow affected by both the Lorentz force and the buoyancy force is modeled by the MHD flow equations coupled with the temperature equation including the viscous dissipation term. The numerical results for all MHD flow problems are simulated in terms of streamlines, equivorticity lines, isotherms, pressure and electric potential contours in different geometries for several values of physical parameters.

The use of radial basis function approximation is also extended to transient Navier-Stokes, MHD convection flow and full MHD flow equations. Since the explicit Euler method is used for the time discretization, the numerical stability analysis is performed computationally through the spectral radius of the coefficient matrices in the RBF discretized systems for the optimal values of the time increment, relaxation parameters and the non-dimensional physical parameters.

Keywords: RBF approximation, DRBEM, DIBEM, MHD Stokes flow, MHD convection flow, viscous dissipation, stability

ÖZ

AKIŞKANLAR MEKANİĞİ PROBLEMLERİNİN RADYAL BAZ FONKSİYONU VE KARŞILIKLI SINIR ELEMANLARI YÖNTEMİ İLE ÇÖZÜMLERİ

Gürbüz, Merve
Doktora, Matematik Bölümü
Tez Yöneticisi : Prof. Dr. Münevver Tezer-Sezgin

Haziran 2017 , 173 sayfa

Bu tezde, viskoz, sıkıştırılamaz, elektrik ileten, farklı yönlerde uygulanan manyetik alan etkisindeki sıvının değişik geometrilere sahip kanal içindeki iki boyutlu zamana bağlı ya da zamandan bağımsız akışı incelenmiştir. Hidrodinamik ve elektromanyetik denklemler tarafından yönetilen magnetohidrodinamik (MHD) akış, Stokes yaklaştırımı ve manyetik indüksiyon olup olmamasıyla birlikte Reynolds ve manyetik Reynolds sayılarının büyük veya küçük değerleri için sayısal olarak hesaplanmıştır. MHD akış problemlerinin nümerik sonuçları radyal baz fonksiyonları (RBF) yaklaştırımı, karşılıklı sınır elemanları yöntemi (DRBEM) ve doğrudan interpolasyon sınır elemanları yöntemi (DIBEM) kullanılarak elde edilmiştir. RBF yaklaştırımının hesaplama verimliliği ve kolay uygulanabilir olması, MHD akış problemlerinin bütün ilkel değişkenler cinsinden çözümlerini elde etmede kullanılmıştır. Kanal yönündeki manyetik alan etkisi altında kalan MHD Stokes ve MHD sıkıştırılamaz akışlar elektrik potensiyelinin eklenmesiyle birlikte çalışılmıştır. RBF yaklaştırımı kesit içindeki MHD ve MHD Stokes konveksiyon akışlarını çözmek için de uygulanmıştır. Lorentz ve buoyancy kuvvetlerinden etkilenen MHD konveksiyonel akış, viskoz yayılımını da içeren ısı denklemi ve MHD denklemleri kullanılarak modellenmiştir. Bütün MHD akış problemlerinin sayısal çözümleri farklı parametreler için sıvı akımı çizgileri, eş vortisiti çizgileri, eş ısı eğrileri, basınç ve elektrik potansiyel konturları cinsinden

farklı geometrilerde gösterilmiştir.

RBF yaklaştırımının kullanımı zamana bağlı Navier-Stokes, MHD konveksiyon akış ve tam MHD akış denklemleri için de genişletilmiştir. Zaman ayrıklaştırması için açık Euler yöntemi kullanılmasından dolayı sayısal kararlılık analizi, ayrıklaştırılmış RBF sistemlerindeki katsayı matrislerinin spektral yarıçapları doğrultusunda zaman aralığı, yumuşama katsayıları ve boyutsal olmayan fiziksel parametrelerin optimal değerlerine göre yapılmıştır.

Anahtar Kelimeler: Radyal baz fonksiyonları yaklaştırımı, Karşılıklı sınır elemanları yöntemi, Doğrudan interpolasyon sınır elemanı yöntemi, Magnetohidrodinamik Stokes akış, Magnetohidrodinamik konveksiyon akış, viskoz dağılım, kararlılık

To my parents, Nurkan and Kenan,

my sister, Meltem,

and my brother, Murat

ACKNOWLEDGMENTS

I would like to express my sincere gratitude to my supervisor Prof. Dr. Münevver Tezer-Sezgin for her precious guidance, continuous support and enthusiastic encouragement during my research. Her great motivation and understanding makes this study possible for me. I shall never forget her invaluable advices for not only academic research but also social life.

I would also like to thank my thesis defense committee members Prof. Dr. Hakan Işık Tarman, Prof. Dr. Tanıl Ergenç, Assoc. Prof. Dr. Canan Bozkaya and Assoc. Prof. Dr. Niyazi Şahin for their suggestions and guidance.

I gratefully acknowledge the financial support of The Scientific and Technology Research Council of Turkey (TÜBİTAK).

I would like to express my deepest gratitude to my best friend Şükran Gül for always being near me when I need someone to talk and for her continuous motivation during the undergraduate and Ph.D. process. Many thanks to Pelin Şenel and Sidre Oğlakkaya for their sincere friendships and their fruitful discussions.

I offer my special thanks to my mother Nurkan and my father Kenan for their unconditional love and endless support which provide me success and happiness in my life. I also thank to my sister Meltem and my brother Murat for their friendships and encouragements during my research.

Last but not least, I would like to thank my pretty nieces Eylül, Ekin and Zeynep, and my handsome nephew Kenan for making my life more colorful and cheerful.

TABLE OF CONTENTS

LIST OF TABLES

TABLES

LIST OF FIGURES

FIGURES

LIST OF ABBREVIATIONS

A	magnetic potential
$\boldsymbol{B}$	magnetic induction
c_p	specific heat
$\boldsymbol{E}$	electric field
Ec	Eckert number
$\boldsymbol{g}$	gravitational acceleration vector
$\boldsymbol{H}$	magnetic field
H_0	magnetic field intensity
$\boldsymbol{J}$	electric current density
L	characteristic length
M	Hartmann number
N	Stuart number
N_b	number of boundary points
N_i	number of interior points
p	pressure
Pr	Prandtl number
Re	Reynolds number
Re_m	magnetic Reynolds number
Ri	Richardson number
T	temperature
T_{hot}	temperature of the hot wall
T_{cold}	temperature of the cold wall
$\boldsymbol{u}$	velocity field
u	x-component of the velocity of the fluid
U_0	characteristic velocity
v	y-component of the velocity of the fluid
ω	vorticity
ψ	stream function

ϕ	electric potential
Φ	viscous dissipation
ρ	density
μ	magnetic permeability
ν	kinematic viscosity
σ	electric conductivity
β	thermal expansion coefficient
λ	thermal conductivity
Δt	time increment
ΔT	temperature difference

CHAPTER 1

INTRODUCTION

Fluid dynamics (or Hydrodynamics) is the branch of the physics which is concerned with the motion of fluids classified as liquids and gases, and the energy exchange in the fluid. The governing equations of fluid dynamics are based on the global laws of conservation of mass, conservation of momentum and conservation of energy. When there exists an external magnetic field around the fluid medium, the Maxwell's equations of elecrtomagnetics are combined with the momentum equations through Ohm's law.

In this thesis, the steady or unsteady laminar flow of a viscous, incompressible fluid is considered under the effect of an applied magnetic field. If the motion of the fluid varies with the time, then the flow is unsteady. Otherwise, it is called steady. Laminar flow has a smooth motion of the fluid. Viscosity arises from internal friction in the fluid particle. Fluid is called incompressible if the density of the fluid is constant.

In this Chapter, we first introduce the Navier-Stokes equations in both primitive (velocity-pressure) and stream function-vorticity formulations. Then, the magnetic field effect on the Stokes flow is considered and the mathematical formulation of MHD Stokes flow is given in Section 1.2. Electric potential equation is also derived for the MHD incompressible flow in Section 1.3. MHD convection flow equations are included with or without viscous dissipation in Section 1.4. MHD convection flow equations are obtained by including the energy equation to the MHD equations. Section 1.5 presents the full MHD equations in which the induced magnetic field satisfies the induction equations added to the momentum equations. Finally, the literature survey, the plan of the thesis and the contributions in the thesis are given in Sections 1.6,

1.7 and 1.8, respectively.

1.1 The Navier-Stokes Equations

The Navier-Stokes equations are the basic equations of the fluid dynamics. The applications of the laws of the conservation of mass and momentum (Newton second law) result in the continuity and momentum equations. These equations are nonlinear partial differential equations in terms of velocity field and pressure of the fluid. The nonlinearity due to the convective acceleration makes the equations difficult to solve. Analytical solutions are available only for some special regions and dimensions with some simplified physical assumptions. Thus, the solution of Navier-Stokes equations are usually obtained by using numerical methods.

Many engineering problems are governed by the Navier-Stokes equations such as ocean currents, motion of stars inside a galaxy, weather movement, the study of blood flow, fluid flows in channels, the analysis of the effects of pollution and the design of the cars, aircraft, and power stations, etc.

The two-dimensional, unsteady Navier-Stokes equations are given together with the continuity equation as [57]

$$\nabla \cdot \boldsymbol{u} = 0 \tag{1.1}$$

$$\rho(\frac{\partial \boldsymbol{u}}{\partial t} + (\boldsymbol{u} \cdot \nabla)\boldsymbol{u}) = -\nabla p + \rho\nu\nabla^2\boldsymbol{u} \tag{1.2}$$

in terms of primitive variables $(\boldsymbol{u}, p)$. Here, $\boldsymbol{u} = (u, v, 0)$ is the velocity field and p is the pressure of the fluid. ρ and ν are the density and kinematic viscosity of the fluid, respectively.

Now, we introduce the scaled transformations with a characteristic length L and a characteristic velocity U_0 as [61]

$$\boldsymbol{x} \to \boldsymbol{x}L, \quad t \to tL/U_0, \quad \boldsymbol{u} \to \boldsymbol{u}U_0, \quad p \to p\rho\nu U_0/L \tag{1.3}$$

and substitute into the equations (1.1)-(1.2) to obtain non-dimensional Navier-Stokes

equations as

$$\frac{\partial u}{\partial x} + \frac{\partial u}{\partial y} = 0 \tag{1.4}$$

$$\nabla^2 u = Re(\frac{\partial u}{\partial t} + u\frac{\partial u}{\partial x} + v\frac{\partial u}{\partial y}) + \frac{\partial p}{\partial x} \tag{1.5}$$

$$\nabla^2 v = Re(\frac{\partial v}{\partial t} + u\frac{\partial v}{\partial x} + v\frac{\partial v}{\partial y}) + \frac{\partial p}{\partial y} \tag{1.6}$$

where $Re = LU_0/\nu$ is the Reynolds number which expresses the ratio of inertia forces to viscous forces. When the viscous forces are dominant ($Re < 2100$), flow regime is laminar this means that fluid has a smooth behavior. Otherwise, the flow is called turbulent. The equations (1.4)-(1.6) in the primitive variables velocity and pressure have the drawback of missing pressure equation although the pressure is also an unknown.

The two-dimensional flow allows one to define the stream function ψ satisfying the continuity equation as

$$u = \frac{\partial \psi}{\partial y}, \qquad v = -\frac{\partial \psi}{\partial x} \tag{1.7}$$

which shows the trajectories of particles in the flow.

The vorticity represents the rotation of the fluid and is defined as

$$\omega = \frac{\partial v}{\partial x} - \frac{\partial u}{\partial y} \tag{1.8}$$

which is the non-zero third component of the vorticity field $\boldsymbol{\omega} = \nabla \times \boldsymbol{u}$.

Substitution the stream function definition (1.7) into the equation (1.8) gives the stream function equation as

$$\nabla^2 \psi = -w. \tag{1.9}$$

The vorticity transport equation can be derived by differentiating the momentum equations (1.6) and (1.5) with respect to x and y, respectively, and subtracting from each other

$$\frac{1}{Re}\nabla^2 \omega = \frac{\partial \omega}{\partial t} + u\frac{\partial \omega}{\partial x} + v\frac{\partial \omega}{\partial y} \tag{1.10}$$

so that pressure terms in the momentum equations are eliminated. This is the main advantage of stream function-vorticity formulation.

Thus, the unsteady Navier-Stokes equations in terms of stream function and vorticity are given as

$$\nabla^2\psi = -\omega \tag{1.11}$$

$$\frac{1}{Re}\nabla^2\omega = \frac{\partial\omega}{\partial t} + u\frac{\partial\omega}{\partial x} + v\frac{\partial\omega}{\partial y}. \tag{1.12}$$

The stream function has Dirichlet type boundary conditions since the stream function is natural streamline on the walls with a constant value and can be taken as zero. However, the vorticity boundary conditions are not known physically. The unknown vorticity boundary values are obtained from the definition of the vorticity with the help of coordinate matrix $\boldsymbol{F}$ of RBF

$$\omega = \frac{\partial v}{\partial x} - \frac{\partial u}{\partial y} = \frac{\partial \boldsymbol{F}}{\partial x}\boldsymbol{F}^{-1}v - \frac{\partial \boldsymbol{F}}{\partial y}\boldsymbol{F}^{-1}u \tag{1.13}$$

where the coordinate matrix $\boldsymbol{F}$ is constructed by radial basis function as $F_{ij} = 1+r_{ij}$, r_{ij} being the distance between the points 'i' and 'j'.

Alternatively, the vorticity boundary conditions can be obtained using Taylor series expansion of the stream function equation ($\nabla^2\psi = -\omega$).

In this approach [6], we first approximate $\dfrac{\partial^2\psi}{\partial n^2} = \psi_{nn}$ on the boundary point 'b' as

$$\psi_{nn}|_b = a_0\psi_b + a_1\psi_s + a_2\psi_q + a_3\psi_n|_b \tag{1.14}$$

where ψ_b is the boundary value, ψ_n is the normal derivative of ψ, ψ_s and ψ_q are interior values which are sh and qh distances away from the boundary, respectively (Figure 1.1).

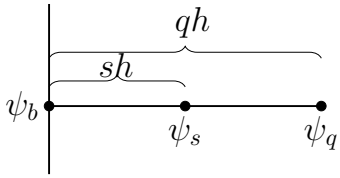

Figure 1.1: ψ_b boundary value ψ_s and ψ_q interior values

Then, the Taylor series expansion of ψ_s and ψ_q around the boundary point 'b' are written and rearranged to obtain

$$\psi_{nn}|_b = (a_0+a_1+a_2)\psi_b+(sha_1+qha_2+a_3)\psi_n|_b+(\frac{s^2h^2}{2}a_1+\frac{q^2h^2}{2}a_2)\psi_{nn}|_b+\mathcal{O}(h^3). \tag{1.15}$$

Equating the coefficients of the corresponding derivatives gives the undetermined coefficients a_0, a_1, a_2, a_3 as

$$a_0 = \frac{-2(s^3 - q^3)}{h^2 s^2 q^2 (s-q)}, \qquad a_1 = \frac{-2q}{h^2 s^2 (s-q)},$$
$$a_2 = \frac{2s}{h^2 q^2 (s-q)}, \qquad a_3 = \frac{-2(s+q)}{hsq} \quad .$$

Thus, the boundary values for ω can be obtained from

$$\omega_b = -(a_0 \psi_b + a_1 \psi_s + a_2 \psi_q + a_3 \psi_n|_b) \tag{1.16}$$

when the boundary values ψ and ψ_n are known in the problem.

1.2 The MHD Stokes Flow

Magnetohydrodynamics (MHD) is the branch of fluid mechanics that focuses on the flow of electrically conducting fluids in the presence of magnetic field. Its popularity comes from the wide range of industrial applications such as MHD pumps, geothermal energy extraction, liquid metal productions (mercury, liquid sodium, etc.), plasma physics and nuclear fusion, etc. The governing coupled MHD equations are the continuity equation, the Navier-Stokes equations of hydrodynamics and Maxwell's equations of electromagnetics through Ohm's law [35, 52]. The analytical solution of MHD equations is difficult to obtain due to the nonlinear terms and Lorentz force term. Another difficulty is satisfying the divergence-free conditions on magnetic field and velocity. Thus, the numerical methods are used to solve MHD equations.

The motion of the fluid satisfies the equation of continuity

$$\nabla \cdot \boldsymbol{u} = 0 \tag{1.17}$$

and the momentum equations

$$\rho(\boldsymbol{u} \cdot \nabla)\boldsymbol{u} = -\nabla p + \rho\nu\nabla^2 \boldsymbol{u} + \boldsymbol{J} \times \boldsymbol{B} \tag{1.18}$$

where $\boldsymbol{J} \times \boldsymbol{B}$ is the Lorentz force which comes from the interaction between the electrically conducting fluid and uniform magnetic field. $\boldsymbol{u} = (u, v, 0)$, $\boldsymbol{B}$, $\boldsymbol{J}$ and p are the velocity field, magnetic field, electric current density and pressure, respectively. ρ is the density, and ν is the kinematic viscosity.

Since the fluid is electrically conducting, electric current density is induced and given by Ohm's law

$$\boldsymbol{J} = \sigma(\boldsymbol{E} + \boldsymbol{u} \times \boldsymbol{B}) \tag{1.19}$$

with the Ampere's law $\boldsymbol{J} = \nabla \times \boldsymbol{H}$ where $\boldsymbol{B} = \mu \boldsymbol{H}$. Here, σ and μ are the electric conductivity and magnetic permeability of the fluid.

The electric field is defined as $\boldsymbol{E} = -\nabla\phi$ where ϕ is the electric potential since the electric filed is irrotational, this means that $\nabla \times \boldsymbol{E} = 0$.

Introducing dimensionless variables as [61]

$$\boldsymbol{x} \to \boldsymbol{x}L, \quad \boldsymbol{u} \to \boldsymbol{u}U_0, \quad \boldsymbol{H} \to \boldsymbol{H}H_0 \tag{1.20}$$

$$p \to p\rho\nu U_0/L, \quad \phi \to \phi\mu L U_0 H_0 \tag{1.21}$$

and substituting into equations (1.17)-(1.19), we obtain the non-dimensional MHD equations as

$$\nabla \cdot \boldsymbol{u} = 0 \tag{1.22}$$

$$Re(\boldsymbol{u} \cdot \nabla)\boldsymbol{u} = -\nabla p + \nabla^2 \boldsymbol{u} + M^2(-\nabla\phi + \boldsymbol{u} \times \boldsymbol{H}) \times \boldsymbol{H} \tag{1.23}$$

$$Re_m(-\nabla\phi + \boldsymbol{u} \times \boldsymbol{H}) = \nabla \times \boldsymbol{H} \tag{1.24}$$

where the non-dimensional parameters are the Reynolds number, the magnetic Reynolds number and the Hartmann number, and represent physically as [14]

$$Re = \frac{LU_0}{\nu} \sim \frac{\text{inertia force}}{\text{viscous force}},$$

$$Re_m = LU_0\sigma\mu \sim \frac{\text{advection}}{\text{diffusion of } \boldsymbol{B}},$$

and

$$M = L\mu H_0\sqrt{\sigma/\rho\nu} \sim \frac{\text{Lorentz force}}{\text{shear force}}$$

where L and U_0 are the characteristic length and the characteristic velocity, and H_0 is externally applied magnetic field intensity.

Induced magnetic field is neglected in the equation (1.24) due to the small magnetic Reynolds number $Re_m << 1$ which indicates that externally applied magnetic field is dominant.

Stokes flow approximation is the assumption of very small values of Reynolds number ($Re << 1$) so that the convective terms $(\boldsymbol{u} \cdot \nabla)\boldsymbol{u}$ in the equation (1.23) are neglected. Hence, the MHD Stokes flow equations in terms of primitive variables velocity and pressure are from the equations (1.22)-(1.24) as

$$\nabla \cdot \boldsymbol{u} = 0 \tag{1.25}$$

$$-\nabla p + \nabla^2 \boldsymbol{u} + M^2(-\nabla\phi \times \boldsymbol{H} + \mathbf{u} \times \boldsymbol{H} \times \boldsymbol{H}) = 0 \quad . \tag{1.26}$$

When the magnetic field is applied horizontally or vertically, from Ohm's law (1.19) and the conservation of electric current $\nabla \cdot \boldsymbol{J} = 0$ we obtain the harmonic electric potential equation $\nabla^2\phi = 0$. With the homogeneous boundary conditions the solution becomes the zero electric potential, $\phi = 0$, dropping the gradient of the electric potential in the equation (1.26), $(\nabla\phi = 0)$.

When the magnetic field is applied in the $x-$direction, $\boldsymbol{H_0} = (1, 0, 0)$, the equations can be written component-wise

$$\frac{\partial u}{\partial x} + \frac{\partial v}{\partial y} = 0 \tag{1.27}$$

$$\nabla^2 u = \frac{\partial p}{\partial x} \tag{1.28}$$

$$\nabla^2 v = \frac{\partial p}{\partial y} + M^2 v. \tag{1.29}$$

Introducing 2D stream function ψ to satisfy continuity equation and vorticity ω as $u = \dfrac{\partial \psi}{\partial y}$, $v = -\dfrac{\partial \psi}{\partial x}$ and $\omega = \dfrac{\partial v}{\partial x} - \dfrac{\partial u}{\partial y}$, we obtain the stream function equation $\nabla^2\psi = -\omega$.

Differentiation of vorticity definition with respect to x and y with the use of continuity equation gives velocity-vorticity equations as

$$\nabla^2 u = -\frac{\partial \omega}{\partial y} \quad , \qquad \nabla^2 v = \frac{\partial \omega}{\partial x} \quad . \tag{1.30}$$

Pressure Poisson's equation is obtained by differentiating equation (1.28) and equation (1.29) with respect to x and y, respectively, and adding

$$\nabla^2 p = -M^2 \frac{\partial v}{\partial y} \quad . \tag{1.31}$$

Similarly, vorticity Poisson's equation can be derived from cross-differentiation of equations (1.28) and (1.29) as

$$\nabla^2 \omega = M^2 \frac{\partial v}{\partial x} \quad . \tag{1.32}$$

Thus, the two-dimensional steady MHD Stokes flow under the horizontal magnetic field is represented with Poisson's type equations in terms of all fluid variables; velocity components (u, v), stream function ψ, vorticity ω and pressure p

$$\nabla^2 u = -\frac{\partial \omega}{\partial y} \quad , \qquad \nabla^2 v = \frac{\partial \omega}{\partial x} \tag{1.33}$$

$$\nabla^2 \psi = -\omega \tag{1.34}$$

$$\nabla^2 \omega = M^2 \frac{\partial v}{\partial x} \quad , \qquad \nabla^2 p = -M^2 \frac{\partial v}{\partial y} \quad . \tag{1.35}$$

Again, the unknown vorticity boundary values are either taken from vorticity definition by using coordinate matrix $\boldsymbol{F}$ or stream function equation by using finite difference approximation as explained in previous section (Section 1.1).

The unknown pressure boundary values are computed by a finite difference scheme for the pressure derivatives and coordinate matrix $\boldsymbol{F}$ for the space derivatives in the equations (1.28)-(1.29) as

$$p_b = p_i - \Delta y(\boldsymbol{C}v - M^2 v) \qquad \text{for the lower boundary} \tag{1.36}$$

$$p_b = p_i + \Delta x \boldsymbol{C} u \qquad \text{for the right boundary} \tag{1.37}$$

$$p_b = p_i + \Delta y(\boldsymbol{C}v - M^2 v) \qquad \text{for the upper boundary} \tag{1.38}$$

$$p_b = p_i - \Delta x \boldsymbol{C} u \qquad \text{for the left boundary} \tag{1.39}$$

where p_b is the boundary value, p_i is the interior value which is Δx or Δy distances away from the boundary and $\boldsymbol{C} = \dfrac{\partial \boldsymbol{F}}{\partial x}\boldsymbol{F}^{-1}\dfrac{\partial \boldsymbol{F}}{\partial x}\boldsymbol{F}^{-1} + \dfrac{\partial \boldsymbol{F}}{\partial y}\boldsymbol{F}^{-1}\dfrac{\partial \boldsymbol{F}}{\partial y}\boldsymbol{F}^{-1}$.

When the magnetic field is acted in the $y-$direction, $\boldsymbol{H_0} = (0, 1, 0)$, the equations (1.25)-(1.26) take the form

$$\frac{\partial u}{\partial x} + \frac{\partial v}{\partial y} = 0 \tag{1.40}$$

$$\nabla^2 u = \frac{\partial p}{\partial x} + M^2 u \tag{1.41}$$

$$\nabla^2 v = \frac{\partial p}{\partial y} \tag{1.42}$$

which are put again into Poisson's equations for the velocity components, stream

function, vorticity and pressure

$$\nabla^2 u = -\frac{\partial \omega}{\partial y} \quad , \qquad \nabla^2 v = \frac{\partial \omega}{\partial x} \tag{1.43}$$

$$\nabla^2 \psi = -\omega \tag{1.44}$$

$$\nabla^2 \omega = -M^2 \frac{\partial u}{\partial y} \quad , \qquad \nabla^2 p = -M^2 \frac{\partial u}{\partial x} \quad . \tag{1.45}$$

The direction of the magnetic field affects the vorticity and pressure Poisson's equations as $M^2\frac{\partial v}{\partial x}$, $-M^2\frac{\partial v}{\partial y}$ replaced by $-M^2\frac{\partial u}{\partial y}$, $-M^2\frac{\partial u}{\partial x}$.

The unknown vorticity and pressure boundary conditions are obtained from the stream function equation by using finite difference method and from the momentum equations (1.41)-(1.42) using the coordinate matrix for the Laplacian, and finite differences for the pressure gradients, respectively.

When the external magnetic field is applied in the pipe-axis direction, $\boldsymbol{H_0} = (0, 0, 1)$, the continuity equation (1.25) and the momentum equations (1.26) are written in terms of primitive variables with electric potential as

$$\frac{\partial u}{\partial x} + \frac{\partial v}{\partial y} = 0 \tag{1.46}$$

$$\nabla^2 u = \frac{\partial p}{\partial x} - M^2(-\frac{\partial \phi}{\partial y} - u) \tag{1.47}$$

$$\nabla^2 v = \frac{\partial p}{\partial y} - M^2(\frac{\partial \phi}{\partial x} - v) \quad . \tag{1.48}$$

Taking the divergence of Ohm's law (1.19) and using the conservation of electric current $\nabla \cdot \mathbf{J} = 0$ give electric potential Poisson's equation as

$$\nabla^2 \phi = \nabla \cdot (\boldsymbol{u} \times \boldsymbol{H}) = \frac{\partial v}{\partial x} - \frac{\partial u}{\partial y} \quad . \tag{1.49}$$

Thus, the contribution of the electric potential can not be neglected in the momentum equations when the magnetic field applies in the pipe-axis direction.

Now, the harmonic pressure and vorticity equations are obtained by differentiating equations (1.47)-(1.48)

$$\nabla^2 p = 0 \quad , \qquad \nabla^2 \omega = 0 \quad . \tag{1.50}$$

Thus, MHD Stokes flow equations in terms of stream function, electrical potential, velocity components, vorticity and pressure are coupled with electric potential through

vorticity in the flow as

$$\nabla^2 u = -\frac{\partial \omega}{\partial y} \ , \qquad \nabla^2 v = \frac{\partial \omega}{\partial x} \tag{1.51}$$

$$\nabla^2 \psi = -\omega \ , \qquad \nabla^2 \phi = \omega \tag{1.52}$$

$$\nabla^2 \omega = 0 \ , \qquad \nabla^2 p = 0 \tag{1.53}$$

where pressure is affected from electric potential in obtaining its boundary conditions from equations (1.47)-(1.48). Boundary conditions for the vorticity are obtained from the stream function equation. For the electric potential both insulated ($\frac{\partial \phi}{\partial n} = 0$) and conducting ($\phi = c$) wall conditions are considered.

1.3 The MHD incompressible Flow with Electric Potential

MHD Stokes flow equations generating the electric potential is given in the previous section due to the external magnetic field in the pipe-axis direction. Now, we extend the problem by adding the convective terms ($(\boldsymbol{u} \cdot \nabla)\boldsymbol{u}$) in the momentum equations of MHD Stokes flow with the assumption of large Reynolds number value.

The MHD coupled equations are obtained from the conservation of mass, momentum and the electric charges with Ohm's law [35, 61].

$$\nabla \cdot \boldsymbol{u} = 0 \tag{1.54}$$

$$\rho(\mathbf{u} \cdot \nabla)\boldsymbol{u} = -\nabla p + \rho\nu\nabla^2 \boldsymbol{u} + \boldsymbol{J} \times \mu \boldsymbol{H} \tag{1.55}$$

$$\nabla \cdot \boldsymbol{J} = 0 \tag{1.56}$$

$$\boldsymbol{J} = \sigma(-\nabla\phi + \boldsymbol{u} \times \mu \boldsymbol{H}) \tag{1.57}$$

where $\boldsymbol{u} = (u, v, 0)$, $\boldsymbol{H} = (H_x, H_y, H_z)$, p, $\boldsymbol{J}$ and ϕ are the fluid velocity, magnetic field, pressure of the fluid, electric current density and electric potential, respectively. ρ, ν, μ and σ are the density, the kinematic viscosity, the magnetic permeability and the electric conductivity of the fluid.

The non-dimensional MHD equations neglecting the induced magnetic field due to

the small magnetic Reynolds number can be written as

$$\frac{\partial u}{\partial x}+\frac{\partial v}{\partial y}=0 \tag{1.58}$$

$$\frac{1}{N}(u\frac{\partial u}{\partial x}+v\frac{\partial u}{\partial y})=-\frac{1}{M^2}\frac{\partial p}{\partial x}+\frac{1}{M^2}\nabla^2 u+\left(-u-\frac{\partial \phi}{\partial y}\right) \tag{1.59}$$

$$\frac{1}{N}(u\frac{\partial v}{\partial x}+v\frac{\partial v}{\partial y})=-\frac{1}{M^2}\frac{\partial p}{\partial y}+\frac{1}{M^2}\nabla^2 v+\left(-v+\frac{\partial \phi}{\partial x}\right) \tag{1.60}$$

with the electric potential equation

$$\nabla^2\phi=\nabla\cdot(\boldsymbol{u}\times\boldsymbol{H})=\frac{\partial v}{\partial x}-\frac{\partial u}{\partial y}\ . \tag{1.61}$$

In the equations (1.58)-(1.60) the following dimensionless variables are used

$$\mathbf{x}\to\mathbf{x}L,\quad \mathbf{u}\to\mathbf{u}U_0,\quad \mathbf{H}\to\mathbf{H}H_0$$
$$p\to p\rho\nu U_0/L,\quad \phi\to\phi\mu L U_0 H_0$$

where L and U_0 are the characteristic length and velocity, respectively, and H_0 is the intensity of the applied magnetic field. The dimensionless parameters are the Hartmann number $M=L\mu H_0\sqrt{\sigma/\rho\nu}$ and the Stuart number (or the interaction parameter) $N=M^2/Re$ which is the ratio of the electromagnetic force to the inertia force.

The two-dimensional MHD flow together with an electric potential can be also given in terms of velocity components, stream function, electric potential, vorticity and pressure

$$\nabla^2 u=-\frac{\partial\omega}{\partial y},\qquad \nabla^2 v=\frac{\partial\omega}{\partial x} \tag{1.62}$$

$$\nabla^2\psi=-\omega,\qquad \nabla^2\phi=\omega \tag{1.63}$$

$$\frac{1}{M^2}\nabla^2\omega=\frac{1}{N}\left(u\frac{\partial\omega}{\partial x}+v\frac{\partial\omega}{\partial y}\right) \tag{1.64}$$

$$\frac{1}{M^2}\nabla^2 p=\frac{2}{N}\left(\frac{\partial u}{\partial x}\frac{\partial v}{\partial y}-\frac{\partial u}{\partial y}\frac{\partial v}{\partial x}\right). \tag{1.65}$$

The harmonic vorticity and pressure equations (1.53) in the MHD Stokes flow equations convert to the Poisson's type equations due to the convection terms.

The unknown boundary conditions for the vorticity are obtained from the finite difference approximation of the stream function equation including interior values of

the stream function. Pressure boundary values are computed by using the finite difference scheme for the gradient of pressure and the coordinate matrix for the space derivatives of velocity components and electric potential in the momentum equations (1.59)-(1.60).

1.4 MHD Convection Flow with Viscous Dissipation

MHD convection flow occurs when the temperature variation of the electrically conducting fluid in the presence of the magnetic field and the gravitation force are introduced. Convective heat transfer can be divided into three categories such as natural (or free), forced and mixed convection. If the fluid motion is produced by the density differences due to the change in the temperature of the fluid, then the convection is called natural. Forced convection is characterized by the fluid motion which is the result of the external force such as blower, pump, wind and lid, etc. When the forced convection and the natural convection occur at the same time, the process is called mixed convection.

The analysis of the fluid flow under the influence of a magnetic field and heat transfer in enclosures is one of the most widely studied problems in thermo-fluids area. It has recently attracted the interest of many researchers because of the wide range of industrial applications such as crystal growth, cooling of electronic systems, air conditioning, solar technology, chemical processing equipment, flat-plate solar collectors, geophysical applications etc.

MHD convection flow affected by the both Lorentz force and buoyancy force is modeled by the MHD flow equations given in Section 1.2 with the use of the Boussinesq approximation coupled with the temperature equations obtained from the first law of thermodynamics (the conservation of energy). In the Boussinesq approximation, variations of all fluid properties due to the temperature difference are neglected except for the density in the buoyancy force term.

Thus, the governing equations are given in vector from as [35, 45]

$$\nabla \cdot \boldsymbol{u} = 0 \tag{1.66}$$

$$\rho(\boldsymbol{u} \cdot \nabla)\boldsymbol{u} = -\nabla p + \rho\nu\nabla^2\boldsymbol{u} + \boldsymbol{J} \times \mu\boldsymbol{H} - \boldsymbol{g}\rho\beta(T - T_{cold}) \tag{1.67}$$

$$\rho c_p((\boldsymbol{u} \cdot \nabla)T) = \nabla \cdot (\lambda\nabla T) + \frac{1}{\sigma}\boldsymbol{J}^2 + \rho\nu\Phi + \rho Q \tag{1.68}$$

where $\boldsymbol{u} = (u, v)$, p, $\boldsymbol{H} = (H_x, H_y)$ and T are the velocity, pressure, the magnetic field and the temperature of the fluid, respectively. The electric current density $\boldsymbol{J}$ is defined as $\boldsymbol{J} = \sigma(\boldsymbol{u} \times \mu\boldsymbol{H})$ in the absence of electric field $\boldsymbol{E}$. Here ν, σ, μ, ρ, c_p, β, λ and $\boldsymbol{g}$ are kinematic viscosity, electrical conductivity, magnetic permeability, the density, specific heat, thermal expansion coefficient, the thermal conductivity of the fluid and the gravitational acceleration vector, respectively.

The last two terms in the momentum equation (1.67) are Lorentz and buoyancy force terms, respectively. Buoyancy force is the net force between the movement due to the heat and gravitation force. In the energy equation (1.68), the viscous dissipation Φ is a transformation of kinetic energy into internal energy and expressed as [45]

$$\Phi = 2(\frac{\partial u}{\partial x})^2 + 2(\frac{\partial v}{\partial y})^2 + (\frac{\partial v}{\partial x} + \frac{\partial u}{\partial y})^2.$$

The terms $\frac{1}{\sigma}\boldsymbol{J}^2 = \frac{1}{\sigma}\boldsymbol{J} \cdot \boldsymbol{J}$ and Q represents the Joule dissipation and other sources of volumetric energy release like chemical reactions or nuclear radiation, respectively, [35]. In this thesis, volumetric energy is neglected.

In order to get dimensionless form of the equations (1.66)-(1.68), the non-dimensional scales are defined as

$$\mathbf{x} \to \mathbf{x}L, \quad \mathbf{u} \to \mathbf{u}U_0, \quad \mathbf{H} \to \mathbf{H}H_0, \quad p \to p\rho\nu U_0/L, \quad T - T_{cold} \to T\Delta T$$

where U_0, L and H_0 are the characteristic velocity, the characteristic length and externally applied magnetic field intensity, respectively. Temperature difference between the hot wall T_{hot} and the cold wall T_{cold} is defined as $\Delta T = (T_{hot} - T_{cold})$.

Thus, the steady, non-dimensional, MHD convection flow equations neglecting the induced magnetic field are

$$\frac{\partial u}{\partial x}+\frac{\partial v}{\partial y}=0 \tag{1.69}$$

$$Re(u\frac{\partial u}{\partial x}+v\frac{\partial u}{\partial y})=-\frac{\partial p}{\partial x}+\nabla^2 u+M^2(-u{H_y}^2+vH_xH_y) \tag{1.70}$$

$$Re(u\frac{\partial v}{\partial x}+v\frac{\partial v}{\partial y})=-\frac{\partial p}{\partial y}+\nabla^2 v+M^2(uH_xH_y-v{H_x}^2)+\frac{Gr}{Re}T \tag{1.71}$$

$$\begin{aligned}\nabla^2 T=&PrRe(u\frac{\partial T}{\partial x}+v\frac{\partial T}{\partial y})-M^2EcPr(uH_y-vH_x)^2\\&-EcPr(2(\frac{\partial u}{\partial x})^2+2(\frac{\partial v}{\partial y})^2+(\frac{\partial v}{\partial x}+\frac{\partial u}{\partial y})^2)\end{aligned} \tag{1.72}$$

where the non-dimensional parameters, Reynolds number Re and Hartmann number M are defined in Section 1.2. The physical interpretation and the definition of the Grashof number Gr, the Prandtl number Pr, and the Eckert number Ec are given as [23, 35]

$$Gr=\frac{g\beta(T_{hot}-T_{cold})L^3}{\nu^2}\sim\frac{\text{buoyancy force}}{\text{viscous force}},$$
$$Pr=\frac{\rho c_p\nu}{\lambda}\sim\frac{\text{viscous}}{\text{thermal diffusivity}},$$

and

$$Ec=\frac{U_0^2}{c_p(T_{hot}-T_{cold})}\sim\frac{\text{Kinetic energy}}{\text{accumulated enthalpy}},$$

respectively.

Richardson number Ri is defined as $Ri=Gr/Re^2$ and determines the convection types. If $Ri<<1$, $Ri\approx 1$ or $Ri>>1$, then the flow is dominated by forced, mixed or natural convection, respectively.

When the convection flow is subjected to the horizontal magnetic field, $\boldsymbol{H_0}=(1,0)$, the equations (1.69)-(1.72) take the form

$$\frac{\partial u}{\partial x}+\frac{\partial v}{\partial y}=0 \tag{1.73}$$

$$Re(u\frac{\partial u}{\partial x}+v\frac{\partial u}{\partial y})=-\frac{\partial p}{\partial x}+\nabla^2 u \tag{1.74}$$

$$Re(u\frac{\partial v}{\partial x}+v\frac{\partial v}{\partial y})=-\frac{\partial p}{\partial y}+\nabla^2 v-M^2v+\frac{Gr}{Re}T \tag{1.75}$$

$$\begin{aligned}\nabla^2 T=&PrRe(u\frac{\partial T}{\partial x}+v\frac{\partial T}{\partial y})-M^2EcPrv^2\\&-EcPr(2(\frac{\partial u}{\partial x})^2+2(\frac{\partial v}{\partial y})^2+(\frac{\partial v}{\partial x}+\frac{\partial u}{\partial y})^2).\end{aligned} \tag{1.76}$$

Following the similar procedure described in Section 1.2, equations (1.73)-(1.76) can be transformed to the equations containing velocity components, stream function, temperature, vorticity and pressure

$$\nabla^2 u = -\frac{\partial \omega}{\partial y} \ , \qquad \nabla^2 v = \frac{\partial \omega}{\partial x} \tag{1.77}$$

$$\nabla^2 \psi = -\omega \tag{1.78}$$

$$\begin{aligned}\nabla^2 T = PrRe(u\frac{\partial T}{\partial x} + v\frac{\partial T}{\partial y}) - M^2 EcPrv^2 \\ - EcPr(2(\frac{\partial u}{\partial x})^2 + 2(\frac{\partial v}{\partial y})^2 + (\frac{\partial v}{\partial x} + \frac{\partial u}{\partial y})^2)\end{aligned} \tag{1.79}$$

$$\nabla^2 \omega = Re(u\frac{\partial \omega}{\partial x} + v\frac{\partial \omega}{\partial y}) + M^2\frac{\partial v}{\partial x} - \frac{Gr}{Re}\frac{\partial T}{\partial x} \tag{1.80}$$

$$\nabla^2 p = -2Re(\frac{\partial v}{\partial x}\frac{\partial u}{\partial y} - \frac{\partial u}{\partial x}\frac{\partial v}{\partial y}) - M^2\frac{\partial v}{\partial y} + \frac{Gr}{Re}\frac{\partial T}{\partial y}. \tag{1.81}$$

In Chapter 4, we will consider the unsteady MHD convection flow equations for the purpose of the stability analysis as time progress. When the convection flow is unsteady, time derivatives of temperature and vorticity are included in the temperature equation (1.79) and the vorticity equation (1.80), respectively. Thus, the two-dimensional unsteady MHD convection flow equations neglecting the viscous dissipation and joule heating terms are given in terms of stream function, temperature, vorticity and pressure as

$$\nabla^2 \psi = -\omega \tag{1.82}$$

$$\nabla^2 T = PrRe(\frac{\partial T}{\partial t} + u\frac{\partial T}{\partial x} + v\frac{\partial T}{\partial y}) \tag{1.83}$$

$$\nabla^2 \omega = Re(\frac{\partial \omega}{\partial t} + u\frac{\partial \omega}{\partial x} + v\frac{\partial \omega}{\partial y}) + M^2\frac{\partial v}{\partial x} - \frac{Gr}{Re}\frac{\partial T}{\partial x} \tag{1.84}$$

$$\nabla^2 p = -2Re(\frac{\partial v}{\partial x}\frac{\partial u}{\partial y} - \frac{\partial u}{\partial x}\frac{\partial v}{\partial y}) - M^2\frac{\partial v}{\partial y} + \frac{Gr}{Re}\frac{\partial T}{\partial y}. \tag{1.85}$$

When the magnetic field is acted on the y-direction, $\boldsymbol{H_0} = (0, 1)$, the Hartmann effect can be seen in the x-component momentum equations instead of y-component. Also, Joule heating term $M^2 EcPrv^2$ is replaced by the $M^2 EcPru^2$ in the temperature equation. Thus, the steady MHD convection flow equations are given in the primitive

variables form as

$$\frac{\partial u}{\partial x}+\frac{\partial v}{\partial y}=0 \tag{1.86}$$

$$Re(u\frac{\partial u}{\partial x}+v\frac{\partial u}{\partial y})=-\frac{\partial p}{\partial x}+\nabla^2 u-M^2u \tag{1.87}$$

$$Re(u\frac{\partial v}{\partial x}+v\frac{\partial v}{\partial y})=-\frac{\partial p}{\partial y}+\nabla^2 v+\frac{Gr}{Re}T \tag{1.88}$$

$$\begin{aligned}\nabla^2 T &= PrRe(u\frac{\partial T}{\partial x}+v\frac{\partial T}{\partial y})-M^2EcPru^2 \\ &\quad -EcPr(2(\frac{\partial u}{\partial x})^2+2(\frac{\partial v}{\partial y})^2+(\frac{\partial v}{\partial x}+\frac{\partial u}{\partial y})^2)\end{aligned} \tag{1.89}$$

which can be similarly expressed in terms of the all fluid variables (u, v, ψ, T, ω, p)

$$\nabla^2 u=-\frac{\partial \omega}{\partial y}\ , \qquad \nabla^2 v=\frac{\partial \omega}{\partial x} \tag{1.90}$$

$$\nabla^2\psi=-\omega \tag{1.91}$$

$$\begin{aligned}\nabla^2 T &= PrRe(u\frac{\partial T}{\partial x}+v\frac{\partial T}{\partial y})-M^2EcPru^2 \\ &\quad -EcPr(2(\frac{\partial u}{\partial x})^2+2(\frac{\partial v}{\partial y})^2+(\frac{\partial v}{\partial x}+\frac{\partial u}{\partial y})^2)\end{aligned} \tag{1.92}$$

$$\nabla^2\omega=Re(u\frac{\partial \omega}{\partial x}+v\frac{\partial \omega}{\partial y})-M^2\frac{\partial u}{\partial y}-\frac{Gr}{Re}\frac{\partial T}{\partial x} \tag{1.93}$$

$$\nabla^2 p=-2Re(\frac{\partial v}{\partial x}\frac{\partial u}{\partial y}-\frac{\partial u}{\partial x}\frac{\partial v}{\partial y})-M^2\frac{\partial u}{\partial x}+\frac{Gr}{Re}\frac{\partial T}{\partial y}\ . \tag{1.94}$$

In both cases, boundary conditions of velocity components, stream function and the temperature are prescribed in the problem. However, the vorticity boundary conditions are not known physically and evaluated from the stream function equation using the finite difference method. The pressure boundary conditions are given (with the physical assumption $\frac{\partial p}{\partial n}=0$) in some cavities [17]. If they are not known, we obtain from the momentum equations using the finite difference method for the space derivatives of pressure and coordinate matrix for the Laplacian and the other space derivatives.

1.5 Full MHD Flow with Magnetic Potential

Full MHD flow equations are the extension of the MHD flow equations in the sense that induction equation is included in terms of the induced magnetic field components

or magnetic potential due to the large values of magnetic Reynolds number.

The unsteady MHD flow is governed by the the Navier-Stokes equations including Lorentz force [52]

$$\nabla \cdot \boldsymbol{u} = 0 \qquad \text{Continuity equation} \tag{1.95}$$

$$\rho(\frac{\partial \boldsymbol{u}}{\partial t} + (\boldsymbol{u} \cdot \nabla)\boldsymbol{u}) = -\nabla p + \rho\nu\nabla^2\boldsymbol{u} + \boldsymbol{J} \times \boldsymbol{B} \qquad \text{Momentum equations} \tag{1.96}$$

coupled with Maxwell's equations of electromagnetics through Ohm's law

$$\nabla \times \boldsymbol{E} = -\frac{\partial \boldsymbol{B}}{\partial t} \qquad \text{Faraday's Law} \tag{1.97}$$

$$\nabla \times \boldsymbol{B} = \mu \boldsymbol{J} \qquad \text{Ampere's Law} \tag{1.98}$$

$$\nabla \cdot \boldsymbol{B} = 0 \qquad \text{Solenoidal nature of } \boldsymbol{B} \tag{1.99}$$

$$\boldsymbol{J} = \sigma(\boldsymbol{E} + \boldsymbol{u} \times \boldsymbol{B}) \qquad \text{Ohm's Law,} \tag{1.100}$$

where ρ, ν, μ and σ are the density, the kinematic viscosity, the magnetic permeability and the electric conductivity of the fluid, respectively. $\boldsymbol{u} = (u, v, 0)$ is the velocity field, p is the pressure of the fluid, $\boldsymbol{B} = (B_x, B_y, 0)$ is the magnetic induction, $\boldsymbol{E}$ is the electric field and $\boldsymbol{J}$ is the electric current density.

Taking the curl of Ohm's law (1.100) and using the Faraday's, and Ampere's laws with the solenoidal nature of $\boldsymbol{B}$, we obtain the induction equation

$$\nabla^2\boldsymbol{B} = \mu\sigma(\frac{\partial \boldsymbol{B}}{\partial t} - \nabla \times (\boldsymbol{u} \times \boldsymbol{B})). \tag{1.101}$$

Thus, the unsteady full MHD flow equations are given in the non-dimensional form

$$\nabla \cdot \boldsymbol{u} = 0 \tag{1.102}$$

$$\frac{1}{Re}\nabla^2\boldsymbol{u} = \frac{\partial \boldsymbol{u}}{\partial t} + (\boldsymbol{u} \cdot \nabla)\boldsymbol{u} + \frac{1}{Re}\nabla p - \frac{M^2}{ReRe_m}(\nabla \times \boldsymbol{B}) \times \boldsymbol{B} \tag{1.103}$$

$$\frac{1}{Re_m}\nabla^2\boldsymbol{B} = \frac{\partial \boldsymbol{B}}{\partial t} - \nabla \times (\boldsymbol{u} \times \boldsymbol{B}) \tag{1.104}$$

by using the dimensionless variables defined as

$$\mathbf{x} \to \mathbf{x}L, \quad t \to tL/U_0, \quad \mathbf{u} \to \mathbf{u}U_0, \quad \mathbf{B} \to \mathbf{B}B_0, \quad p \to p\rho\nu U_0/L$$

where $B_0 = (B_x^2 + B_y^2)^{1/2}$ is the magnitude of the applied magnetic field, L is the characteristic length and U_0 is the characteristic velocity. The dimensionless parameters are the Reynolds number $Re = U_0L/\nu$, the magnetic Reynolds number

$Re_m = U_0 L\sigma\mu$ and the Hartmann number $LB_0\sqrt{\sigma/\rho\nu}$. The physical interpretation of the magnetic Reynolds number is the ratio of the induced magnetic field to applied magnetic field.

Using the similar stream function-vorticity formulation explained in Section 1.2, the full MHD equations can be expressed

$$\nabla^2\psi = -\omega \tag{1.105}$$

$$\frac{1}{Re}\nabla^2\omega = \frac{\partial\omega}{\partial t} + u\frac{\partial\omega}{\partial x} + v\frac{\partial\omega}{\partial y} - \frac{M^2}{ReRe_m}[B_x\frac{\partial}{\partial x}(\frac{\partial B_y}{\partial x} - \frac{\partial B_x}{\partial y}) + B_y\frac{\partial}{\partial y}(\frac{\partial B_y}{\partial x} - \frac{\partial B_x}{\partial y})] \tag{1.106}$$

$$\frac{1}{Re_m}\nabla^2 B_x = \frac{\partial B_x}{\partial t} + u\frac{\partial B_x}{\partial x} + v\frac{\partial B_x}{\partial y} - B_x\frac{\partial u}{\partial x} - B_y\frac{\partial u}{\partial y} \tag{1.107}$$

$$\frac{1}{Re_m}\nabla^2 B_y = \frac{\partial B_y}{\partial t} + u\frac{\partial B_y}{\partial x} + v\frac{\partial B_y}{\partial y} - B_x\frac{\partial v}{\partial x} - B_y\frac{\partial v}{\partial y} \tag{1.108}$$

in terms of velocity components, stream function, vorticity and the induced magnetic field components.

Induction equation (1.104) can be represented by the magnetic potential A instead of the induced magnetic field components to reduce the number of equations. The magnetic potential A is the nonzero third component of the potential vector $\boldsymbol{A} = (0, 0, A)$ defined as [39, 52]

$$\boldsymbol{B} = \nabla \times \boldsymbol{A} \tag{1.109}$$

which is automatically satisfied by the solenoidal nature of $\boldsymbol{B}$, ($\nabla \cdot \boldsymbol{B} = 0$). Substituting $B_x = \dfrac{\partial A}{\partial y}$ and $B_y = -\dfrac{\partial A}{\partial x}$ into the one of the induction equations (1.107)-(1.108), the magnetic potential equation is obtained

$$\frac{1}{Re_m}\nabla^2 A = \frac{\partial A}{\partial t} + u\frac{\partial A}{\partial x} + v\frac{\partial A}{\partial y}. \tag{1.110}$$

Thus, the non-dimensional MHD full equations are given in terms of stream function ψ, vorticity ω, induced magnetic field components (B_x, B_y) and magnetic potential A as

$$\nabla^2\psi = -\omega \tag{1.111}$$

$$\frac{1}{Re_m}\nabla^2 A = \frac{\partial A}{\partial t} + u\frac{\partial A}{\partial x} + v\frac{\partial A}{\partial y} \tag{1.112}$$

$$\frac{1}{Re}\nabla^2\omega = \frac{\partial \omega}{\partial t} + u\frac{\partial \omega}{\partial x} + v\frac{\partial \omega}{\partial y} - \frac{M^2}{ReRe_m}[B_x\frac{\partial}{\partial x}(\frac{\partial B_y}{\partial x} - \frac{\partial B_x}{\partial y}) + B_y\frac{\partial}{\partial y}(\frac{\partial B_y}{\partial x} - \frac{\partial B_x}{\partial y})] \tag{1.113}$$

with the prescribed boundary conditions for the stream function and magnetic potential. The unknown vorticity boundary conditions are obtained from its definition ($\omega = \frac{\partial v}{\partial x} - \frac{\partial u}{\partial y}$) with the help of coordinate matrix $\boldsymbol{F}$.

1.6 Literature Survey

The lid-driven cavity flow governed by the Navier-Stokes equations is a benchmark problem in the computational fluid dynamics (CFD) for the validation of numerical methods. The oldest study of the lid-driven cavity problem is given by Ghia et al. [19]. They applied the implicit multigrid (CSI-MG) method to unsteady Navier-Stokes equations in stream function-vorticity formulation for the high values of Reynolds number in the range of $100 \leq Re \leq 10^4$. Sahin et al. [47] solved both the steady and unsteady Navier-Stokes equations using a novel fully implicit finite volume method. In this procedure, the momentum equation is multiplied by the unit normal vector and integrated around the control volume boundary in order to eliminate the pressure term in the momentum equations. DRBEM is implemented to solve the two-dimensional unsteady Navier-Stokes equations in terms of primitive variables by Choi et. [12]. The fractional step algorithm and Adam-Bashforth is used for the time discretization and the non-linear convective term, respectively. In order to obtain stable solution, the time increment Δt is taken as 10^{-3} with the use of 10 or 20 boundary elements. When the Reynolds number increases up to 400, the computations are required small time increment as $\Delta t = 10^{-4}$ for 20 boundary elements or 0.5×10^{-5} for 40 boundary nodes. Yun-Xin et al. [66] presented the application of the radial basis function (RBF) approximation to the unsteady Navier-Stokes equations in stream function-vorticity formulation. They used different RBFs depending on the parameters α and β to ob-

tain the accurate and efficient numerical results. In [53], the numerical comparison of least square-based finite difference (LSFD) and radial basis function-based finite difference (RBFFD) methods are given in terms of accuracy and efficiency. The two-dimensional incompressible flow in a lid-driven cavity is used for the test problem. In this study, multiquadratic (MQ) RBF is used by taking the shape parameter $c = 0.2$ for the uniformly distributed nodes and $c = 0.03$ for randomly distributed nodes. They indicated that LSFD method is more efficient in terms of the iteration number, whereas the RBFFD method gives more accurate results. Sanyasiraju et al. [49] developed the local RBF to solve Navier-Stokes equations in primitive variables with the use of fractional step algorithm. This method has been validated with the lid-driven cavity problem by taking the MQ RBF. The domain is discretized by 41 non-uniform nodes for $Re = 100$ and 129 non-uniform or uniform points for $Re = 1000$. They observed that non-uniform distribution of nodes gives more accurate results compared to the uniform distribution. Javed et al. [25] presented the numerical solution of two dimensional Navier-Stokes equations in primitive variables form by using the radial basis function in a finite difference mode (RBF-FD). They analyzed both the explicit and implicit RBF-FD schemes with a constant or adaptive shape parameters to make a comparison. They conclude that implicit RBF-FD gives more accurate results with low computational cost than the explicit scheme. Also, the use of adaptive shape parameters gives better results since this scheme leads to use finer nodal points.

Stokes (or creeping) flow refers to fluid motion that is dominated by viscosity and modeled by Navier-Stokes equations neglecting the convective terms due the small values of Reynolds number. In the literature, creeping flow has been studied by several numerical approaches. Smyrlis et al. [54] have transformed 2D Stokes equations into the biharmonic equation using the stream function formulation and solved with the method of fundamental solutions (MFS). Tsai et al. [58] applied MFS to 3D Stokes flow in velocity-vorticity formulation. The method of fundamental solution for 2D Stokes flow in cavities have been presented in [4, 11, 62]. Young et al. [64] extended MFS solution to 2D irregular geometry and 3D Stokes flows in terms of all field variables. In these studies the effects of number of source points in MFS and their locations on the numerical accuracy have been discussed. The behavior of the Stokes flow in cavities is also analyzed by using the dual reciprocity boundary

element method (DRBEM) in [15, 65]. Eldho et al. [15] obtained the numerical results from the velocity-vorticity formulation of the Navier-Stokes equations by taking $Re = 0$ and $Re = 1$ (Stokes approximation). They used 11×11 and 21×21 uniform meshes. In [65], the compactly-supported, positive definite radial basis function approximation is used for the approximation of the non-linear terms. The boundaries of the lid-driven square cavity and circular cavity were discretized by 40 and 80 boundary nodes related to 21×21 and 1600 RBF collocation points, respectively. The RBF approximation have been applied to Stokes flow equations in the velocity-vorticity formulation by Young et al. [63]. They used the multiquadratic RBF for three numerical examples as lid-driven square and circular cavities in 2D, and cubic cavity in 3D. Kutanaei et al. [55] considered 2D Stokes flow in a circular cavity using the mesh-free local RBF based differential quadrature (RBF-DQ). In this study, multiquadratic RBF is taken with the shape parameter $c = 0.12$. Bustamante et al. [9] utilized the global method of approximate particular solutions (MAPS) to Stokes flow in a lid-driven cavity and backward-facing step channel. They observed that the proposed MAPS provides stable and accurate results for the wide range of shape parameters. Kolodziej et al. [30] carried the method of fundamental solutions (MFS) and the radial basis functions for solving creeping flow in a wavy channel. In this method, homogeneous solution of stream function-vorticity formulation is obtained by MFS and particular solution is approximated by the RBF with the use of inverse multiquadarics. The effect of the wavy channel on the Stokes flow behavior was analyzed for different amplitudes of corrugation by taking $Re = 0$ in the Navier-Stokes equations.

An externally applied magnetic field affects the flow behavior when the fluid is electrically conducting. Yosinobu et al. [61] considered the two-dimensional Stokes flow of an electrically conducting fluid past a cylinder in the presence of uniform magnetic field. They found the expansion formula for the drag in terms of Hartmann number. Sellier et al. [50] gave an analytical approach for solving 2D MHD Stokes flow produced by the rigid body motion of a solid particle.

The magnetic field in the pipe-axis direction produces the electric potential which can be made use of in fusion blanket and MHD generators. Layton et al. [31] performed the error and stability analysis of MHD flow with electric potential . In the numerical computations, they used the software package FreeFEM++ for the Hartman number

20 and 200. In [28], three dimensional liquid metal magnetohydrodynamic flow in a suddenly contracting duct under a uniform magnetic field. The commercial software CFX code is used to obtain numerical results in terms of velocity, pressure distribution, electric potential and current by taking the Hartmann number as 300 and 1000 with fixed Reynolds number. It is observed that fluid recirculation occurs with lower electric potential after the sharp edge of the contraction. Tezer-Sezgin et al. [56] applied the DRBEM for solving the MHD flow equations in terms of stream function, vorticity and electric potential for several values of Hartmann number ranging from $20 \leq Ha \leq 200$ with fixed Stuart number $N = 16$. They found that electric potential has the same behavior of streamlines.

Interaction between the convection flow and the magnetic field has been studied by many researchers. At most of this studies, induced magnetic field, Joule heating and viscous dissipation effect are neglected. Rudraiah et al. [46] studied unsteady natural convection flow in a rectangular cavity heated from the right wall in the presence of vertical magnetic field. A modified Alternating Direction Implicit (ADI) method and Successive Line Over Relaxation (SLOR) method have been applied to the stream function, vorticity and temperature equations for several values of Hartmann number $(0 \leq Ha \leq 100)$ and Grashof number $(2 \times 10^4 \leq Gr \leq 2 \times 10^6)$ with fixed Prandtl number $Pr = 0.733$. In [5] the two-dimensional steady natural convection flow in a horizontal shallow cavity under the effect of a vertical magnetic field is investigated by using the method of matched asymptotic expansions for the analytical solution and finite volume technique for the numerical results. They found that analytical results are in well agreement with the numerical results for different values of Rayleigh, Prandtl and Hartmann numbers. Colaço et al. [13] used the radial basis function approximation to solve the stream function, temperature equations of the MHD convection flow in a square cavity under the impact of magnetic field in the horizontal direction. Computations are carried out for several Hartmann number and Grashof number at fixed $Pr = 0.71$ by using multiquadratic RBF. The numerical results obtained by the RBF approximation and the finite volume method are compared in terms of computational time. They concluded that RBF approximation gives an accurate result with a low computational cost. The effect of horizontal magnetic field on the unsteady natural convection flow in a square cavity is analyzed by Alsoy-Akgün

et al. [3]. They imposed the dual reciprocity boundary element (DRBEM) and the differential quadrature method to the modified Helmholtz equations transforming from the vorticity and temperature equations. In this study, flow and temperature behaviors are presented for $10^3 \leq Ra \leq 10^6$ and $0 \leq Ha \leq 300$ at fixed $Pr = 1$. DRBEM and DQM results are compared in terms od accuracy and computational time. It is observed that DQM requires less computational time, although two methods give same accuracy. Alchaar et al. [2] examined the unsteady natural convection in a shallow cavity under a magnetic field inclined with angle. The finite difference method is used to solve the governing equations in terms of velocity, stream function, vorticity and temperature for the wide range of the Hartmann, Rayleigh and Prandtl numbers with fixed aspect ratio of the cavity $A = 6$. They showed that the number of convection rolls increases when the magnetic field is applied in the vertical direction. The increase in the Prandtl number increases the heat transfer. Al-Najem et al. [1] used the alternating direction implicit (ADI) scheme to analyze natural convection flow inside tilted enclosures in the presence of a magnetic field. They observed that the effect of the magnetic field on the heat transfer is negligible for small inclination angles. Lo et al. [32] studied MHD free convection flow in a rectangular enclosure. The numerical results are obtained for different values of Hartmann number $(0 \leq Ha \leq 100)$, Grashof number $(10^4 \leq Gr \leq 10^5)$, Prandtl number $(0.01 \leq Pr \leq 10)$ and the aspect ratio $A = 1 - 3$ by using DQM. It is found that Nusselt number increases as Prandtl number increases. In the above studies, it is concluded that the rate of the convective heat transfer decreases, when the magnetic field intensity increases or Grashof number decreases.

The effect of the magnetic field on mixed convection flow is also analyzed by researchers. Kefayati et al. [27] solved MHD mixed convection in a lid-driven cavity for linearly heated wall using the Lattice Boltzmann method (LBM). Numerical results are obtained for several values of the Hartman and Richardson numbers varying from $Ha = 0$ to 100 and $Ri = 0.01$ to 100, respectively, with fixed $Re = 100$ and $Pr = 0.71$ in the case of applied magnetic field in x- or y-direction. They observed that the increase in the Richardson number increases the heat transfer. In [48], the Lattice Boltzmann method is also employed to the mixed convection flow in a two sided lid-driven cavity under the effect of horizontal magnetic field. The bottom and the top

wall moves in same direction or opposite direction. In the numerical computations, the ranges of the non-dimensional parameters are $Ha = 0 - 10$, $Ri = 0.01 - 100$ with fixed $Pr = 0.71$. It is concluded that when the Hartmann number increases, the new circulations on the streamlines occur for both cases.

MHD flow and heat transfer from irregular surfaces have attracted the considerable interest of many researchers due to the engineering applications such as flat-plate solar collectors, micro-electronic devices, geophysical applications, cooling system etc. Gajbhiye et al. [17] presented the numerical solution of the MHD flow and heat transfer in a rectangular constricted enclosure heated from the below by using ANUPARAVAHA which is a finite volume solver. The magnetic field is acted in the x- or y-direction. They investigated the effects of the constriction ratios $(0\% \leq C \leq 50\%)$ and Rayleigh number $(1500 \leq C \leq 10000)$ on MHD convection flow for fixed $Pr = 0.01$ and the aspect ratio $A = 4$. It is observed that the velocity is suppressed as the Hartmann number or constriction ratio increases. The direction of the magnetic field does not significantly change the flow behavior. In [36], MHD mixed convection flow in a lid-driven cavity with wavy bottom surface is analyzed. The numerical results are given for several values of the Hartmann number, Reynolds number and the number of the undulations of the cavity by using Galerkin finite element method (FEM). It is found that the average Nusselt number decreases with increasing the Hartmann number, whereas increases with increasing the number of undulations and Reynolds number. Galerkin FEM is also applied to MHD convection flow in a triangular wavy channel by Parvin et al. [41]. The numerical solutions are depicted in terms of streamlines, isotherms and local Nusselt number for several values of Reynolds, Grashof and Prandtl numbers with fixed $Ha = 50$. They observed that streamlines spreads in whole channel with increasing Reynolds number and decreasing Prandtl number.

In the above studies, viscous dissipation term has been neglected in the energy equation. Viscous dissipation represents a source of heat because of the friction between the fluid particles. It is characterized by Eckert number. The effect of viscous dissipation was first studied by Gebhart [18] by using a perturbation method. Later, Hitesh [22] analyzed the heat transfer of the boundary layer flow over stretching plate with viscous dissipation effect in the presence of magnetic field. The effect of vis-

cous dissipation has been considered on a natural convection flow along a heated vertical plate by Pantokratoras [40]. The finite difference method (FDM) is applied for solving the boundary layer equations. They observed that viscous dissipation assists the upward flow and opposes the downward flow. Kishore et al. [29] and Nyabuto et al. [38] have also investigated the effects of viscous dissipation on MHD natural convection flow by using the FDM. They showed that temperature increases with increasing values of Eckert number. Viscous dissipation in slow flow (creeping flow) is considered in [26] which indicated the effect of viscous dissipation for highly viscous fluids having Brinkman number of order unity. Vasudeviah et al. [59] also studied convective heat transfer for Stokes flow together with viscous dissipation. The perturbation method is imposed to the stream function-temperature formulation.

In some MHD flow problems, magnetic induction is taken into consideration by taking large magnetic Reynolds number. Navarro et al. [37] have used the generalized Peaceman and Rachford alternating-direction implicit (ADI) scheme to solve the equations in the stream function-vorticity formulation. They presented the behavior of the MHD flow with low Reynolds and magnetic Reynolds numbers. Bozkaya et al. [7] have applied a dual reciprocity boundary element method (DRBEM) to full MHD flow equations with the use of an implicit backward time integration scheme for the time derivatives. The numerical results are obtained for several values of Reynolds, magnetic Reynolds and Hartmann numbers and shown in terms of stream function, vorticity, current density and magnetic induction contours.

Sharp [51] has considered the stability analysis of boundary element method (BEM) for the diffusion equation. It is concluded that the decrease in the time step causes the quality of the approximation to deteriorate which indicates the state of the instability. In [43], the numerical stability of BEM for one-dimensional advection-diffusion problems is studied by Peratta et al. They observed that as the Courant and Peclet numbers decrease, the stability characteristics of the method increases. Ramesh et al. [44] have performed the stability analysis of the multiple reciprocity method for transient heat conduction through an eigenvalue decomposition of the system matrix. They showed that the stability analysis of the direct and indirect boundary integral formulations are identical, and the multiple reciprocity method is stable only for appropriately taken large time steps.

In this thesis, the numerical solutions of the MHD Stokes and the MHD incompressible flow equations in terms of all the fluid variables are obtained using RBF approximation which are not available in the literature. In the above studies, viscous dissipation effect on both the MHD Stokes and the MHD convection flows is considered by using the FDM or perturbation techniques without giving the behaviors of fluid variables. In this thesis, we cover the case of MHD flows of viscous dissipative fluids by using the RBF approximation. Finally, the numerical stability analysis of the RBF approximation for the unsteady MHD flow problems is a new study given in this thesis.

1.7 Plan of the Thesis

In Chapter 2, The three numerical techniques as the radial basis function (RBF) approximation, the dual reciprocity boundary element method (DRBEM) and the direct interpolation boundary element method (DIBEM) are explained on the Poisson type equations. RBF approximation is also imposed to the time dependent equations. For the time discretization explicit Euler method is used .

Chapter 3 presents the applications of the RBF approximation, the DRBEM and the DIBEM to some fluid dynamics problems. First of all, these methods are imposed to solve MHD Stokes in a lid-driven cavity to make a comparison. Then, the other test problems for the MHD Stokes and the MHD incompressible flows are solved by using RBF approximation. Finally, the method is applied to the solution of the MHD convection flow with viscous dissipation.

In Chapter 4, we present the RBF solutions of the unsteady Navier-Stokes equations, time dependent MHD convection flow and full MHD flow problems and also perform the stability analysis in terms of the maximum eigenvalues of the coefficient matrices containing the time increment, relaxation parameters and the problem variables.

In Chapter 5, we summarize the overall important numerical results obtained in the thesis.

1.8 Contributions in the Thesis

In the thesis, we first analyze the behavior of the Stokes flow under the impact of the uniform magnetic field applied in different directions. The MHD Stokes flow equations in terms of all the fluid variables such as velocity components, stream function, vorticity and pressure are solved by using the RBF approximation, the DRBEM and the DIBEM and compared in terms of computational cost. The pressure equation which is not given physically is derived and its unknown boundary conditions are obtained from the momentum equations by using the finite difference scheme for the pressure gradients and the RBF coordinate matrix for the space derivatives. This enables to include the solution the pressure behaviors with respect to the variations of problem variables. Also, the solution of the MHD flow generating electric potential due to the magnetic field in the pipe-axis direction is obtained using the RBF approximation although the flow is two-dimensional. The RBF solution of the MHD flow is given in its complete set of physical unknowns which constitutes one of the original contribution in the thesis.

In the second part of the thesis, the RBF approximation is generalized to solve the convection flow with or without Stokes approximation in the presence of a magnetic field. The effect of viscous dissipation, which is generally neglected in the literature, is also studied together with the buoyancy force and magnetic field effects.

Finally, the RBF approximation solution of transient full MHD flow equations adopting magnetic potential is achieved at steady-state as well as at transient levels. Thus, the stability analysis of the RBF approximation of unsteady MHD flow problems is carried which is a new contribution to the transient MHD flow in pipes.

CHAPTER 2

THE RBF APPROXIMATION, THE DRBEM AND THE DIBEM FORMULATIONS

The radial basis function approximation (RBF) is based on the meshless method and is an attractive technique for the solution of partial differential equations (PDEs) even in complex irregular geometries due to the mesh independence and flexibility in programming. In this method, particular solution, which is approximated with RBFs depending on the distance between the points to satisfy both differential equation and boundary conditions, becomes also the solution of the equation. The choice of radial basis function is important for the accuracy and convergence in the approximation.

The boundary element method (BEM) is an alternative numerical technique for solving PDEs. The main idea of this method is to transform the differential equation defined in the domain into an integral equation defined on the boundary. Thus, the BEM reduces the dimension of the problem and the computational cost. When this technique is applied to the inhomogeneous PDE, the integral equation contains the domain integral. In this case, the advantage of BEM is lost.

The dual reciprocity boundary element method (DRBEM) avoids this domain integral problem. In this method, all the terms except Laplacian are treated as inhomogeneity which is approximated by RBFs. These radial basis functions are related to particular solution of the differential equation through the Laplace operator. Then, the boundary element procedure is applied to both sides of the equation with the fundamental solution of Laplace equation.

The direct interpolation boundary element method (DIBEM) is another numerical

technique to transform the domain integral due to the inhomogeneity of the differential equation into the boundary integral directly. In this method, the complete kernel of the domain integral is interpolated directly by using radial basis function.

In this Chapter, the basic theories of the radial basis function approximation, the dual reciprocity boundary element method and the direct interpolation boundary element method are given. We first derive the RBF formulation for the general boundary value problem $Lu = f$ in Section 2.1. Then, the method is extended to Poisson type equation with the inhomogeneity including space derivatives of unknown function in Section 2.1.1. The application of the RBF to time dependent Poisson type equation results in a discretized system of ordinary differential equations as explained in Section 2.1.2. Then, the Euler method is used for the discretization of the time derivative. The DRBEM and the DIBEM are explained for Poisson type equations in Sections 2.2 and 2.3, respectively.

2.1 The Radial Basis Function (RBF) Approximation

In this Section, the radial basis function approximation is going to be described on the Poisson equation as in [8, 10]. Let us consider a general boundary value problem

$$Lu(x, y) = f(x, y), \qquad (x, y) \in \Omega \tag{2.1}$$

$$Bu(x, y) = g(x, y), \qquad (x, y) \in \partial\Omega \tag{2.2}$$

where L and B are linear partial differential and boundary operators, respectively, f and g are known functions in the domain Ω and the boundary $\partial\Omega$, respectively.

In this method, the inhomogeneity in the equation (2.1) is a function $f(x, y)$ of space variables and is approximated by a finite series of RBFs $\{\varphi_j\}$ as

$$f(x, y) \simeq \sum_{j=1}^{n} a_j \varphi_j(r), \quad (x, y) \in \Omega \tag{2.3}$$

where $r = ((x - x_j)^2 + (y - y_j)^2)^{1/2}$ is the Euclidean distance and n is the number of unknown coefficients $a_j's$.

Then, we can write the approximate particular solution u_p as

$$u_p(x,y) = \sum_{j=1}^{n} a_j \Psi_j(r) \tag{2.4}$$

where $\{\Psi_j\}$ is obtained by the back substitution through the differential equation $L\Psi_j(r) = \varphi_j(r)$ and u_p is forced to satisfy the boundary condition in (2.2), i.e,

$$\sum_{j=1}^{n} a_j B\Psi_j(r) = g(x,y), \qquad (x,y) \in \partial\Omega \quad . \tag{2.5}$$

Since the approximate particular solution u_p satisfies both the differential equation and the boundary condition, it also becomes the approximate solution u of the equation (2.1). The undetermined coefficients a_j's in the approximation (2.4) are obtained from the collocation method. Taking arbitrarily $n = N_b + N_i$ points (x_k, y_k) on the boundary and the interior of the domain, we have two linear systems

$$\sum_{j=1}^{n} a_j B\Psi_j(r_k) = g(x_k, y_k), \qquad 1 \le k \le N_b \tag{2.6}$$

and

$$\sum_{j=1}^{n} a_j \varphi_j(r_k) = f(x_k, y_k), \qquad 1 + N_b \le k \le n \tag{2.7}$$

which are combined to give one linear system

$$\tilde{\boldsymbol{A}}\boldsymbol{a} = \boldsymbol{d} \tag{2.8}$$

for the solution vector $\boldsymbol{a}$=$(a_1 \cdots a_n)^T$.

The coefficient matrix $\tilde{\boldsymbol{A}}$ and the right hand side vector $\boldsymbol{d}$ are given as

$$\tilde{\boldsymbol{A}} = \begin{bmatrix} B\Psi_1(r_1) & B\Psi_2(r_1) & \cdots & B\Psi_n(r_1) \\ \vdots & \vdots & \ddots & \vdots \\ B\Psi_1(r_{N_b}) & B\Psi_2(r_{N_b}) & \cdots & B\Psi_n(r_{N_b}) \\ \varphi_1(r_{N_b+1}) & \varphi_2(r_{N_b+1}) & \cdots & \varphi_n(r_{N_b+1}) \\ \vdots & \vdots & \ddots & \vdots \\ \varphi_1(r_n) & \varphi_2(r_n) & \cdots & \varphi_n(r_n) \end{bmatrix}_{n\times n}, \boldsymbol{d} = \begin{bmatrix} g(x_1, y_1) \\ \vdots \\ g(x_{N_b}, y_{N_b}) \\ f(x_{N_b+1}, y_{N_b+1}) \\ \vdots \\ f(x_n, y_n) \end{bmatrix}_{n\times 1} .$$

The solution $\boldsymbol{a} = \tilde{\boldsymbol{A}}^{-1}\boldsymbol{d}$ of the system (2.8) gives the coefficients a_j, $1 \leq j \leq n$. Substituting the vector $\boldsymbol{a}$ into the equation (2.4) we obtain the approximate solution (particular solution also) as

$$\boldsymbol{u} = \tilde{\boldsymbol{U}}\tilde{\boldsymbol{A}}^{-1}\boldsymbol{d} \tag{2.9}$$

where $\tilde{U}_{ij} = \Psi_j(r_i), \quad 1 \leq i, j \leq n.$

Several types of RBFs, $\varphi_j(r)$, $j = 1, \ldots, n$ as polynomial, multiquadratics, inverse multiquadratics, conical, Gaussian, polyharmonic splines can be used in the approximation of right hand side function as in (2.3) but the appropriate choice of RBF is important for obtaining the nonsingular matrix $\tilde{\boldsymbol{A}}$ and for the accuracy of the approximation.

In Chapter 3, all of the system of PDEs contain the Laplace operator as the dominant term. Thus, we apply the RBF approximation to the Poisson's type equation $\nabla^2 u = f$. That is, $L = \nabla^2$ is the Laplace operator. The relation between the radial basis functions (φ, Ψ) for the approximation of the function f and the solution u are obtained as follows.

Let us take a polynomial RBF of degree m as $\varphi(r) = 1 + r + r^2 + \cdots + r^m$ satisfying the equation

$$\nabla^2 \Psi = \varphi \tag{2.10}$$

which can be written in a polar coordinates for the axisymmetric case

$$\frac{1}{r}\frac{\partial}{\partial r}\left(r\frac{\partial \Psi}{\partial r}\right) = 1 + r + r^2 + \cdots + r^m. \tag{2.11}$$

Integration backwards gives

$$\Psi = \frac{r^2}{4} + \frac{r^3}{9} + \cdots + \frac{r^{m+2}}{(m+2)^2}. \tag{2.12}$$

The list of different types of RBFs and related approximate solutions for $L = \nabla^2$ are given in Table 2.1, [8, 10].

	φ	Ψ
Polynomial	$1 + r + r^2 + \cdots + r^m$	$\frac{r^2}{4} + \frac{r^3}{9} + \cdots + \frac{r^{m+2}}{(m+2)^2}$
Multiquadratics	$\sqrt{r^2 + c^2}$ c: shape parameter	$\frac{1}{9}(4c^2 + r^2)\sqrt{r^2 + c^2}$ $-\frac{c^3}{3} ln(c^2 + c\sqrt{r^2 + c^2})$
Inverse Multiquadratics	$1/\sqrt{r^2 + c^2}$	$-c\ ln(c^2 + c\sqrt{r^2 + c^2})$ $+\sqrt{r^2 + c^2}$
Conical	r^{2m-1} $m = 1, 2, 3, \ldots$	$\frac{r^{2m+1}}{(2m+1)^2}$
Polyharmonic Splines	$r^{2m} lnr$	$\frac{r^{2m+2} lnr}{4(m+1)^2} - \frac{r^{2m+2}}{4(m+1)^3}$
Gaussian	$e^{-c^2 r^2}$	$\frac{1}{4c^2} E_1(c^2 r^2)$

Table 2.1: Radial basis functions for $\nabla^2 \Psi = \varphi$.

In Table 2.1, E_1 is the exponential integral defined by $E_1(x) = \int_x^\infty \frac{e^{-t}}{t} dt$.

2.1.1 The RBF Approximation for the Equation $\nabla^2 u = f(x, y, u_x, u_y)$

We consider the two-dimensional Poisson type equation where the right hand side function includes the space derivatives of the problem variable

$$\nabla^2 u = f(x, y, u_x, u_y) \ \text{ in } \ \Omega \tag{2.13}$$

where

$$f(x, y, u_x, u_y) = \frac{\partial u}{\partial x} + \frac{\partial u}{\partial y}. \tag{2.14}$$

The boundary condition $Bu(x, y) = g(x, y)$ on $\partial\Omega$ is also supplied. Approximating the right hand side function as in (2.3)

$$f(x, y, u_x, u_y) = \sum_{j=1}^{n} a_j \varphi_j(r), \quad (x, y) \in \Omega \tag{2.15}$$

results in a system

$$\boldsymbol{f} = \boldsymbol{F}\boldsymbol{a} \tag{2.16}$$

where $\boldsymbol{F}$ is the coordinate matrix constructed by $F_{ij} = \varphi_j(r_i), \quad 1 \leq i, j \leq N_b + N_i$ and $\boldsymbol{a}$ contains the undetermined coefficients in the approximation of $\boldsymbol{f}$.

A similar approximation can be used for the problem variable u

$$u(x, y) = \sum_{j=1}^{n} \tilde{\beta}_j \varphi_j(r) \tag{2.17}$$

giving the system

$$\boldsymbol{u} = \boldsymbol{F}\tilde{\boldsymbol{\beta}} \tag{2.18}$$

where $\tilde{\boldsymbol{\beta}} \neq \boldsymbol{a}$, and $\tilde{\boldsymbol{\beta}}$ contains the undetermined coefficients b_j's in the approximation of the solution $\boldsymbol{u}$.

Differentiation of the equation (2.18) with respect to x and y gives

$$\frac{\partial \boldsymbol{u}}{\partial x} = \frac{\partial \boldsymbol{F}}{\partial x}\tilde{\boldsymbol{\beta}} \qquad \text{and} \qquad \frac{\partial \boldsymbol{u}}{\partial y} = \frac{\partial \boldsymbol{F}}{\partial y}\tilde{\boldsymbol{\beta}}, \tag{2.19}$$

respectively.

The vector $\tilde{\boldsymbol{\beta}}$ is obtained from (2.18) by inverting the nonsingular coordinate matrix $\boldsymbol{F}$ as

$$\tilde{\boldsymbol{\beta}} = \boldsymbol{F}^{-1}\boldsymbol{u} \tag{2.20}$$

and substituting into (2.19) to obtain the space derivatives of $\boldsymbol{u}$ as vectors

$$\frac{\partial \boldsymbol{u}}{\partial x} = \frac{\partial \boldsymbol{F}}{\partial x}\boldsymbol{F}^{-1}\boldsymbol{u} \qquad \text{and} \qquad \frac{\partial \boldsymbol{u}}{\partial y} = \frac{\partial \boldsymbol{F}}{\partial y}\boldsymbol{F}^{-1}\boldsymbol{u}. \tag{2.21}$$

Then, the inhomogeneity function in (2.14) is expressed as a system containing the unknown vector $\boldsymbol{u}$

$$\boldsymbol{f} = \frac{\partial \boldsymbol{F}}{\partial x}\boldsymbol{F}^{-1}\boldsymbol{u} + \frac{\partial \boldsymbol{F}}{\partial y}\boldsymbol{F}^{-1}\boldsymbol{u}. \tag{2.22}$$

The boundary condition is also discretized as in (2.6)

$$\sum_{j=1}^{n} a_j B\Psi_j(r_k) = g(x_k, y_k), \qquad 1 \leq k \leq N_b \tag{2.23}$$

and added to the discretized system (2.15) at the point r_k, for $1 + N_b \leq k \leq n$ which is

$$\sum_{j=1}^{n} a_j \varphi_j(r_k) = f(x_k, y_k, u_x|_{(x_k,y_k)}, u_y|_{(x_k,y_k)}), \quad 1 + N_b \leq k \leq n. \tag{2.24}$$

Now, the system of equations (2.23) and (2.24) constitute the final system of equations

$$\tilde{\boldsymbol{A}}\boldsymbol{a} = \boldsymbol{d} \tag{2.25}$$

and then

$$\boldsymbol{u} = \tilde{\boldsymbol{U}}\tilde{\boldsymbol{A}}^{-1}\boldsymbol{d} \tag{2.26}$$

to be solved for the solution $\boldsymbol{u}$. Thus, the linear system of equations (2.26) is solved iteratively by taking the lower part of the vector $\boldsymbol{d}$ as

$$d_j = f_j, \qquad N_b \leq j \leq N_b + N_i \tag{2.27}$$

since f_j's contain unknown solution values u_j's.

2.1.2 The RBF Approximation for the Equation $\nabla^2 u = f(x, y, t, \dot{u})$

Now, the RBF approximation will be extended to the time dependent Poisson type equations

$$\nabla^2 u = \underbrace{\frac{\partial u}{\partial t} + \tilde{f}(x, y)}_{f(x,y,t,\dot{u})} \tag{2.28}$$

where $\dot{u}$ denotes the time derivative of u.

The application of the RBF to the equation (2.28) gives the discretized system in matrix-vector form as

$$\boldsymbol{u} = \tilde{\boldsymbol{U}}\tilde{\boldsymbol{A}}^{-1}\boldsymbol{d} \tag{2.29}$$

where the vector $\boldsymbol{d} = (\boldsymbol{u_{bc}} \;\; \bar{\boldsymbol{f}})^{\boldsymbol{T}}$, $\boldsymbol{u_{bc}}$ is the boundary values of the solution vector $\boldsymbol{u}$, and the vector $\bar{\boldsymbol{f}}$ is of length N_i and contains the time derivative of $\boldsymbol{u}$.

Let us define the coefficient matrix $\boldsymbol{R} = \tilde{\boldsymbol{U}}\tilde{\boldsymbol{A}}^{-1}$ which can be divided into two submatrices $\boldsymbol{R_1}$ of size $n \times N_b$ and $\boldsymbol{R_2}$ of size $n \times N_i$ as $\boldsymbol{R} = [\boldsymbol{R_1} \;\; \boldsymbol{R_2}]$. Thus, the system (2.29) is rearranged as

$$\begin{aligned} \boldsymbol{u} &= \begin{bmatrix} \boldsymbol{R_1} & \boldsymbol{R_2} \end{bmatrix} \begin{bmatrix} \boldsymbol{u_{bc}} \\ \bar{\boldsymbol{f}} \end{bmatrix} \\ &= \boldsymbol{R_1 u_{bc}} + \boldsymbol{R_2}\bar{\boldsymbol{f}} \end{aligned} \tag{2.30}$$

where $\bar{\boldsymbol{f}}$ is evaluated only at the interior points. To include the contribution from the boundary points to the vector $\bar{\boldsymbol{f}}$, the last term of the system (2.30) is extended by using an enlarged matrix $\boldsymbol{K} = [\underset{n\times N_b}{\boldsymbol{0}} \;\; \underset{n\times N_i}{\boldsymbol{R_2}}]$ and an enlarged vector $\boldsymbol{f} = \{f_i\} = \left\{\tilde{f}_i + \dfrac{\partial u_i}{\partial t}\right\}, 1 \leq i \leq N_b + N_i$.

Thus, the new enlarged system is given as

$$\begin{aligned} \boldsymbol{u} &= \boldsymbol{R_1 u_{bc}} + \boldsymbol{K f} \\ &= \boldsymbol{g_u} + \boldsymbol{K}(\dot{\boldsymbol{u}} + \tilde{\boldsymbol{f}}) \end{aligned} \tag{2.31}$$

where the vectors $\boldsymbol{g_u} = \boldsymbol{R_1 u_{bc}}$ and $\dot{\boldsymbol{u}} = \{\partial u_i/\partial t\}, \quad i = 1, 2, \ldots, N_b + N_i$ are of the size $N_b + N_i$.

The solution of the system (2.31) will be obtained at transient time levels and at the steady-state by using the Euler method for the time discretization.

The Euler method is the first order, explicit time integration method and is derived from Taylor series expansion.

The Taylor series expansion of $u(x, y, t_{m+1})$ around $t_m = m\Delta t$ is written as

$$u^{m+1} = u^m + \Delta t \frac{\partial u}{\partial t}\bigg|_m + \frac{\Delta t^2}{2!}\frac{\partial^2 u}{\partial t^2}\bigg|_m + \dots \tag{2.32}$$

where Δt is the time increment and 'm' indicates the time level.

Taking terms of order $(\Delta t)^2$ we have

$$\frac{\partial u}{\partial t}\bigg|_m = \frac{u^{m+1} - u^m}{\Delta t} + \mathcal{O}(\Delta t) \tag{2.33}$$

which is called the Euler method (forward difference for the first order derivative).

Substitution of the first order approximation (2.33) in the equation (2.31) results in a matrix-vector equation

$$\boldsymbol{u} = \boldsymbol{g}_{\boldsymbol{u}}^m + \boldsymbol{K}\left(\frac{\boldsymbol{u}^{m+1} - \boldsymbol{u}^m}{\Delta t}\right) + \boldsymbol{K}\tilde{\boldsymbol{f}}^m. \tag{2.34}$$

We use relaxation parameter α_u for accelerating the convergence for the iterations to reach steady-state as

$$\boldsymbol{u} = (1 - \alpha_u)\boldsymbol{u}^m + \alpha_u \boldsymbol{u}^{m+1}, \;\; 0 \leq \alpha_u \leq 1. \tag{2.35}$$

This will lead to the system of equations

$$\boldsymbol{S1}\boldsymbol{u}^{m+1} = \boldsymbol{g}_{\boldsymbol{u}}^m - \boldsymbol{S2}\boldsymbol{u}^m + \boldsymbol{K}\tilde{\boldsymbol{f}}^m \tag{2.36}$$

where $\boldsymbol{S1} = \alpha_u \boldsymbol{I} - \frac{1}{\Delta t}\boldsymbol{K}$ and $\boldsymbol{S2} = (1 - \alpha_u)\boldsymbol{I} + \frac{1}{\Delta t}\boldsymbol{K}$.

Since the Euler method is an explicit method, stability problems are occurred for large Δt values. We will consider the stability analysis in Chapter 4 for the solutions of time dependent MHD problems depending on the choice of Δt, the relaxation parameter α_u and other problem parameters.

2.2 The Dual Reciprocity Boundary Element Method (DRBEM)

In this Section, boundary integral formulation for Poisson type equations is given, and then the dual reciprocity boundary element method is explained as in [42]. The

DRBEM transforms the domain integral due to the inhomogeneity in the BEM equation into the boundary integral.

Consider the Poisson equation in two-dimensions

$$\nabla^2 u = b(x, y), \qquad (x, y) \in \Omega \tag{2.37}$$

with Dirichlet and Neumann boundary conditions (Figure 2.1)

$$u(x, y) = \overline{u}(x, y), \qquad (x, y) \in \Gamma_1 \tag{2.38}$$

$$q(x, y) = \frac{\partial u}{\partial n} = \overline{q}(x, y), \qquad (x, y) \in \Gamma_2 \tag{2.39}$$

where n is the unit outward normal to the boundary $\Gamma = \Gamma_1 + \Gamma_2$ of the domain Ω, $b(x, y)$, $\overline{u}(x, y)$ and $\overline{q}(x, y)$ are given functions.

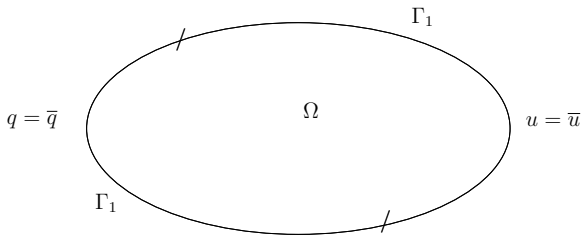

Figure 2.1: The geometry of the domain and boundary conditions

The boundary conditions can be defined as

$$u = \begin{cases} \overline{u} & \text{on } \Gamma_1 \\ \tilde{u} & \text{on } \Gamma_2 \end{cases}, \qquad q = \begin{cases} \tilde{q} & \text{on } \Gamma_1 \\ \overline{q} & \text{on } \Gamma_2 \end{cases} \tag{2.40}$$

where $\tilde{u}$ and $\tilde{q}$ denote unknown values.

Now, the weighted residual statement for the equation (2.37) is obtained by multiplying the equation with a weight function u^* and integrating over the region Ω as

$$\int_\Omega (\nabla^2 u - b) u^* \, d\Omega = 0 \tag{2.41}$$

where $u^* = \frac{1}{2\pi}\ln(\frac{1}{r})$ is the fundamental solution of the Laplace equation and satisfies

$$\nabla^2 u^* = -\Delta(x - x_i) = -\Delta^i. \tag{2.42}$$

Here, Δ^i is the Dirac delta function and defined as

$$\Delta^i = \begin{cases} \infty & \text{if } x = x_i \\ 0 & \text{if } x \neq x_i \end{cases} \tag{2.43}$$

and

$$\int_\Omega f(x)\Delta^i d\Omega = \begin{cases} f(x_i) & \text{if } x_i \in \Omega \\ 0 & \text{if } x_i \notin \Omega \end{cases} \tag{2.44}$$

where $f(x)$ is a continuous function at x_i.

Applying the Green's first identity two times to the equation (2.41) and substituting the boundary conditions given in (2.40) , we obtain

$$\int_\Omega u\nabla^2 u^* d\Omega - \int_\Omega bu^* d\Omega = -\int_{\Gamma_1} \tilde{q}u^* d\Gamma_1 - \int_{\Gamma_2} \overline{q}u^* d\Gamma_2 + \int_{\Gamma_1} \overline{u}q^* d\Gamma_1 + \int_{\Gamma_2} \tilde{u}q^* d\Gamma_2 \tag{2.45}$$

where $q^* = \dfrac{\partial u^*}{\partial n}$ is the normal derivative of u^*.

Using the property (2.44) of Dirac delta function, the equation (2.45) becomes

$$c_i u_i + \int_\Omega bu^* d\Omega = \int_{\Gamma_1} \tilde{q}u^* d\Gamma_1 + \int_{\Gamma_2} \overline{q}u^* d\Gamma_2 - \int_{\Gamma_1} \overline{u}q^* d\Gamma_1 - \int_{\Gamma_2} \tilde{u}q^* d\Gamma_2 \tag{2.46}$$

where the subscript 'i' denotes the source point and the constant c_i is

$$c_i = \begin{cases} \dfrac{1}{2} & \text{if } i \in \Gamma \\ 1 & \text{if } i \in \Omega - \Gamma. \end{cases} \tag{2.47}$$

The equation (2.46) can be rewritten as

$$c_i u_i + \int_\Gamma uq^* d\Gamma - \int_\Gamma qu^* d\Gamma = -\int_\Omega bu^* d\Omega. \tag{2.48}$$

The domain integral is still occurred in the equation (2.48) due to the inhomogeneity function $b(x, y)$. The main aim of the DRBEM is to reduce this domain integral to a boundary integral.

Now, we approximate the function $b(x, y)$ by a linear combination of the radial basis functions φ_j as in [42]

$$b \simeq \sum_{j=1}^{N_b+N_i} \alpha_j \varphi_j \tag{2.49}$$

where α_j's are unknown coefficients, N_b and N_i are the number of boundary and interior points, respectively. The radial basis function φ_j is connected to the particular solution $\hat{u}_j$ through the Laplace operator

$$\nabla^2 \hat{u}_j = \varphi_j, \qquad j = 1, 2, \ldots, N_b + N_i. \tag{2.50}$$

Thus, the right hand side function $b(x, y)$ is expressed also with the same Laplace operator applied on the set of particular solutions

$$b(x, y) = \sum_{j=1}^{N_b+N_i} \alpha_j \nabla^2 \hat{u}_j. \tag{2.51}$$

The substitution of this approximation of $b(x, y)$ from (2.51) into the equation (2.48) results in

$$c_i u_i + \int_\Gamma u q^* d\Gamma - \int_\Gamma q u^* d\Gamma = - \sum_{j=1}^{N_b+N_i} \alpha_j \int_\Omega \nabla^2 \hat{u}_j u^* d\Omega, \quad i = 1, \ldots, N_i + N_b. \tag{2.52}$$

The application of the Green's first identity two times again to the Laplacian on the right hand side reduces the domain integral to the boundary integral for each source i,

$$c_i u_i + \int_\Gamma u q^* d\Gamma - \int_\Gamma q u^* d\Gamma = \sum_{j=1}^{N_b+N_i} \alpha_j (c_i \hat{u}_{ij} + \int_\Gamma q^* \hat{u}_j d\Gamma - \int_\Gamma u^* \hat{q}_j d\Gamma), \quad i = 1, \ldots, N_i + N_b \tag{2.53}$$

where $\hat{q}_j$ is the normal derivative of $\hat{u}_j$ and defined as

$$\hat{q}_j = \frac{\partial \hat{u}_j}{\partial n} = \frac{\partial \hat{u}_j}{\partial x}\frac{\partial x}{\partial n} + \frac{\partial \hat{u}_j}{\partial y}\frac{\partial y}{\partial n}. \tag{2.54}$$

We use constant boundary elements for the discretization of the boundary Γ. That is, the boundary is divided into N_e elements and the nodes are taken in the middle of these elements shown in Figure 2.2.

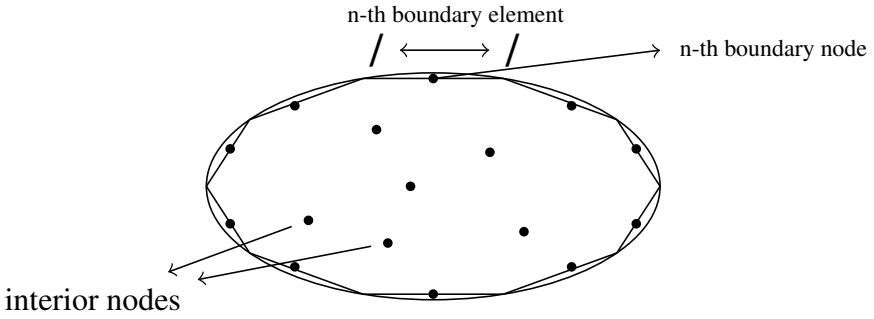

Figure 2.2: Constant boundary element case

The discretization of the boundary to N_e boundary integrals will give the discretized system of equations

$$\begin{aligned} c_i u_i + \sum_{k=1}^{N_e} \int_{\Gamma_k} q^* u \, d\Gamma_k - \sum_{k=1}^{N_e} \int_{\Gamma_k} u^* q \, d\Gamma_k \\ = \sum_{j=1}^{N_b+N_i} \alpha_j (c_i \hat{u}_{ij} + \sum_{k=1}^{N_e} \int_{\Gamma_k} q^* \hat{u}_j \, d\Gamma_k - \sum_{k=1}^{N_e} \int_{\Gamma_k} u^* \hat{q}_j \, d\Gamma_k), \\ i = 1, \ldots, N_i + N_b \end{aligned} \tag{2.55}$$

where $N_e = N_b$ for the constant element case.

The equation (2.55) can be rewritten as

$$c_i u_i + \sum_{k=1}^{N_b} \overline{H}_{ik} u_k - \sum_{k=1}^{N_b} G_{ik} q_k = \sum_{j=1}^{N_b+N_i} \alpha_j (c_i \hat{u}_{ij} + \sum_{k=1}^{N_b} \overline{H}_{ik} \hat{u}_{kj} - \sum_{k=1}^{N_b} G_{ik} \hat{q}_{kj}) \tag{2.56}$$

with entries of the matrices $\overline{\boldsymbol{H}}$ and $\boldsymbol{G}$

$$\overline{H}_{ik} = \begin{cases} \int_{\Gamma_k} q^* d\Gamma_k & \text{if} \quad i \neq k \\ 0 & \text{if} \quad i = k, \end{cases} \qquad G_{ik} = \begin{cases} \int_{\Gamma_k} u^* d\Gamma_k & \text{if} \quad i \neq k \\ \dfrac{1}{2\pi}(ln\dfrac{1}{l_e} + 1) & \text{if} \quad i = k \end{cases} \tag{2.57}$$

where l_e is the length of the element.

We take $c_i = 1/2$ for the boundary points and obtain the linear system

$$\boldsymbol{H^{BS}u^{BS} - G^{BS}q^{BS} = \left(H^{BS}\hat{U}^{BS} - G^{BS}\hat{Q}^{BS}\right)\alpha} \tag{2.58}$$

where $\boldsymbol{BS}$ represents the boundary, and the matrices $\boldsymbol{H^{BS}}$ and $\boldsymbol{G^{BS}}$ with the size $N_b \times N_b$ are constructed as

$$H^{BS}_{ik} = \overline{H}_{ik} + \frac{1}{2}\delta_{ik}, \qquad G^{BS}_{ik} = G_{ik}, \qquad 1 \leq i, k \leq N_b. \tag{2.59}$$

Here, δ is the Kronecker delta function which is 1 if the variables are equal; otherwise 0.

$\hat{\boldsymbol{U}}^{\boldsymbol{BS}}$ and $\hat{\boldsymbol{Q}}^{\boldsymbol{BS}}$ are formed from $\hat{u}_j$ and $\hat{q}_j$ columnwise, respectively. Their size are $N_b \times (N_i + N_b)$. The vectors $\boldsymbol{u^{BS}}$, $\boldsymbol{q^{BS}}$ and $\boldsymbol{\alpha}$ are of length N_b, N_b, $N_b + N_i$, respectively.

The interior solution is obtained from the discretized system (2.56) with $c_i = 1$ ($i = 1, 2, \ldots, N_i$) as

$$u_i = -\sum_{k=1}^{N_b} \overline{H}_{ik}u_k + \sum_{k=1}^{N_b} G_{ik}q_k + \sum_{j=1}^{N_b+N_i} \alpha_j(c_i\hat{u}_{ij} + \sum_{k=1}^{N_b} \overline{H}_{ik}\hat{u}_{kj} - \sum_{k=1}^{N_b} G_{ik}\hat{q}_{kj}) \tag{2.60}$$

which is expressed in matrix-vector form as

$$\boldsymbol{Iu^{IS} = -H^{IS}u^{BS} + G^{IS}q^{BS} + \left(I\hat{U}^{IS} + H^{IS}\hat{U}^{BS} - G^{IS}\hat{Q}^{BS}\right)\alpha} \tag{2.61}$$

where $\boldsymbol{IS}$ denotes interior, and the matrices $\boldsymbol{H^{IS}}$, $\hat{\boldsymbol{G}}^{\boldsymbol{IS}}$, $\hat{\boldsymbol{U}}^{\boldsymbol{IS}}$ and the identity matrix $\boldsymbol{I}$ have the size $N_i \times N_b$, $N_i \times N_b$, $N_i \times (N_i + N_b)$ and $N_i \times N_i$, respectively. The

distance r in the matrices $\overline{\boldsymbol{H}}$ and $\boldsymbol{G}$ is measured now from an interior point to the boundary elements.

Combining the systems (2.58) and (2.61), we obtain the enlargement system as

$$\begin{bmatrix} \boldsymbol{H}^{BS} & \mathbf{0} \\ \boldsymbol{H}^{IS} & \boldsymbol{I} \end{bmatrix} \begin{Bmatrix} \boldsymbol{u}^{BS} \\ \boldsymbol{u}^{IS} \end{Bmatrix} - \begin{bmatrix} \boldsymbol{G}^{BS} & \mathbf{0} \\ \boldsymbol{G}^{IS} & \mathbf{0} \end{bmatrix} \begin{Bmatrix} \boldsymbol{q}^{BS} \\ \mathbf{0} \end{Bmatrix}$$
$$= \left(\begin{bmatrix} \boldsymbol{H}^{BS} & \mathbf{0} \\ \boldsymbol{H}^{IS} & \boldsymbol{I} \end{bmatrix} \begin{Bmatrix} \hat{\boldsymbol{U}}^{BS} \\ \hat{\boldsymbol{U}}^{IS} \end{Bmatrix} - \begin{bmatrix} \boldsymbol{G}^{BS} & \mathbf{0} \\ \boldsymbol{G}^{IS} & \mathbf{0} \end{bmatrix} \begin{Bmatrix} \hat{\boldsymbol{Q}}^{BS} \\ \mathbf{0} \end{Bmatrix} \right) \boldsymbol{\alpha} \tag{2.62}$$

which is written in a compact form as

$$\boldsymbol{Hu} - \boldsymbol{Gq} = (\boldsymbol{H}\hat{\boldsymbol{U}} - \boldsymbol{G}\hat{\boldsymbol{Q}})\boldsymbol{\alpha}. \tag{2.63}$$

The vector $\boldsymbol{\alpha}$ is obtained from the approximation (2.49) which is also expressed in a matrix-vector form as

$$\boldsymbol{b} = \boldsymbol{F}\boldsymbol{\alpha} \tag{2.64}$$

where $\boldsymbol{F}$ is constructed by φ_j as columns.

Inverting the equation (2.64) and substituting into (2.63), we get

$$\boldsymbol{Hu} - \boldsymbol{Gq} = (\boldsymbol{H}\hat{\boldsymbol{U}} - \boldsymbol{G}\hat{\boldsymbol{Q}})\boldsymbol{F}^{-1}\boldsymbol{b}. \tag{2.65}$$

If the right hand side function b includes the space derivatives of the solution u such that $b = \dfrac{\partial u}{\partial x} + \dfrac{\partial u}{\partial y}$, then the coordinate matrix $\boldsymbol{F}$ is used as explained in the Section 2.1.1, and the vector $\boldsymbol{b}$ is computed as

$$\boldsymbol{b} = \frac{\partial \boldsymbol{F}}{\partial x}\boldsymbol{F}^{-1}\boldsymbol{u} + \frac{\partial \boldsymbol{F}}{\partial y}\boldsymbol{F}^{-1}\boldsymbol{u}. \tag{2.66}$$

In the system (2.65), the vectors $\boldsymbol{u}$ and $\boldsymbol{q}$ contain both known and unknown u and q values at the nodes. Shuffling the known and unknown values with the related columns of the matrices $\boldsymbol{H}$ and $\boldsymbol{G}$, we obtain a new system such that $\hat{\boldsymbol{A}}\boldsymbol{x} = \hat{\boldsymbol{d}}$. Here, the vector $\boldsymbol{x}$ contains only the unknown nodal values on the boundary in the form of solution or its normal derivative, and the vector $\hat{\boldsymbol{d}}$ contains only the given boundary information. Solution of this system gives unknown u and q values on the boundary, and interior u values.

2.3 The Direct Interpolation Boundary Element Method (DIBEM)

In this Section, the direct interpolation boundary element method (DIBEM) is going to be explained for the Poisson type equations. This technique is the combination of the boundary element method and the radial basis function approximation. The difference from DRBEM is that the domain integral due to the right hand side function of Poisson equation is solved by using direct interpolation [33, 34].

Let us consider Poisson equation

$$\nabla^2 u = z(x, y) \quad \text{in} \quad \Omega \tag{2.67}$$

with boundary conditions

$$\begin{aligned} u &= \bar{u} && \text{on} \quad \Gamma_1 \\ \frac{\partial u}{\partial n} &= \bar{q} && \text{on} \quad \Gamma_2 \end{aligned} \tag{2.68}$$

where $\Gamma = \Gamma_1 + \Gamma_2$ is the boundary of the domain Ω.

Applying the procedure similar to DRBEM to the equation (2.67), we obtain

$$c(\xi)u(\xi) + \int_\Gamma u(X)q^*(\xi; X)\, d\Gamma - \int_\Gamma q(X)u^*(\xi; X)\, d\Gamma = -\int_\Omega z(X)u^*(\xi; X)\, d\Omega \tag{2.69}$$

where ξ and X are the source and field points in Ω or Γ, and u^*, q^* are the fundamental solution and its normal derivative of Laplace equation, respectively. The coefficient $c(\xi)$ depends on the position of the source point ξ and given as in (2.47).

In the right hand side domain integral of the equation (2.69), the integrand is directly interpolated using the linear combination of radial basis functions F^i

$$z(X)u^*(\xi; X) = \sum_{i=1}^{n} \alpha_i(\xi) F^i(X^i; X) \tag{2.70}$$

where X^i and X are the interpolation and field points, respectively. n is the number of points used in the interpolation. The undetermined coefficients $\alpha_i(\xi)$'s change for each source point ξ, $\xi = 1, \ldots, \tilde{n}$. Here, $\tilde{n}$ is the total number of boundary and interior nodes and is equal to the number of interpolation points n, that is $n = \tilde{n}$. Since $z(X)$ is a known function, collocation of the approximation (2.70) with the interpolation

points X^j, $j = 1, \ldots, n$ results in the matrix-vector form

$$\boldsymbol{\Lambda}(\xi)\boldsymbol{z} = \boldsymbol{F}\boldsymbol{\alpha}(\xi) \tag{2.71}$$

where the vectors $\boldsymbol{z} = (z_1, \ldots, z_n)^T$ and $\boldsymbol{\alpha}(\xi) = (\alpha_1(\xi), \ldots, \alpha_n(\xi))^T$ are of the size $n \times 1$. The diagonal matrix $\boldsymbol{\Lambda}(\xi)$ is constructed by the fundamental solution of Laplace equation u^* for each ξ

$$\boldsymbol{\Lambda}(\xi) = \begin{bmatrix} u^*(\xi, X^1) & \ldots & 0 \\ & \ddots & \\ 0 & \ldots & u^*(\xi, X^n) \end{bmatrix} \tag{2.72}$$

where the interpolation point X^j is different from the source point ξ due to the singularities of the fundamental solution.

In the approximation (2.70) the interpolation radial basis function F^i is related to primitive interpolation function Ψ^i as $\nabla^2\Psi^i = F^i, \quad i = 1, \ldots, n$. Thus, the domain integral of the source term in the equation (2.69) is also expressed with the set of Ψ^i

$$\int_\Omega z(X)u^*(\xi; X)d\Omega = \int_\Omega \sum_{i=1}^{n} \alpha_i(\xi)\nabla^2\Psi^i(X^i; X)d\Omega \tag{2.73}$$

and this domain integral converts to a boundary integral with the application of the Green's first identity

$$\int_\Omega z(X)u^*(\xi; X)d\Omega = \sum_{i=1}^{n} \alpha_i(\xi) \int_\Omega \nabla^2\Psi^i(X^i; X)d\Omega = \sum_{i=1}^{n} \alpha_i(\xi) \int_\Gamma \frac{\partial\Psi^i}{\partial n}(X^i; X)d\Gamma \tag{2.74}$$

where $\dfrac{\partial\Psi^i}{\partial n}(X^i; X)$ is the normal derivative of interpolation function $\Psi^i(X^i; X)$.

Substituting the boundary integral relation (2.74) into the domain integral of the source term in the equation (2.69), we obtain the boundary integral equation

$$c(\xi)u(\xi) + \int_\Gamma u(X)q^*(\xi; X)\, d\Gamma - \int_\Gamma q(X)u^*(\xi; X)\, d\Gamma = -\alpha_i(\xi) \int_\Gamma \frac{\partial\Psi^i}{\partial n}(X^i; X)\, d\Gamma. \tag{2.75}$$

for each source node ξ, $\xi = 1, \ldots, n$.

Using a similar discretization procedure for boundary integrals like DRBEM explained in Section 2.2, the equation (2.75) can be expressed in discretized system

as

$$
\begin{aligned}
H_{11}u_1 + \cdots + H_{1n}u_n - G_{11}q_1 - \cdots - G_{1n}q_n &= \alpha_1(1)\overline{N}_1 + \cdots + \alpha_n(1)\overline{N}_n \\
H_{21}u_1 + \cdots + H_{2n}u_n - G_{21}q_1 - \cdots - G_{2n}q_n &= \alpha_1(2)\overline{N}_1 + \cdots + \alpha_n(2)\overline{N}_n \\
&\vdots \\
H_{n1}u_1 + \cdots + H_{nn}u_n - G_{n1}q_1 - \cdots - G_{nn}q_n &= \alpha_1(n)\overline{N}_1 + \cdots + \alpha_n(n)\overline{N}_n
\end{aligned}
\tag{2.76}
$$

where $\overline{N}_i = -\sum_{j=1}^{N_e} \int_{\Gamma_j} \frac{\partial \Psi^i}{\partial n}(X^i; X_j)\, d\Gamma_j, \quad 1 \leq i \leq n$. Here, N_e is the number of boundary elements, and X^i and X_j are the interpolation and field points, respectively.

The discretized system (2.76) can be rewritten in a matrix-vector form as

$$
\boldsymbol{Hu - Gq = \bar{A}\overline{N}} \tag{2.77}
$$

where $\boldsymbol{H}$ and $\boldsymbol{G}$ are the DRBEM matrices given in (2.62), the vector $\overline{\boldsymbol{N}} = \{\overline{N}_i\}$, $i = 1, \ldots, n$. The matrix $\bar{\boldsymbol{A}}$ is formed from the vector $\boldsymbol{\alpha}(\xi)$ as rows, i.e, $\bar{\boldsymbol{A}} = (\boldsymbol{\alpha}(1), \ldots, \boldsymbol{\alpha}(n))^T$ and the unknown vectors $\boldsymbol{\alpha}(\xi)$ is obtained from the solution of the system (2.71) for each source point ξ.

The system (2.77) is rearranged as a linear system $\boldsymbol{Ax = b}$ shuffling the known and unknown boundary informations like DRBEM. Here, $\boldsymbol{x}$ is the vector of unknown boundary values $\boldsymbol{u}$ or $\boldsymbol{q}$ and unknown interior values of $\boldsymbol{u}$. The vector $\boldsymbol{b}$ contains only the known values.

In the next Chapter, the RBF approximation, DRBEM and DIBEM are going to be applied to the MHD Stokes, MHD incompressible and MHD convection flow problems which are modeled by the Poisson's type differential equations. The numerical solution of the MHD Stokes flow in a lid-driven cavity will be obtained by using three types of methods explained in this chapter. In comparison with the DRBEM and DIBEM for this problem, the RBF approximation gives more accurate results with considerably low computational time and cost. Thus, the other MHD flow problems will be solved by the RBF approximation.

CHAPTER 3

MHD STOKES, MHD INCOMPRESSIBLE AND MHD CONVECTION CHANNEL FLOWS

In this Chapter, we are going to present the numerical solution of the two dimensional steady, laminar flow of incompressible, viscous, electrically conducting fluid under the effect of uniform magnetic field in channels by using the numerical methods explained in the previous chapter. First, the RBF approximation will be applied to the MHD Stokes flow in a lid-driven cavity. Also, the applications of the other numerical techniques as DRBEM and DIBEM to the same problems will be considered and the comparison will be carried between these methods in terms of accuracy and the computational cost in Section 3.1. Since RBF approximation gives the solution with quite less computational expense compared to other numerical methods, we will continue using the RBF approximation to solve the other MHD Stokes and incompressible flow problems in the thesis. Sections 3.2 and 3.3 present the RBF approximation of MHD Stokes flow channels with different geometries. Then, the RBF solutions of the MHD Stokes and MHD incompressible flow under the magnetic field applied in the pipe-axis direction generating the electric potential are presented in Section 3.4 and Section 3.5. Applications are given in a lid-driven cavity and in a constricted enclosure with a moving left wall. Finally, the RBF approximation will be extended to solve the MHD convection flow equations in Section 3.6 with or without the viscous dissipation term in the temperature equation. The MHD convection problem is also solved by using Stokes approximation to analyze the heat transfer for the slow flow in different type of cavities. The numerical results for all MHD flow problems mentioned above are simulated in terms of streamlines, equivorticity lines, pressure and temperature contours, and the centerline velocities for several values of physical

parameters.

3.1 The MHD Stokes Flow in a Lid-driven Cavity

The incompressible, highly viscous flow in slow motion is called Stokes flow (or creeping flow) which has many industrial applications such as lubrication, food-processing materials, etc. MHD Stokes flow equations are hydrodynamic and electromagnetic equations neglecting the convection terms due to the small values of Reynolds number ($Re << 1$). Induced magnetic filed is also neglected due to the small magnetic Reynolds number values. In this Section, the numerical results of the Stokes flow are obtained in cavities (cross-section of channels) under the impact of a uniform magnetic field in the x-direction by using three numerical methods as the RBF approximation, the DRBEM or the DIBEM.

MHD Stokes flow in a lid-driven square cavity (cross-section of the square channel which has a moving top lid shown in Figure 3.1) is considered. Flow is subjected to a magnetic field in the horizontal direction.

The non-dimensional governing equations for the two-dimensional, steady MHD Stokes flow in terms of primitive variables (velocity components (u, v), pressure p) are given in Chapter 1 (equations (1.27)-(1.29)) as

$$\frac{\partial u}{\partial x} + \frac{\partial v}{\partial y} = 0 \qquad (3.1)$$

$$\nabla^2 u = \frac{\partial p}{\partial x}, \quad \nabla^2 v - M^2 v = \frac{\partial p}{\partial y} \qquad \text{in} \quad \Omega \qquad (3.2)$$

which can be rewritten in terms of velocity components (u, v), stream function ψ, vorticity ω and pressure p

$$\nabla^2 u = -\frac{\partial \omega}{\partial y} \ , \qquad \nabla^2 v = \frac{\partial \omega}{\partial x} \qquad (3.3)$$

$$\nabla^2 \psi = -\omega \qquad \text{in} \quad \Omega \qquad (3.4)$$

$$\nabla^2 \omega = M^2 \frac{\partial v}{\partial x} \ , \qquad \nabla^2 p = -M^2 \frac{\partial v}{\partial y} \qquad (3.5)$$

where $M = L\mu H_0\sqrt{\sigma/\rho\nu}$ is the Hartmann number, and $\Omega = \{(x, y) : 0 \leq x \leq 1, 0 \leq y \leq 1\}$.

The related boundary conditions are the no-slip condition giving u, v, ψ imposed zero on the walls except the top wall which has movement with velocity $u = 1$. Pressure and vorticity wall conditions are not known.

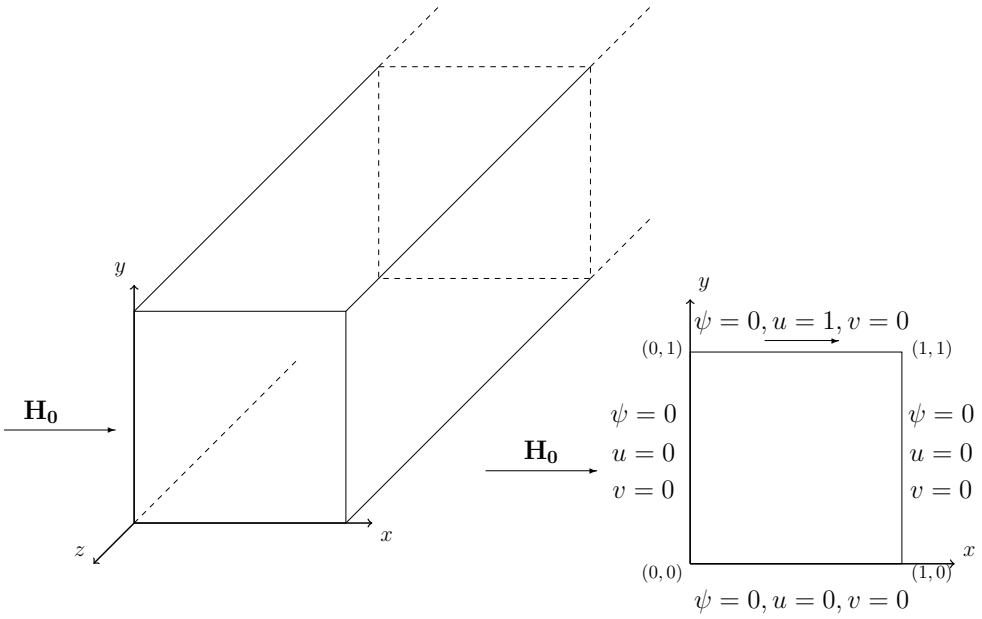

Figure 3.1: Problem 3.1: Lid-driven cavity and boundary conditions.

The unknown vorticity boundary conditions are obtained from the stream function equation (3.4) by using the finite difference scheme which includes also interior ψ values. Thus, the boundary values for ω are explained in Chapter 1, equation (1.16)

$$\omega_b = -(a_0\psi_b + a_1\psi_s + a_2\psi_q + a_3\psi_n|_b) \tag{3.6}$$

where ψ_b is the boundary value, ψ_n is the normal derivative of ψ, and ψ_s and ψ_q are interior values which are sh and qh distances away from the boundary. The coefficients are defined as

$$a_0 = \frac{-2(s^3 - q^3)}{h^2 s^2 q^2 (s - q)}, \qquad a_1 = \frac{-2q}{h^2 s^2 (s - q)}, \tag{3.7}$$

$$a_2 = \frac{2s}{h^2 q^2 (s - q)}, \qquad a_3 = \frac{-2(s + q)}{hsq} \quad . \tag{3.8}$$

The unknown pressure boundary values are found by a finite difference scheme for the pressure derivatives and coordinate matrix $\boldsymbol{F}$ for the space derivatives in the equations (3.2). Then, we have

$$p_b = p_i - \Delta y(\boldsymbol{C}v - M^2 v) \qquad \text{for the lower boundary} \tag{3.9}$$

$$p_b = p_i + \Delta x \boldsymbol{C}u \qquad \text{for the right boundary} \tag{3.10}$$

$$p_b = p_i + \Delta y(\boldsymbol{C}v - M^2 v) \qquad \text{for the upper boundary} \tag{3.11}$$

$$p_b = p_i - \Delta x \boldsymbol{C}u \qquad \text{for the left boundary} \tag{3.12}$$

where p_b is the boundary value, p_i is the interior value which is Δx or Δy distances away from the boundary and $\boldsymbol{C} = \dfrac{\partial \boldsymbol{F}}{\partial x}\boldsymbol{F}^{-1}\dfrac{\partial \boldsymbol{F}}{\partial x}\boldsymbol{F}^{-1} + \dfrac{\partial F}{\partial y}\boldsymbol{F}^{-1}\dfrac{\partial \boldsymbol{F}}{\partial y}\boldsymbol{F}^{-1}$.

In the next Section, the two-dimensional steady MHD Stokes flow equations are going to be solved iteratively by using RBF approximation, DRBEM and DIBEM. We make a comparison of these methods in terms of computational cost and accuracy.

3.1.1 RBF Solution of the MHD Stokes Flow in a Lid-Driven Cavity

The RBF approximation (2.31) is applied to the two-dimensional steady MHD Stokes flow equations (3.3)-(3.5) by taking the right hand side functions as

$$f_u = -\frac{\partial \omega}{\partial y} \quad , \qquad f_v = \frac{\partial \omega}{\partial x} \tag{3.13}$$

$$f_\psi = -\omega, \tag{3.14}$$

$$f_\omega = M^2 \frac{\partial v}{\partial x}, \qquad f_p = -M^2 \frac{\partial v}{\partial y} \tag{3.15}$$

which results in matrix-vector equations with the help of the coordinate matrix $\boldsymbol{F}$ for the space derivatives of unknowns

$$\boldsymbol{u} = \boldsymbol{g_u} - \boldsymbol{K}(\frac{\partial \boldsymbol{F}}{\partial y}\boldsymbol{F^{-1}}\boldsymbol{\omega}) \tag{3.16}$$

$$\boldsymbol{v} = \boldsymbol{g_v} + \boldsymbol{K}(\frac{\partial \boldsymbol{F}}{\partial x}\boldsymbol{F^{-1}}\boldsymbol{\omega}) \tag{3.17}$$

$$\boldsymbol{\psi} = \boldsymbol{g_\psi} + \boldsymbol{K}(\boldsymbol{-\omega}) \tag{3.18}$$

$$\boldsymbol{\omega} = \boldsymbol{g_\omega} + M^2\boldsymbol{K}(\frac{\partial \boldsymbol{F}}{\partial x}\boldsymbol{F^{-1}}\boldsymbol{v}) \tag{3.19}$$

$$\boldsymbol{p} = \boldsymbol{g_p} - M^2\boldsymbol{K}(\frac{\partial \boldsymbol{F}}{\partial y}\boldsymbol{F^{-1}}\boldsymbol{v}) \tag{3.20}$$

where the vector $\boldsymbol{g}_{\xi}$, $\boldsymbol{\xi}$ denotes $\boldsymbol{u}$, $\boldsymbol{v}$, $\boldsymbol{\psi}$, $\boldsymbol{\omega}$, $\boldsymbol{p}$ and the matrices $\boldsymbol{K}$ and $\boldsymbol{F}$ are defined in Section 2.1.2.

The RBF system of MHD Stokes flow equations (3.16)-(3.20) are solved iteratively.

Now, we shall describe the iterative procedure:

1. Start with initial estimates for vorticity $\boldsymbol{\omega}^0$.
2. Solve the velocity equations (3.16)-(3.17) to obtain $\boldsymbol{u}^{m+1}$ and $\boldsymbol{v}^{m+1}$ with $\boldsymbol{\omega}^m$.
3. Solve the stream function equation (3.18) to obtain $\boldsymbol{\psi}^{m+1}$ with $\boldsymbol{\omega}^m$.
4. Calculate the new vorticity boundary conditions by using finite difference procedure (3.6).
5. Solve the vorticity equation (3.19) to obtain $\boldsymbol{\omega}^{m+1}$ with $\boldsymbol{v}^{m+1}$.
6. Use a relaxation parameter $0 < \alpha_{\omega} < 1$ to accelerate the convergence
$$\boldsymbol{\omega}^{m+1} = (1 - \alpha_{\omega})\boldsymbol{\omega}^m + \alpha_{\omega}\boldsymbol{\omega}^{m+1}.$$
7. Obtain the new pressure boundary conditions from (3.9)-(3.12) by using coordinate matrix $\boldsymbol{F}$ for the space derivatives of velocities and finite difference scheme for pressure derivatives.
8. Solve the pressure equation (3.20) to obtain $\boldsymbol{p}^{m+1}$ with $\boldsymbol{v}^{m+1}$.
9. Use a relaxation parameter $0 < \alpha_p < 1$ to accelerate the convergence
$$\boldsymbol{p}^{m+1} = (1 - \alpha_p)\boldsymbol{p}^m + \alpha_p\boldsymbol{p}^{m+1}.$$
10. Check the stopping criteria by using absolute error
$$||\boldsymbol{z}^{m+1} - \boldsymbol{z}^m||_{\infty} < \epsilon$$
where $\boldsymbol{z}$ denotes either $\boldsymbol{u}$, $\boldsymbol{v}$, $\boldsymbol{\psi}$, $\boldsymbol{\omega}$ or $\boldsymbol{p}$ and preassigned tolerance is taken $\epsilon = 10^{-3}$.
11. If the stopping criterion is satisfied, then stop; otherwise go to step 1.

In the numerical computations, linear polynomial radial basis function $\varphi = 1 + r$ is used. We take $N_b = 60, 60, 80, 80, 120, 140$ boundary points and $N_i = 196, 196, 361, 361, 841, 1156$ interior points for the Hartmann number values $M = 0, 1, 10, 30, 50, 80$, respectively. The relaxation parameters for vorticity and pressure are given as $\alpha_\omega = 0.01$ and $\alpha_p = 0.001$. The numerical results are shown in terms of streamlines, vorticity and pressure contours.

First, the proposed numerical procedure is validated for the Stokes flow problem by taking $M = 0$ (absence of external magnetic field) and the numerical results in terms of stream function, vorticity and pressure are in well agreement with the ones in [64]. Figure 3.2 shows the flow symmetry with respect to vertical centerline which is expected in the Stokes flow. The effect of only the moving top lid is observed on the Stokes flow. Pressure is naturally concentrated near the upper corners.

In Figure 3.3, the impact of magnetic field on the Stokes flow is analyzed by taking several values of Hartmann number. One can observe that as M increases, the main vortex of the flow shifts through the moving top lid with a decreasing magnitude and a secondary flow with small magnitude is developed. With a further increase in M this secondary flow squeezes through the top lid and the rest of the cavity is almost stagnant. The increase in M develops boundary layers in the direction of magnetic field (side layers) near the moving lid. These are the well-known characteristics of the MHD flow (flattening tendency of the flow and the boundary layer formation for increasing M).

As the intensity of applied magnetic field increases, vorticity profile is distorted appreciably. Boundary layer is developed towards moving boundary, and a secondary vortex starts to be seen just below the boundary layer. For $M \geq 30$ vorticity action is completely in front of the moving top lid in terms of two opposite direction bunch of vorticity lines. Again, the lower part of the cavity is stagnant.

When the magnetic field is neglected ($M = 0$), pressure contours are observed at the upper corners of the cavity. The increase in the magnetic field intensity extends the pressure on the flow also to the lower part of the cavity. Thus, there are four antisymmetric vortices with respect to $x = 0.5$ line, two of them are separated from the others close to the moving lid. Hence, it may be regarded as a boundary layer in

the separation region which is approximately $0.8 \leq y \leq 1.0$.

Figure 3.4 shows the centerline velocity behaviors for increasing values of Hartmann number. One can see from the $u-$centerline velocity that the fluid motion is enforced through the moving top lid by increasing the Hartmann number. The well known flattening tendency of MHD flow is observed from the decrease of magnitude of v as M increases. The centerline velocity profiles for $M = 0$ (Stokes flow) is the same as the centerline velocities in Stokes flow obtained by [64].

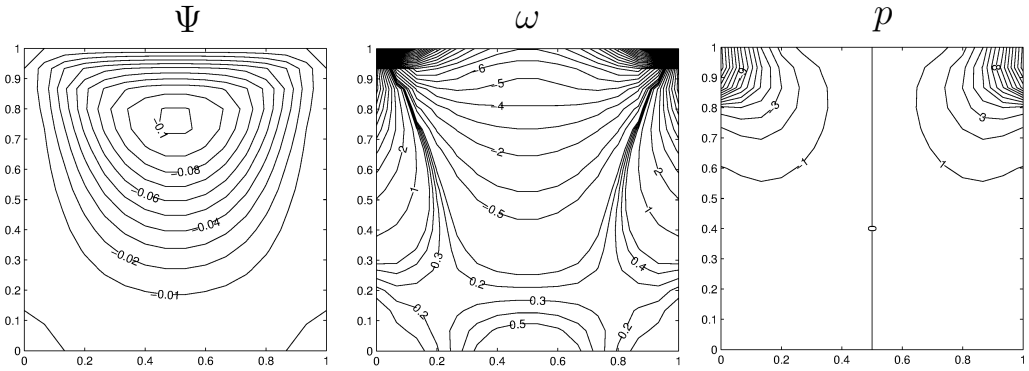

Figure 3.2: Problem 3.1: RBF solution of the MHD Stokes flow for $M = 0$.

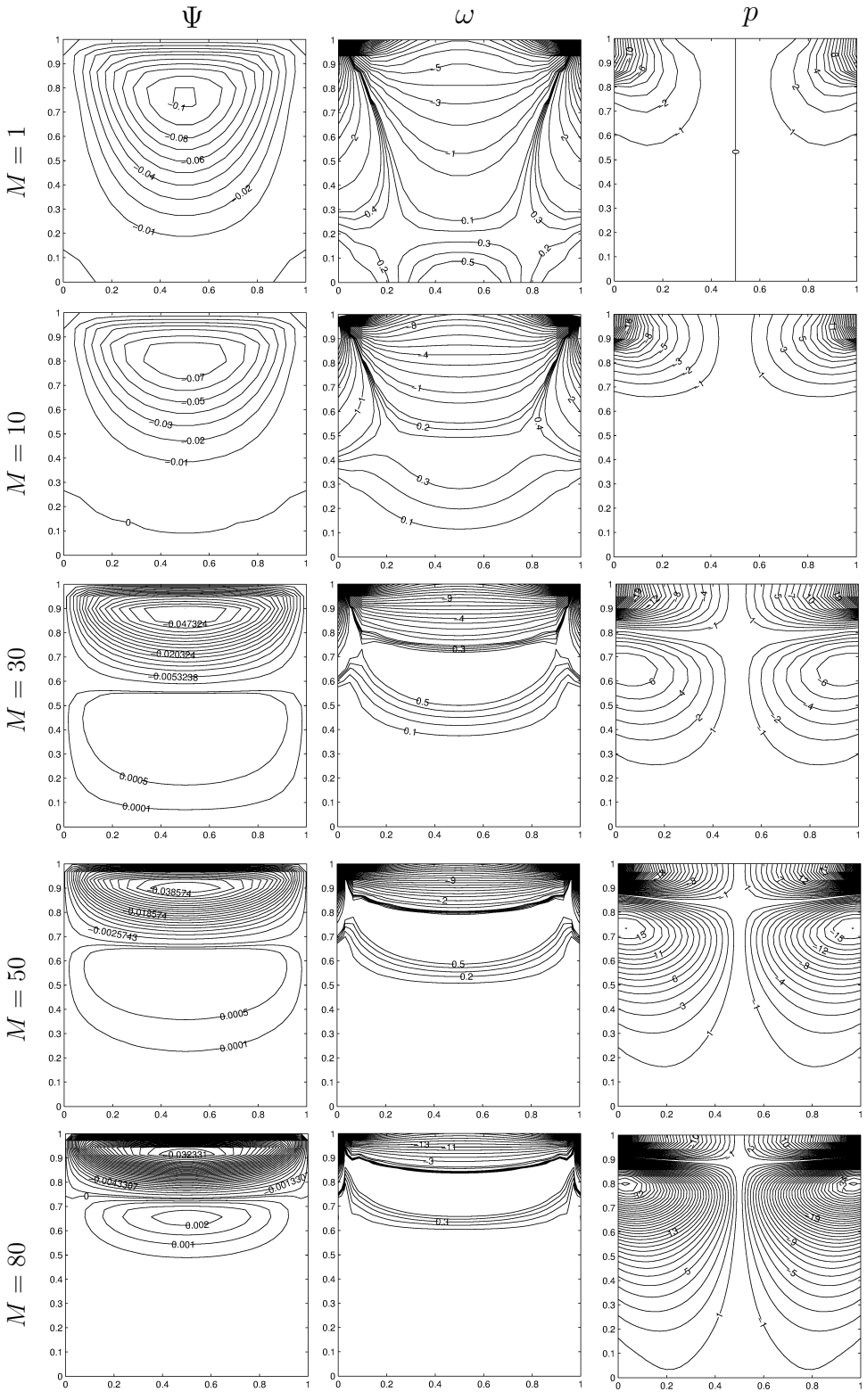

Figure 3.3: Problem 3.1: RBF solution of the MHD Stokes flow for $1 \leq M \leq 80$.

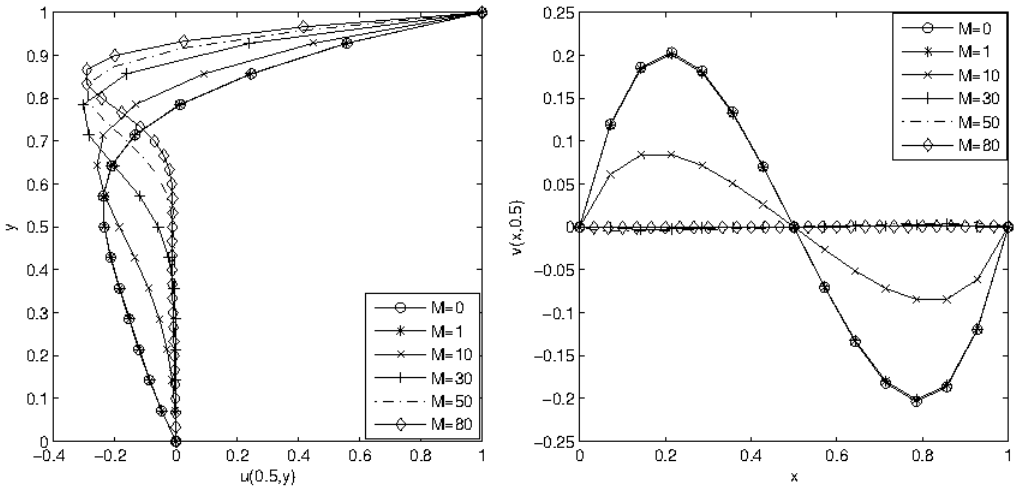

Figure 3.4: Problem 3.1: Centerline velocities for the MHD Stokes flow in a lid-driven cavity.

The radial basis function approximation of MHD Stokes flow in a lid-driven square cavity is also carried by taking radial basis functions as quadratic polynomial $\varphi = 1 + r + r^2$, multiquadratics $\varphi = \sqrt{r^2 + c^2}$ with the shape parameter c is taken as $c = 0.01$ in [9] and polyharmonic splines $\varphi = r^2 lnr$. The numerical results are shown in Figures 3.5-3.6. The solutions obtained by linear radial basis functions (in Figures 3.2-3.3) and by quadratic polynomial, multiquadratics and polyharmonic spline functions have the same behaviors with little magnitude differences in the flow only for $M = 30$.

The computational cost of different radial basis functions and the corresponding iteration numbers as well as the 2-norm condition numbers of the coefficient matrices required for reaching steady-state solution are calculated and shown in Table 3.1. It is observed that the linear polynomial RBF takes less computational time and number of iterations for converging to steady-state solution with a small condition number. Thus, the rest of the computations in thesis is carried with the linear polynomial RBF.

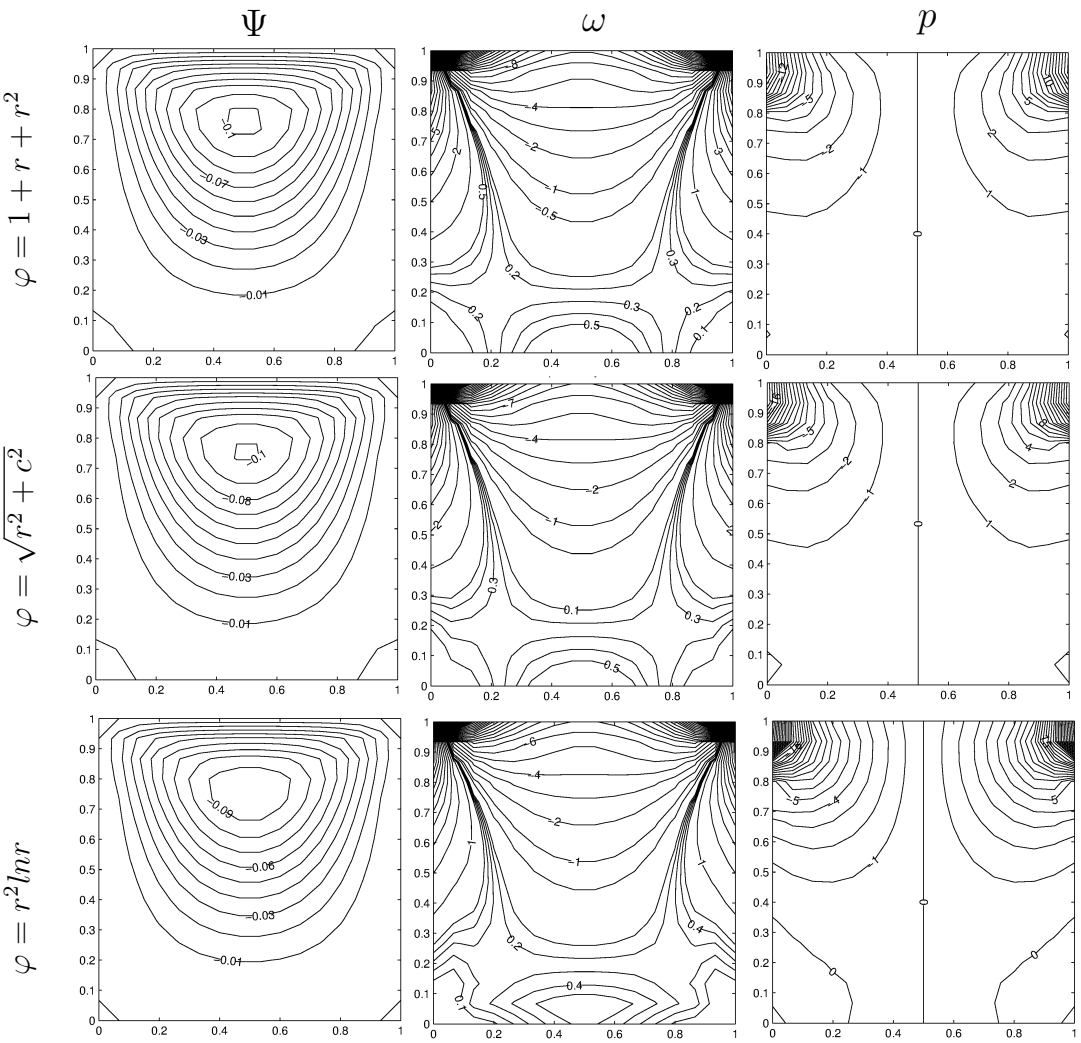

Figure 3.5: Problem 3.1: RBF solution of the MHD Stokes flow for $M = 0$ using $\varphi = 1 + r + r^2$, $\varphi = \sqrt{r^2 + c^2}$ and $\varphi = r^2 lnr$.

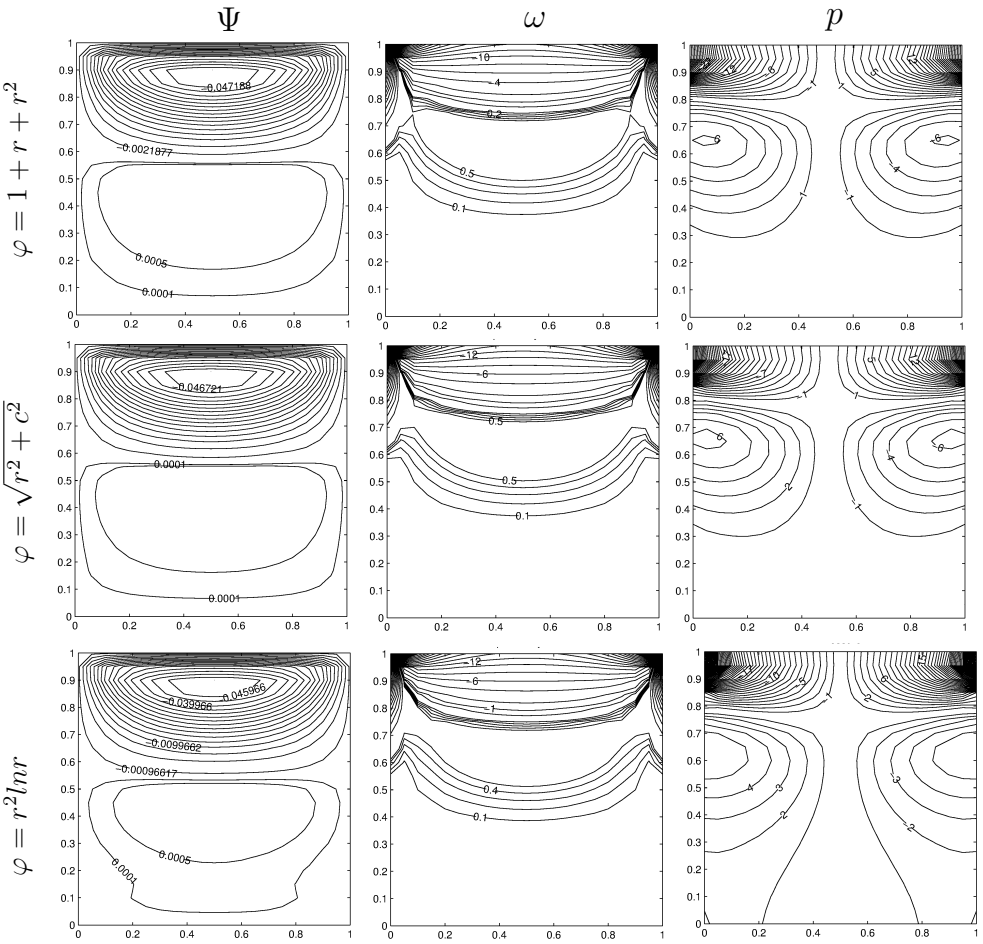

Figure 3.6: Problem 3.1: RBF solution of the MHD Stokes flow for $M = 30$ using $\varphi = 1 + r + r^2$, $\varphi = \sqrt{r^2 + c^2}$ and $\varphi = r^2 lnr$.

	$M = 0$			$M = 30$		
RBFs	CPU(s)	Iteration Number	Condition Number	CPU(s)	Iteration Number	Condition Number
$1 + r$	242.5796	6764	4105×10^4	1669.9183	10954	1762×10^5
$1 + r + r^2$	266.4113	7182	5039×10^4	1789.9155	11391	2163×10^5
$\sqrt{r^2 + c^2}$	281.0303	7408	1639×10^4	1873.9552	11523	7611×10^4
$r^2 lnr$	371.5490	9500	4732×10^4	2116.7653	13352	2726×10^5

Table 3.1: CPU times, iteration numbers and 2-norm condition numbers for $M = 0, 30$ using different RBFs.

3.1.2 DRBEM Solution of the MHD Stokes Flow in a Lid-Driven Cavity

The DRBEM is also used as a numerical technique for solving MHD Stokes flow equations since the governing differential operator is the Laplacian in equations (3.3)-(3.5). The application of DRBEM to the Poisson type equations (3.3)-(3.5) gives the discretized system (2.65) in matrix-vector form as

$$\boldsymbol{Hu - Gq = (H\hat{U} - G\hat{Q})F^{-1}b} \tag{3.21}$$

with the non-homogeneous term b denoting

$$b_u = -\frac{\partial \omega}{\partial y} \quad , \qquad b_v = \frac{\partial \omega}{\partial x} \tag{3.22}$$

$$b_\psi = -\omega, \tag{3.23}$$

$$b_\omega = M^2 \frac{\partial v}{\partial x}, \qquad b_p = -M^2 \frac{\partial v}{\partial y}. \tag{3.24}$$

Using the coordinate matrix $\boldsymbol{F}$ for the space derivatives of the unknowns, the discretized form of the equations (3.3)-(3.5) are written as

$$\boldsymbol{Hu - Gq_u = (H\hat{U} - G\hat{Q})F^{-1}\frac{\partial F}{\partial y}F^{-1}(-\omega)} \tag{3.25}$$

$$\boldsymbol{Hv - Gq_v = (H\hat{U} - G\hat{Q})F^{-1}\frac{\partial F}{\partial x}F^{-1}\omega} \tag{3.26}$$

$$\boldsymbol{H\psi - Gq_\psi = (H\hat{U} - G\hat{Q})F^{-1}(-\omega)} \tag{3.27}$$

$$\boldsymbol{H\omega - Gq_\omega = (H\hat{U} - G\hat{Q})F^{-1}(}M^2\frac{\partial \boldsymbol{F}}{\partial x}\boldsymbol{F^{-1}v}) \tag{3.28}$$

$$\boldsymbol{Hp - Gq_p = (H\hat{U} - G\hat{Q})F^{-1}(}M^2\frac{\partial \boldsymbol{F}}{\partial y}\boldsymbol{F^{-1}(-v)}) \tag{3.29}$$

where the matrices $\boldsymbol{F, H, G, \hat{U}, \hat{Q}}$ are given in Section 2.2.

These system of equations (3.25)-(3.29) are solved iteratively by using $N_b = 60$ constant boundary elements and $N_i = 225$ interior nodes with preassigned tolerance $\epsilon = 10^{-3}$ for the convergence. The numerical results are obtained for $M = 0$ and $M = 30$.

Figure 3.7 presents the Stokes flow and pressure behaviors by taking $M = 0$ in MHD Stokes equations and are in well agreement with the ones in [64].

In Figure 3.8, DRBEM and RBF solutions of MHD Stokes flow equations for $M = 30$ are given. The same flow and pressure behaviors are captured. It is observed that, the

DRBEM has the weakness to capture the secondary flow in the lower part of the cavity and some disturbances are occurred in the vorticity profiles near the bottom wall due to the singularities in the boundary conditions at the corners when constant elements are used. These inconveniences may be handled by using linear boundary elements.

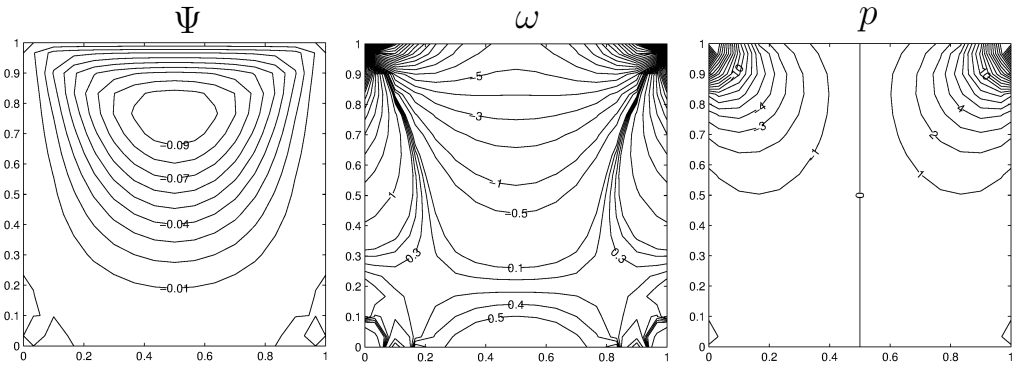

Figure 3.7: Problem 3.1: DRBEM solution of the MHD Stokes flow for $M = 0$.

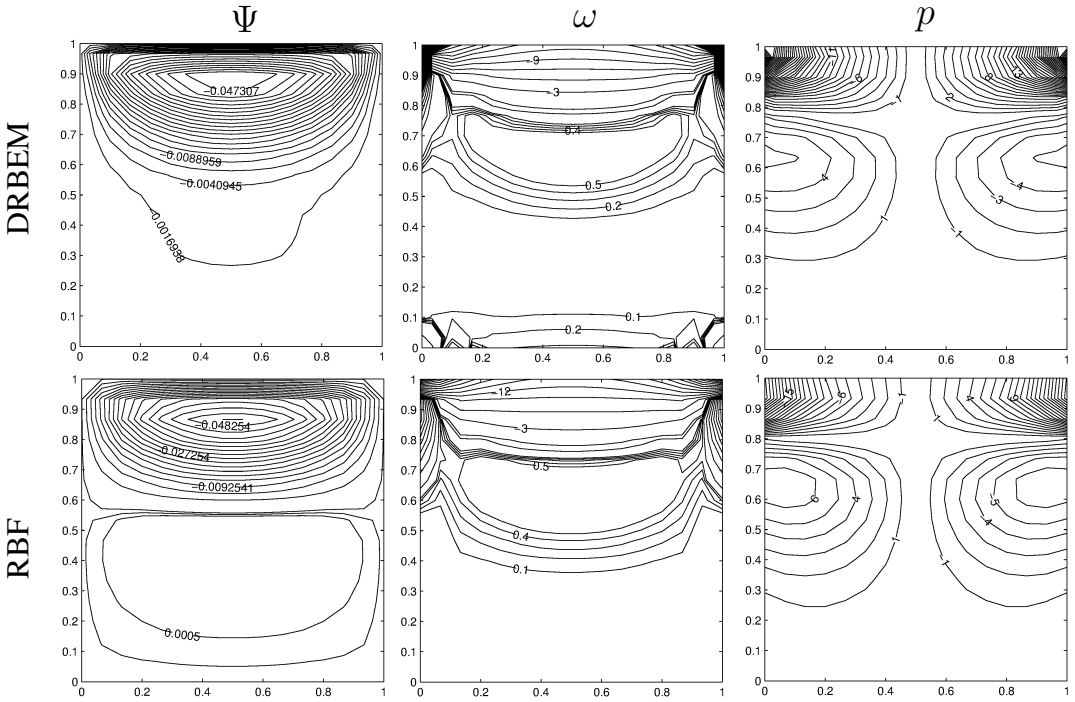

Figure 3.8: Problem 3.1: DRBEM and RBF solutions of the MHD Stokes flow for $M = 30$.

3.1.3 DIBEM Solution of the MHD Stokes Flow in a Lid-Driven Cavity

In this Section, we apply the DIBEM to the same lid-driven cavity problem and the numerical results are compared with the results obtained by RBF and DRBEM.

The application of the DIBEM to the Poisson type equation $\nabla^2 u = z$ is given in equation (2.77) as

$$\boldsymbol{Hu - Gq = \bar{A}\overline{N}} \tag{3.30}$$

where $\bar{\boldsymbol{A}} = (\boldsymbol{\alpha}(1), \ldots, \boldsymbol{\alpha}(n))^T$ and the unknown vectors $\boldsymbol{\alpha}(\xi)$ is obtained from the interpolation of right hand side function as explained in Section 2.3

$$\boldsymbol{\alpha}(\xi) = \boldsymbol{F^{-1}\Lambda}(\xi)\boldsymbol{z} \tag{3.31}$$

for each source point ξ.

Now, we apply the DIBEM to the steady MHD Stokes flow equations (3.3)-(3.5) by taking the non-homogeneous terms as

$$z_u = -\frac{\partial \omega}{\partial y} \ , \qquad z_v = \frac{\partial \omega}{\partial x} \tag{3.32}$$

$$z_\psi = -\omega, \tag{3.33}$$

$$z_\omega = M^2 \frac{\partial v}{\partial x}, \qquad z_p = -M^2 \frac{\partial v}{\partial y} \tag{3.34}$$

which results in discretized systems

$$\boldsymbol{Hu - Gq_u = \bar{A}_u \overline{N}} \tag{3.35}$$

$$\boldsymbol{Hv - Gq_v = \bar{A}_v \overline{N}} \tag{3.36}$$

$$\boldsymbol{H\psi - Gq_\psi = \bar{A}_\psi \overline{N}} \tag{3.37}$$

$$\boldsymbol{H\omega - Gq_\omega = \bar{A}_\omega \overline{N}} \tag{3.38}$$

$$\boldsymbol{Hp - Gq_p = \bar{A}_p \overline{N}}. \tag{3.39}$$

The matrices $\boldsymbol{\bar{A}_u}, \boldsymbol{\bar{A}_v}, \boldsymbol{\bar{A}_\psi}, \boldsymbol{\bar{A}_\omega}$ and $\boldsymbol{\bar{A}_p}$ are constructed by the unknown vectors $\boldsymbol{\alpha_u}(\xi)$, $\boldsymbol{\alpha_v}(\xi)$, $\boldsymbol{\alpha_\psi}(\xi)$, $\boldsymbol{\alpha_\omega}(\xi)$ and $\boldsymbol{\alpha_p}(\xi)$ as rows and these vectors are obtained from the interpolation equation (3.31) with the help of coordinate matrix $\boldsymbol{F}$ for the space

derivatives of the unknowns

$$\boldsymbol{\alpha_u}(\xi) = \boldsymbol{F^{-1}\Lambda}(\xi)\frac{\partial \boldsymbol{F}}{\partial y}\boldsymbol{F^{-1}}(-\boldsymbol{\omega}) \tag{3.40}$$

$$\boldsymbol{\alpha_v}(\xi) = \boldsymbol{F^{-1}\Lambda}(\xi)\frac{\partial \boldsymbol{F}}{\partial x}\boldsymbol{F^{-1}}\boldsymbol{\omega} \tag{3.41}$$

$$\boldsymbol{\alpha_\psi}(\xi) = \boldsymbol{F^{-1}\Lambda}(\xi)(-\boldsymbol{\omega}) \tag{3.42}$$

$$\boldsymbol{\alpha_\omega}(\xi) = \boldsymbol{F^{-1}\Lambda}(\xi)\frac{\partial \boldsymbol{F}}{\partial x}\boldsymbol{F^{-1}}(M^2\boldsymbol{v}) \tag{3.43}$$

$$\boldsymbol{\alpha_p}(\xi) = \boldsymbol{F^{-1}\Lambda}(\xi)\frac{\partial \boldsymbol{F}}{\partial y}\boldsymbol{F^{-1}}(-M^2\boldsymbol{v}) \tag{3.44}$$

for each source point $1 \leq \xi \leq N_b + N_i = n$. Here, the Lagrange interpolation is used for obtaining the unknown values of $\boldsymbol{\omega}$ and $\boldsymbol{v}$ at the interpolation points which are different from the source points.

The DIBEM system of MHD Stokes flow equations (3.35)-(3.39) are solved by the same iteration process described in 3.1.1 with preassigned tolerance $\epsilon = 10^{-3}$. We take $N_b = 60$ boundary nodes and $N_i = 225$ interior nodes for the Hartmann number values $M = 0, 30$. The numerical results are shown in terms of streamlines, vorticity and pressure contours in Figures 3.9-3.10.

In Figure 3.9, DIBEM results for $M = 0$ are in well agreement with the solutions given in [64].

Figure 3.10 shows the comparison of DIBEM and RBF solutions of MHD Stokes flow equations for $M = 30$. The flow and pressure behaviors obtained by DIBEM show the agreement with the behaviors obtained by RBF.

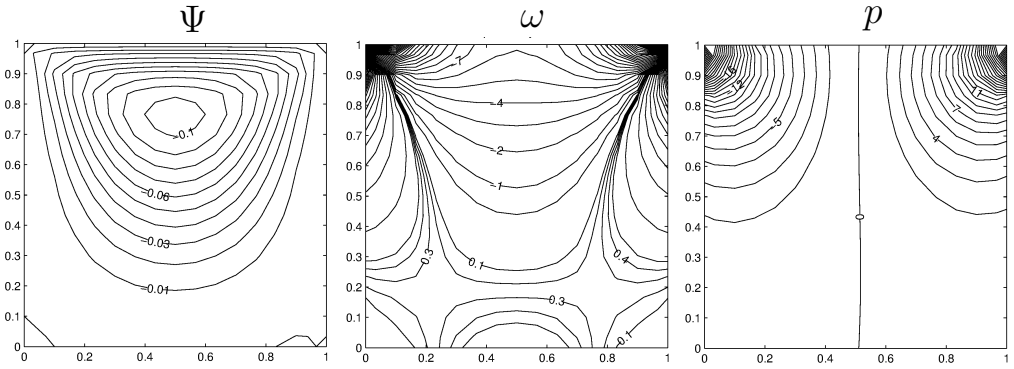

Figure 3.9: Problem 3.1: DIBEM solution of the MHD Stokes flow for $M = 0$.

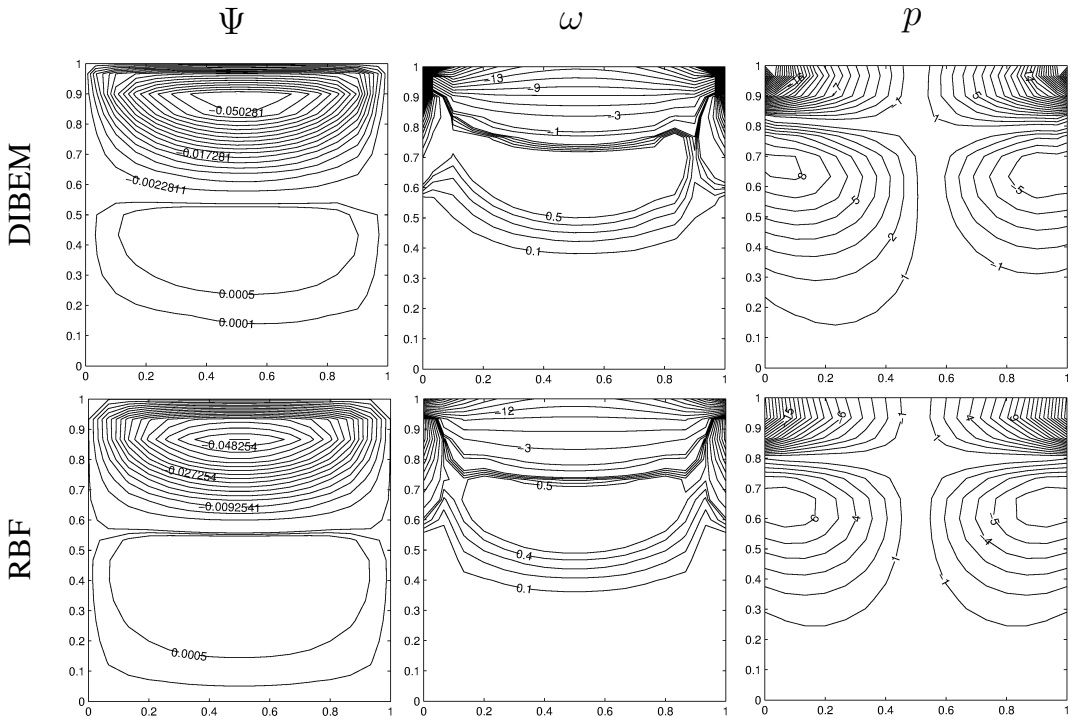

Figure 3.10: Problem 3.1: DIBEM and RBF solutions of the MHD Stokes flow for $M = 30$.

Table 3.2 shows the computational cost for the RBF, DRBEM and DIBEM solutions of MHD Stokes flow problem. We observe that DIBEM procedure takes much more computational time compared to DRBEM and RBF due to the interpolation for the domain integral. On the other hand, the RBF approximation gives solution of MHD Stokes flow problem with considerably less computational expense. Hence, we continue with the RBF approximation method for the rest of the MHD problem solutions in this thesis.

	CPU(s)	
	$M = 0$	$M = 30$
RBF	242.58	293.83
DRBEM	519.66	720.20
DIBEM	76116.88	99721.87

Table 3.2: CPU times for RBF, DRBEM and DIBEM solutions of MHD Stokes flow.

3.2 RBF Solution of the MHD Stokes Flow in a Constricted Cavity

We consider in this Section, the steady slow flow of a viscous, incompressible and electrically conducting fluid in channels with a constriction. The uniform magnetic field is applied in the x- or y- direction.

When the magnetic field is acted horizontally, that is $\boldsymbol{H_0} = (1, 0, 0)$, the non-dimensional governing MHD Stokes flow equations which are given in Chapter 1 (equations (1.27)-(1.29)) as

$$\frac{\partial u}{\partial x} + \frac{\partial v}{\partial y} = 0 \tag{3.45}$$

$$\nabla^2 u = \frac{\partial p}{\partial x}, \quad \nabla^2 v - M^2 v = \frac{\partial p}{\partial y} \quad . \tag{3.46}$$

Defining the stream function and vorticity in the $2D$ cross-section of the channel, these equations can be represented in terms of velocity components (u, v), stream function ψ, vorticity ω and pressure p as

$$\nabla^2 u = -\frac{\partial \omega}{\partial y} \ , \qquad \nabla^2 v = \frac{\partial \omega}{\partial x} \tag{3.47}$$

$$\nabla^2 \psi = -\omega \tag{3.48}$$

$$\nabla^2 \omega = M^2 \frac{\partial v}{\partial x} \ , \qquad \nabla^2 p = -M^2 \frac{\partial v}{\partial y} \tag{3.49}$$

where the Hartmann number $M = L\mu H_0 \sqrt{\sigma/\rho\nu}$ is the non-dimensional parameter.

When the magnetic field is applied vertically, $\boldsymbol{H_0} = (0, 1, 0)$, the steady MHD Stokes flow equations take the form (Chapter 1, equations (1.40)-(1.42))

$$\frac{\partial u}{\partial x} + \frac{\partial v}{\partial y} = 0 \tag{3.50}$$

$$\nabla^2 u = \frac{\partial p}{\partial x} + M^2 u, \quad \nabla^2 v = \frac{\partial p}{\partial y} \tag{3.51}$$

which can be also represented in terms of velocity components (u, v), stream function

ψ, vorticity ω and pressure p as

$$\nabla^2 u = -\frac{\partial \omega}{\partial y} \quad , \qquad \nabla^2 v = \frac{\partial \omega}{\partial x} \tag{3.52}$$

$$\nabla^2 \psi = -\omega \tag{3.53}$$

$$\nabla^2 \omega = -M^2 \frac{\partial u}{\partial y} \quad , \qquad \nabla^2 p = -M^2 \frac{\partial u}{\partial x}. \tag{3.54}$$

The difference is only in the right hand sides of vorticity and pressure Poisson's equations. Velocity and stream function equations are not affected with the direction of magnetic field.

Application of the RBF approximation (2.31) to the equations (3.47)-(3.49) and (3.52)-(3.54), and using the coordinate matrix $\boldsymbol{F}$ for the required space derivatives of the unknowns, we get the discretized systems of MHD Stokes flow equations when the magnetic field applies in the $x-$direction

$$\boldsymbol{u} = \boldsymbol{g_u} - \boldsymbol{K}(\frac{\partial \boldsymbol{F}}{\partial y}\boldsymbol{F^{-1}}\boldsymbol{\omega}) \tag{3.55}$$

$$\boldsymbol{v} = \boldsymbol{g_v} + \boldsymbol{K}(\frac{\partial \boldsymbol{F}}{\partial x}\boldsymbol{F^{-1}}\boldsymbol{\omega}) \tag{3.56}$$

$$\boldsymbol{\psi} = \boldsymbol{g_\psi} + \boldsymbol{K}(\boldsymbol{-\omega}) \tag{3.57}$$

$$\boldsymbol{\omega} = \boldsymbol{g_\omega} + M^2\boldsymbol{K}(\frac{\partial \boldsymbol{F}}{\partial x}\boldsymbol{F^{-1}}\boldsymbol{v}) \tag{3.58}$$

$$\boldsymbol{p} = \boldsymbol{g_p} - M^2\boldsymbol{K}(\frac{\partial \boldsymbol{F}}{\partial y}\boldsymbol{F^{-1}}\boldsymbol{v}), \tag{3.59}$$

and when the magnetic field applies in the $y-$direction

$$\boldsymbol{u} = \boldsymbol{g_u} - \boldsymbol{K}(\frac{\partial \boldsymbol{F}}{\partial y}\boldsymbol{F^{-1}}\boldsymbol{\omega}) \tag{3.60}$$

$$\boldsymbol{v} = \boldsymbol{g_v} + \boldsymbol{K}(\frac{\partial \boldsymbol{F}}{\partial x}\boldsymbol{F^{-1}}\boldsymbol{\omega}) \tag{3.61}$$

$$\boldsymbol{\psi} = \boldsymbol{g_\psi} + \boldsymbol{K}(\boldsymbol{-\omega}) \tag{3.62}$$

$$\boldsymbol{\omega} = \boldsymbol{g_\omega} - M^2\boldsymbol{K}(\frac{\partial \boldsymbol{F}}{\partial y}\boldsymbol{F^{-1}}\boldsymbol{u}) \tag{3.63}$$

$$\boldsymbol{p} = \boldsymbol{g_p} - M^2\boldsymbol{K}(\frac{\partial \boldsymbol{F}}{\partial x}\boldsymbol{F^{-1}}\boldsymbol{u}) \tag{3.64}$$

where the vectors $\boldsymbol{g_u}$, $\boldsymbol{g_v}$, $\boldsymbol{g_\psi}$, $\boldsymbol{g_\omega}$, $\boldsymbol{g_p}$ and the matrices$\boldsymbol{K}$, $\boldsymbol{F}$ are derived in the Section 2.1.2.

The iterative process starts with an initial estimate for the vorticity, then the velocity equations (3.55)-(3.56) or (3.60)-(3.61) and the stream function equation (3.57) or

(3.62) are solved. After the unknown vorticity boundary conditions are obtained from the stream function equation by using the finite difference scheme or vorticity definition by using coordinate matrix $\boldsymbol{F}$, the vorticity equation (3.58) or (3.63) is solved. In order to accelerate the convergence we use a relaxation parameter α_ω, $0 < \alpha_\omega < 1$ for the vorticity. Then, the unknown pressure boundary values are derived by using coordinate matrix $\boldsymbol{F}$ for the Laplacian of u and v, and the finite difference scheme for the pressure derivatives in (3.46) or (3.51). Since the boundary of the constricted channel is a curved boundary , the Taylor series expansion of the pressure is written on the boundary points by using the interior points in the perpendicular axis direction. Finally, the pressure equation (3.59) or (3.64) is solved. The relaxation parameter α_p, $0 < \alpha_p < 1$ is used for the pressure to accelerate the convergence. The iteration continues until a preassigned tolerance ϵ is reached between two successive iterations.

The iterative process is applied to solve the MHD Stokes flow in a constricted cavity under the influence of external magnetic field applied horizontally or vertically. The two-dimensional steady Stokes flow of a viscous, incompressible and electrically conducting fluid is considered in a constricted square cavity with a moving left wall. Stokes flow is subjected to the uniform magnetic field in the horizontal or vertical direction. The middle section of the square cavity is symmetrically constricted using functions f_b and f_t, which are the vertical coordinates of the bottom and top walls, respectively. These functions are given as,

$$f_b(x) = \frac{1}{2}h(1 + \cos(2\pi(x - \frac{1}{2}))) \ ,$$
$$f_t(x) = 1 - f_b(x)$$

where $0 \leq x \leq 1$ and the constriction ratio(CR) of the cavity is defined as $CR = 2h \times 100$. The problem geometry and the boundary conditions are shown in the Figure 3.11. The vorticity boundary values are obtained from the stream function equation by using the finite difference method including interior values of stream function. The unknown pressure boundary values are found by a finite difference scheme for the pressure derivatives and coordinate matrix for the space derivatives in (3.46) (or (3.51) for the applied magnetic field in the y-direction).

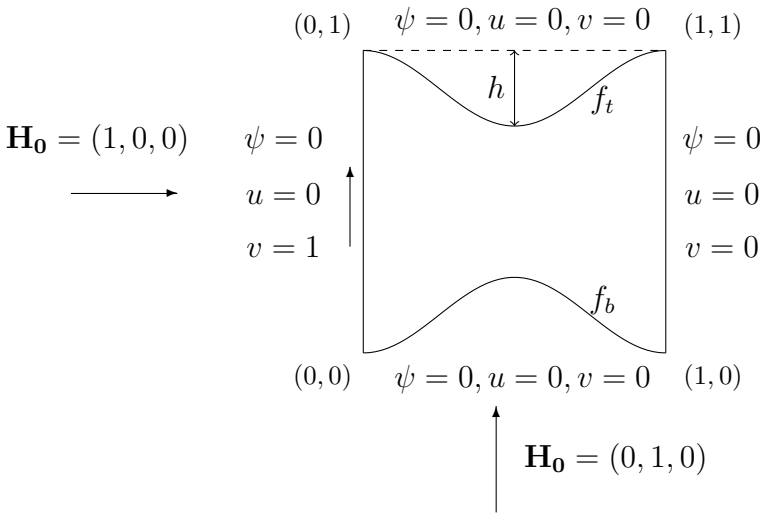

Figure 3.11: Problem 3.2: Schematic of the square cavity with constriction and the boundary conditions

The numerical results are obtained from the RBF iteration process which is explained in the previous section by using a linear polynomial radial basis function ($\varphi = 1 + r$). The tolerance for the stopping criteria is taken as 10^{-3}. We use relaxation parameters $\alpha_\omega = 0.01$ and $\alpha_p = 0.001$ for the vorticity and pressure convergence acceleration. The boundary of the cavity is discretized by $N_b = 96$ boundary points. To see the effects of both magnetic field in the x- or y-direction and the constriction of the channel on the Stokes flow we take several values of Hartmann number ($0 \leq M \leq 100$) and the constriction ratio of the cavity ($0\% \leq CR \leq 75\%$).

First, we consider MHD Stokes flow in a square cavity with 0% constriction and moving left wall upwards under the effect of horizontally applied magnetic field. The numerical solution is depicted in terms of streamlines, vorticity and pressure contours in Figure 3.12 for increasing values of Hartmann number. Figure 3.12 shows the effect of magnetic field on the Stokes flow in a non-constricted cavity. In the absence of the magnetic field, Stokes flow is concentrated in front of the left moving wall with a similar profile as obtained in a cavity with moving top lid [64]. Pressure profiles are antisymmetric with respect to $y = 0.5$ line. As the intensity of the magnetic field increases, fluid flows in almost all parts of the cavity. Also, the main vortex of the flow shifts through the center of the cavity with an increasing magnitude. Further increase in M causes side layers to be formed on the walls parallel to the applied magnetic

field and also Hartmann layers on the vertical walls especially pronounced on the left wall with the effect of its movement upwards. The vorticity has the expected behavior due to the movement of the left wall when M is small. But, it forms the boundary layers leaving the central part of the cavity almost stagnant as M increases. Pressure is uniformly distributed with an increasing value between the top and the bottom walls as M increases.

In Figure 3.13, we fix the constriction ratio to $CR = 25\%$ and increase Hartmann number to analyze the impact of the horizontal magnetic field on the Stokes flow in a constricted cavity. When the channel is constricted, pressure tends to be increased at the right corners, the behavior of the flow does not change significantly, but the flow is mostly concentrated near the left moving wall and in the constricted area leaving the parts close to the right corners stagnant. Horizontally applied magnetic field with an increasing intensity retards the effect of moving left wall as in the case of non-constricted cavity (Figure 3.12) extending the flow to the whole cavity.

The effect of the constriction ratio on the MHD Stokes flow under the effect of horizontal magnetic field is depicted in Figure 3.14 for a fixed Hartmann number $M = 10$. When the constriction is further increased, the fluid completely flows in the left constricted part and the rest of the cavity is stagnant. Constriction deteriorates the uniform distribution of pressure. Pressure contours are anti-symmetrically squeezed through the corners of the cavity with respect to $y = 0.5$ line.

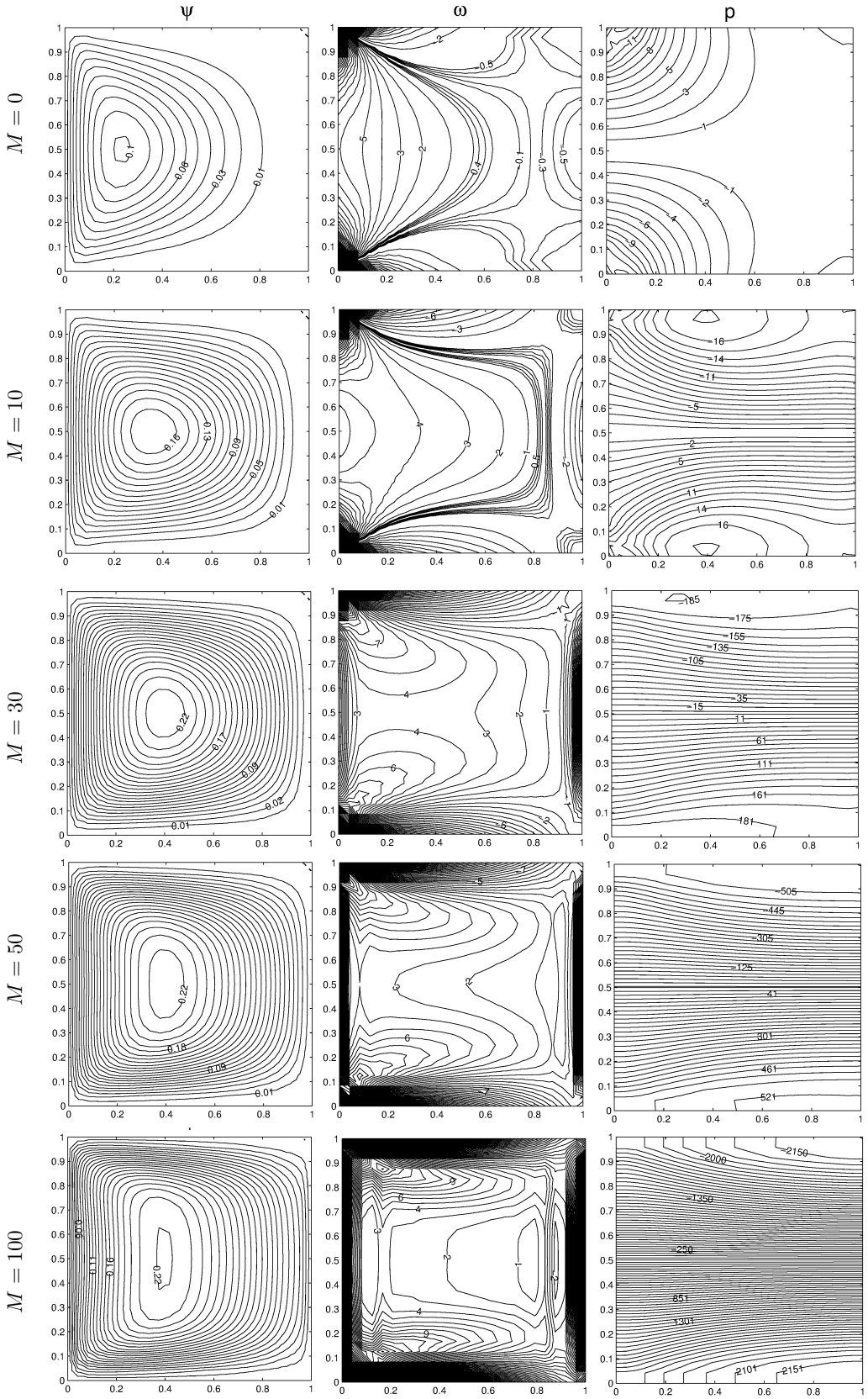

Figure 3.12: Problem 3.2: MHD Stokes flow with $CR = 0\%$, $\mathbf{H_0} = (1, 0, 0)$.

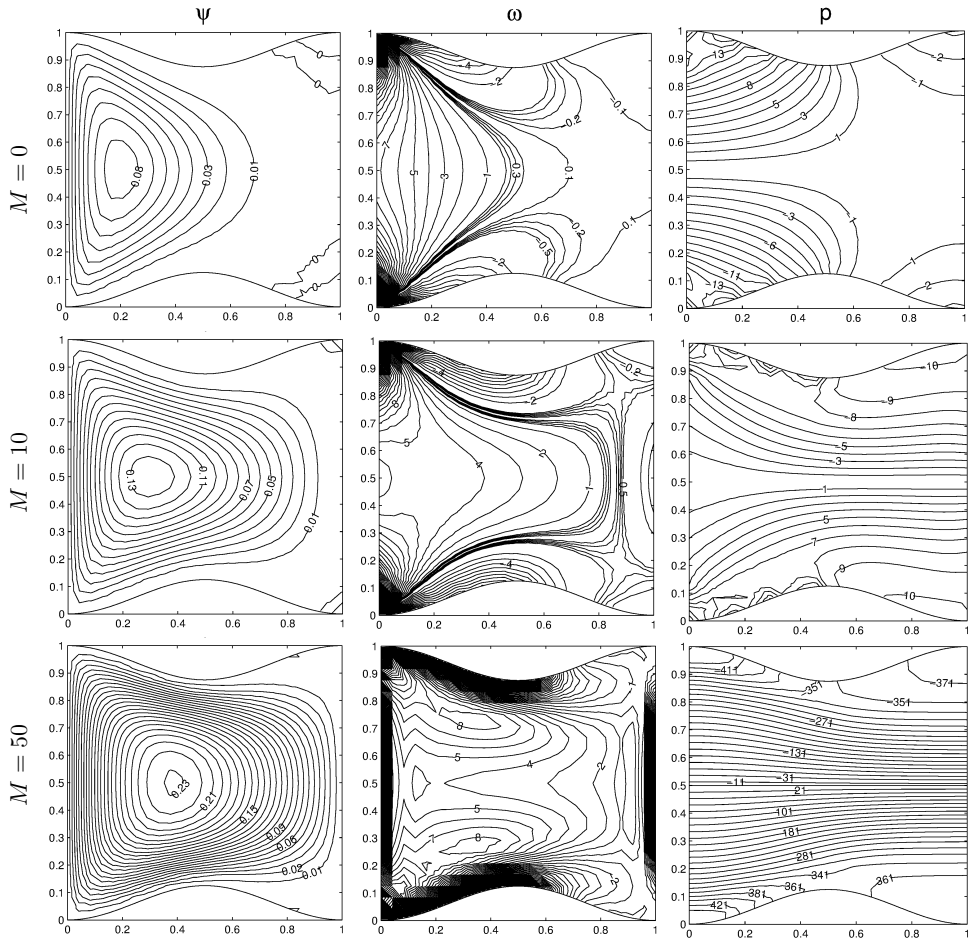

Figure 3.13: Problem 3.2: MHD Stokes flow with $CR = 25\%$, $\mathbf{H_0} = (1, 0, 0)$.

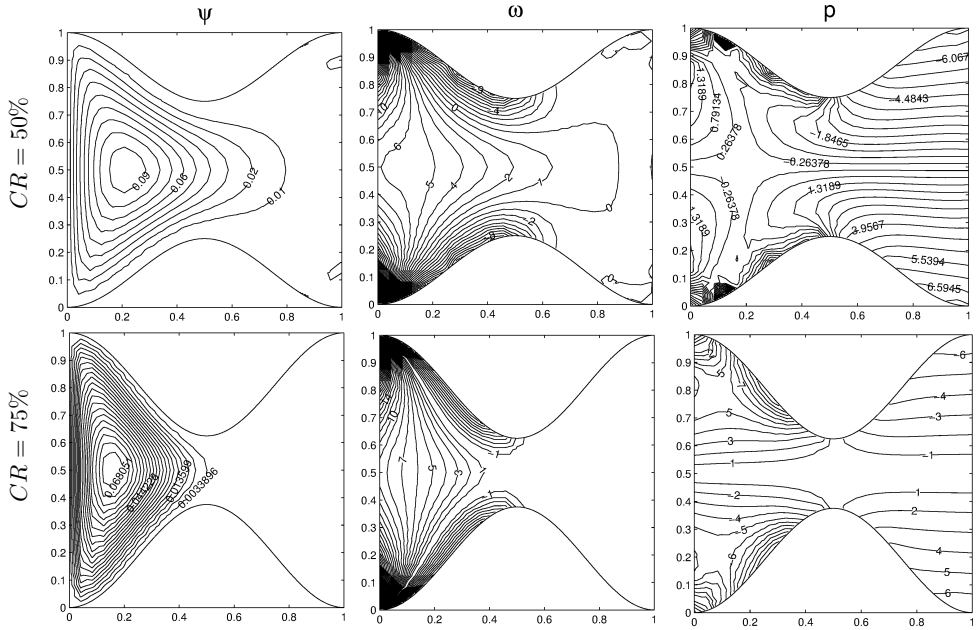

Figure 3.14: Problem 3.2: MHD Stokes flow with $M = 10$, $\mathbf{H_0} = (1, 0, 0)$.

The impact of the vertical magnetic field on the Stokes flow in the constricted cavity is also analyzed in Figures 3.15-3.17.

The influence of the vertical magnetic field on the creeping flow in the non-constricted cavity with a moving left lid is shown in Figure 3.15. The behaviors of the flow and pressure are completely different from the ones obtained with horizontally applied magnetic field which can be seen by comparing the results given in Figure 3.12 and Figure 3.15. As M increases, the flow is completely concentrated through the moving left wall forming boundary side layer. This is due to the direction of magnetic field which is the same with the moving left wall. Further increase in M, secondary flow with a small magnitude occurs and the rest of the cavity is stagnant. As the strength of the vertical magnetic field increases, pressure is distributed anti-symmetrically with respect to horizontal centerline of the cavity in terms of two loops mostly concentrated near the left moving wall.

Figure 3.16 shows that constricted cavity with the ratio $CR = 25\%$ causes secondary flow and pressure appearance near the right corners when the magnetic field effect is absent. As M increases, secondary flow near the right wall enlarges first due to the constriction, but a further increase in M again pushes the flow through the moving left wall contrary to the effect of horizontally applied magnetic field. It was observed in Figure 3.13 that magnetic field acted in the $x-$direction retards the effect of moving lid and causes the fluid to flow in the whole cavity.

In Figure 3.17, we see the influence of further constrictions of the cavity on the MHD Stokes flow when the Hartmann number is fixed as $M = 10$. Secondary flow in front of the right wall enlarges first when the cavity is constricted. Then, 75% constriction and moving left wall effects weaken this secondary flow and move the fluid through the left wall. The vorticity and pressure concentrate in front of the left moving lid as in the case of magnetic field acted in $x-$direction (Figure 3.14). Pressure appears at the right corners with an increasing value due to increase in the constriction showing the anti-symmetric profile again with respect to $y = 0.5$.

As a result, we conclude that horizontal magnetic field causes the flow to be spreaded to the whole channel, but this effect is weakened when the cavity is further constricted in the sense that flow is completely squeezed through the moving left wall. On the

other hand, vertical magnetic field forces the flow to concentrate in front of the moving left wall, and the constriction leads to flow to the right part of the constricted channel.

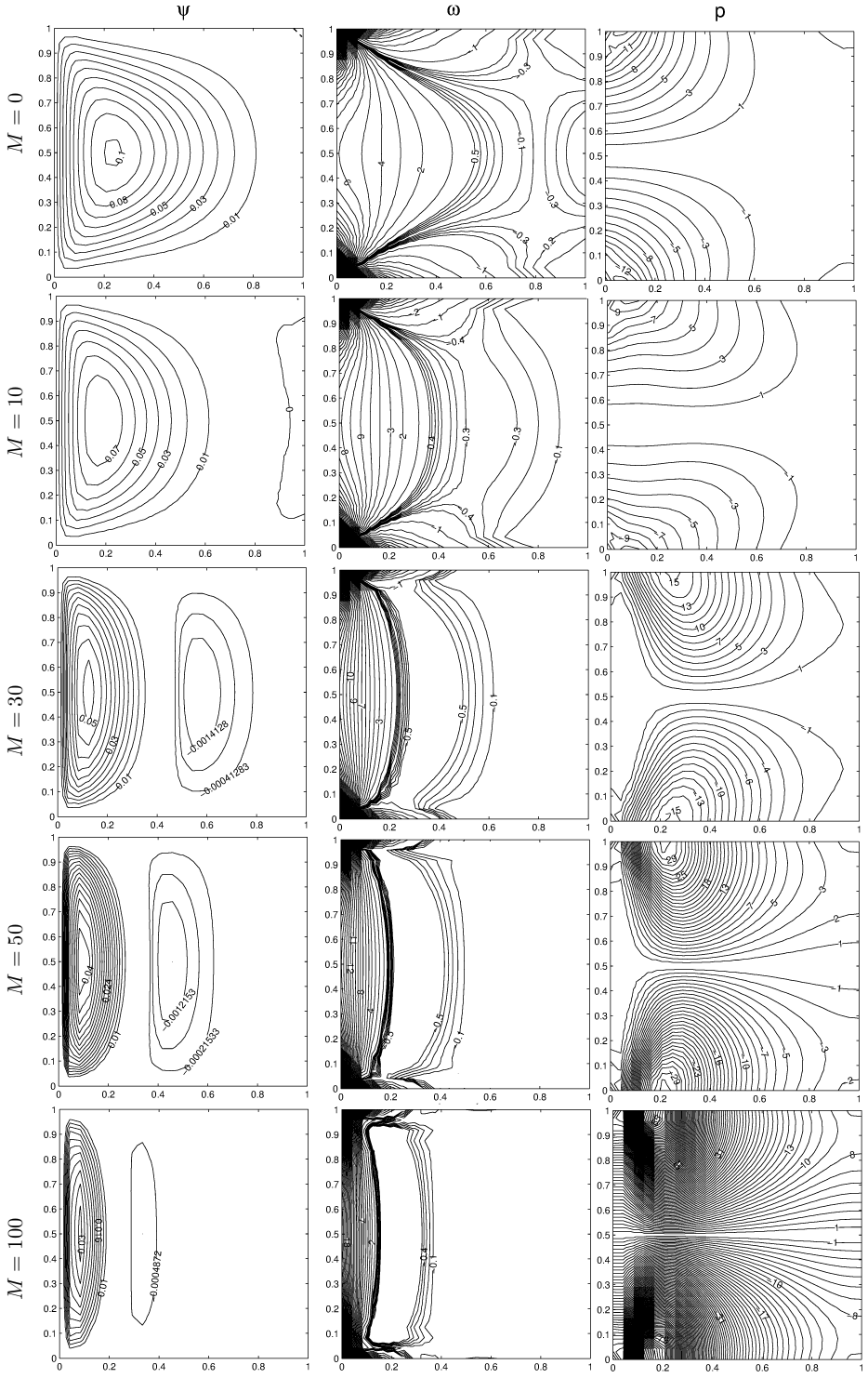

Figure 3.15: Problem 3.2: MHD Stokes flow with $CR = 0\%$, $\mathbf{H_0} = (0, 1, 0)$.

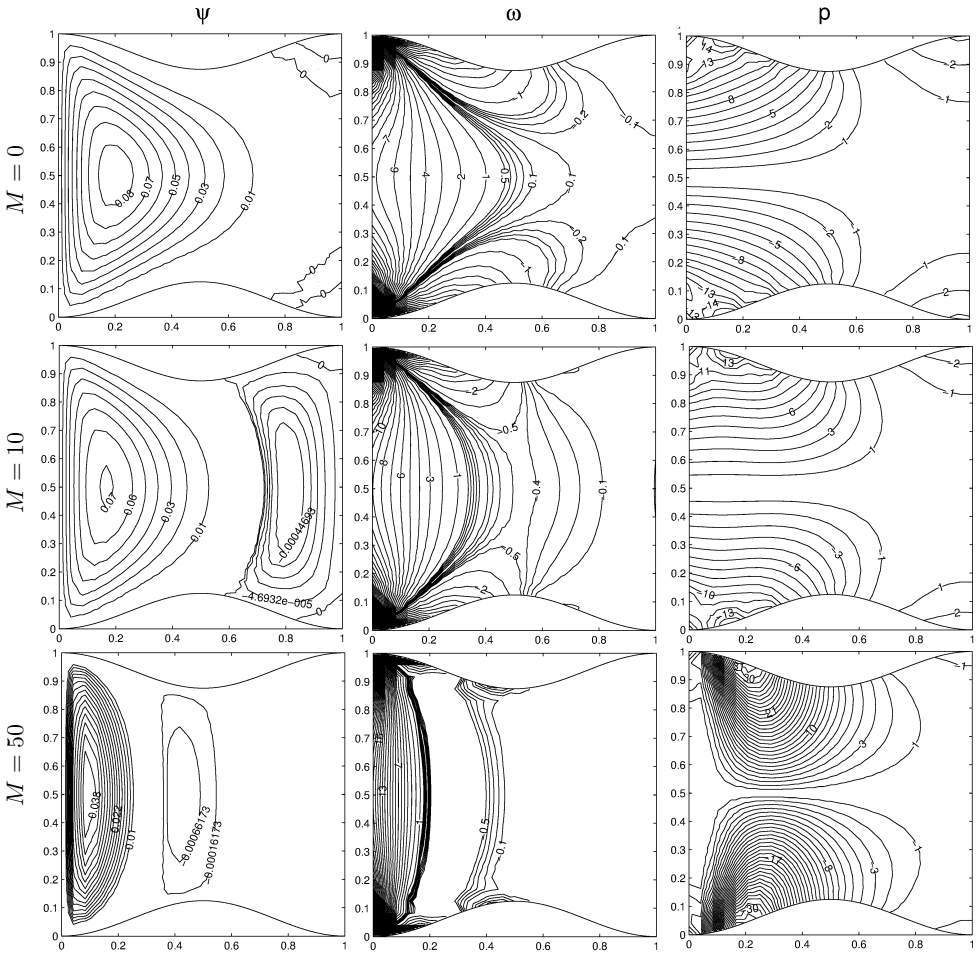

Figure 3.16: Problem 3.2: MHD Stokes flow with $CR = 25\%$, $\mathbf{H_0} = (0, 1, 0)$.

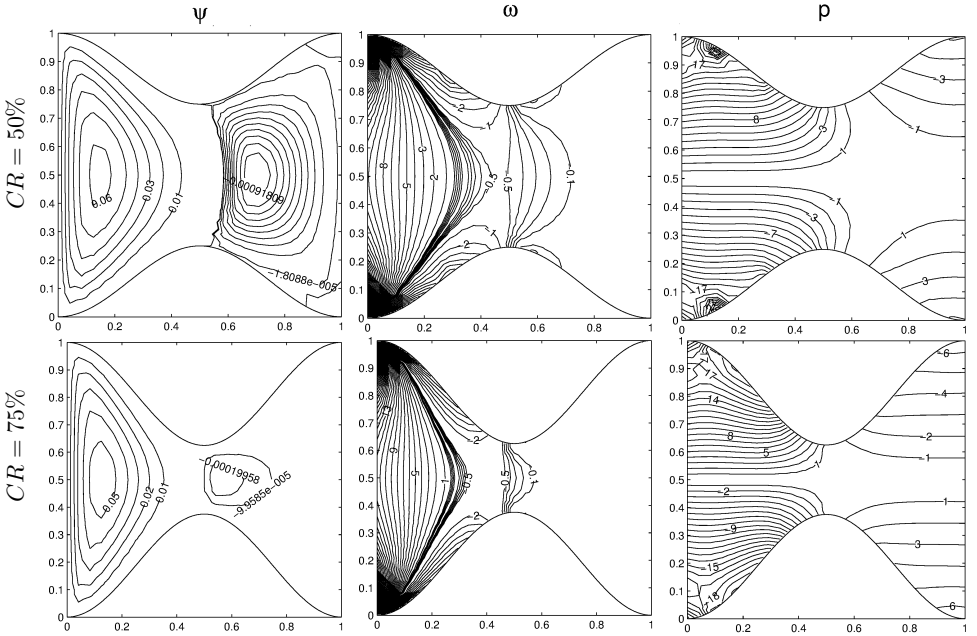

Figure 3.17: Problem 3.2: MHD Stokes flow with $M = 10$, $\mathbf{H_0} = (0, 1, 0)$.

3.3 RBF Solution of the MHD Stokes Flow in a Backward-Facing Step Channel

In this Section, we analyze Stokes flow over backward-facing step channel under the effect of a horizontally or vertically applied magnetic field. The problem configuration and boundary values are shown in Figure 3.18. At the inlet, a parabolic velocity profile is prescribed so that vorticity varies linearly ($\omega = \dfrac{\partial v}{\partial x} - \dfrac{\partial u}{\partial y}$). No-slip boundary conditions for u and v are imposed on the channel walls. At the exit, Neumann boundary conditions are imposed for u, w and ψ with the assumption of fully developed flow. Pressure reduces to zero and the v velocity component is obviously zero at the exit. The unknown vorticity boundary conditions are obtained from the vorticity definition by using the coordinate matrix $\boldsymbol{F}$ which gives better results than obtained from the stream function equation by using finite difference scheme. The unknown pressure boundary values are obtained from equations (3.46) (or (3.51) for magnetic field in the y-direction) by using coordinate matrix $\boldsymbol{F}$ for the space derivatives and the finite difference scheme for the pressure gradients.

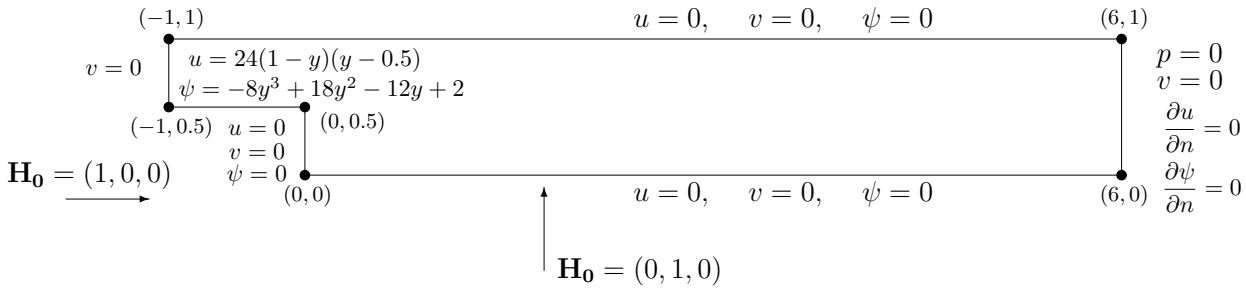

Figure 3.18: Problem 3.3: Backward-Facing step channel and boundary conditions

Numerical solutions are obtained by taking stopping criteria as 10^{-3} for fixed relaxation parameters of vorticity and pressure as $\alpha_\omega = 0.01$ and $\alpha_p = 0.5$. In the case of horizontally applied magnetic field we take $N_b = 224$ boundary and $N_i = 1163$ interior points for the several values of Hartmann numbers.

Figure 3.19 is in well agreement with the ones in [9], since $M = 0$ for $Re << 1$ corresponds to the Stokes flow over a backward-facing step. Streamlines starts the channel with a negative value. Effect of the step is small at $M = 0$ due to the slow motion of the fluid. In front of the step the same direction recirculated flow appears

(drops), but a secondary opposite direction flow is developed in the upper part of the channel starting around the step. Centerline velocities for $M = 0$ are presented in Figure 3.20. One can observe that parabolic profile of u velocity is maintained through the channel which is in well agreement with the Stokes step channel flow centerline velocities obtained by [9].

In Figures 3.21-3.23, we see that, as the horizontal magnetic field intensity increases, the recirculation flow in front of the step enlarges. The secondary flow developed in front of the channel is squeezed through the upper wall and through the entrance. As M is increased further ($M = 90$), the same direction flow in front of the step which is small in magnitude tends to reach fully-developed profile through the exit of the channel. This shows the effect of external magnetic field which is applied in the direction of the flow. The main flow gets fully developed in a much shorter length of the channel as can be seen from Figure 3.23.

From the $u-$velocity figures we also notice the drop of the fluid in front of the step from its parabolic profile. It reaches fully developed profile through the exit. A further increase in M leaves a small stagnant region in front of the step and then overwhelms the effect of the step pushing the fluid above the bottom plate (Figure 3.23).

It can be concluded that the MHD flow in a step channel is subjected to the following variations. Fluid enters the channel with a constant pressure ($p = 48$). The step causes small disturbance at the corner even at $M = 0$, and then, pressure diminishes smoothly ($p = 0$) through the exit in Figure 3.19. Pressure of the fluid increases as M increases, and the disturbance due to the step is more pronounced in the narrow entrance region and around the step. This is the expected behavior of the pressure in a channel containing a step.

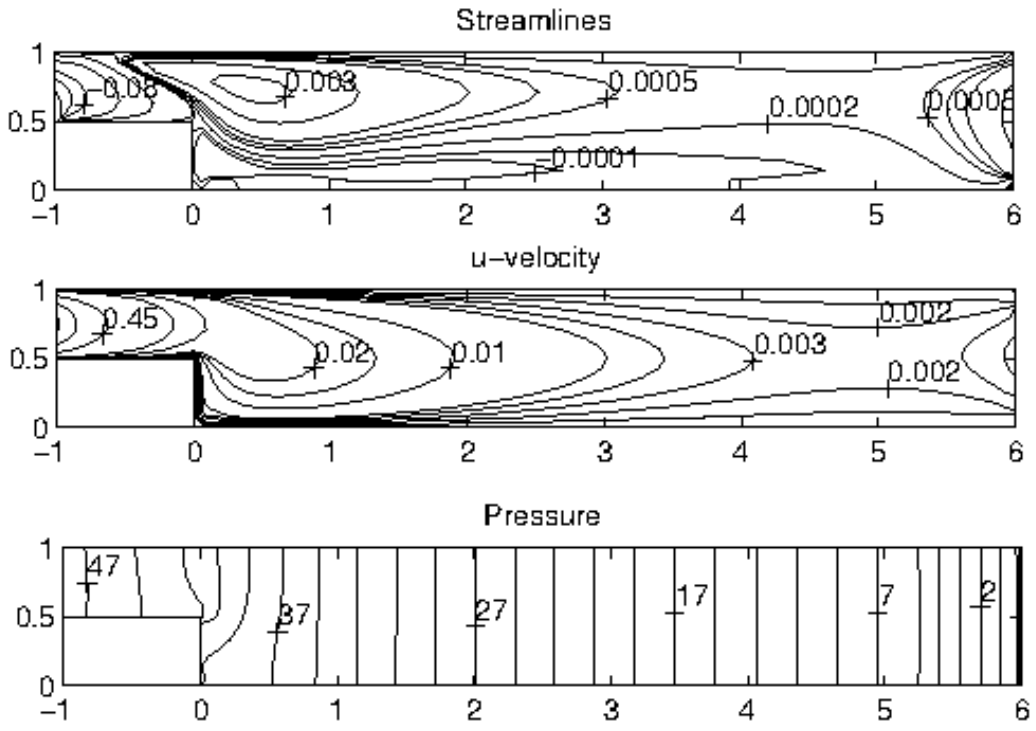

Figure 3.19: Problem 3.3: MHD Stokes flow with $M = 0$, $\mathbf{H_0} = (1, 0, 0)$.

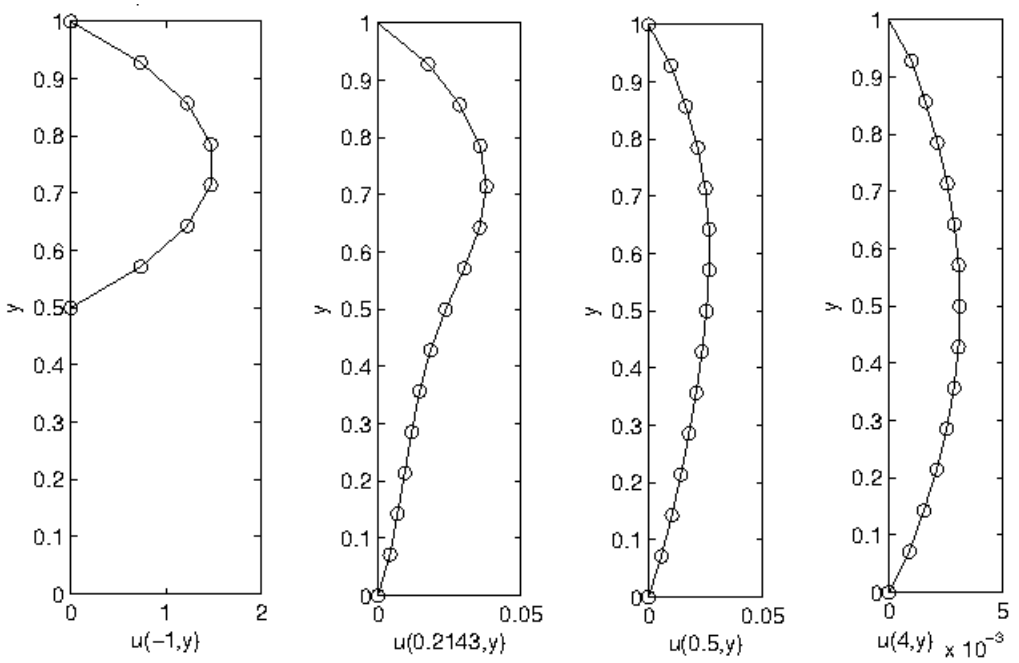

Figure 3.20: Problem 3.3: Centerline velocities for $M = 0$, $\mathbf{H_0} = (1, 0, 0)$.

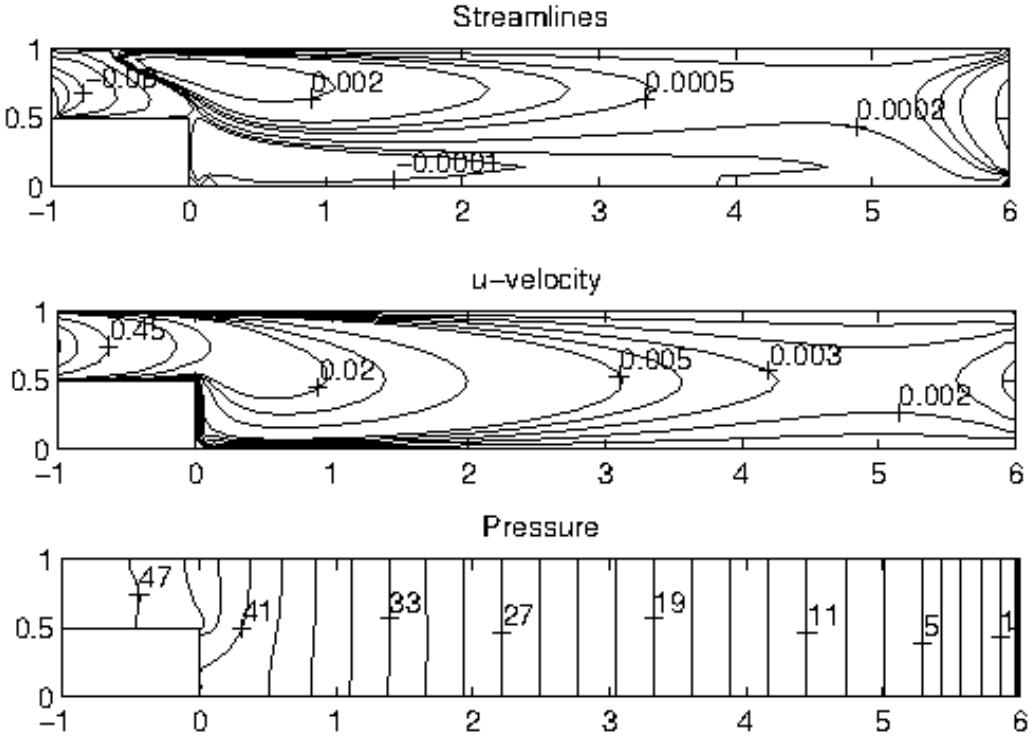

Figure 3.21: Problem 3.3: MHD Stokes flow with $M = 10$, $\mathbf{H_0} = (1, 0, 0)$.

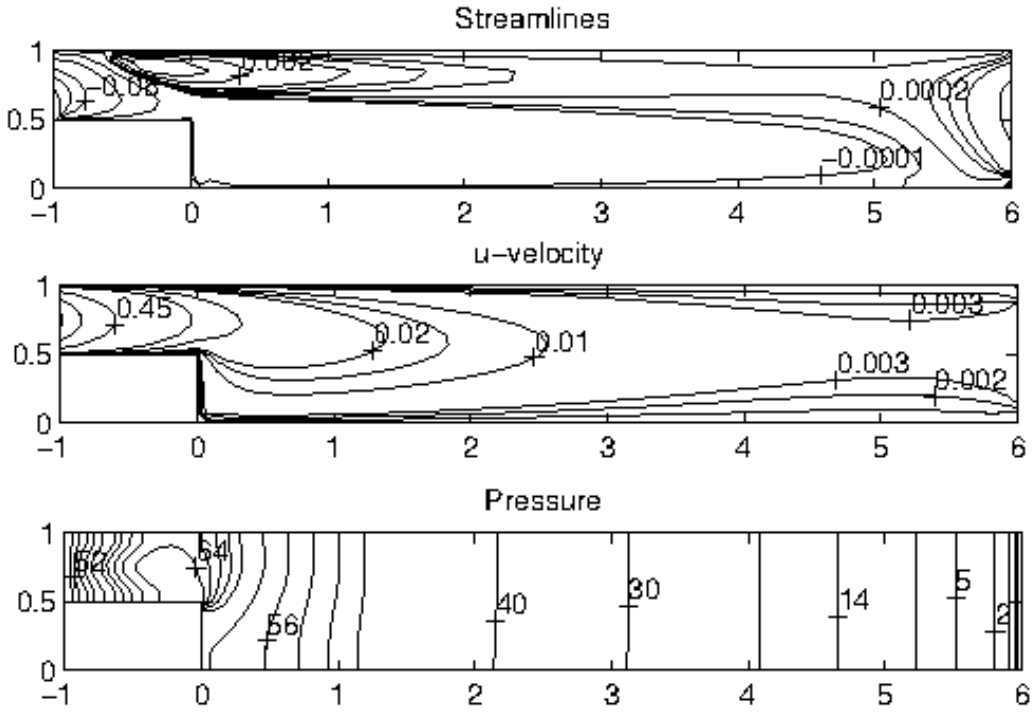

Figure 3.22: Problem 3.3: MHD Stokes flow with $M = 30$, $\mathbf{H_0} = (1, 0, 0)$.

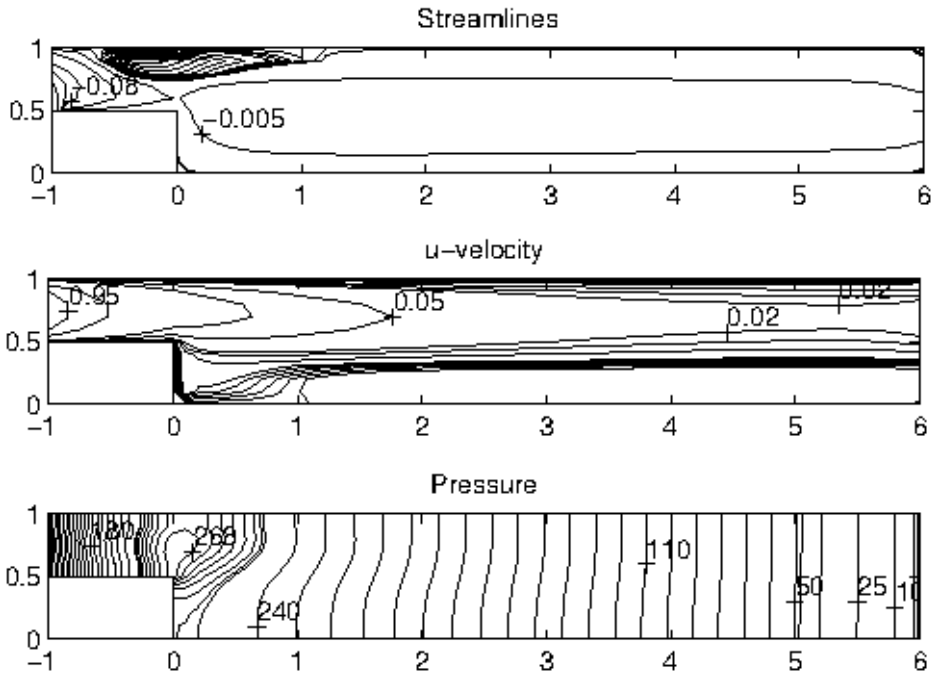

Figure 3.23: Problem 3.3: MHD Stokes flow with $M = 90$, $\mathbf{H_0} = (1, 0, 0)$.

The behavior of Stokes flow over the step channel under the effect of vertical magnetic field is simulated by taking $N_b = 200$ boundary and $N_i = 1463$ interior points for $M = 0, 10, 30$. When the Harmann number increases up to 50, more discretization points ($N_b = 224, N_i = 1649$) are taken to obtain smooth results.

In Figure 3.24, we again present $M = 0$ case which is the Stokes flow as in Figure 3.19. The entrance (main) flow drops in front of the step, a secondary flow close to the upper plate extends through the channel. As M increases, secondary flow covers almost whole channel after the step. Meantime, the main flow in front of the step is getting smaller as M gets larger, as can be seen from Figures 3.25-3.27.

From the $u-$velocity profiles we deduce that as Hartmann number increases, fluid is pushed through the entrance and the flow is concentrated in front of the entrance region. Thus, the flow is retarded with decreasing magnitude throughout the channel.

Pressure shows the same behavior as in the case of horizontal magnetic field. The increase in the intensity of the vertical magnetic field increases pressure values due to square of Hartmann number in front of the non-homogeneous term of pressure equation.

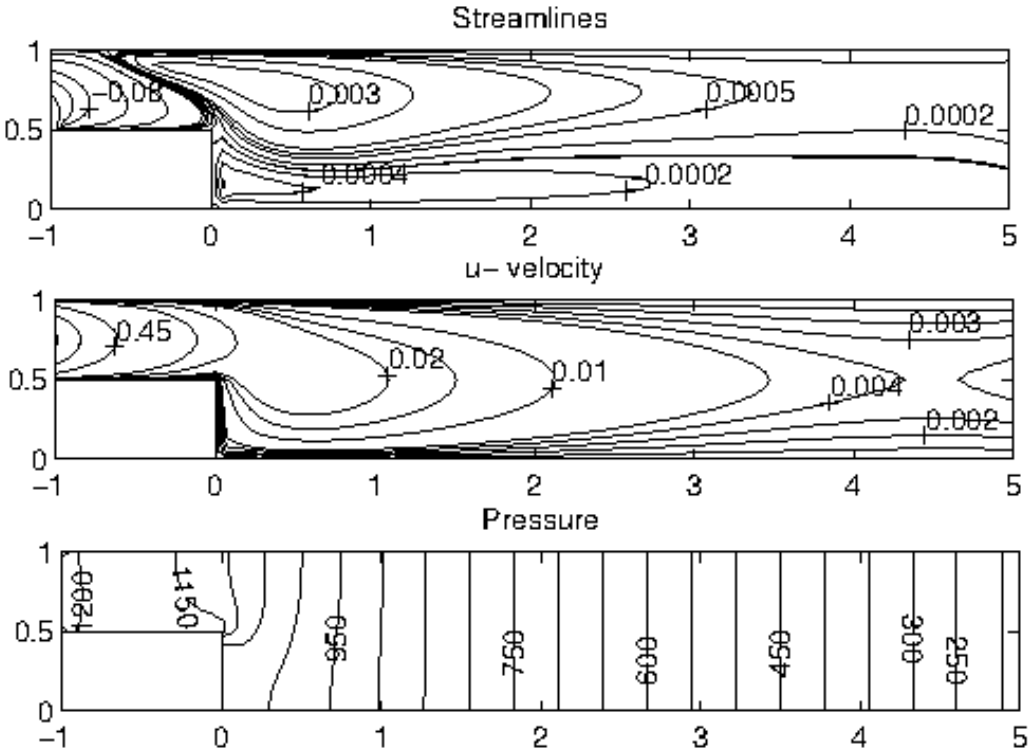

Figure 3.24: Problem 3.3: MHD Stokes flow with $M = 0$, $\mathbf{H_0} = (0, 1, 0)$.

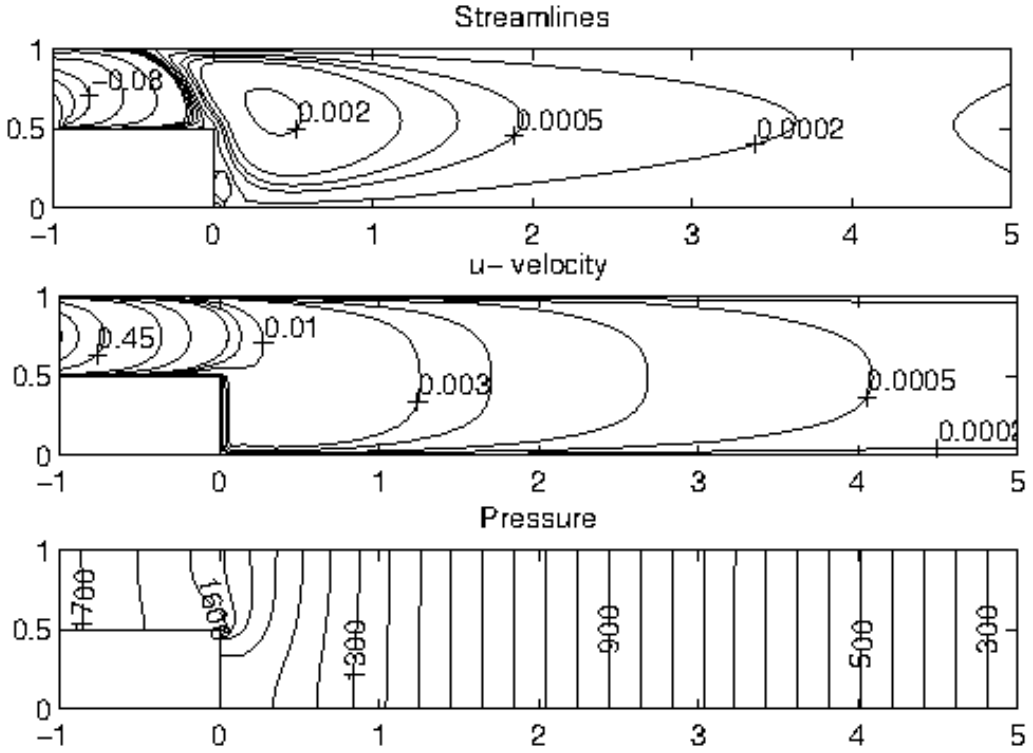

Figure 3.25: Problem 3.3: MHD Stokes flow with $M = 10$, $\mathbf{H_0} = (0, 1, 0)$.

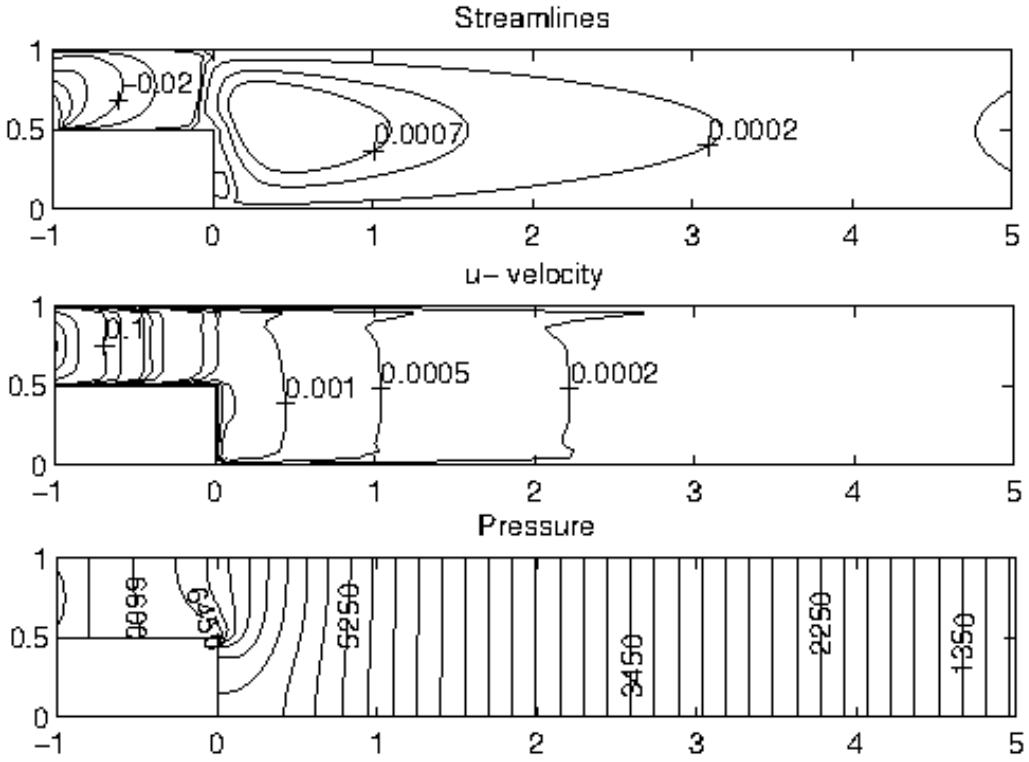

Figure 3.26: Problem 3.3: MHD Stokes flow with $M = 30$, $\mathbf{H_0} = (0, 1, 0)$.

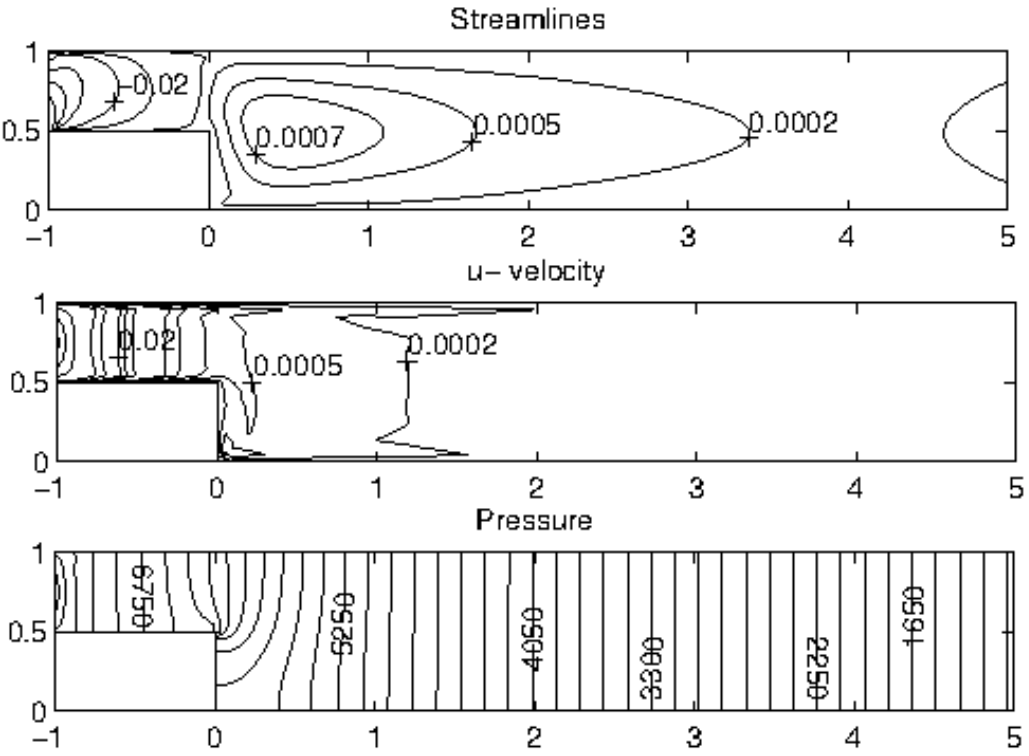

Figure 3.27: Problem 3.3: MHD Stokes flow with $M = 50$, $\mathbf{H_0} = (0, 1, 0)$.

3.4 RBF Solution of the MHD Stokes flow with Electric Potential

Finally, the effect of the external magnetic field applied in the pipe-axis direction is analyzed on the Stokes flow in a lid-driven cavity. This problem differs from the Stokes flow only with the generation of electric potential due to the application of the magnetic field in the $z-$direction.

The steady slow flow of a viscous, incompressible and electrically conducting fluid is considered in a lid-driven square cavity under the influence of a uniform magnetic field in the pipe-axis direction (Figure 3.28).

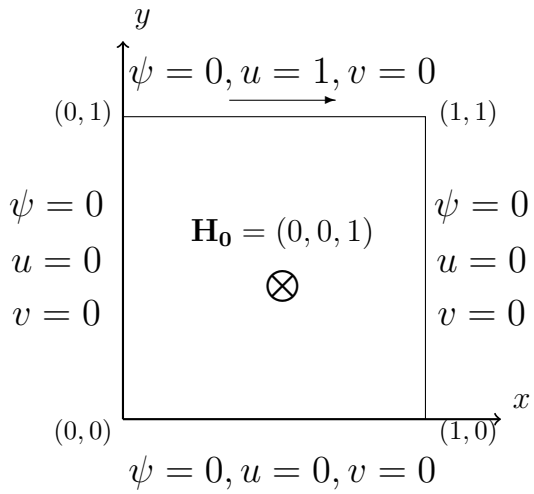

Figure 3.28: Problem 3.4: Lid-driven cavity with electric potential and boundary conditions.

The non-dimensional governing equations of MHD Stokes flow in terms of velocity components (u, v), pressure p and electric potential ϕ are given in Chapter 1 (equations (1.46)-(1.48)) as

$$\frac{\partial u}{\partial x} + \frac{\partial v}{\partial y} = 0 \tag{3.65}$$

$$\nabla^2 u = \frac{\partial p}{\partial x} - M^2(-\frac{\partial \phi}{\partial y} - u) \tag{3.66}$$

$$\nabla^2 v = \frac{\partial p}{\partial y} - M^2(\frac{\partial \phi}{\partial x} - v) \tag{3.67}$$

which can be written in all fluid variables u, v, ψ, ϕ, ω and p

$$\nabla^2 u = -\frac{\partial \omega}{\partial y} \ , \qquad \nabla^2 v = \frac{\partial \omega}{\partial x} \tag{3.68}$$

$$\nabla^2 \psi = -\omega \ , \qquad \nabla^2 \phi = \omega \tag{3.69}$$

$$\nabla^2 \omega = 0 \ , \qquad \nabla^2 p = 0. \tag{3.70}$$

Since the Hartmann number is disappeared in this formulation, the increase in the magnetic field intensity can not affect the flow behavior.

The boundary conditions for the velocity and stream function are shown in the Figure 3.28. The unknown boundary conditions for the vorticity are obtained from the finite difference approximation of the stream function equation including interior values of stream function. Pressure boundary values are computed by using the finite difference scheme for the gradient of pressure and the coordinate matrix for the space derivatives in the momentum equations (3.66)-(3.67). For the electric potential both insulated ($\frac{\partial \phi}{\partial n} = 0$) and conducting ($\phi = 0$) wall conditions are considered.

The application of the RBF approximation (2.31) to MHD Stokes flow equations with electric potential (3.68)-(3.70) with the help of coordinate matrix $\boldsymbol{F}$ for space derivatives of ω gives the matrix system

$$\boldsymbol{u} = \boldsymbol{g_u} - \boldsymbol{K}(\frac{\partial \boldsymbol{F}}{\partial y}\boldsymbol{F^{-1}}\boldsymbol{\omega}) \tag{3.71}$$

$$\boldsymbol{v} = \boldsymbol{g_v} + \boldsymbol{K}(\frac{\partial \boldsymbol{F}}{\partial x}\boldsymbol{F^{-1}}\boldsymbol{\omega}) \tag{3.72}$$

$$\boldsymbol{\psi} = \boldsymbol{g_\psi} + \boldsymbol{K}(-\boldsymbol{\omega}) \tag{3.73}$$

$$\boldsymbol{\phi} = \boldsymbol{g_\phi} + \boldsymbol{K}\boldsymbol{\omega} \tag{3.74}$$

$$\boldsymbol{\omega} = \boldsymbol{g_\omega} \tag{3.75}$$

$$\boldsymbol{p} = \boldsymbol{g_p} \tag{3.76}$$

where the vectors $\boldsymbol{g_\xi} = \boldsymbol{R_1}\boldsymbol{\xi_{bc}}$, $\boldsymbol{\xi}$ denotes $\boldsymbol{u}$, $\boldsymbol{v}$, $\boldsymbol{\psi}$, $\boldsymbol{\phi}$, $\boldsymbol{\omega}$, $\boldsymbol{p}$, and the matrices$\boldsymbol{K}$, $\boldsymbol{R_1}$ and $\boldsymbol{F}$ are given in the Section 2.1.2.

The iteration starts with an initial estimate for the vorticity to solve the velocity equations (3.71)-(3.72). Then, the stream function and the electric potential equations are solved. After the vorticity boundary values are computed from the stream function equation by using finite difference scheme, vorticity equation (3.75) is solved. Then,

pressure boundary conditions are obtained from the momentum equations (3.66)-(3.67). With these boundary values pressure equation (3.76) is solved. The iteration continues until the stopping criteria in terms of maximum error

$$||\boldsymbol{z}^{m+1} - \boldsymbol{z}^{m}||_{\infty} < \epsilon \tag{3.77}$$

is satisfied where $\boldsymbol{z}$ denotes $\boldsymbol{u}$, $\boldsymbol{v}$, $\boldsymbol{\psi}$, $\boldsymbol{\phi}$, $\boldsymbol{\omega}$ and $\boldsymbol{p}$. Preassigned tolerance is taken $\epsilon = 10^{-3}$ to reach steady solutions.

In the computations, we use linear polynomial RBF ($\varphi = 1 + r$). The domain is discretized by $N_b = 60$ boundary points and $N_i = 196$ interior points for several values of Hartmann numbers $M = 0, 30, 50$. The numerical results are depicted in terms of streamlines, equvorticity, electric equipotential lines and pressure contours.

Figures 3.29-3.30 present the flow behavior for conducting or insulating wall conditions in the absence of the magnetic field ($M = 0$). In Figure 3.29 the numerical results show the flow symmetry expected in the Stokes flow in the case of electrically conducting walls ($\phi = 0$). Streamlines and electric equipotential lines have the same magnitude with opposite sign since $\nabla^2\phi = \omega$, $\nabla^2\psi = -\omega$. When the top and bottom walls are conducting and the parallel walls are insulated, the electric potential obeys the boundary condition leaving the same behavior of the flow (Figure3.30).

We deduce that the effect of magnetic field applied in the pipe-axis direction which enables to generate the electric potential with the interaction of electrically conducting fluid even in the Stokes flow. However, the flow and pressure behaviors stay the same due to the Lorentz force terms canceling each other in vorticity equation.

In Figure 3.31 we demonstrate the flow, electric potential and pressure profiles for increasing values of Hartmann number. One can see that the flow, electric potential and pressure are not affected from the variation of M since the Hartmann number is diminished in the construction of the equations containing velocity components, vorticity, stream function, electric potential and pressure. This is an expected situation. Because the equations (3.66)-(3.67) containing Lorentz force terms vanish which are multiplied by Hartmann number. This problem case (application of the external magnetic field in the pipe-axis direction) is considered for the reason of generating electric potential in the Stokes flow. It is seen that electric potential is in the same behavior of

streamlines with opposite magnitude.

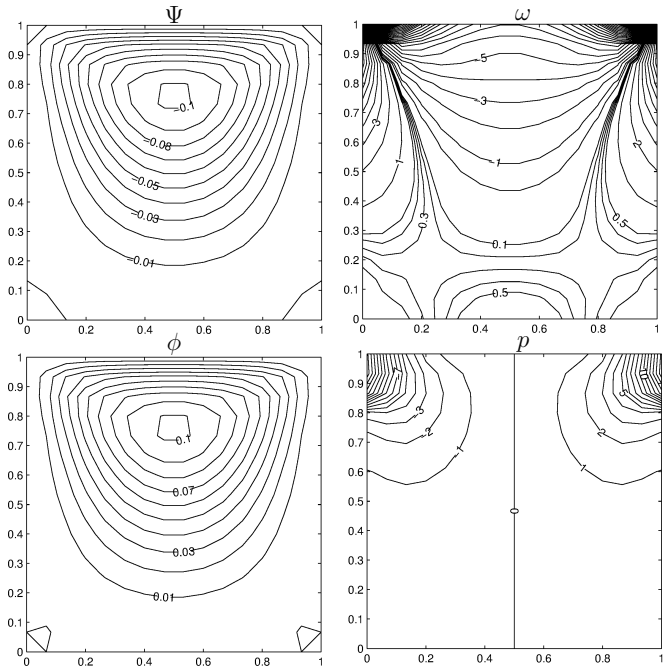

Figure 3.29: Problem 3.4: Stokes flow with electric potential ($\phi|_{wall} = 0$), $M = 0$.

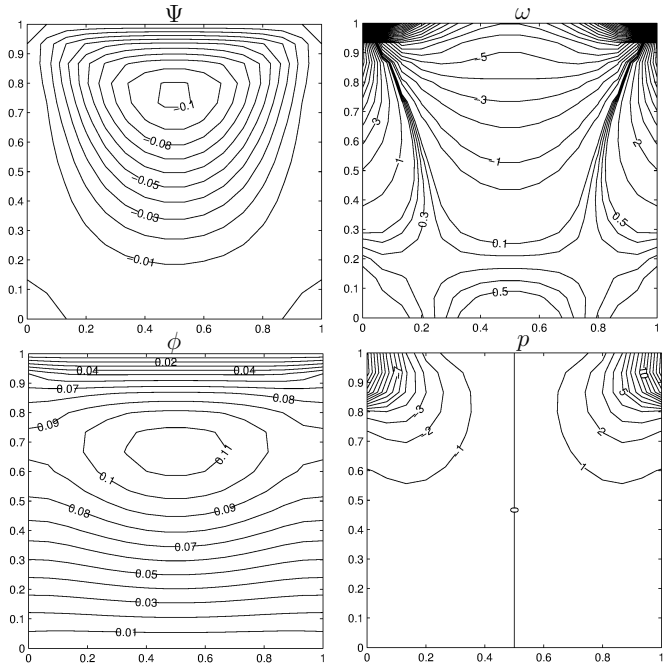

Figure 3.30: Problem 3.4: Stokes flow with electric potential ($\frac{\partial \phi}{\partial n}|_{x=0,1}, \phi|_{y=0,1} = 0$), $M = 0$.

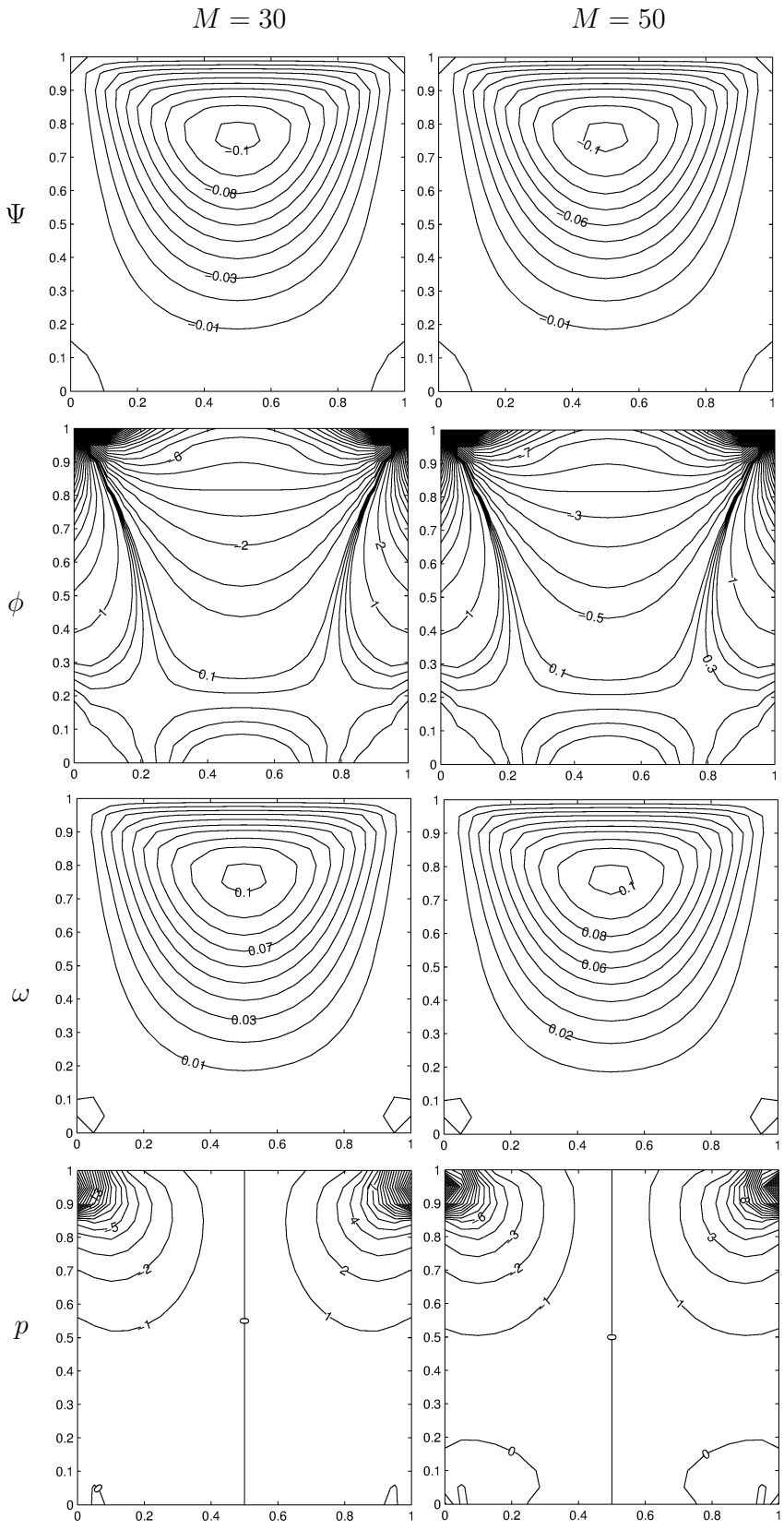

Figure 3.31: Problem 3.4: MHD Stokes flow with electric potential ($\phi|_{wall} = 0$).

3.5 MHD Incompressible Flow with Electric Potential

In this Section, the steady, laminar fully-developed flow of an incompressible, viscous, electrically conducting fluid in the cross-section of a long pipe (enclosure) is considered. A uniform magnetic field is applied in the pipe-axis direction which generates the electric potential. This problem is an extension of the MHD Stokes flow with electric potential given in Section 3.4 in the sense that convection terms are included in the MHD Stokes momentum equations due to the large values of Reynolds number. Only the RBF approximation procedure is going to be used for the MHD incompressible flow problems in the rest of this chapter.

The non-dimensional governing equations of MHD flow in terms of velocity component (u, v), pressure p and electric potential ϕ are given in Chapter 1 (equations (1.58)-(1.60)) as

$$\frac{1}{N}(u\frac{\partial u}{\partial x} + v\frac{\partial u}{\partial y}) = -\frac{1}{M^2}\frac{\partial p}{\partial x} + \frac{1}{M^2}\nabla^2 u + (-u - \frac{\partial \phi}{\partial y}) \tag{3.78}$$

$$\frac{1}{N}(u\frac{\partial v}{\partial x} + v\frac{\partial v}{\partial y}) = -\frac{1}{M^2}\frac{\partial p}{\partial y} + \frac{1}{M^2}\nabla^2 v + (-v + \frac{\partial \phi}{\partial x}). \tag{3.79}$$

where N is the Stuart number given by $N = M^2/Re$ as the ratio of Hartmann number square to Reynolds number.

The equations of Ohm's law $\boldsymbol{J} = \sigma(-\nabla\phi + \boldsymbol{u} \times \mu\boldsymbol{H})$, and the conservation of charge $\nabla \cdot \boldsymbol{J} = 0$ are combined to obtain the electric potential Poisson's equation $\nabla^2\phi = \omega$ by using the vorticity definition.

Thus, the two-dimensional MHD flow together with an electric potential is governed by the equations

$$\nabla^2 u = -\frac{\partial \omega}{\partial y}, \qquad \nabla^2 v = \frac{\partial \omega}{\partial x} \tag{3.80}$$

$$\nabla^2 \psi = -\omega, \qquad \nabla^2 \phi = \omega \tag{3.81}$$

$$\frac{1}{M^2}\nabla^2 \omega = \frac{1}{N}(u\frac{\partial \omega}{\partial x} + v\frac{\partial \omega}{\partial y}) \tag{3.82}$$

$$\frac{1}{M^2}\nabla^2 p = \frac{2}{N}(\frac{\partial u}{\partial x}\frac{\partial v}{\partial y} - \frac{\partial u}{\partial y}\frac{\partial v}{\partial x}) \tag{3.83}$$

under the effect of a magnetic field applied perpendicular to the enclosure.

The RBF approximation (2.31) is applied to the equations (3.80)-(3.83) by evaluating the space derivatives in the inhomogeneities with the help of coordinate matrix $\boldsymbol{F}$. We obtain the discretized matrix-vector systems for the MHD equations in terms of vectors of velocity components, stream function, electric potential, vorticity and pressure as

$$\boldsymbol{u} = \boldsymbol{g_u} - \boldsymbol{K}(\frac{\partial \boldsymbol{F}}{\partial y}\boldsymbol{F^{-1}}\boldsymbol{\omega}) \tag{3.84}$$

$$\boldsymbol{v} = \boldsymbol{g_v} + \boldsymbol{K}(\frac{\partial \boldsymbol{F}}{\partial x}\boldsymbol{F^{-1}}\boldsymbol{\omega}) \tag{3.85}$$

$$\boldsymbol{\psi} = \boldsymbol{g_\psi} + \boldsymbol{K}(-\boldsymbol{\omega}) \tag{3.86}$$

$$\boldsymbol{\phi} = \boldsymbol{g_\phi} + \boldsymbol{K}\boldsymbol{\omega} \tag{3.87}$$

$$\boldsymbol{\omega} = \boldsymbol{g_\omega} + \frac{M^2}{N}\boldsymbol{K}([\boldsymbol{u}]_{\boldsymbol{d}}\frac{\partial \boldsymbol{F}}{\partial x}\boldsymbol{F^{-1}}\boldsymbol{\omega} + [\boldsymbol{v}]_{\boldsymbol{d}}\frac{\partial \boldsymbol{F}}{\partial y}\boldsymbol{F^{-1}}\boldsymbol{\omega}) \tag{3.88}$$

$$\boldsymbol{p} = \boldsymbol{g_p} + \frac{2M^2}{N}\boldsymbol{K}(\frac{\partial \boldsymbol{F}}{\partial x}\boldsymbol{F^{-1}}[\boldsymbol{u}]_{\boldsymbol{d}}\frac{\partial \boldsymbol{F}}{\partial y}\boldsymbol{F^{-1}}\boldsymbol{v} - \frac{\partial \boldsymbol{F}}{\partial y}\boldsymbol{F^{-1}}[\boldsymbol{u}]_{\boldsymbol{d}}\frac{\partial \boldsymbol{F}}{\partial x}\boldsymbol{F^{-1}}\boldsymbol{v}) \tag{3.89}$$

where the diagonal matrices $[\boldsymbol{u}]_{\boldsymbol{d}}$, $[\boldsymbol{v}]_{\boldsymbol{d}}$ are constructed with the diagonal elements of $\boldsymbol{u}$, $\boldsymbol{v}$ and the matrices $\boldsymbol{K}$, $\boldsymbol{F}$, and the vectors $\boldsymbol{g_u}$, $\boldsymbol{g_v}$, $\boldsymbol{g_\psi}$, $\boldsymbol{g_\phi}$, $\boldsymbol{g_\omega}$, $\boldsymbol{g_p}$ are defined as in Section 2.1.2. Vorticity and pressure equations differ from the MHD Stokes flow equations (3.75), (3.76) due to the convection terms.

The iterative process starts with an initial estimate for the vorticity to solve the velocity equations (3.84)-(3.85), the stream function equation (3.86) and the electric potential equation (3.87). Then, the unknown vorticity boundary values are obtained from the stream function equation by using finite difference scheme. The vorticity equation (3.88) is solved with these boundary values and then we use a relaxation parameter α_ω for the vorticity to accelerate the convergence. After pressure boundary values are computed by using the finite difference scheme for the gradient of pressure and the coordinate matrix for the space derivatives in the momentum equations (3.78)-(3.79), pressure equation (3.89) is solved. We use again a relaxation parameter α_p for pressure. The iteration is stopped when the preassigned tolerance ϵ is reached between two successive iterations for reaching the steady solutions.

The present iterative process is applied to two test problems: MHD flow in a lid-driven cavity and MHD flow in a constricted cavity with a moving left wall.

3.5.1 MHD Flow in a Lid-Driven Cavity with Electric Potential

The two-dimensional square cavity with moving top lid shown in Figure 3.32 is filled with a viscous, electrically conducting fluid. Flow is subjected to the external magnetic field in the z-direction generating the electric potential. Dirichlet boundary conditions are imposed for the velocity components, stream function and electric potential. The unknown vorticity and pressure boundary conditions are computed from the stream function and momentum equations, respectively.

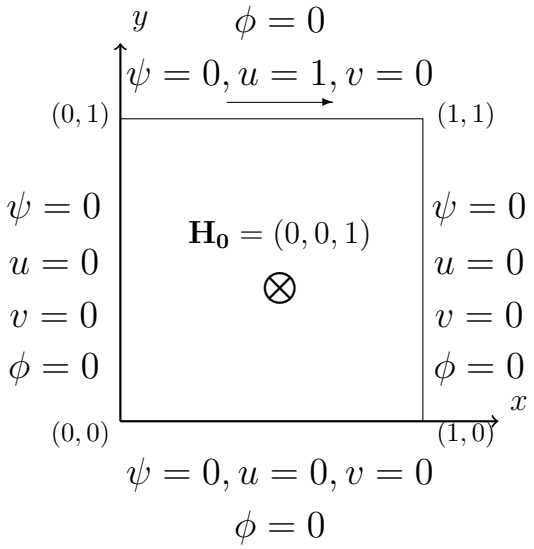

Figure 3.32: Problem 3.5.1: Lid-driven cavity and boundary conditions.

Numerical calculations are carried by using linear polynomial radial basis functions ($\varphi = 1 + r$) with the preassigned tolerance $\epsilon = 10^{-3}$. We take $N_b = 80$ boundary nodes and $N_i = 361$ interior points. For fixed Stuart number $N = 16$ we use several Hartman number values as $M = 20, 40, 100$ corresponding to Reynolds number values $Re = 25, 100, 625$, respectively, since $Re = M^2/N$.

Figure 3.33 shows the effect of the increase of Hartmann number on the flow, electric potential and pressure behaviors. One can observe that as M increases, the main flow shifts through the center of the cavity with an increasing magnitude. With a further increase in M secondary flow occurs at the bottom right corner. The vorticity moves away from the center towards the walls which indicates the strong vorticity gradients as M increases. Electric potential has the same behavior of streamlines with opposite

direction, since $\nabla^2\psi = -\omega$, $\nabla^2\phi = \omega$ with zero boundary conditions. These results are in good agreement with the ones in [56]. When it is compared with the MHD Stokes flow case (Figure 3.31), both the effects of magnetic field applying in the pipe-axis direction and the moving top lid accelerate the flow and electric potential through the right upper corner of the cavity.

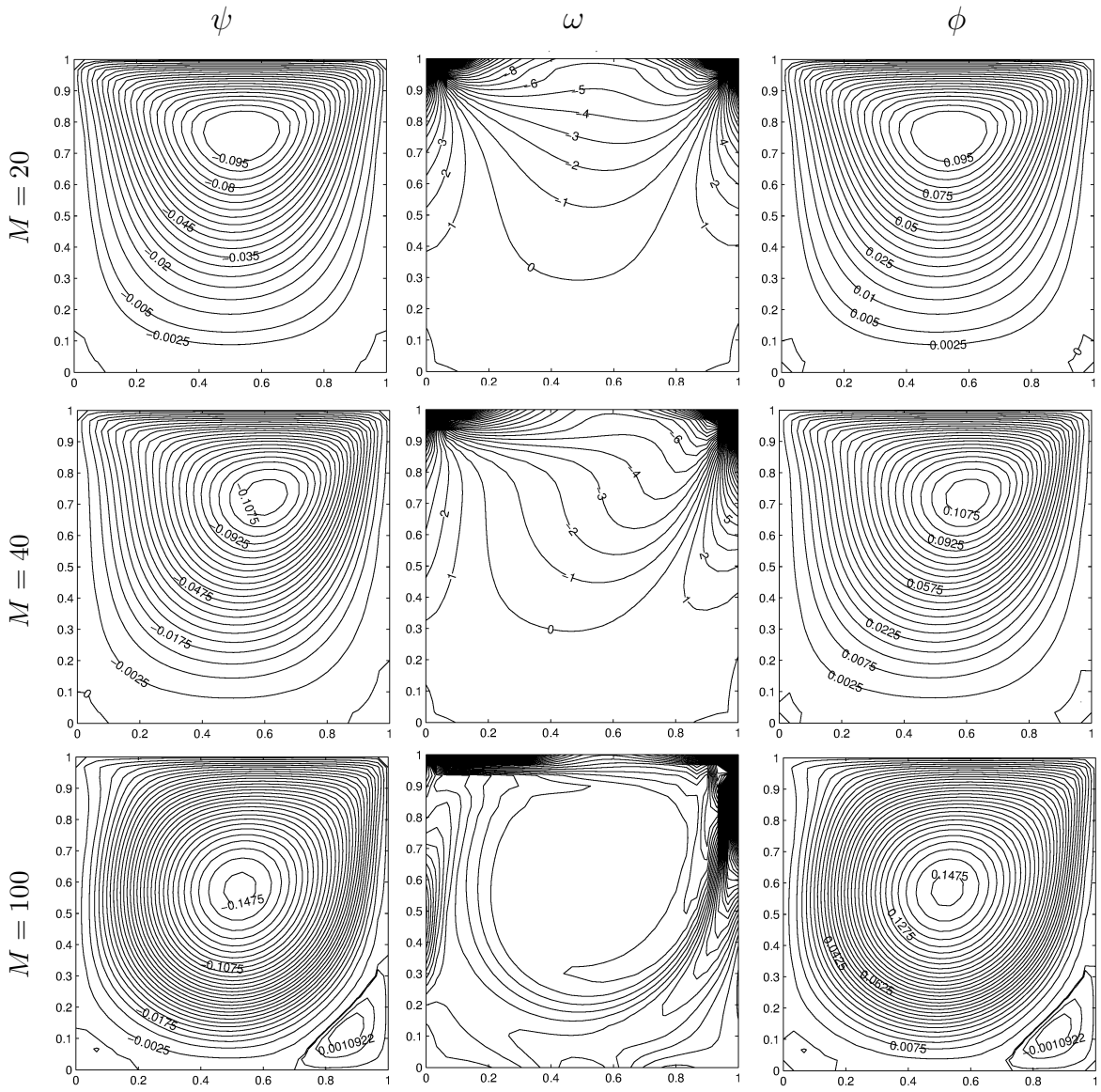

Figure 3.33: Problem 3.5.1: MHD flow with electric potential, $\mathbf{H_0} = (0, 0, 1)$.

3.5.2 MHD Flow in a Constricted Cavity with Electric Potential

In this Section, we discuss the MHD flow in a square cavity with moving left wall in the presence of the pipe- axis direction magnetic field. The bottom and top walls are constricted by using the functions f_b and f_t defined as

$$f_b(x) = \frac{1}{2}h(1 + \cos(2\pi(x - \frac{1}{2}))) \ , \qquad f_t(x) = 1 - f_b(x)$$

where $x \in [0, 1]$, and the constriction ratio(CR) of the enclosure is defined as $CR = 2h \times 100$. Figure 3.34 shows the configuration of the cavity and boundary conditions.

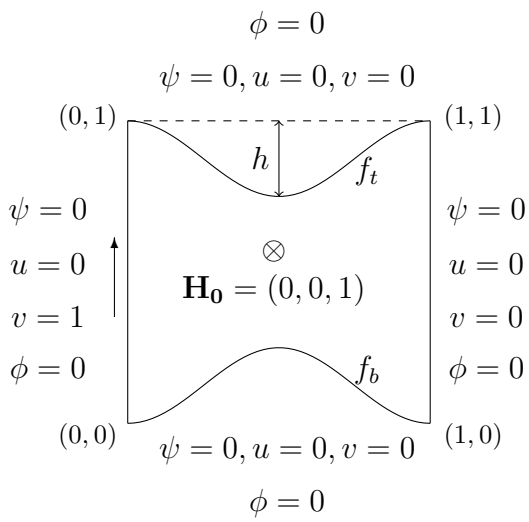

Figure 3.34: Problem 3.5.2: Constricted cavity and boundary conditions.

In the numerical computations, we use linear radial basis functions $\varphi = 1 + r$. The boundary is discretized by taking $N_b = 120$ boundary points for several values of constriction ratios. The relaxation parameters for the vorticity and pressure are taken as $\alpha_\omega = \alpha_p = 0.01$ with the preassigned tolerance $\epsilon = 10^{-3}$. We fix the Stuart number as $N = 16$ and take the Hartmann number values $M = 20$ and 40 with corresponding Reynolds numbers $Re = 25$ and 100. From the obtained numerical results, the flow, electric potential and pressure are simulated in Figures 3.35-3.37.

In Figure 3.35, the effects of perpendicularly applied magnetic field (z-direction) on the flow, electric potential and pressure are analyzed in a non-constricted cavity ($CR = 0\%$). As Hartmann number increases, streamlines and equivorticity lines move through the moving left wall forming boundary layer and the rest of the cavity

is stagnant. The electric potential has the same behavior and magnitude of stream function. This is an expected behavior since $\nabla^2\psi = -\omega$, $\nabla^2\phi = \omega$ and both ψ and ϕ vanish on the boundary. This behavior is the result of strong magnetic field applied perpendicular to the cross-section (cavity) of the pipe. Increase in the strength of the magnetic field increases the pressure values, but decreases magnitudes of stream function and electric potential. Pressure is unevenly distributed in the cavity and highly concentrated at the moving left corner of the cavity as M increases.

Figure 3.36-3.37 show the effect of constriction on the incompressible MHD flow for fixed $M = 20$ and $M = 40$. It is observed that an increase in the constriction ratio of the cavity leads to the development of secondary vortex in the right part of the enclosure for the flow and the electric potential. When the pipe is constricted further, this secondary vortex moves through the constricted area with the effect of moving left wall. Pressure is pronounced completely in the left part with descending values when the constriction of the cavity is increased.

When this study is compared with the MHD Stokes flow in a constricted channel under the x- or y-directed magnetic field given in Section 3.2, we deduce that the effect of magnetic field in the pipe-axis direction on the flow is similar to the effect of the vertical magnetic field. That is, the flow moves through the moving lid as magnetic field intensity increases, but the uniform distribution of the pressure profiles is destroyed comparing with the Figures 3.15. Magnetic field in the x-direction prevents the formation of the secondary flow in front of the right part of the cavity which is observed in the case of the both y-directed and z-directed magnetic fields due to the constriction when we compare the results with the ones given in Figures 3.13-3.14 and 3.16-3.17. However, further constriction forces the flow to squeeze through the left wall regardless of the direction of the magnetic field.

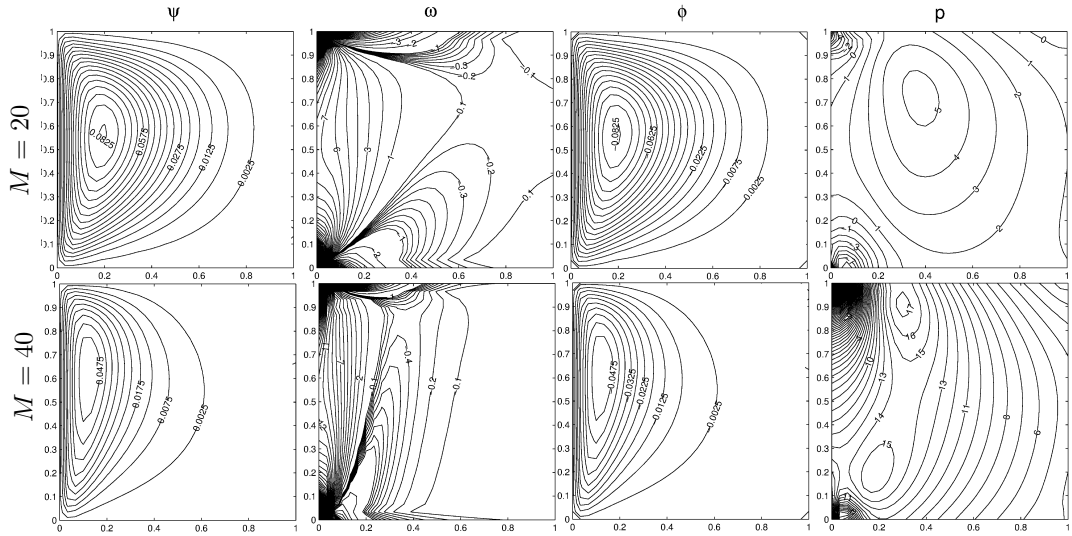

Figure 3.35: Problem 3.5.2: MHD flow with electric potential for $CR = 0\%$, $\mathbf{H_0} = (0, 0, 1)$.

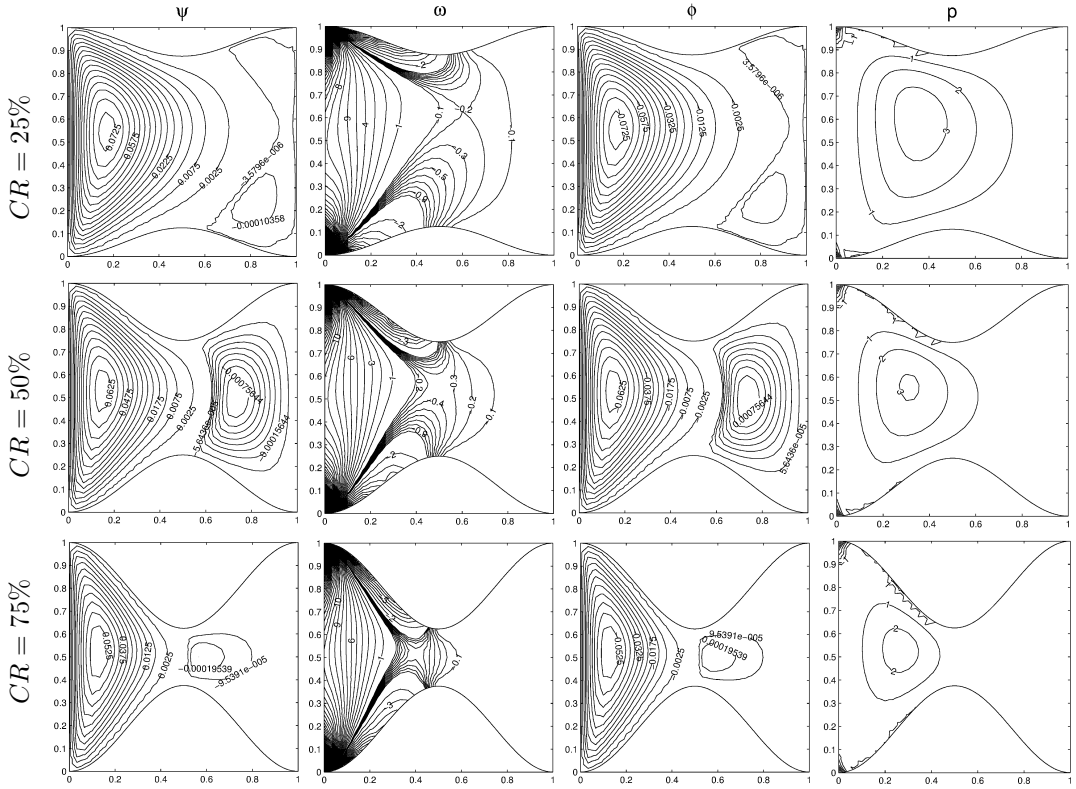

Figure 3.36: Problem 3.5.2: MHD flow with electric potential for $M = 20$, $\mathbf{H_0} = (0, 0, 1)$.

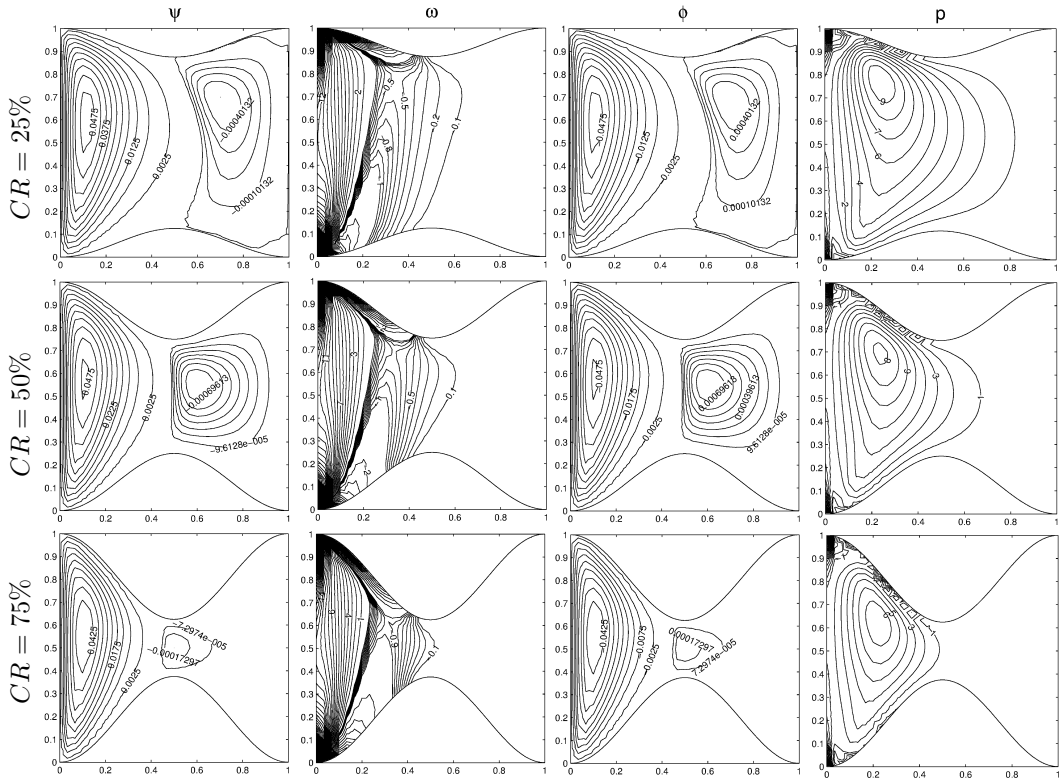

Figure 3.37: Problem 3.5.2: MHD flow with electric potential for $M = 40$, $\mathbf{H_0} = (0, 0, 1)$.

3.6 MHD Convection Flow with Viscous Dissipation

In this Section, MHD convection flow for an incompressible dissipative fluid is considered in cavities when the temperature of the fluid is subjected to variations in the channel due to the wall temperature differences. A uniform magnetic field is applied in the x- or y-direction. The continuity equation and the equations of motion are combined for the MHD flow including buoyancy and Lorentz forces together with the energy equation containing Joule heating and viscous dissipation terms for an incompressible dissipative viscous fluid [35, 45].

When the external magnetic field is applied in the x-direction, the two-dimensional, steady MHD convection flow is represented with Poisson's type equations in terms of velocity components, stream function, temperature, vorticity and pressure (Chapter 1, equations (1.77)-(1.81))

$$\nabla^2 u = -\frac{\partial \omega}{\partial y} \quad , \qquad \nabla^2 v = \frac{\partial \omega}{\partial x} \tag{3.90}$$

$$\nabla^2 \psi = -\omega \tag{3.91}$$

$$\begin{aligned} \nabla^2 T =& PrRe(u\frac{\partial T}{\partial x} + v\frac{\partial T}{\partial y}) - M^2 EcPrv^2 \\ & -EcPr(2(\frac{\partial u}{\partial x})^2 + 2(\frac{\partial v}{\partial y})^2 + (\frac{\partial v}{\partial x} + \frac{\partial u}{\partial y})^2) \end{aligned} \tag{3.92}$$

$$\nabla^2 \omega = Re(u\frac{\partial \omega}{\partial x} + v\frac{\partial \omega}{\partial y}) + M^2 \frac{\partial v}{\partial x} - \frac{Gr}{Re}\frac{\partial T}{\partial x} \tag{3.93}$$

$$\nabla^2 p = -2Re(\frac{\partial v}{\partial x}\frac{\partial u}{\partial y} - \frac{\partial u}{\partial x}\frac{\partial v}{\partial y}) - M^2 \frac{\partial v}{\partial y} + \frac{Gr}{Re}\frac{\partial T}{\partial y} \tag{3.94}$$

where the non-dimensional parameters are the Reynolds number $Re = LU_0/\nu$, the Hartmann number $M = L\mu H_0\sqrt{\sigma/\rho\nu}$, the Eckert number $Ec = U_0^2/(c_p(T_{hot} - T_{cold}))$ which can be interpreted as the ratio of kinetic energy to the accumulated enthalpy, the Grashof number $Gr = g\beta(T_{hot} - T_{cold})L^3/\nu^2$ which is the ratio of buoyancy force to viscous force and the Prandtl number $Pr = \rho c_p \nu/\lambda$.

When the magnetic field is acted in the y-direction, the steady MHD convection flow equations take the form (Chapter 1, equations (1.90)-(1.94)). The differences are only in the second terms of energy, vorticity and pressure equations as v^2, $\frac{\partial v}{\partial x}$ and $\frac{\partial v}{\partial y}$ replaced by u^2, $\frac{\partial u}{\partial y}$ and $\frac{\partial u}{\partial x}$, respectively.

$$\nabla^2 u = -\frac{\partial \omega}{\partial y} \quad , \qquad \nabla^2 v = \frac{\partial \omega}{\partial x} \tag{3.95}$$

$$\nabla^2 \psi = -\omega \tag{3.96}$$

$$\begin{aligned}\nabla^2 T = {} & PrRe(u\frac{\partial T}{\partial x} + v\frac{\partial T}{\partial y}) - M^2 EcPr u^2 \\ & - EcPr(2(\frac{\partial u}{\partial x})^2 + 2(\frac{\partial v}{\partial y})^2 + (\frac{\partial v}{\partial x} + \frac{\partial u}{\partial y})^2)\end{aligned} \tag{3.97}$$

$$\nabla^2 \omega = Re(u\frac{\partial \omega}{\partial x} + v\frac{\partial \omega}{\partial y}) - M^2 \frac{\partial u}{\partial y} - \frac{Gr}{Re}\frac{\partial T}{\partial x} \tag{3.98}$$

$$\nabla^2 p = -2Re(\frac{\partial v}{\partial x}\frac{\partial u}{\partial y} - \frac{\partial u}{\partial x}\frac{\partial v}{\partial y}) - M^2 \frac{\partial u}{\partial x} + \frac{Gr}{Re}\frac{\partial T}{\partial y} \quad . \tag{3.99}$$

The second and third terms in the energy equation (3.92), (3.97) are due to the magnetic field and viscous dissipation. Similarly, in the vorticity and pressure equations (3.93)- (3.94) and (3.98)-(3.99) the last two terms are the magnetic force and buoyancy force terms, respectively.

RBF application to the MHD convection equations (3.90)-(3.94) with the help of the coordinate matrix $\boldsymbol{F}$ for the space derivatives of unknowns results in the matrix-vector equations

$$\boldsymbol{u} = \boldsymbol{g_u} - \boldsymbol{K}(\boldsymbol{D_y}\boldsymbol{\omega}) \tag{3.100}$$

$$\boldsymbol{v} = \boldsymbol{g_v} + \boldsymbol{K}(\boldsymbol{D_x}\boldsymbol{\omega}) \tag{3.101}$$

$$\boldsymbol{\psi} = \boldsymbol{g_\psi} + \boldsymbol{K}(-\boldsymbol{\omega}) \tag{3.102}$$

$$\begin{aligned}\boldsymbol{T} = {} & \boldsymbol{g_T} + PrRe\boldsymbol{K_T}([\boldsymbol{u}]_d\boldsymbol{D_x}\boldsymbol{T} + [\boldsymbol{v}]_d\boldsymbol{D_y}\boldsymbol{T}) - M^2 EcPr\boldsymbol{K_T}\boldsymbol{v^2} \\ & - EcPr\boldsymbol{K_T}(2((\boldsymbol{D_x}\boldsymbol{u})^2 + (\boldsymbol{D_y}\boldsymbol{v})^2) + (\boldsymbol{D_x}\boldsymbol{v} + \boldsymbol{D_y}\boldsymbol{u})^2)\end{aligned} \tag{3.103}$$

$$\begin{aligned}\boldsymbol{\omega} = {} & \boldsymbol{g_\omega} + Re\boldsymbol{K}([\boldsymbol{u}]_d\boldsymbol{D_x}\boldsymbol{\omega} + [\boldsymbol{v}]_d\boldsymbol{D_y}\boldsymbol{\omega}) + M^2\boldsymbol{K}\boldsymbol{D_x}\boldsymbol{v} \\ & - \frac{Gr}{Re}\boldsymbol{K}\boldsymbol{D_x}\boldsymbol{T}\end{aligned} \tag{3.104}$$

$$\begin{aligned}\boldsymbol{p} = {} & \boldsymbol{g_p} - 2Re\boldsymbol{K_p}(\boldsymbol{D_x}[\boldsymbol{v}]_d\boldsymbol{D_y}[\boldsymbol{u}]_d) + 2Re\boldsymbol{K_p}(\boldsymbol{D_x}[\boldsymbol{u}]_d\boldsymbol{D_y}[\boldsymbol{v}]_d) \\ & - M^2\boldsymbol{K_p}\boldsymbol{D_y}\boldsymbol{v} + \frac{Gr}{Re}\boldsymbol{K_p}\boldsymbol{D_y}\boldsymbol{T}\end{aligned} \tag{3.105}$$

where $\boldsymbol{D_x} = \dfrac{\partial \boldsymbol{F}}{\partial x}\boldsymbol{F^{-1}}$ and $\boldsymbol{D_y} = \dfrac{\partial \boldsymbol{F}}{\partial y}\boldsymbol{F^{-1}}$, and the diagonal matrices $[\boldsymbol{u}]_{\boldsymbol{d}}$, $[\boldsymbol{v}]_{\boldsymbol{d}}$ are constructed with the diagonal elements $\boldsymbol{u}$, $\boldsymbol{v}$ matrices, respectively. The matrices $\boldsymbol{K}$, $\boldsymbol{K_T}$, $\boldsymbol{K_p}$, $\boldsymbol{F}$ and the vectors $\boldsymbol{g_u}$, $\boldsymbol{g_v}$, $\boldsymbol{g_\psi}$, $\boldsymbol{g_\phi}$, $\boldsymbol{g_\omega}$, $\boldsymbol{g_p}$ are defined as given in Section 2.1.2.

When the magnetic field is in the y-direction, RBF discretized system of equations for (3.95)-(3.99) take the form

$$\boldsymbol{u} = \boldsymbol{g_u} - \boldsymbol{K}(\boldsymbol{D_y}\boldsymbol{\omega}) \tag{3.106}$$

$$\boldsymbol{v} = \boldsymbol{g_v} + \boldsymbol{K}(\boldsymbol{D_x}\boldsymbol{\omega}) \tag{3.107}$$

$$\boldsymbol{\psi} = \boldsymbol{g_\psi} + \boldsymbol{K}(-\boldsymbol{\omega}) \tag{3.108}$$

$$\begin{aligned}\boldsymbol{T} = {} & \boldsymbol{g_T} + PrRe\boldsymbol{K_T}([\boldsymbol{u}]_{\boldsymbol{d}}\boldsymbol{D_x}\boldsymbol{T} + [\boldsymbol{v}]_{\boldsymbol{d}}\boldsymbol{D_y}\boldsymbol{T}) - M^2 EcPr\boldsymbol{K_T}\boldsymbol{u^2} \\ & - EcPr\boldsymbol{K_T}(2((\boldsymbol{D_x}\boldsymbol{u})^{\boldsymbol{2}} + (\boldsymbol{D_y}\boldsymbol{v})^{\boldsymbol{2}}) + (\boldsymbol{D_x}\boldsymbol{v} + \boldsymbol{D_y}\boldsymbol{u})^{\boldsymbol{2}})\end{aligned} \tag{3.109}$$

$$\begin{aligned}\boldsymbol{\omega} = {} & \boldsymbol{g_\omega} + Re\boldsymbol{K}([\boldsymbol{u}]_{\boldsymbol{d}}\boldsymbol{D_x}\boldsymbol{\omega} + [\boldsymbol{v}]_{\boldsymbol{d}}\boldsymbol{D_y}\boldsymbol{\omega}) - M^2\boldsymbol{K}\boldsymbol{D_y}\boldsymbol{u} \\ & - \frac{Gr}{Re}\boldsymbol{K}\boldsymbol{D_x}\boldsymbol{T}\end{aligned} \tag{3.110}$$

$$\begin{aligned}\boldsymbol{p} = {} & \boldsymbol{g_p} - 2Re\boldsymbol{K_p}(\boldsymbol{D_x}[\boldsymbol{v}]_{\boldsymbol{d}}\boldsymbol{D_y}[\boldsymbol{u}]_{\boldsymbol{d}}) + 2Re\boldsymbol{K_p}(\boldsymbol{D_x}[\boldsymbol{u}]_{\boldsymbol{d}}\boldsymbol{D_y}[\boldsymbol{v}]_{\boldsymbol{d}}) \\ & - M^2\boldsymbol{K_p}\boldsymbol{D_x}\boldsymbol{u} + \frac{Gr}{Re}\boldsymbol{K_p}\boldsymbol{D_y}\boldsymbol{T}.\end{aligned} \tag{3.111}$$

Now, we shall describe the iterative procedure for both set of equations resulting with x-directed and y-directed magnetic field:

1. Start with initial estimates for vorticity $\boldsymbol{\omega}^0$ and temperature $\boldsymbol{T}^0$.

2. Solve the velocity equations (3.100)-(3.101) or (3.106)-(3.107) to obtain $\boldsymbol{u}^{m+1}$ and $\boldsymbol{v}^{m+1}$ with $\boldsymbol{\omega}^m$.

3. Solve the stream function equation (3.102) or (3.108) to obtain $\boldsymbol{\psi}^{m+1}$ with $\boldsymbol{\omega}^m$.

4. Solve the temperature equation (3.103) or (3.109) to obtain $\boldsymbol{T}^{m+1}$ using $\boldsymbol{T}^m$, and $\boldsymbol{u}^{m+1}$ and $\boldsymbol{v}^{m+1}$.

5. Use a relaxation parameter $0 < \alpha_T < 1$ to accelerate the convergence

$$\boldsymbol{T}^{m+1} = (1 - \alpha_T)\boldsymbol{T}^m + \alpha_T\boldsymbol{T}^{m+1}.$$

6. Calculate the new vorticity boundary conditions from the stream function equation by using finite difference procedure.

7. Solve the vorticity equation (3.104) or (3.110) to obtain $\boldsymbol{\omega}^{m+1}$.

8. Use a relaxation parameter $0 < \alpha_\omega < 1$ to accelerate the convergence

$$\boldsymbol{\omega}^{m+1} = (1 - \alpha_\omega)\boldsymbol{\omega}^m + \alpha_\omega \boldsymbol{\omega}^{m+1}.$$

9. Obtain the unknown pressure boundary conditions from the equations

$$Re(u\frac{\partial u}{\partial x} + v\frac{\partial u}{\partial y}) = -\frac{\partial p}{\partial x} + \nabla^2 u + M^2(-u{H_y}^2 + vH_xH_y)$$
$$Re(u\frac{\partial v}{\partial x} + v\frac{\partial v}{\partial y}) = -\frac{\partial p}{\partial y} + \nabla^2 v + M^2(uH_xH_y - v{H_x}^2) + \frac{Gr}{Re}T$$

   by using the finite difference scheme for the gradient of pressure and the coordinate matrix for the space derivatives. Here, $\boldsymbol{H} = (H_x, H_y)$ is the magnetic field.

10. Solve the pressure equation (3.105) or (3.111) to obtain $\boldsymbol{p}^{m+1}$.

11. Use a relaxation parameter $0 < \alpha_p < 1$ for correcting pressure values

$$\boldsymbol{p}^{m+1} = (1 - \alpha_p)\boldsymbol{p}^m + \alpha_p \boldsymbol{p}^{m+1}.$$

12. Check the maximum error

$$||\boldsymbol{z}^{m+1} - \boldsymbol{z}^m||_\infty < \epsilon$$

    where $\boldsymbol{z}$ denotes either $\boldsymbol{u}$, $\boldsymbol{v}$, $\boldsymbol{\psi}$, $\boldsymbol{T}$, $\boldsymbol{\omega}$ or $\boldsymbol{p}$.

13. When the stopping criterion is satisfied, the solution is obtained.

If the pressure boundary conditions are given (with the physical assumption $\frac{\partial p}{\partial n} = 0$), pressure equation is solved after the iteration is terminated.

The present iterative RBF approximation procedure will be applied to the MHD convection Stokes and incompressible flows in cavities.

3.6.1 MHD Convection Stokes Flow in a Square Cavity

First, the iterative procedure described in the previous section is applied to solve MHD convection equations by taking small Reynolds number ($Re << 1$) to analyze the heat transfer for the Stokes flow under the impact of a magnetic field. The effects of the magnetic field, buoyancy force and viscous dissipation on the slow flow in a square cavity with or without moving top lid are analyzed for several values of the Hartmann number, Grashof number and Eckert number.

In this problem, the RBF solution of MHD convection Stokes flow in a square cavity in the presence of horizontally applied magnetic field is presented. The cavity is heated from the left, and the right wall is kept cooled, while the other walls are adiabatic (Figure 3.38). Normal derivative of pressure is taken as zero on the walls of the cavity which is a physically expected behavior of the pressure as given in [17]. The unknown vorticity conditions are obtained from the stream function equation with the use of finite difference scheme.

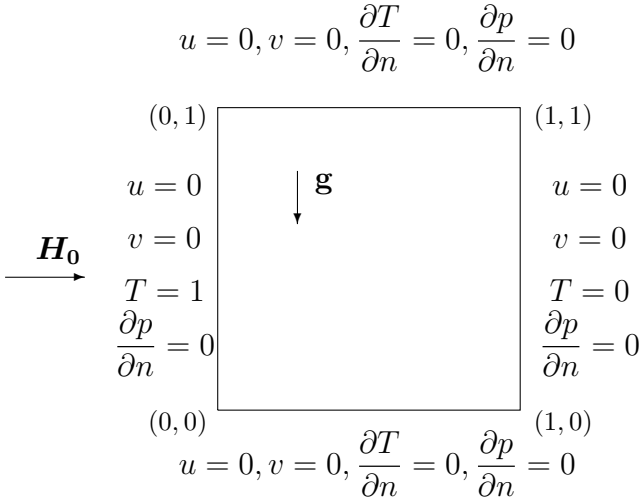

Figure 3.38: Problem 3.6.1: Square cavity and boundary conditions.

In the numerical computations, Reynolds number is taken as 0.6 for the Stokes approximation and the boundary is discretized by $N_b = 80$ points. We use relaxation parameters $\alpha_\omega = 0.01$ and $\alpha_T = 0.1$ for the obtained vorticity and temperature values, respectively, with the convergence tolerance $\epsilon = 10^{-3}$. Flow, temperature and pres-

sure behaviors are visualized for several values of M, Gr, Ec by keeping $Pr = 0.71$ fixed.

We first show in Figure 3.39 that the effect of the increase in Gr (buoyancy force dominance) on the Stokes flow and the temperature whether the fluid is viscous dissipative ($Ec = 1$) or not ($Ec = 0$) in the absence of magnetic field ($M = 0$). The flow circulates at the center of the cavity, isotherms are uniformly distributed from the hot to the cold wall. Pressure extends throughout the cavity and reaches its minimum value at the center. The viscous dissipation effect on the Stokes flow can be noticed when Gr is reached to a value about 90. As Gr increases, dissipative viscous fluid ($Ec = 1$) moves to the cold right wall. When we look at the isotherms, the heat spreads through the center of the cavity with an increase in the magnitude, and splits symmetrically through the top and bottom walls in the left part of the cavity. Then, the temperature value decreases and concentrates through the right cold wall forming thick layer. Pressure profiles are symmetrically distributed in front of the walls obeying the imposed boundary conditions when $Gr = 90$. Thus, one can observe that viscous dissipation causes a significant change on isotherms forming a thermal boundary layer near the cold wall due the transformation of kinetic energy into internal energy.

Figure 3.40 depicts the effect of applied magnetic field on the flow when the viscous dissipation is present. As M increases, center vortex of the streamlines converts to elliptic shape with a decrease in magnitude. Further increase in M forces vorticity to be divided into two vortices in front of the bottom and top walls (adiabatic walls). Boundary layers on the flow are formed near the heated and cooled walls as can be seen in the streamlines and the equivorticity curves for $M \geq 30$. The magnetic field reduces the effect of the buoyancy force and when M reaches to the value of 50, the temperature resumes completely the uniform distribution between the vertical walls. Moreover, an increase in M leads to four symmetric pressure distributions emanating from the cavity corners. Pressure value decreases when the intensity of the magnetic field increases.

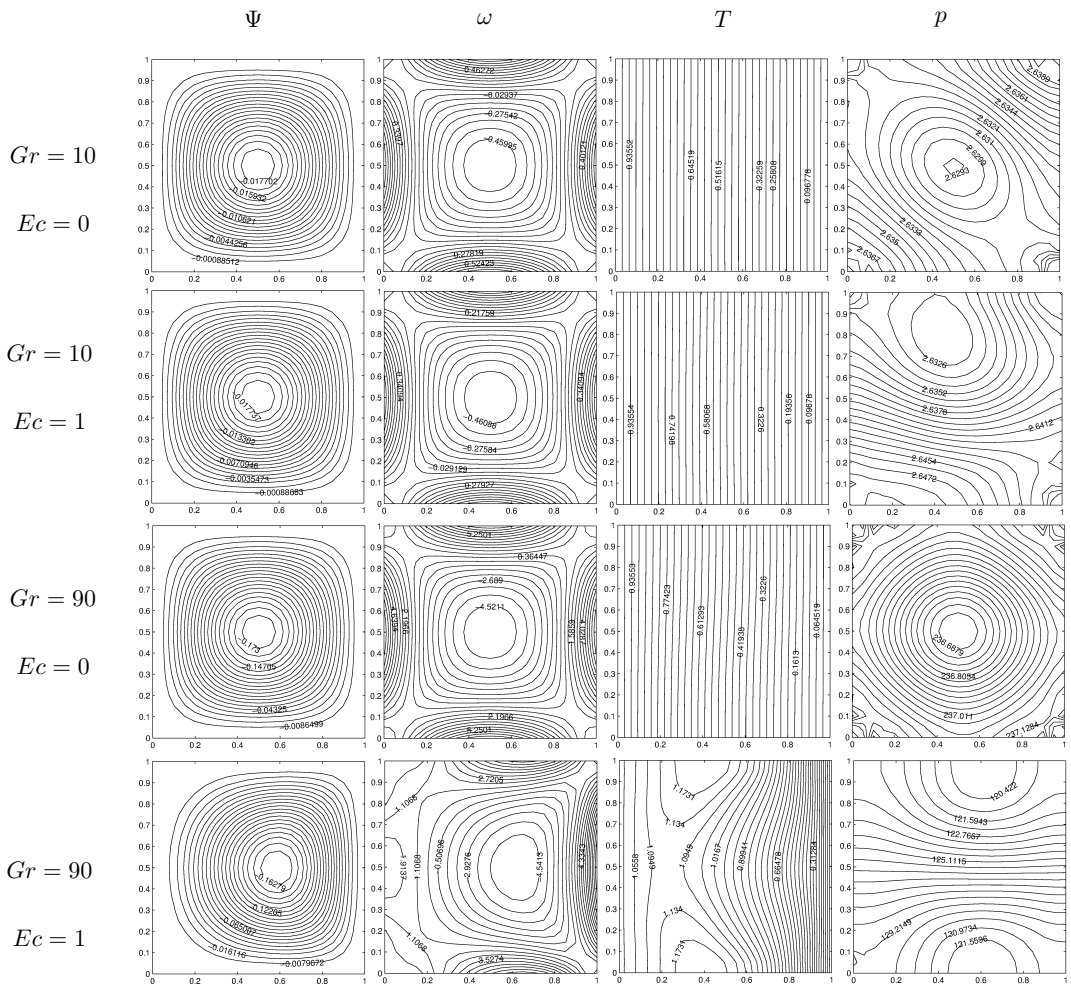

Figure 3.39: Problem 3.6.1: MHD convection Stokes flow for $M = 0$.

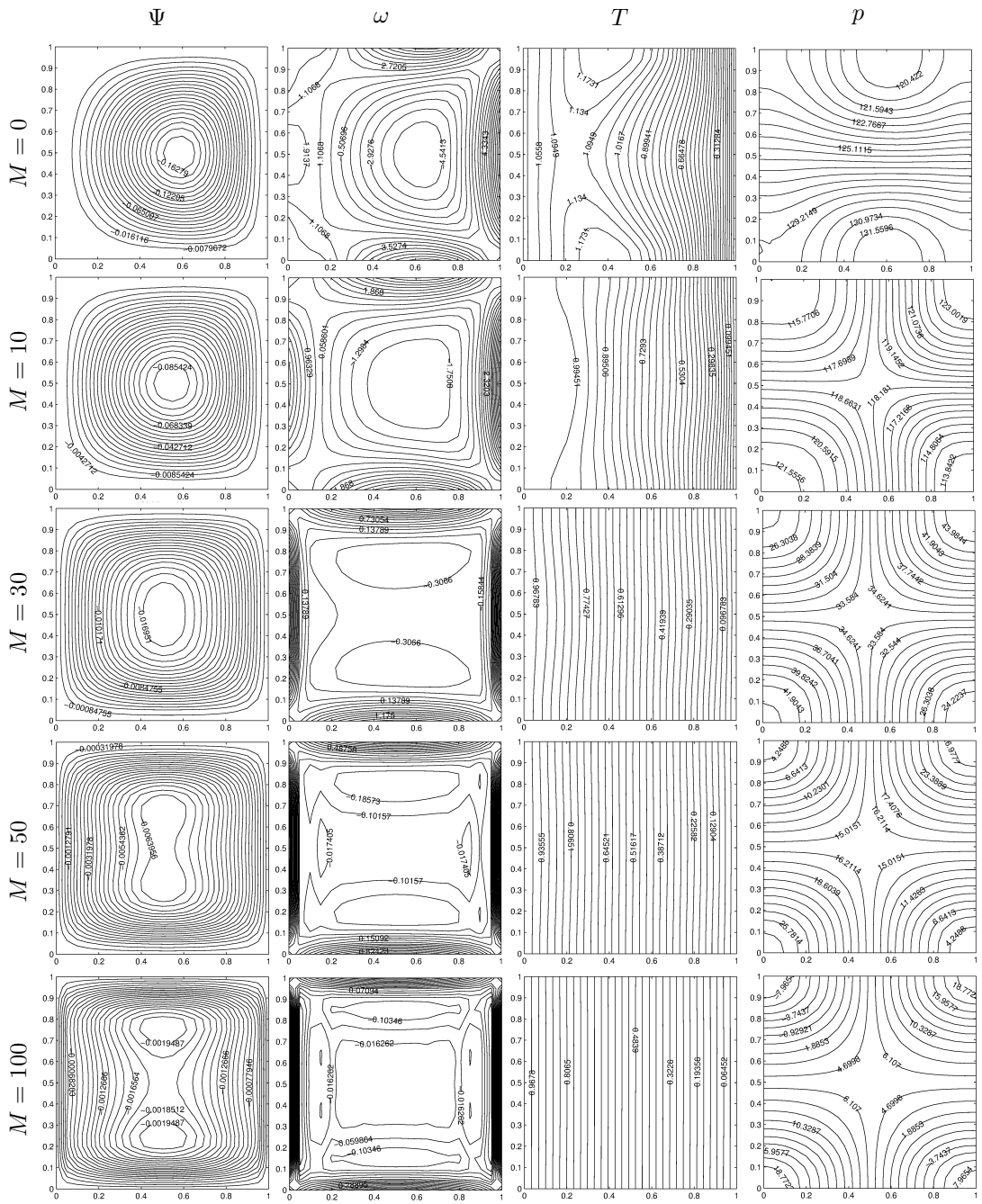

Figure 3.40: Problem 3.6.1: MHD convection Stokes flow for $Gr = 90$, $Ec = 1$.

3.6.2 MHD Convection Stokes Flow in a Lid-Driven Cavity

We consider again the MHD convection Stokes flow in a square cavity whose top lid has a movement with a constant velocity $u = 1$ as shown in Figure 3.41. The effects of the movement of the lid, the x-directed applied magnetic field, buoyancy force and the dissipation of the fluid are considered together.

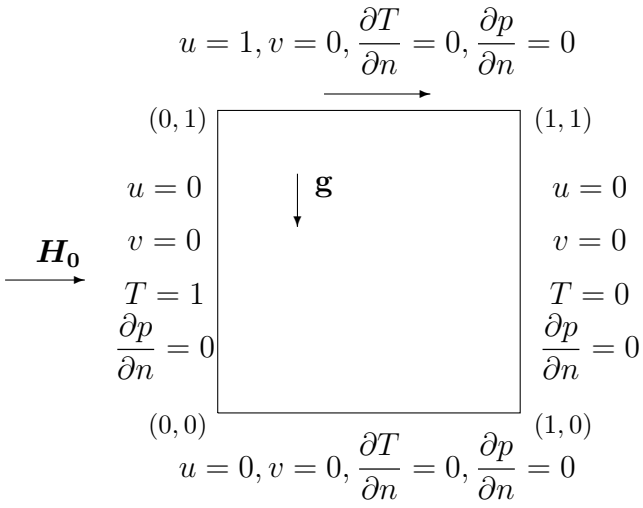

Figure 3.41: Problem 3.6.2: Lid-driven cavity and boundary conditions.

The boundary and domain of the problem are discretized by $N_b = 80$ boundary and $N_i = 361$ interior points, respectively. The RBF discretized equations (3.100)-(3.105) are solved iteratively with the preassigned tolerance $\epsilon = 10^{-3}$. The numerical investigation is carried for different values of Gr, M for fixed $Re = 0.6$ and $Pr = 0.71$.

First, the numerical results for the Stokes flow in the lid-driven cavity are validated for non-dissipative fluid exposed to small magnetic field effect by taking $M = 1$, $Re = Ec = Gr = 0$. The flow behavior is in well agreement with the MHD Stokes flow behavior given in [21].

Figure 3.42 depicts the effects of buoyancy force and viscous dissipation on the Stokes flow when the upper lid of the cavity is moving to the right. When we neglect the viscous dissipation ($Ec = 0$), boundary layer formation for the flow is observed near the moving top lid. As Gr increases, the main vortex of the flow shifts

through the center of the cavity with an increase in the magnitude which indicates that the effect of the moving lid on the flow is reduced. The vorticity and pressure behaviors are significantly changed. Pressure takes its minimum value at the center of the cavity. When the viscous dissipation is present ($Ec = 1$), buoyancy force is more pronounced especially in isotherms and in the flow behaviors for $Gr \approx 90$. The moving lid accelerates the heat transfer from the hot wall to the cold wall. Although the viscous dissipation effect can be seen in the square cavity for $Gr \geq 90$ (Figure 3.39), it is observed even for lower values of $Gr \geq 10$ in the lid-driven cavity. On the other hand, as in the square cavity case the viscous dissipation causes the flow and the temperature to concentrate through the cold wall forming a thin boundary layer which can be observed from the vorticity and the temperature lines. Pressure is almost evenly distributed between the hot and cold walls taking its maximum value near the bottom wall.

The effect of the magnetic field for the dissipative fluid in a lid-driven cavity is presented for fixed $Gr = 90$ in Figure 3.43. The increase in the magnetic field intensity shows a different behavior in the flow and the fluid temperature when it is compared with the square cavity case in Figure 3.40. The flow concentrates near the upper wall forming a boundary layer with the effect of both moving lid and the increasing intensity of the magnetic field acting in the same direction. Further increase in M causes secondary flow development through the center of the cavity. Pressure in the cavity increases with an increase in M. As Hartmann number increases, buoyancy force is still dominant causing the heat transfer from the hot wall to the cold wall unlike the square cavity case. Also, the temperature of the fluid is high near the top moving lid.

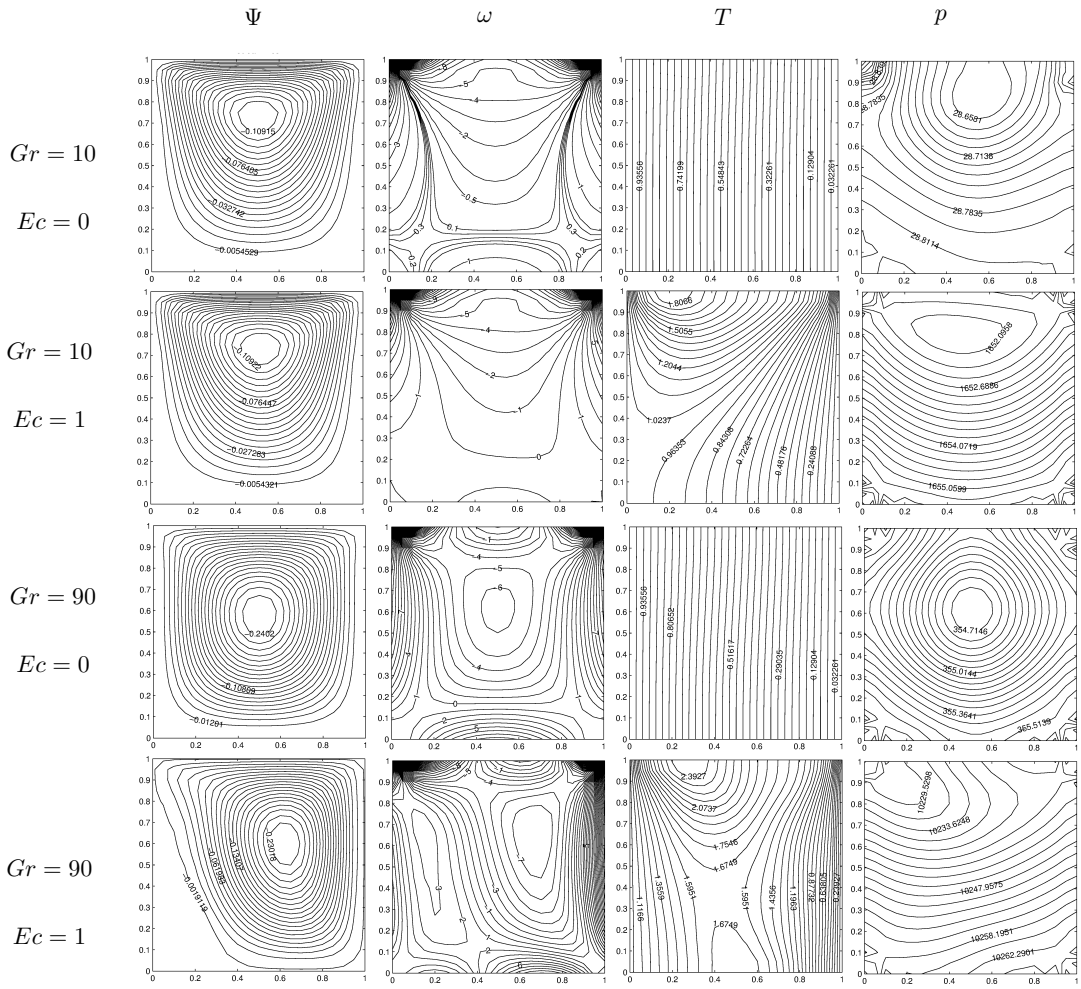

Figure 3.42: Problem 3.6.2: MHD convection Stokes flow for $M = 0$.

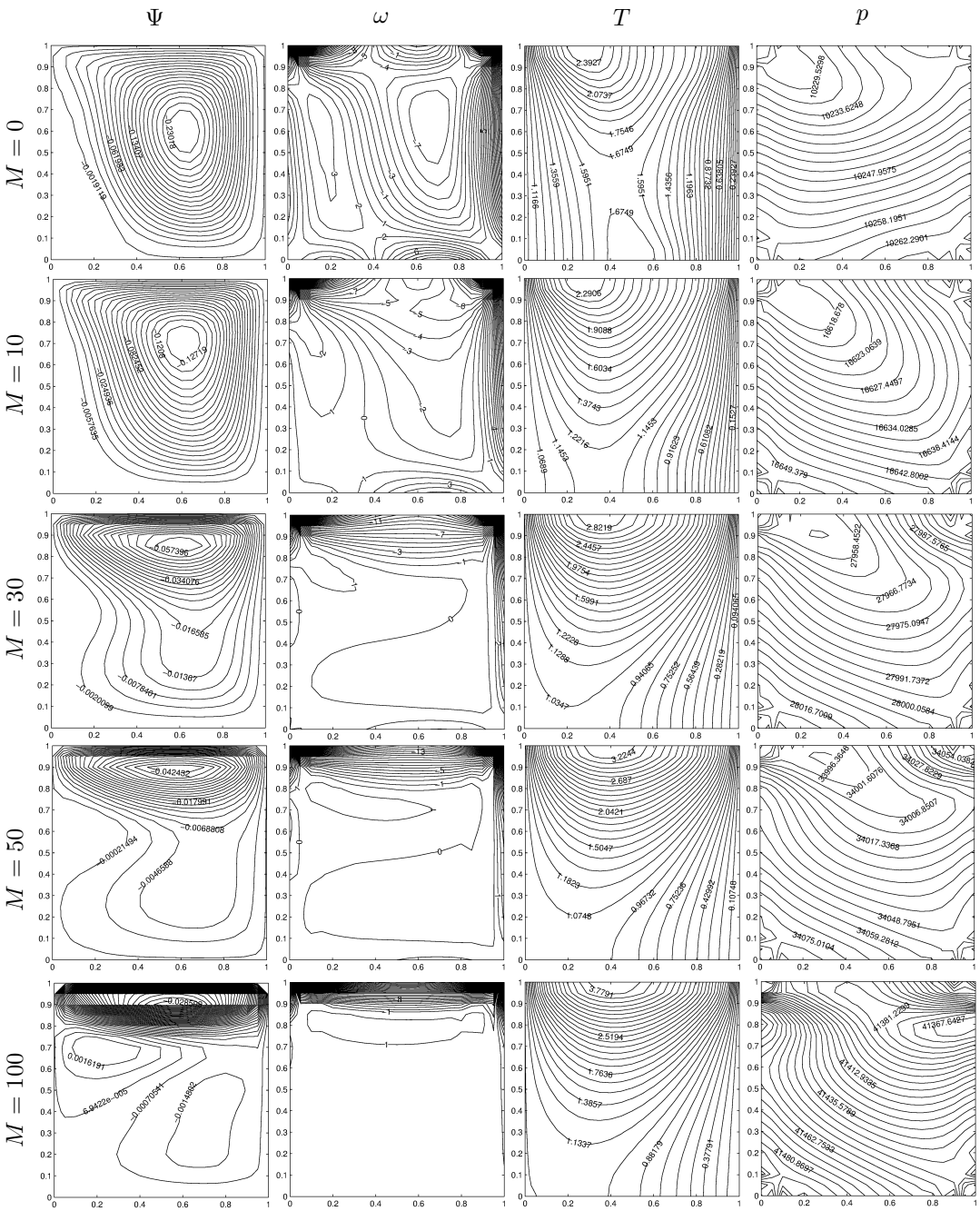

Figure 3.43: Problem 3.6.2: MHD convection Stokes flow for $Gr = 90$, $Ec = 1$.

3.6.3 MHD Convection Incompressible Flow in a Square Cavity

In this Section, the 2D steady, laminar MHD flow of an incompressible, electrically conducting, dissipative viscous fluid and the heat transfer are considered in the cross-section of channels. Flow is subjected to the uniform magnetic field in the x- or y-direction. The impacts of the magnetic field, buoyancy force and viscous dissipation are discussed for the MHD flow in a square cavity and in a lid-driven cavity. Heat transfer for the MHD flow in the constricted channel is also included.

RBF approximation is implemented to the steady convection flow in a square cavity under the effect of horizontally applied magnetic field. The problem domain and the boundary conditions are given in the Figure 3.44. Dirichlet boundary conditions for u, v and ψ are imposed on the walls. The left wall is hot and the right wall is cold, whereas the other walls are adiabatic. The unknown vorticity boundary conditions are obtained from the stream function equation.

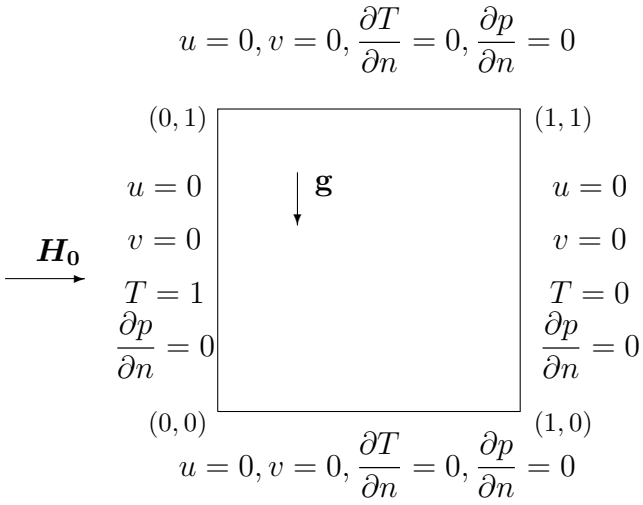

Figure 3.44: Problem 3.6.3: Square cavity and boundary conditions.

Numerical results are obtained by $N_b = 80$ boundary points with the preassigned tolerance $\epsilon = 10^{-3}$. The relaxation parameters for the vorticity and temperature are taken as $\alpha_\omega = 0.01$ and $\alpha_T = 0.1$. The behaviors of the flow, isotherms and pressure are depicted for several values of Gr ($10^3 \leq Gr \leq 10^5$) and M ($0 \leq M \leq 50$) with fixed $Re = 100$, $Pr = 0.71$.

In Figure 3.45, we show convection flow and temperature behaviors in the same square cavity for increasing values of Gr neglecting applied magnetic field and viscous dissipation which are in good agreement with the results in [1]. As Gr increases, the magnitude of stream function also increases and center vortex is divided into two vortices. Similarly, vorticity tends to be divided at the center of the cavity forming vortices and boundary layers near the left and right walls. Isotherms variation is more pronounced with an increase in Grashof number due to dominance of buoyancy effect. Pressure values also increase.

Figure 3.46 indicates the effect of the magnetic field on the flow, temperature and pressure profiles for fixed $Re = 100$, $Gr = 10^4$ and $Ec = 0$. Results are in well agreement with the ones obtained in [1, 13]. Hartmann number effect on the flow is the boundary layer formation near the walls which are perpendicular to the applied magnetic field (Hartmann layers). External magnetic field impact is most pronounced on isotherms. It reduces the dominance of convective heat transfer from the left wall to the right wall (which was observed for large Gr number). When M reaches to the value of 50, the temperature comes back to the uniform distribution between the vertical walls which indicates that heat conduction becomes dominant. When uniform external magnetic field is present, pressure in the channel is divided symmetrically into four pieces emanating from the corners.

When we add viscous dissipation term in the energy equation by taking $Ec = 1$, flow characteristics are shown in Figures 3.47-3.48 with respect to Gr increase and M increase. Main vortex of the streamlines moves to the right bottom corner forming boundary layer with an increase in Gr up to 10^5. Secondary flow occurs in the upper left corner. Similarly, pressure concentrates near the right bottom corner. As Grashof number is taken up to 10^5, both vorticity and isotherms are altered loosing the symmetry and they form boundary layers near the cold wall. Temperature values increase through the center of the cavity, but decrease through the right cold wall showing heat transfer from the left wall through upper adiabatic wall and sharp decrease to the cold wall. This means that the thermal convection is completely changed for dissipative viscous fluid only when Gr is reached to 10^5 which can be seen from the second column of Figure 3.47 with the first column of Figure 3.46.

In Figure 3.48, the impacts of both the magnetic field and the buoyancy force are searched on the solution for dissipative viscous fluid. For $Gr = 10^4$ the magnetic field effect on the dissipative flow is the same as in the case of $Ec = 0$. When Gr reaches to 10^5 viscous dissipation effect starts to be observed. Streamlines, isotherms and equivorticity lines all concentrate near the right bottom corner and form boundary layer near the cold right wall. Values of pressure increase from the right bottom to the left top corner of the cavity with an increase in M.

As a result, it is concluded that viscous dissipation causes significant change on the flow and temperature of the fluid for $Gr \geq 10^4$. A dramatic change is observed when both Gr and M values are large in the sense that the flow and isotherms are pushed through the cold right wall.

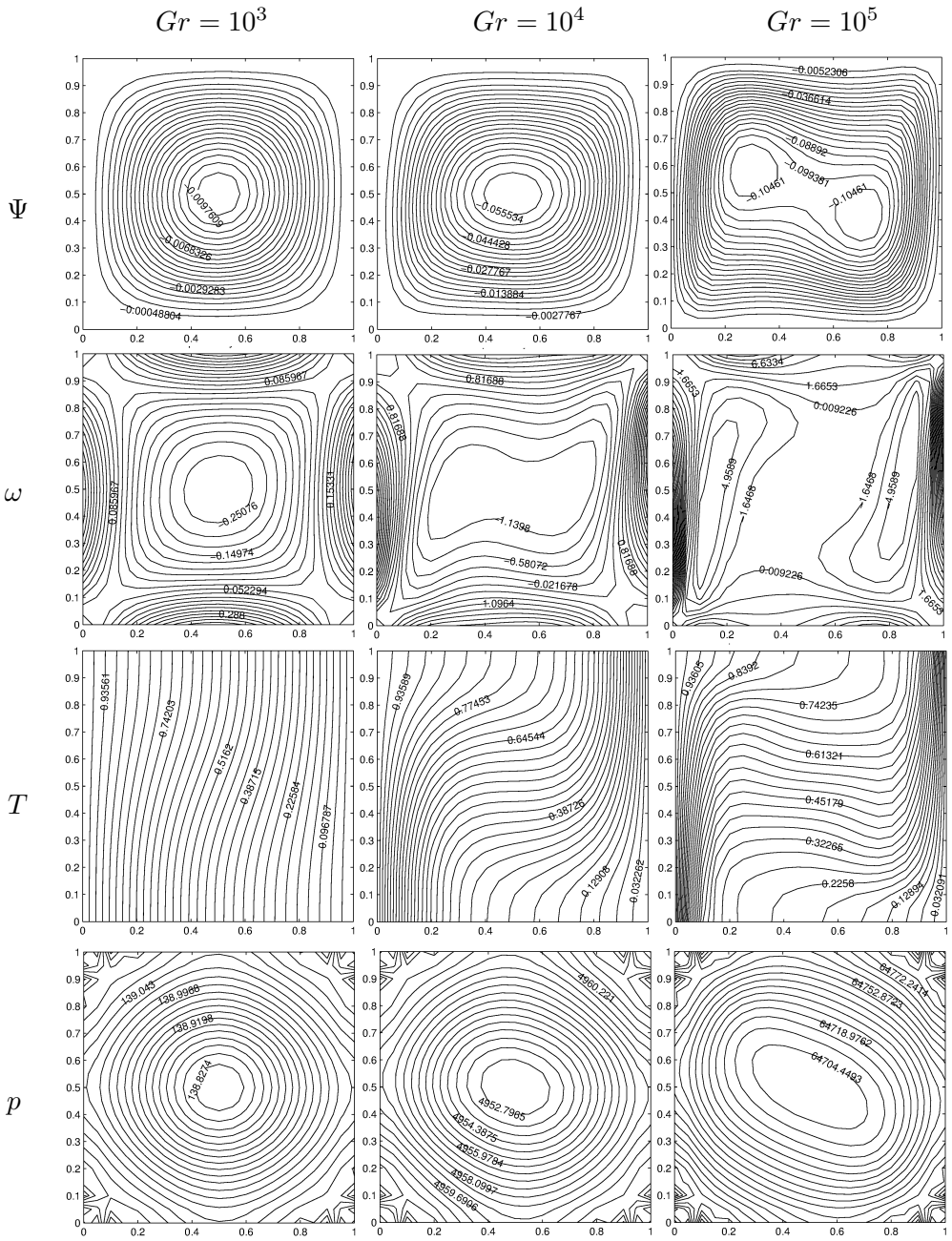

Figure 3.45: Problem 3.6.3: MHD convection flow for $M = 0$, $Ec = 0$.

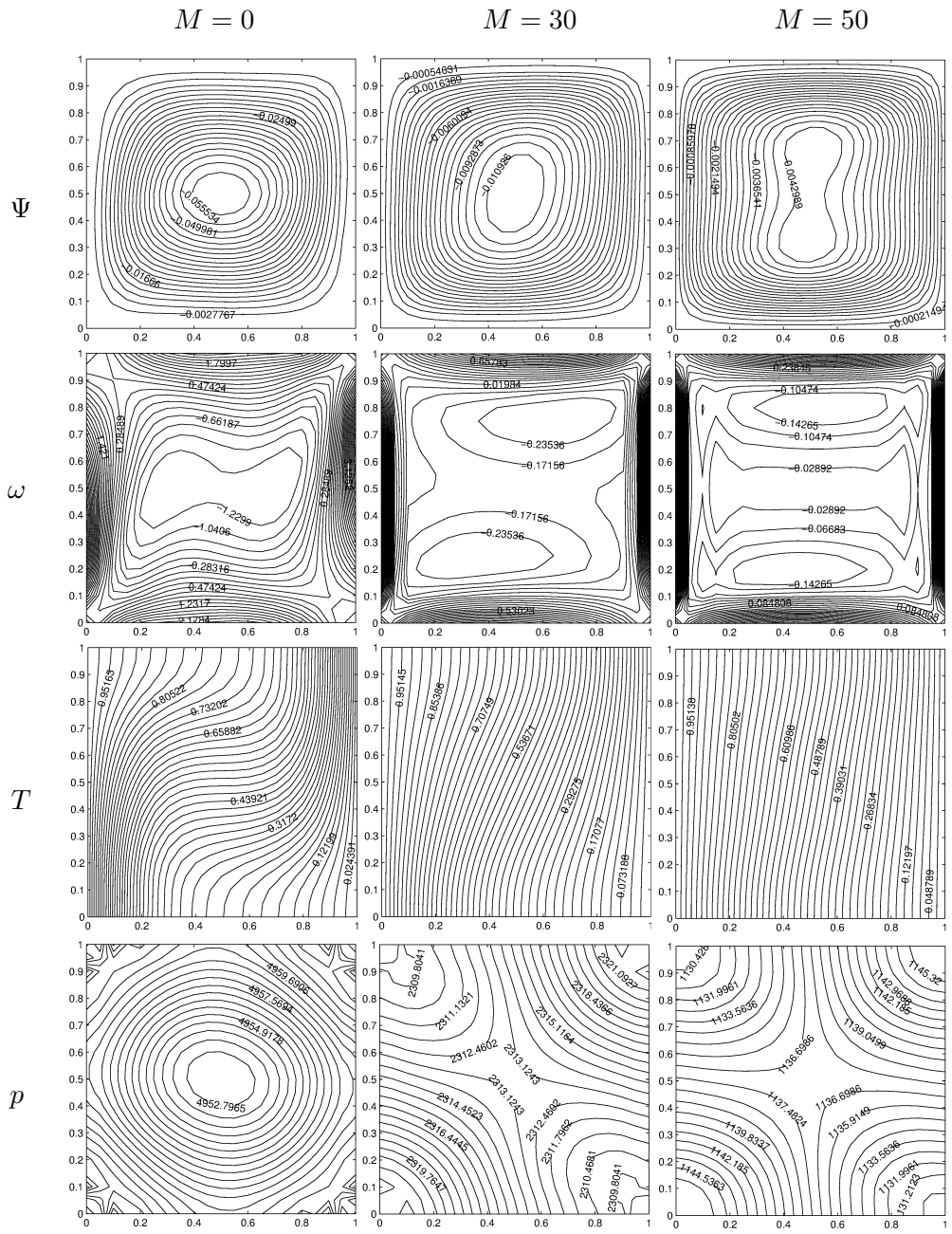

Figure 3.46: Problem 3.6.3: MHD convection flow for $Gr = 10^4$, $Ec = 0$.

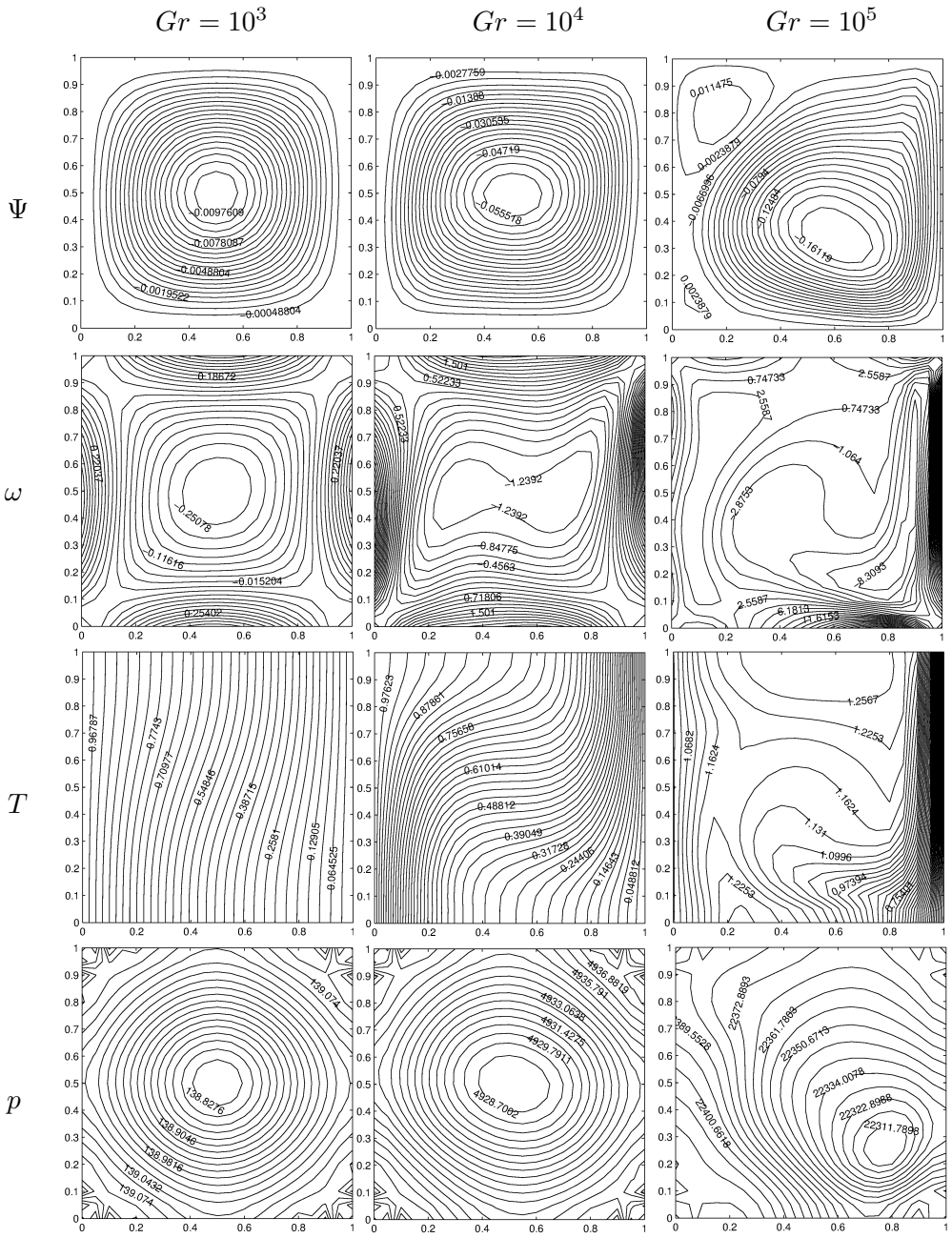

Figure 3.47: Problem 3.6.3: MHD convection flow for $M = 0$, $Ec = 1$.

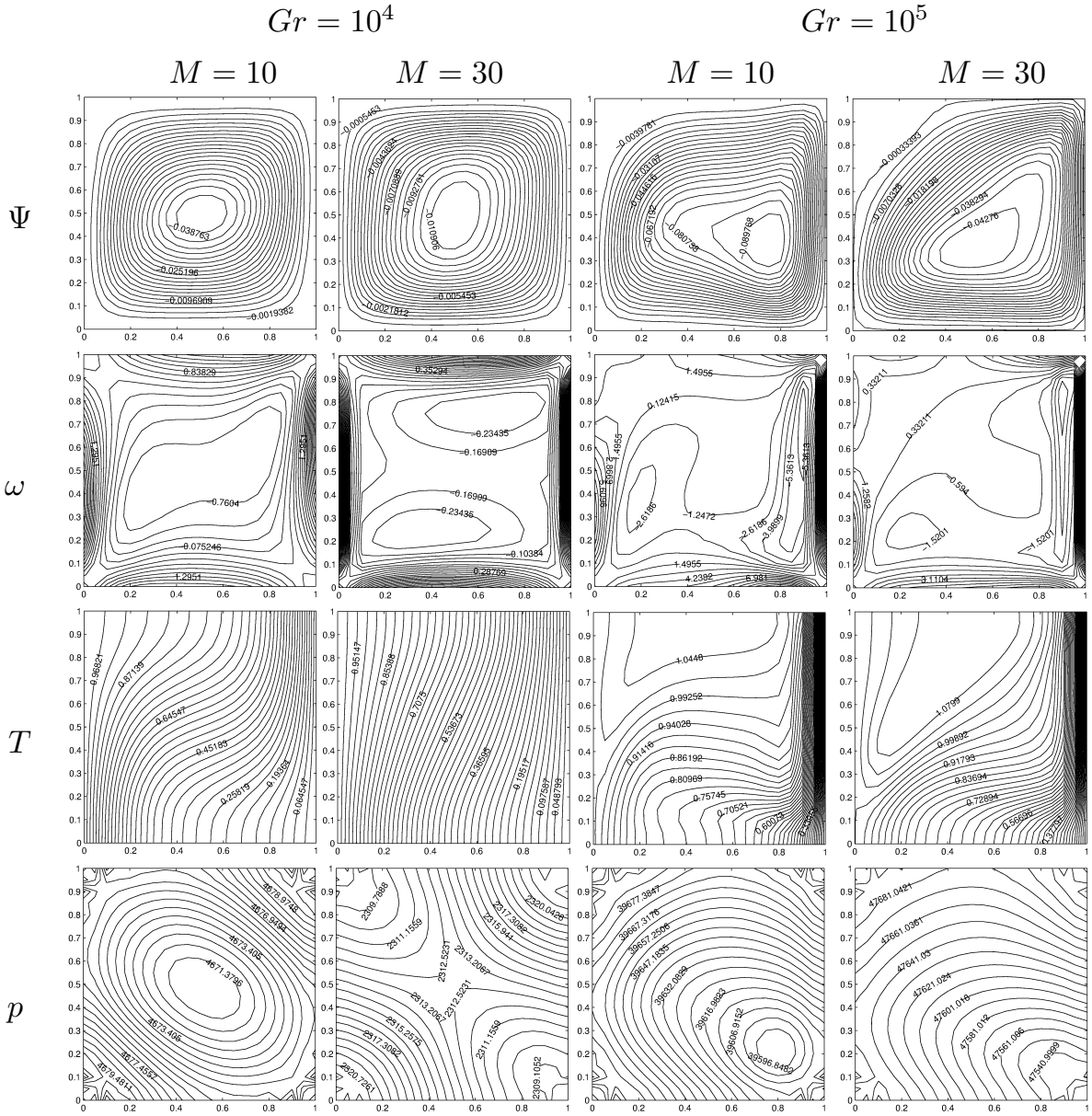

Figure 3.48: Problem 3.6.3: MHD convection flow for $Ec = 1$, $Gr = 10^4$ and $Gr = 10^5$.

3.6.4 MHD Convection Incompressible Flow in a Lid-Driven Cavity

In this problem, MHD convection flow is studied in a lid-driven cavity under the impact of a magnetic field applied in the x-direction. The bottom and top walls are kept at different temperatures, but the left and right walls are insulated. We have stationary boundary conditions for the velocity components except for the top lid which moves from the left to the right as can be seen in Figure 3.49. The vorticity and pressure boundary values are computed from the stream function and momentum equations, respectively.

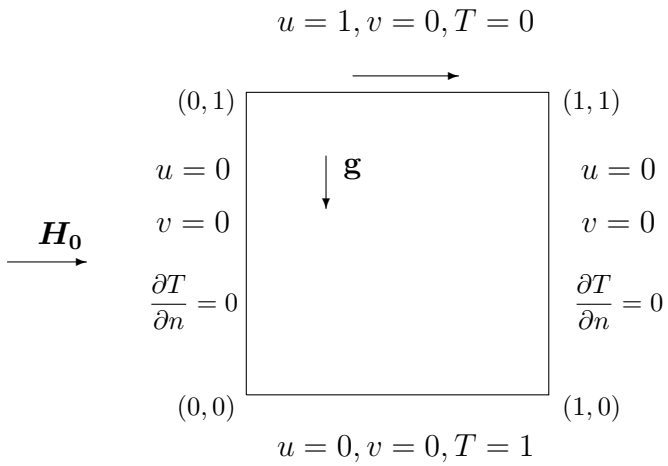

Figure 3.49: Problem 3.6.4: Lid-driven cavity and boundary conditions.

In the numerical computations, we take preassigned tolerance $\epsilon = 10^{-3}$ and relaxation parameters for the vorticity, temperature, and pressure as $\alpha_\omega = 0.01$, $\alpha_T = 0.1$, and $\alpha_p = 0.001$, respectively. The boundary is discretized by $N_b = 80$ points. The numerical results are obtained for Hartmann number values in the range $(0 - 80)$ and Grashof number is taken up to 10^4 ($10 \leq Gr \leq 10^4$) for fixed $Re = 100$ and $Pr = 0.71$. The solution is depicted in terms of streamlines, vorticity, pressure contours and isotherms.

In Figure 3.50, the increase in the Grashof number is considered on the flow, temperature and pressure behaviors in the absence of the magnetic field and viscous dissipation effects. These results are in well agreement with the ones obtained in [60], since

$Ec = 0$ corresponds to the heat transfer without viscous dissipation. As Gr increases, central vortex of stream function moves through the center of the cavity with an increasing magnitude. Lid-driven effect can be seen in the flow. Isotherms bend through the center and concentrate near the hot bottom wall since buoyancy force dominates the flow (Gr contains thermal expansion coefficient and thermal conductivity of the fluid). It can be seen in pressure profiles that pressure values also increase due to the high Gr number, and it extends through the hot wall.

Figure 3.51 presents the variation of the Hartmann number for fixed $Gr = 10^3$ and $Ec = 0$. It is observed that as the magnetic field intensity increases, the main flow shifts through the moving top lid with a decrease in the magnitude. With a further increase in M flow concentrates in front of the moving lid and forming a side layer which is an expected behavior of MHD flow. For larger M even secondary flow with small magnitude starts to develop and the rest of the cavity is almost stagnant. Magnetic field effect on isotherms is opposite to the effect of Gr. This means that further increase in M causes the convection to be suppressed as in the case of a small Gr. Pressure is increased everywhere in the channel and concentrates in front of the lid when M increases.

The effect of viscous dissipation on the MHD convection flow can be seen in Figures 3.52-3.53 by taking $Ec = 1$. Figure 3.52 depicts the variations of Gr on the flow and temperature when $Ec = 1$. One can see that boundary layer is developed near the moving top lid when Gr is increased, and the increase in Gr causes the extension of circulation of the fluid through the center of the cavity as in the case of $Ec = 0$. Thus, viscous dissipation does not cause a significant change on the flow when we compare to Figure 3.50. On the other hand, isotherms tend to bend inside the cavity between adiabatic walls with the effects of moving lid, and an increase in Gr. Viscous dissipation effect together with the buoyancy force cause the temperature values to drop suddenly near the upper lid forming boundary layer instead of concentrating through the hot wall as in the case of $Ec = 0$ (Figure 3.50). As the buoyancy force increases, pressure is extended throughout the cavity.

The effects of both magnetic field and viscous dissipation can be seen in Figure 3.53. The flow behavior is the same as in the case $Ec = 0$ (Figure 3.51). However, viscous

dissipation impact is most pronounced on the temperature contours. Magnetic field has a cooling effect on isotherms pushing the heat through the moving lid and forming a boundary layer near the cold wall. It is seen that pressure profiles do not change significantly when we compare with the Figure 3.51.

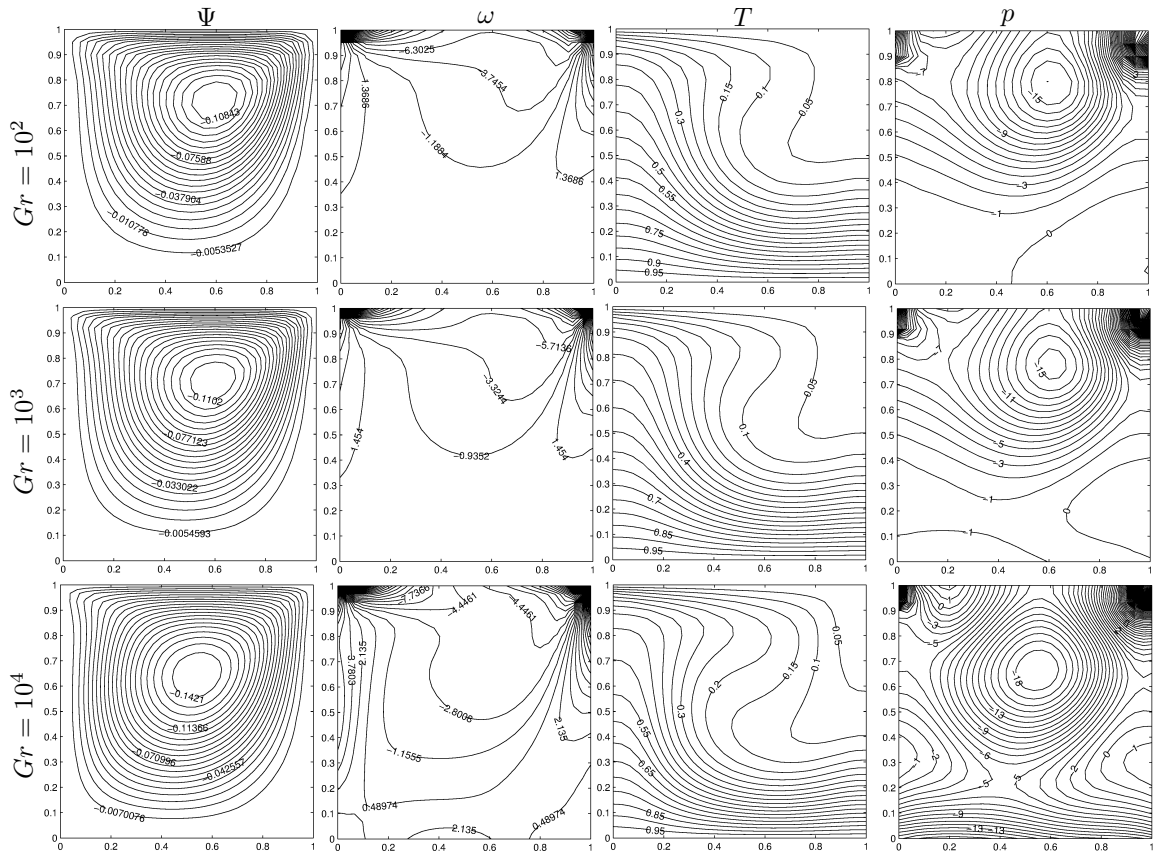

Figure 3.50: Problem 3.6.4: MHD convection flow for $M = 0$, $Ec = 0$.

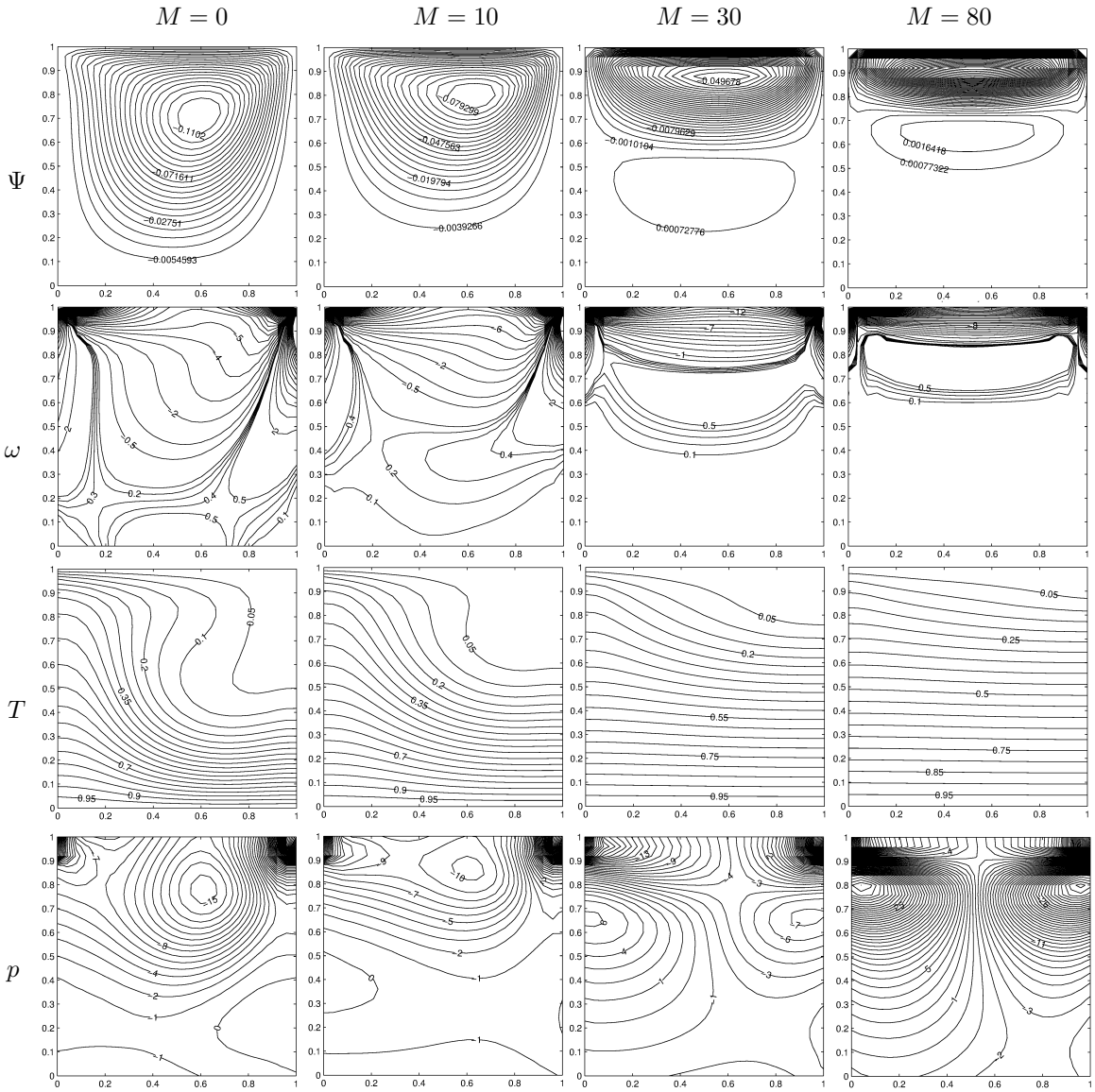

Figure 3.51: Problem 3.6.4: MHD convection flow for $Gr = 10^3$, $Ec = 0$.

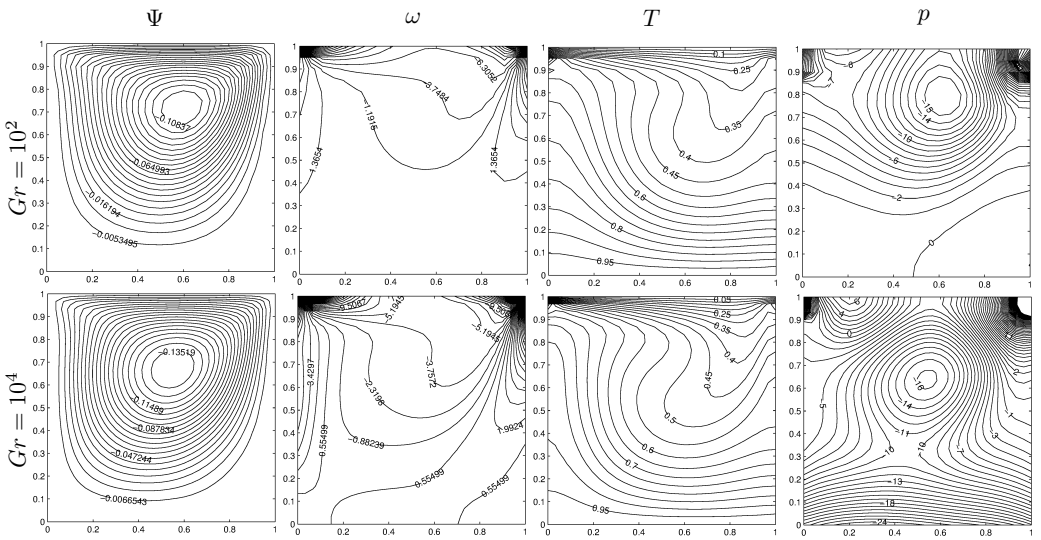

Figure 3.52: Problem 3.6.4: MHD convection flow for $M = 0$, $Ec = 1$.

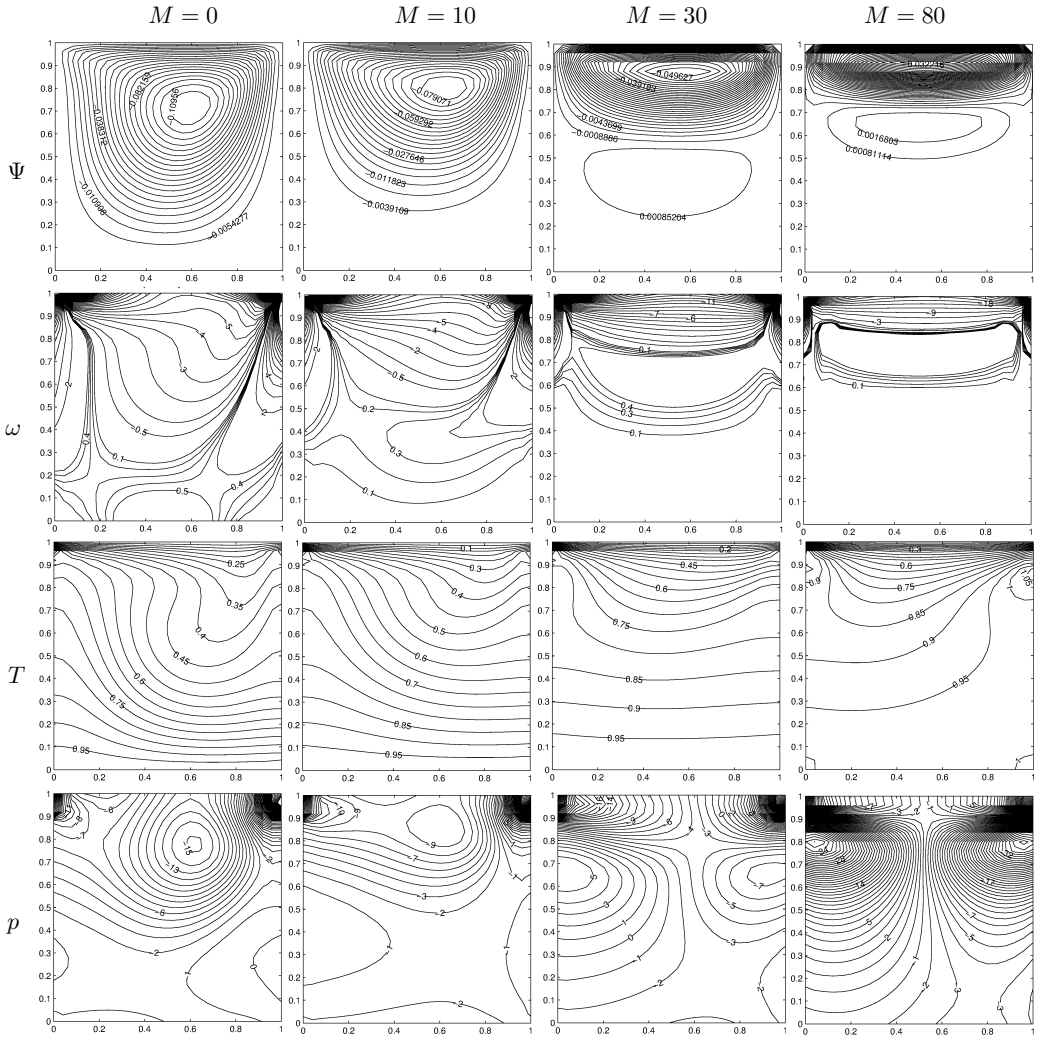

Figure 3.53: Problem 3.6.4: MHD convection flow for $Gr = 10^3$, $Ec = 1$.

3.6.5 MHD Convection Incompressible Flow in a Constricted Channel

Finally, the MHD convection flow is studied in a constricted rectangular cavity under the effect of a uniform x- or y-directed magnetic field. The middle section of the cavity is symmetrically constricted using functions f_b and f_t which are the vertical coordinates of the bottom and top walls, respectively (Figure 3.54). These functions are given as,

$$f_b(x) = \frac{1}{2}h(1 + \cos(2\pi(x - L/2)/L)), \qquad f_t(x) = 1 - f_b(x), \quad x \in [0, L]$$

where L is the horizontal length of the channel. The constriction ratio(CR) of the enclosure is computed as $CR = 2h \times 100$. The vertical walls of the channel are adiabatic while the bottom wall is heated and the top wall is kept cold. Fluid velocity has no-slip condition on the boundary of the cavity and the homogeneous Neumann type boundary condition is given for the pressure ($\frac{\partial p}{\partial n} = 0$). The unknown vorticity values are again obtained from the stream function equation by using finite difference scheme.

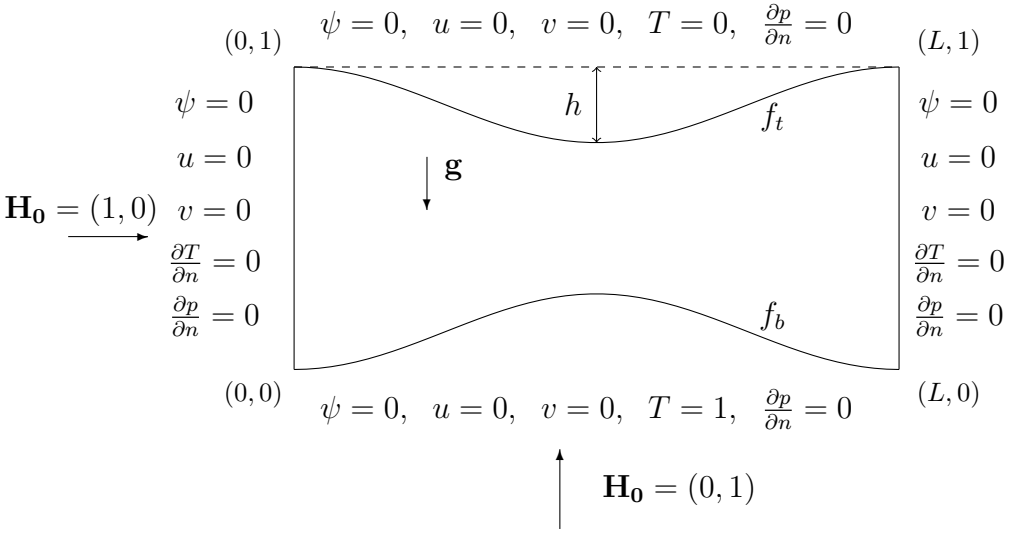

Figure 3.54: Problem 3.6.5: Schematic of the rectangular cavity with constriction and the boundary conditions

The numerical results are obtained for several values of the Hartmann number (M) and the constriction ratios (CR) to see the effects on the flow and isotherms for fixed $Re = 100$ and $Pr = 0.71$. Also we use different values of Grashof number (Gr) to

analyze the behavior of the forced, mixed and natural convection flows since the flow is dominated by the forced, mixed or natural convection if the Richardson number ($Ri = Gr/Re^2$) is less than 1, equal to 1 or greater than 1, respectively.

In all numerical computations, we neglect the joule heating and viscous dissipation terms in the energy equation by taking $Ec = 0$. The convergence tolerance is generally $\epsilon = 10^{-7}$ and $\epsilon = 10^{-11}$ for large values of the parameters Gr and M. Number of boundary points lie in the range $70 \leq N_b \leq 100$.

The proposed numerical procedure is validated first for the natural convection flow in non-constricted rectangular enclosure by taking $L = 4$, $Gr = 25 \times 10^4$, $M = 0$ and $Pr = 0.01$. The flow and temperature behaviors are in well agreement with the ones in [17].

When the magnetic field is applied vertically, $\boldsymbol{H_0} = (0, 1)$, MHD convection flow equations (3.106)-(3.111) are solved iteratively. We take Grashof number in between $5 \times 10^3 \leq Gr \leq 5 \times 10^4$, Hartmann number ranging in $0 \leq M \leq 25$ and the constriction ratio $0\% \leq CR \leq 40\%$. The influence of the horizontal length of the channel is also analyzed by testing with $L = 0, 2, 4$.

Figure 3.55 shows the effect of Grashof number increase in the non-constricted square channel ($CR = 0$) neglecting magnetic field ($M = 0$). As Gr increases, magnitude of the flow and pressure increases. When $Gr > 10^4$, the flow (ψ, ω) is separated into two loops symmetrically with respect to $x = 0.5$. Convection dominance is observed but isotherms show symmetry with respect to $x = 0.5$ as the flow bending at the center of the cavity for $Gr > 10^4$ since the forced convection turns out to be natural convection ($Ri >> 1$).

We show the influence of magnetic field on the flow, temperature and pressure behaviors for fixed $Gr = 10^4$ in Figure 3.56. As the intensity of the magnetic field increases, flow is flattened which is an expected behavior for MHD flow. Further increase in M results in the retardation of the convection dominance which can be observed in isotherms as becoming straight lines parallel to the hot and cold walls. Similarly, pressure behavior is uniformly distributed in the channel.

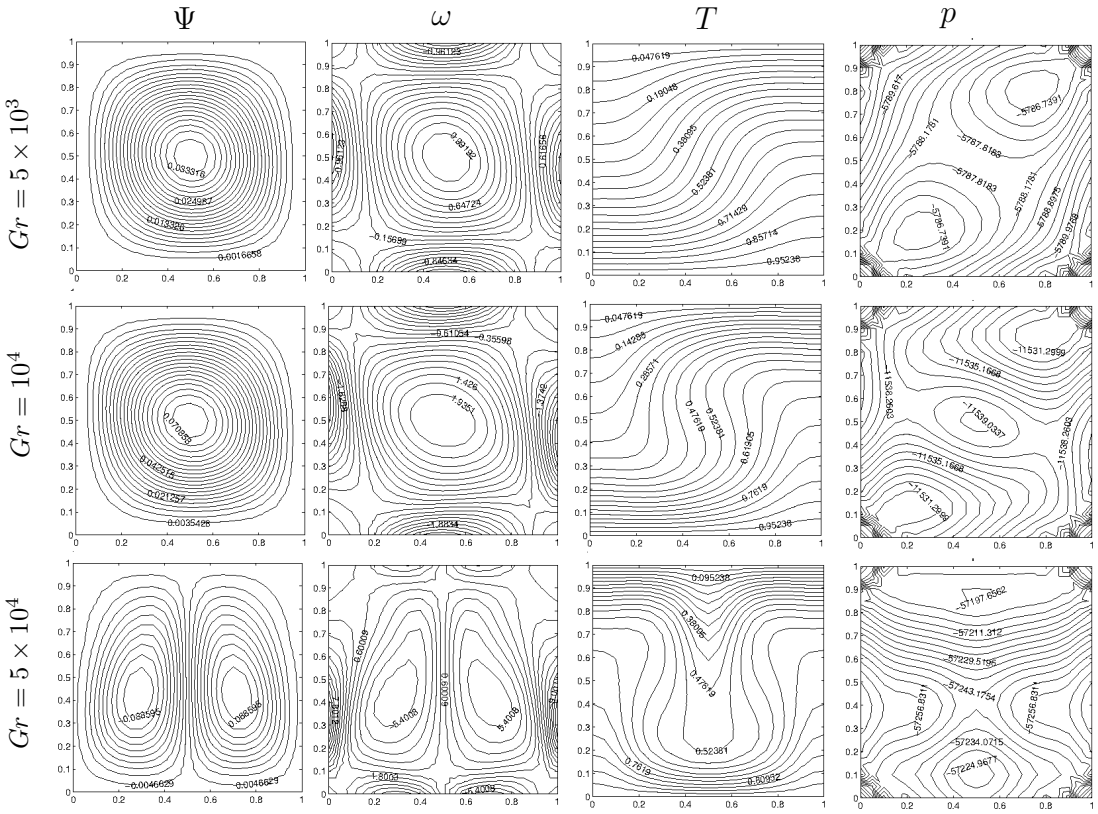

Figure 3.55: Problem 3.6.5: The effect of Gr on the flow, temperature and pressure for $M = 0$ and $L = 1$, $\boldsymbol{H_0} = (0, 1)$.

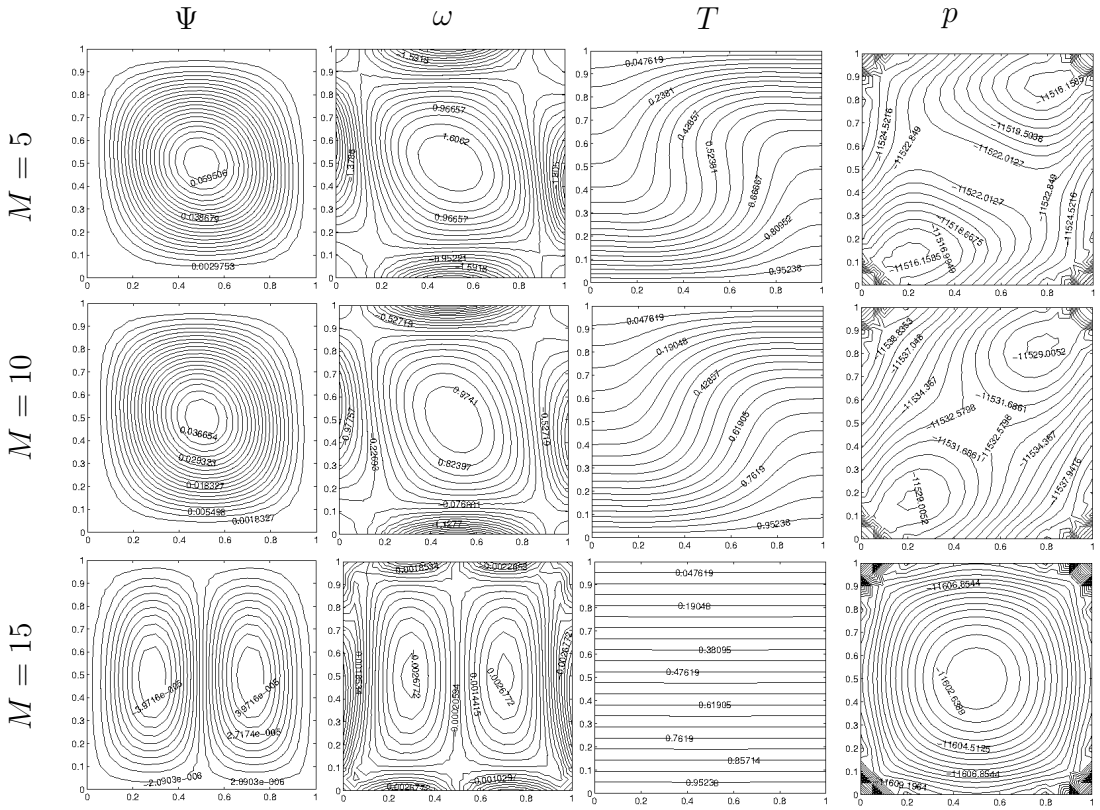

Figure 3.56: Problem 3.6.5: The effect of M on the flow, temperature and pressure for $Gr = 10^4$ and $L = 1$, $\boldsymbol{H_0} = (0, 1)$.

Figures 3.57-3.58 depict the effect of magnetic field for an electrically conducting fluid in a non-constricted rectangular channel for the increase of its horizontal length $L = 2, 4$. When the length of the channel increases, the number of convection rolls increases which can be seen from the first row of Figure 3.57 and Figure 3.58. The same effect of increasing M on the flow and temperature is observed as in the square channel (Figure 3.56). An increase in M causes Hartmann layers near to the top and bottom walls and side layers parallel to the applied magnetic field leaving the central part stagnant. When the Hartmann number value is reached to 15, the number of rolls in the stream function and vorticity also increases for $L = 4$ as can be seen in Figure 3.58.

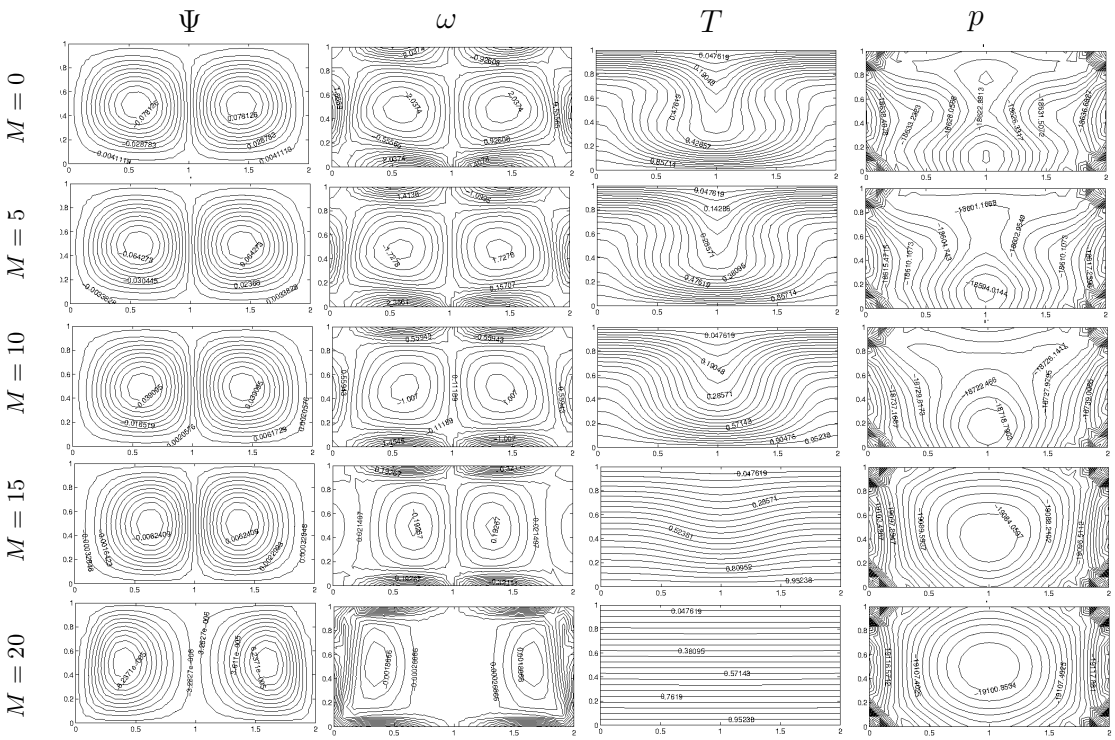

Figure 3.57: Problem 3.6.5: The effect of M on the flow, temperature and pressure for $Gr = 10^4$ and $L = 2$, $\boldsymbol{H_0} = (0, 1)$.

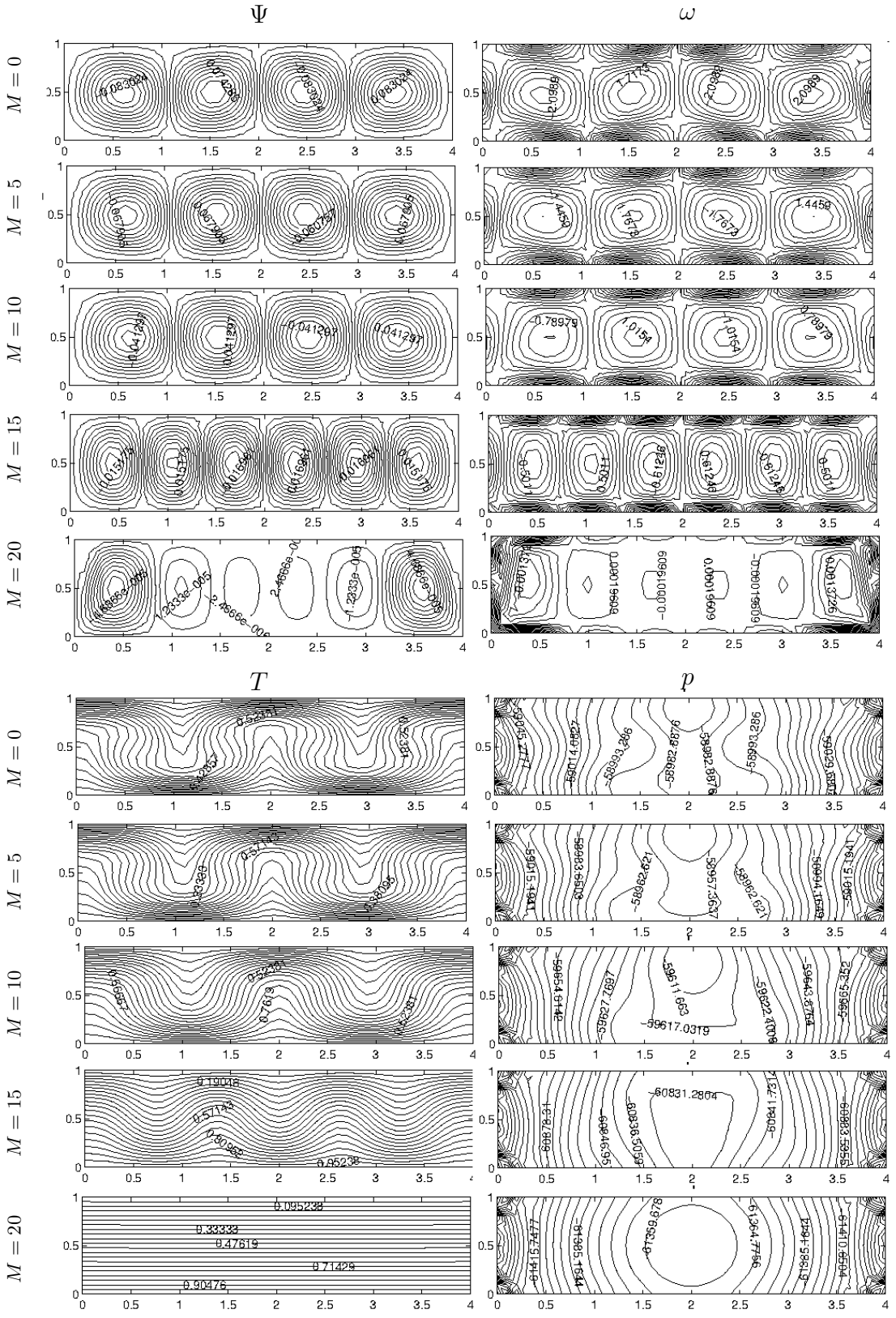

Figure 3.58: Problem 3.6.5: The effect of M on the flow, temperature and pressure for $Gr = 10^4$ and $L = 4$, $\boldsymbol{H_0} = (0, 1)$.

The effect of the constriction ratio on the convection flow under the effect of vertical magnetic field is shown in Figures 3.59-3.60. There is a symmetry in the flow, temperature and pressure with respect to vertical centerline. As the constriction ratio increases, flow vortices in the constriction area are started to be weakened and the fluid becomes almost stagnant at the middle of the channel. Fluid concentrates through the adiabatic walls due to the constriction. This causes the retardation of the convection in the constriction area. Similarly, the magnitude of the pressure is increased through the side walls.

For a fixed $CR = 40\%$, we increase the Hartmann number to see the impact of magnetic field on MHD convection flow in a constricted channel with the length $L = 2, 4$. In Figures 3.61-3.62 as M increases the magnitude of the flow decreases but the pressure increases as in the non-constricted channel shown in Figures 3.57-3.58. The increase in the magnitude of applied magnetic field first weakens and then increases the number of the center vortices in the flow ($M \leq 10$). In the constricted channel, the division of the flow into symmetric vortices and Hartmann layer formation start for a smaller value of $M \geq 10$ when we compare with the rectangular channel case. For $M \geq 15$ the flow vortices are symmetrically located with respect to the vertical and horizontal centerlines. The number of the vortices does not change with the length of the constricted channel contrary to non-constricted channel. Isolines become completely diffusion dominated and are distributed uniformly between the horizontal walls.

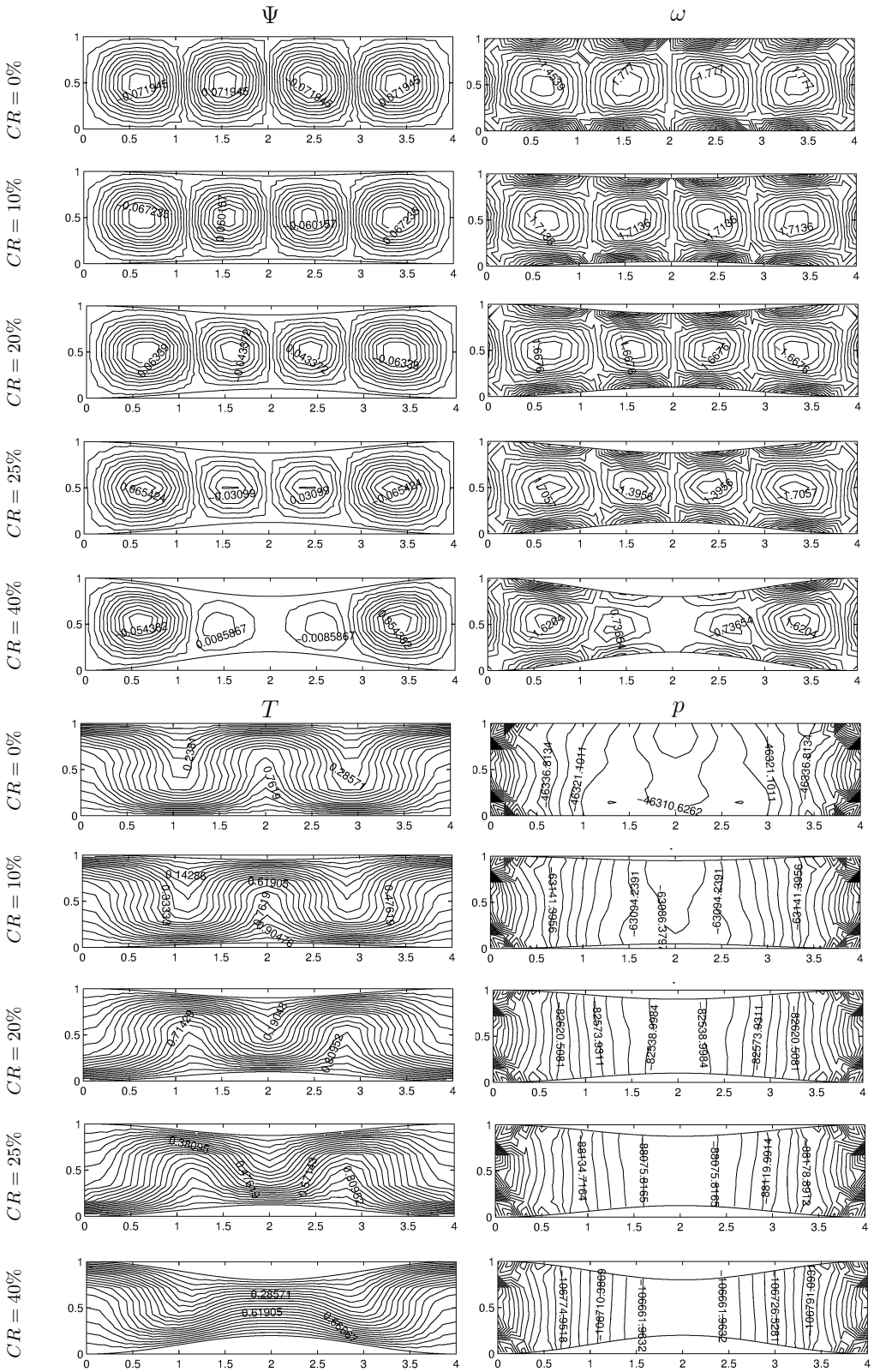

Figure 3.59: Problem 3.6.5: The effect of CR on the flow, temperature and pressure for $Gr = 10^4$, $M = 4$ and $L = 4$, $\boldsymbol{H_0} = (0, 1)$.

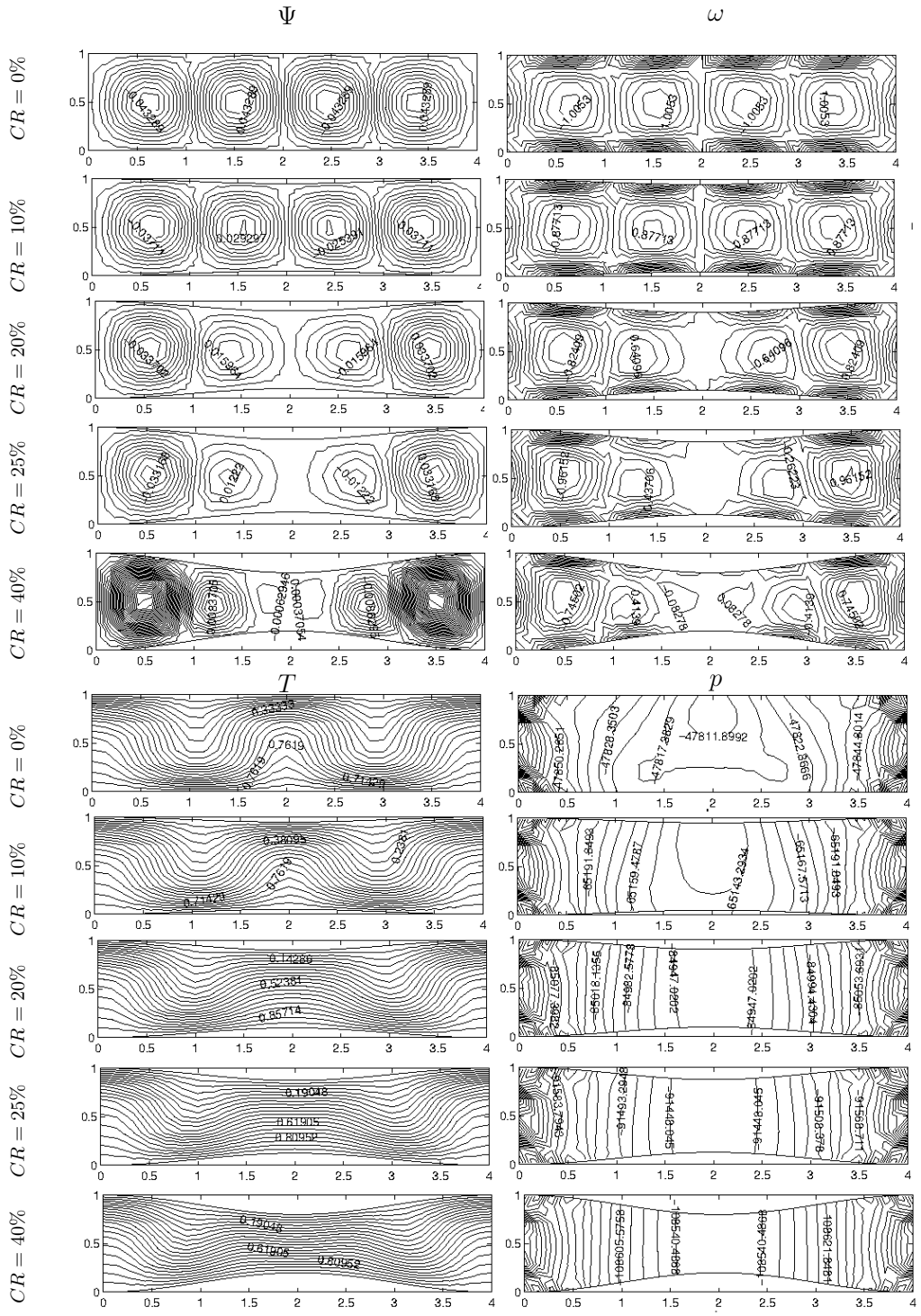

Figure 3.60: Problem 3.6.5: The effect of CR on the flow, temperature and pressure for $Gr = 10^4$, $M = 10$ and $L = 4$, $\boldsymbol{H_0} = (0, 1)$.

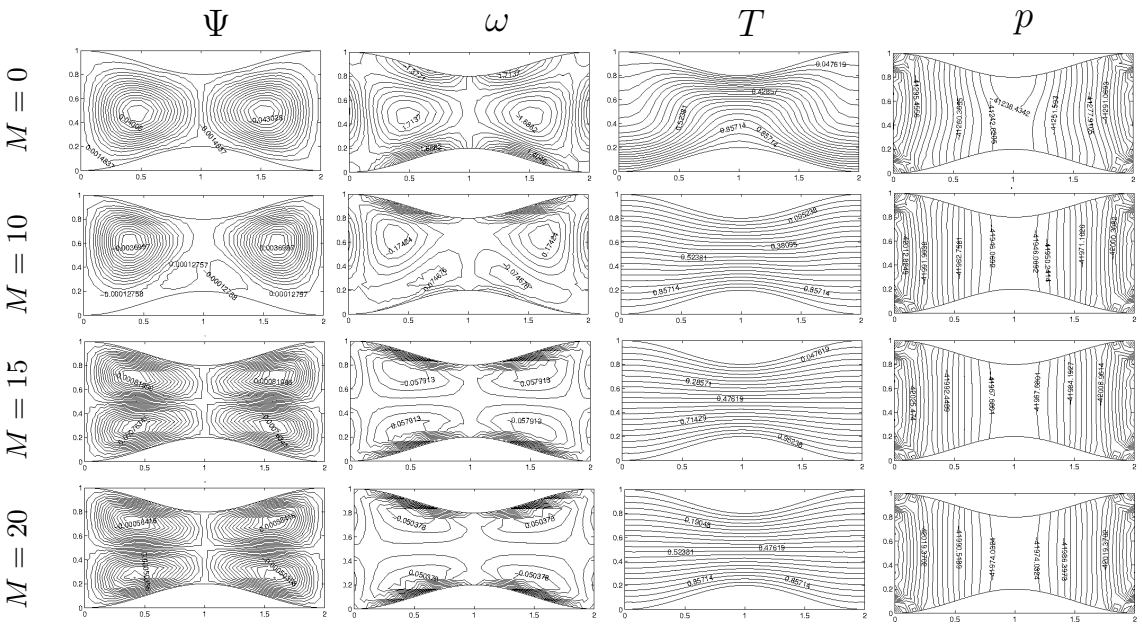

Figure 3.61: Problem 3.6.5: The effect of M on the flow, temperature and pressure for $Gr = 10^4$, $CR = 40\%$ and $L = 2$, $\boldsymbol{H_0} = (0, 1)$.

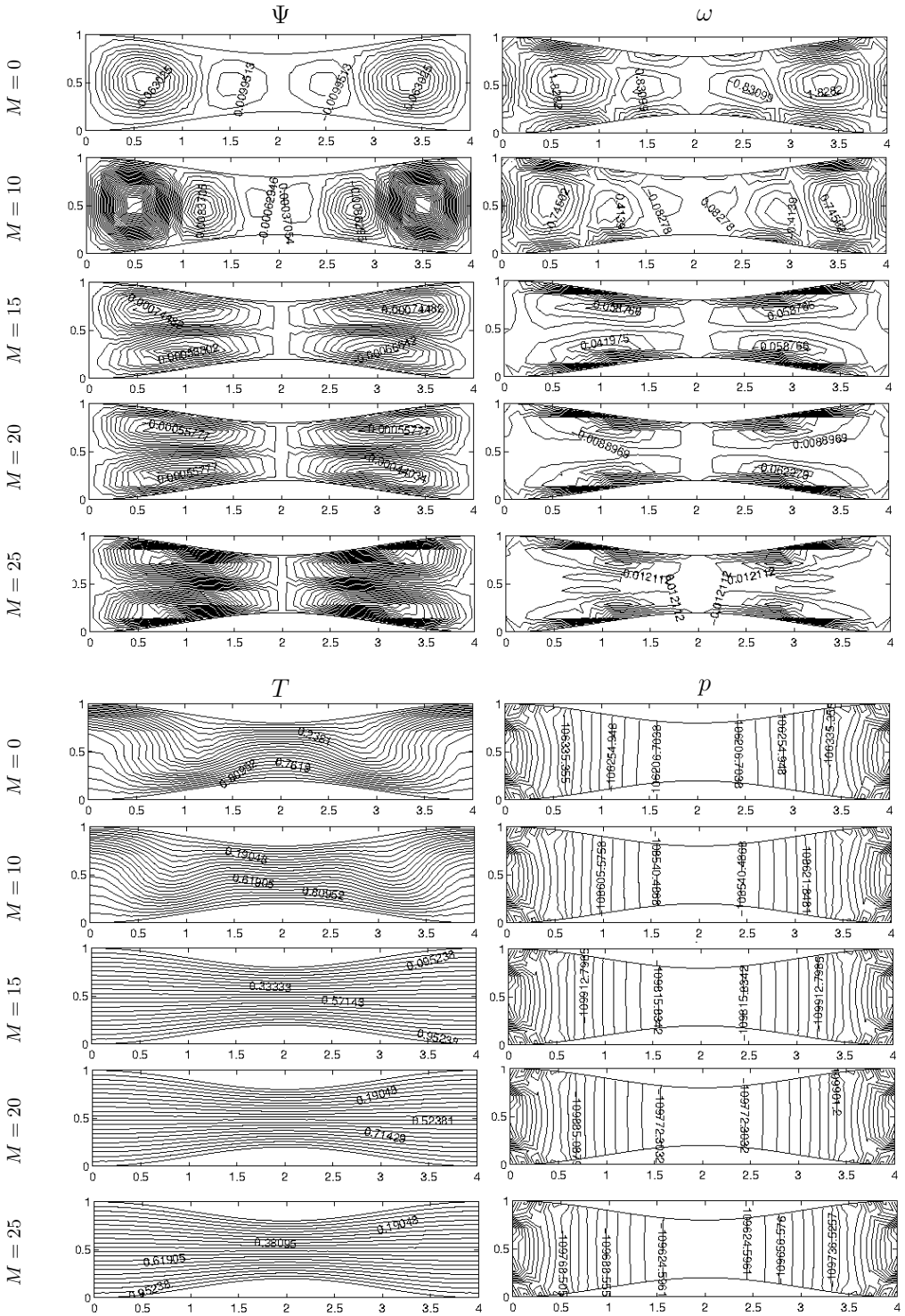

Figure 3.62: Problem 3.6.5: The effect of M on the flow, temperature and pressure for $Gr = 10^4$, $CR = 40\%$ and $L = 4$, $\boldsymbol{H_0} = (0, 1)$.

In Figure 3.63 we fix $CR = 40\%$ and increase Gr for $M = 10$ and $M = 20$ to analyze the effect of magnetic field on the convection flow in a constricted channel. For a small intensity of magnetic field ($M = 10$) the passage from forced convection to natural convection destroys the symmetrically located four loops into two loops symmetric with respect to $x = 1$ in the flow. As M increases, magnetic field forces the mixed convection of the fluid to behave as if forced convection. Due to the increase in both the constriction and buoyancy force the appearance of the new vortices is observed symmetrically at the center (constriction area) of the cavity. Gr increase results in bending in isotherms.

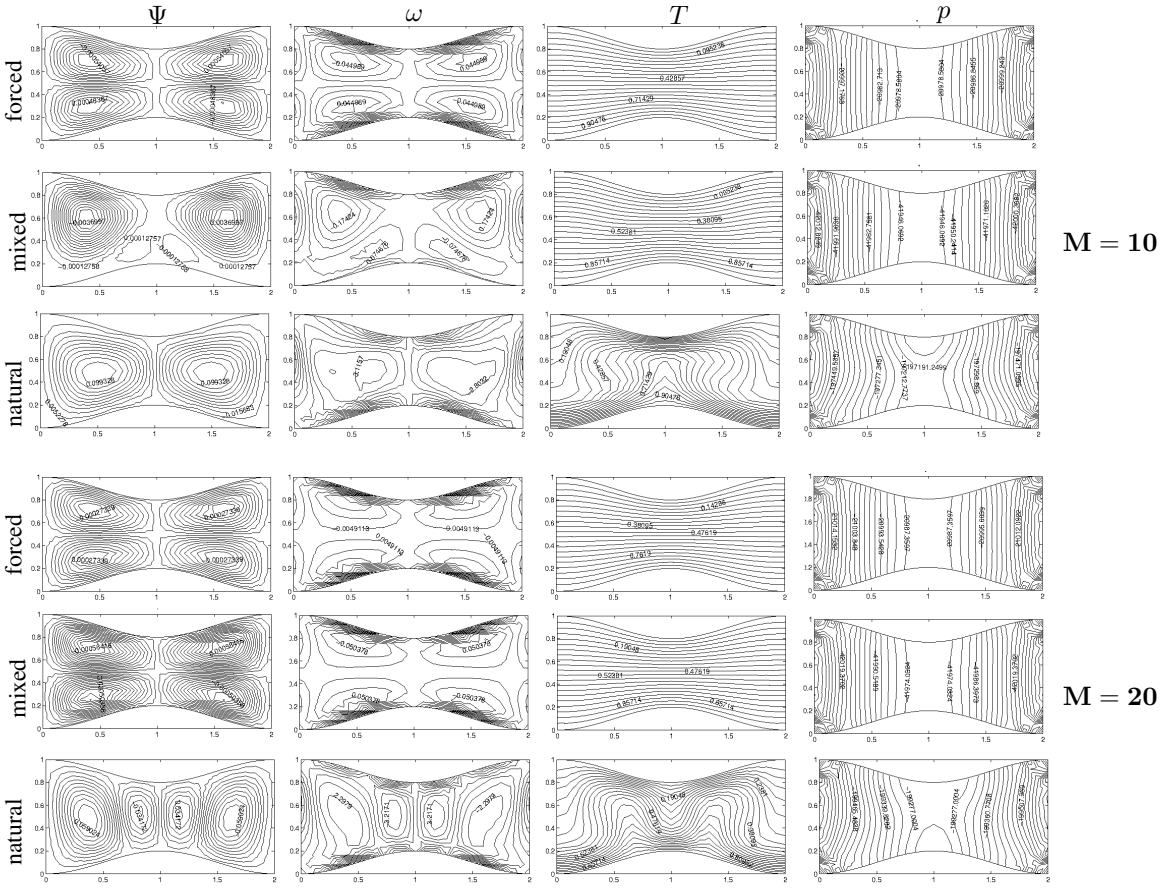

Figure 3.63: Problem 3.6.5: The effect of magnetic field on convection flow for $CR = 40\%$ and $L = 2$, $\boldsymbol{H_0} = (0, 1)$.

Now, the heat transfer on the MHD flow is considered in the constricted channel under the influence of horizontally applied magnetic field. Equations (3.100)-(3.105) are solved for different Hartmann number values for fixed $CR = 40\%$, $Gr = 10^4$

and $L = 2, 4$. The numerical results are depicted in terms of ψ, ω, T, p in Figures 3.64-3.65. It is observed that the effect of horizontal magnetic field is nearly the same as the effect of magnetic field in the y-direction comparing with the results in Figures 3.61-3.62. Boundary layers on the top and bottom walls as M increases are not pronounced much as in the case of vertically applied magnetic field since now these walls are parallel to the magnetic field. However, the fluid flows in terms of equally placed symmetric vortices with respect to axes in horizontally applied magnetic field. Isotherms and pressure are not affected with the direction of applied magnetic field.

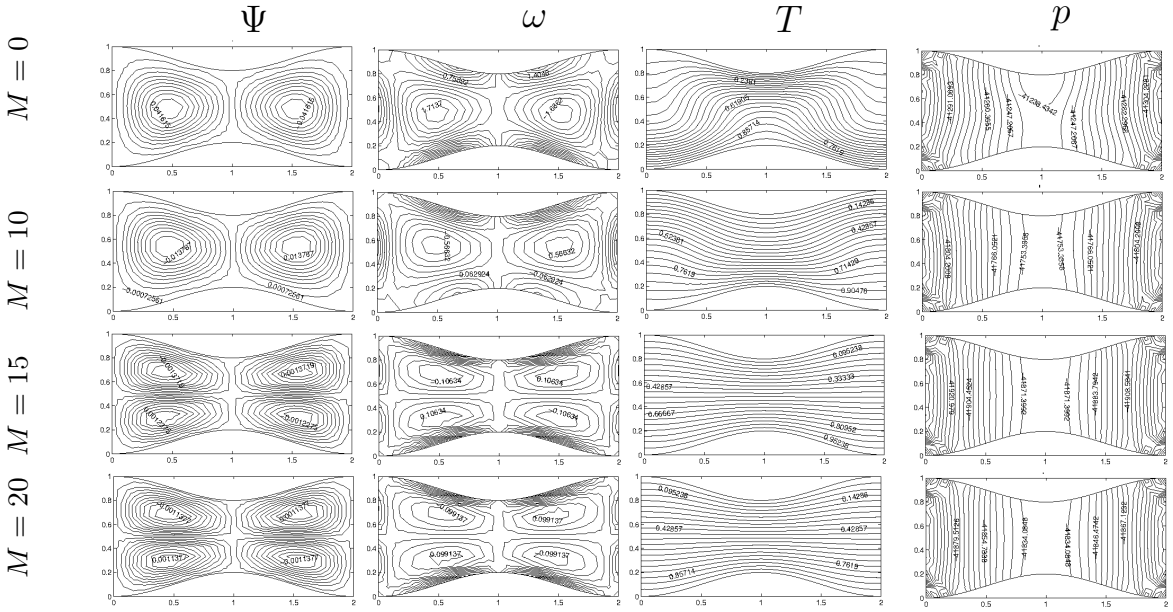

Figure 3.64: Problem 3.6.5: The effect of M on the flow, temperature and pressure for $Gr = 10^4$, $CR = 40\%$ and $L = 2$, $\boldsymbol{H_0} = (1, 0)$.

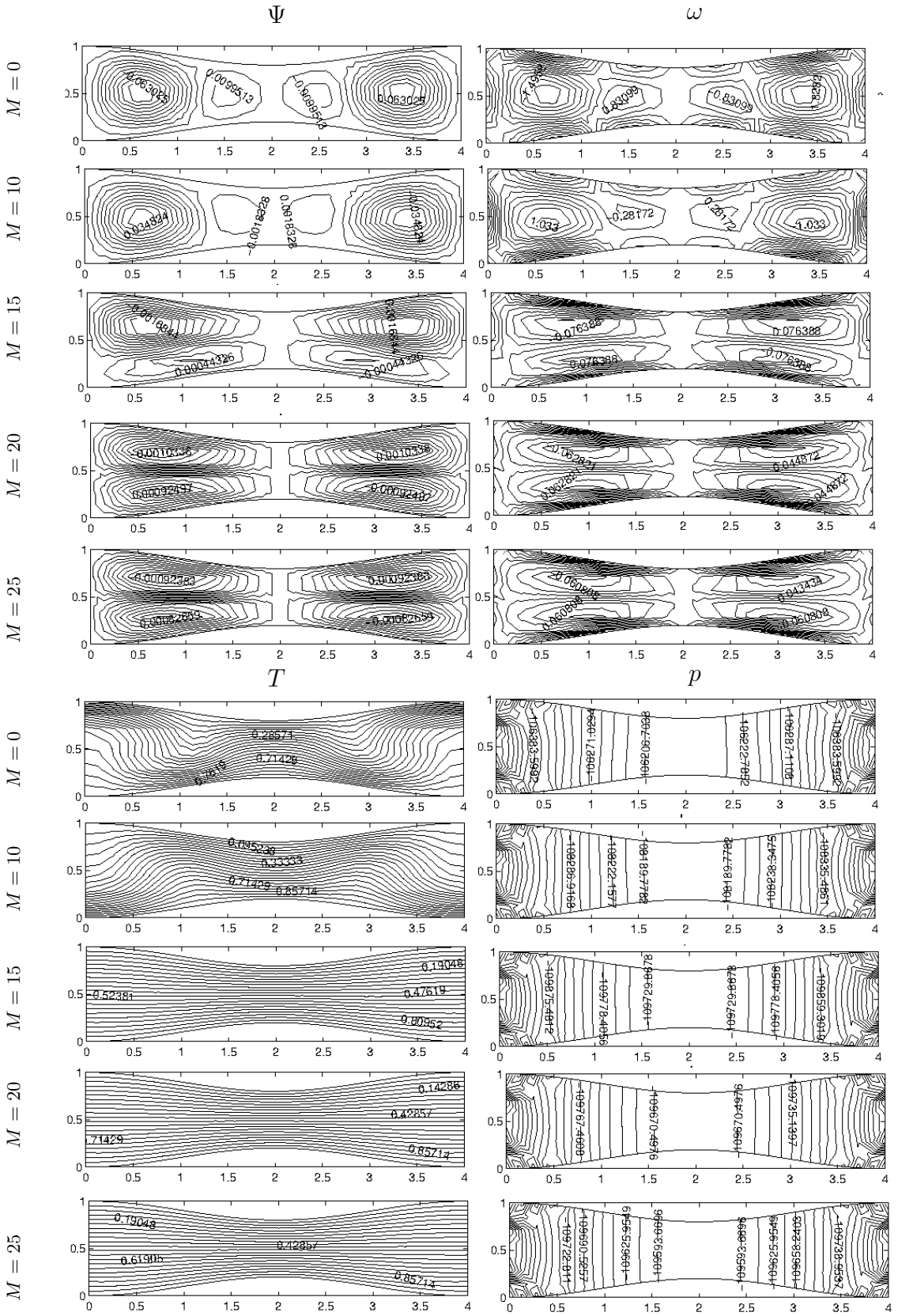

Figure 3.65: Problem 3.6.5: The effect of M on the flow, temperature and pressure for $Gr = 10^4$, $CR = 40\%$ and $L = 4$, $\boldsymbol{H_0} = (1, 0)$.

In this Chapter, we first apply the RBF approximation for solving the MHD Stokes flow in square cavities, in a lid-driven cavity, in a constricted cavity with a moving left wall and in a backward-facing step channel. Stokes flow is subjected to different orientations of external magnetic field. When the magnetic field direction is parallel to the moving lid, the Stokes flow is completely squeezed through the moving wall forming boundary layer. However, this effect is overwhelmed by the horizontal magnetic field (perpendicular to the lid). Secondary flow is developed due to the magnetic field having a same direction with the moving wall or the constriction of the enclosure. Magnetic field in the pipe axis-direction generates the electric potential. It is observed that electric potential has the same behavior of the flow, but it does not show a significant alteration when the intensity of the magnetic field increases, contrary to MHD incompressible flow problem. Secondly, the RBF approximation is implemented to MHD convection Stokes flow and MHD convection incompressible flow by taking $Re = 0.6$ and $Re = 100$, respectively, for fixed $Pr = 0.71$. When the viscous dissipation is present, isotherms concentrate through the cold wall forming a boundary layer in both cases. The increase in the constriction ratio of the channel or the magnetic field intensity causes the retardation of the convection dominance opposing to buoyancy force effect.

CHAPTER 4

STABILITY ANALYSIS FOR THE RBF SOLUTION OF THE UNSTEADY MHD EQUATIONS

In this Chapter, we are going to explain first the stability of the general initial value problem $\frac{du}{dt} = f(t, u)$, and then extend the analysis for unsteady Navier-Stokes equations, time dependent MHD convection flow and full MHD problems. Since the application of radial basis function approximation to these time dependent flow problems gives the systems of ordinary differential equations in time, the stability characteristics of these fluid flow problems are similar to the stability of general initial value problem. In each system of RBF approximation of the above mentioned problems, the explicit Euler method is used for the discretization of the time derivatives, and the stability analysis is performed in terms of the maximum eigenvalues of the coefficient matrices containing the time increment, relaxation parameters and the problem variables. The optimal choices of the time increment and relaxation parameters are given computationally in terms of tables for considered problem parameters. Also, for the range of parameters guaranteeing the stability, the solutions of the considered MHD problems are presented in terms of streamlines, equal vorticity lines, isotherms, pressure and magnetic potential contours.

4.1 Stability Analysis of the System of Initial Value Problems

In this Section, the stability analysis of a single step method applied to the system of ordinary differential equations will be explained.

Let us consider a system of first order differential equations

$$\frac{d\boldsymbol{u}}{dt} = \boldsymbol{f}(t, \boldsymbol{u}) \tag{4.1}$$

with initial boundary condition

$$\boldsymbol{u}(t_0) = \boldsymbol{u}_0 \tag{4.2}$$

where

$$\boldsymbol{u} = \begin{bmatrix} u_1 \\ u_2 \\ \vdots \\ u_{N_b+N_i} \end{bmatrix}, \quad \boldsymbol{f}(t, \boldsymbol{u}) = \begin{bmatrix} f_1(t, u_1, \ldots, u_{N_b+N_i}) \\ f_2(t, u_1, \ldots, u_{N_b+N_i}) \\ \vdots \\ f_{N_b+N_i}(t, u_1, \ldots, u_{N_b+N_i}) \end{bmatrix}, \quad \boldsymbol{u}_0 = \begin{bmatrix} u_{1,0} \\ u_{2,0} \\ \vdots \\ u_{N_b+N_i,0} \end{bmatrix}.$$

We assume that the right hand side functions $f_i(t, \boldsymbol{u})$'s have continuous partial derivatives $\dfrac{\partial f_i(t, \boldsymbol{u})}{\partial u_j} = c_{ij}$, $1 \leq i, j \leq N_b + N_i$ and construct the Jacobian matrix $\boldsymbol{C} = [c_{ij}]$. Then, the linearized form of the equation (4.1) is given by

$$\frac{d\tilde{\boldsymbol{u}}}{dt} = \boldsymbol{C}\tilde{\boldsymbol{u}} \tag{4.3}$$

and the stability characteristics of the equations (4.1) and (4.3) are similar.

The matrix $\boldsymbol{C}$ usually depends on the variables t and $\tilde{\boldsymbol{u}}$, but we consider simple case of the matrix $\boldsymbol{C}$ to estimate the behavior of the solution of equation (4.3). If $\boldsymbol{C}$ is a constant matrix with distinct eigenvalues, then the analytic solution $\tilde{\boldsymbol{u}}(t)$ of the equation (4.3) with the initial approximation $\tilde{\boldsymbol{u}}_{\boldsymbol{0}}$ is given by [24]

$$\tilde{\boldsymbol{u}}(t) = \boldsymbol{e}^{(\boldsymbol{C}t)}\tilde{\boldsymbol{u}}_0 \tag{4.4}$$

where $\boldsymbol{e}^{(\boldsymbol{C}t)}$ is defined as a matrix function

$$\boldsymbol{e}^{(\boldsymbol{C}t)} = \boldsymbol{I} + \boldsymbol{C}t + \frac{(\boldsymbol{C}t)^2}{2!} + \frac{(\boldsymbol{C}t)^3}{3!} + \ldots \tag{4.5}$$

and $\boldsymbol{I}$ is the identity matrix.

If $\boldsymbol{C}$ is diagonalizable, then there exist a matrix $\boldsymbol{P}$ such that

$$\boldsymbol{P^{-1}CP = D} \tag{4.6}$$

where $\boldsymbol{D}$ is the diagonal matrix and constructed by the eigenvalues λ_i of the matrix $\boldsymbol{C}$ as

$$\boldsymbol{D} = \begin{bmatrix} \lambda_1 & \dots & 0 \\ & \ddots & \\ 0 & \dots & \lambda_{N_b+N_i} \end{bmatrix}. \tag{4.7}$$

The transformation $\boldsymbol{P}$ also diagonalizes $\boldsymbol{e}^{(\,\boldsymbol{C}t)}$ with the relation [24]

$$\boldsymbol{P}^{-1}\boldsymbol{e}^{(\,\boldsymbol{C}t)}\boldsymbol{P} = \boldsymbol{e}^{(\,\boldsymbol{D}t)} \tag{4.8}$$

where $\boldsymbol{e}^{(\,\boldsymbol{D}t)}$ is diagonal matrix such that

$$\boldsymbol{e}^{(\,\boldsymbol{D}t)} = \begin{bmatrix} e^{\lambda_1 t} & \dots & 0 \\ & \ddots & \\ 0 & \dots & e^{\lambda_{N_b+N_i} t} \end{bmatrix}. \tag{4.9}$$

Here, the eigenvalues λ_i are assumed to be distinct or possibly complex with negative real parts.

Using the relation $\boldsymbol{C} = \boldsymbol{P}\boldsymbol{D}\boldsymbol{P}^{-1}$ from the equation (4.6), the initial value problem (4.3) can be written as

$$\frac{d\tilde{\boldsymbol{u}}}{dt} = \boldsymbol{C}\tilde{\boldsymbol{u}} = \boldsymbol{P}\boldsymbol{D}\boldsymbol{P}^{-1}\tilde{\boldsymbol{u}} \tag{4.10}$$

Multiplying both sides by $\boldsymbol{P}^{-1}$ and defining $\boldsymbol{v} = \boldsymbol{P}^{-1}\tilde{\boldsymbol{u}}$, we obtain the equation

$$\frac{d\boldsymbol{v}}{dt} = \boldsymbol{D}\boldsymbol{v} \tag{4.11}$$

with initial condition

$$\boldsymbol{v}_0 = \boldsymbol{P}^{-1}\boldsymbol{v}_0. \tag{4.12}$$

Thus, the analytic solution $\boldsymbol{v}(t)$ of the equation (4.11) is

$$\boldsymbol{v}(t) = \boldsymbol{e}^{(\,\boldsymbol{D}t)}\boldsymbol{v}_0. \tag{4.13}$$

Now, the application of the single step method to the equation (4.3) for the vector $\tilde{\boldsymbol{u}}$ gives the numerical values of the function $\tilde{\boldsymbol{u}}$(t) at the time level t_{m+1}

$$\tilde{\boldsymbol{u}}_{m+1} = \boldsymbol{E}(\boldsymbol{C}\Delta t)\tilde{\boldsymbol{u}}_m, \quad m = 0, \dots, N_b + N_i - 1 \tag{4.14}$$

where the growth factor matrix $\boldsymbol{E}(\boldsymbol{C}\Delta t)$ is defined as

$$\boldsymbol{E}(\boldsymbol{C}\Delta t) = \boldsymbol{I} + \boldsymbol{C}\Delta t + \frac{(\boldsymbol{C}\Delta t)^2}{2!} + \cdots + \frac{(\boldsymbol{C}\Delta t)^q}{q!} \tag{4.15}$$

if the method is q-th order.

Similarly, imposing the single step method to the equation (4.11) for the vector $\boldsymbol{v}$, we can compute $\boldsymbol{v}$ at the time level $m+1$ as

$$\boldsymbol{v}_{m+1} = \boldsymbol{E}(\boldsymbol{D}\Delta t)\boldsymbol{v}_m \tag{4.16}$$

where $\boldsymbol{E}(\boldsymbol{D}\Delta t)$ is the diagonal matrix with diagonal elements $E_i(\lambda_i\Delta t)$ which is the approximation to the diagonal elements $e^{(\lambda_i\Delta t)}$, $i = 1, \ldots, N_b + N_i$ of the matrix $\boldsymbol{e}^{(\boldsymbol{D}\Delta t)}$. Thus, the stability analysis of the single step method applied to the system of initial value problems (4.1) can be discussed by applying the method to the scalar equation [24]

$$\frac{d\tilde{u}}{dt} = \lambda_i \tilde{u}, \quad i = 1, \ldots, N_b + N_i \tag{4.17}$$

where λ_i are the eigenvalues of $\boldsymbol{C}$.

Thus, the single step method is absolutely stable if

$$|E_i(\lambda_i\Delta t)| < 1, \quad i = 1, \ldots, N_b + N_i \tag{4.18}$$

where the eigenvalues have negative real parts.

In the next sections, the stability condition (maximum eigenvalue is less than one) will be checked for the system of equations obtained by the RBF applications to the unsteady Navier-Stokes, MHD Convection flow and full MHD flow problems. This stability condition depends on the choice of time increment, relaxation parameters and other problem parameters.

4.2 Stability Analysis of the Transient Navier-Stokes Equations

The two-dimensional, laminar, unsteady flow of a viscous, incompressible fluid is governed by the Navier-Stokes equations [16]. The non-dimensional governing equations in stream function-vorticity formulation are given in Chapter 1, equations (1.11)-(1.12)

$$\nabla^2 \psi = -\omega \tag{4.19}$$

$$\frac{1}{Re}\nabla^2 \omega = \frac{\partial \omega}{\partial t} + u\frac{\partial \omega}{\partial x} + v\frac{\partial \omega}{\partial y} \tag{4.20}$$

where velocity components $u = \dfrac{\partial \psi}{\partial y}$ and $v = -\dfrac{\partial \psi}{\partial x}$ are the coefficients of the convective terms in the vorticity transport equation, and the Reynolds number $Re = \dfrac{LU_0}{\nu}$ is the non-dimensional parameter.

The application of the radial basis function approximation to the Poisson type equation $\nabla^2 u = f$ gives the discretized system in matrix-vector form (equation (2.31)) as

$$\boldsymbol{u} = \boldsymbol{g_u} + \boldsymbol{K}\boldsymbol{f} \tag{4.21}$$

where $\boldsymbol{g_u} = \boldsymbol{R_1}\boldsymbol{u_{bc}}$, $\boldsymbol{u_{bc}}$ is the vector containing boundary values of the solution vector $\boldsymbol{u}$. The right hand side functions of the equations (4.19)-(4.20) are

$$f = -\omega \tag{4.22}$$

and

$$f = Re(\frac{\partial \omega}{\partial t} + u\frac{\partial \omega}{\partial x} + v\frac{\partial \omega}{\partial y}), \tag{4.23}$$

respectively.

Thus, the RBF approximation explained in Section 2.1.2 is applied to the unsteady Navier-Stokes equations (4.19)-(4.20) by using the coordinate matrix $\boldsymbol{F}$ for the space derivatives of unknowns (equation (2.21))

$$\boldsymbol{\psi} = \boldsymbol{g_\psi} + \boldsymbol{K}(-\boldsymbol{\omega}) \tag{4.24}$$

$$\boldsymbol{\omega} = \boldsymbol{g_\omega} + Re\boldsymbol{K}(\frac{\partial \boldsymbol{\omega}}{\partial t} + [\boldsymbol{u}]_{\boldsymbol{d}}\frac{\partial \boldsymbol{F}}{\partial x}\boldsymbol{F^{-1}}\boldsymbol{\omega} + [\boldsymbol{v}]_{\boldsymbol{d}}\frac{\partial \boldsymbol{F}}{\partial y}\boldsymbol{F^{-1}}\boldsymbol{\omega}) \tag{4.25}$$

where $[\boldsymbol{u}]_{\boldsymbol{d}}$, $[\boldsymbol{v}]_{\boldsymbol{d}}$ are the diagonal matrices formed by the vectors $\boldsymbol{u} = \dfrac{\partial \boldsymbol{F}}{\partial y}\boldsymbol{F^{-1}}\boldsymbol{\psi}$ and $\boldsymbol{v} = -\dfrac{\partial \boldsymbol{F}}{\partial x}\boldsymbol{F^{-1}}\boldsymbol{\psi}$. The matrices $\boldsymbol{R_1}$, $\boldsymbol{K}$, $\boldsymbol{F}$ are derived in Chapter 2 (equations (2.30)-(2.31)).

For the simplicity of the notation the equation (4.25) is rearranged as

$$\boldsymbol{S\omega} = \boldsymbol{g_\omega} + Re\boldsymbol{K}\frac{\partial \boldsymbol{\omega}}{\partial t} \tag{4.26}$$

where $\boldsymbol{S} = \boldsymbol{I} - Re\boldsymbol{K}([\boldsymbol{u}]_d\frac{\partial \boldsymbol{F}}{\partial x}\boldsymbol{F^{-1}} + [\boldsymbol{v}]_d\frac{\partial \boldsymbol{F}}{\partial y}\boldsymbol{F^{-1}})$.

Since the vorticity equation (4.26) can be expressed as a first order system of differential equations in time

$$\frac{\partial \boldsymbol{\omega}}{\partial t} = \frac{1}{Re}\boldsymbol{K^{-1}S\omega} - \frac{1}{Re}\boldsymbol{K^{-1}g_\omega} \tag{4.27}$$

and the known vector $\frac{1}{Re}\boldsymbol{K^{-1}g_\omega}$ does not contribute to the stability analysis, the stability characteristic of the vorticity equation (4.27) is similar to the system of the ordinary differential equation (4.3).

Using the explicit Euler method for the time derivative of the vorticity and relaxation parameter α_ω explained in Section 2.1.2, we obtain

$$\boldsymbol{S}((1-\alpha_\omega)\boldsymbol{\omega}^m + \alpha_\omega\boldsymbol{\omega}^{m+1}) = \boldsymbol{g_\omega}^m + Re\boldsymbol{K}(\frac{\boldsymbol{\omega}^{m+1} - \boldsymbol{\omega}^m}{\Delta t}) \tag{4.28}$$

which is rearranged to collect the $(m+1)$ and m time levels in the left and right hand sides, respectively

$$\boldsymbol{C_\omega\omega}^{m+1} = \boldsymbol{g_\omega}^m - \boldsymbol{L_\omega\omega}^m \tag{4.29}$$

where $\boldsymbol{C_\omega} = \alpha_\omega\boldsymbol{S} - \frac{Re}{\Delta t}\boldsymbol{K}$ and $\boldsymbol{L_\omega} = (1-\alpha_\omega)\boldsymbol{S} + \frac{Re}{\Delta t}\boldsymbol{K}$.

Thus, the final discretized system of unsteady Navier-Stokes equations in terms of unknown vectors $\boldsymbol{\psi}$, $\boldsymbol{\omega}$ is given as

$$\boldsymbol{\psi}^{m+1} = \boldsymbol{g_\psi}^m - \boldsymbol{K\omega}^m \tag{4.30}$$

$$\boldsymbol{C_\omega\omega}^{m+1} = \boldsymbol{g_\omega}^m - \boldsymbol{L_\omega\omega}^m. \tag{4.31}$$

In the discretized vorticity equation (4.31), the matrix $\boldsymbol{C_\omega^{-1}L_\omega}$ can be assumed to be constant and the known vector $\boldsymbol{C_\omega^{-1}g_\omega}^m$ does not contribute to the stability analysis. Thus, the stability characteristic of (4.31) is similar to the equation (4.14) ($\tilde{\boldsymbol{u}}_{m+1} = \boldsymbol{E}(\boldsymbol{C}\Delta t)\tilde{\boldsymbol{u}}_m$).

Therefore, the stability analysis of RBF approximation for unsteady Navier-Stokes equations is reduced to check the condition, [20, 44]

$$\rho(\boldsymbol{C}_{\boldsymbol{\omega}}^{-\mathbf{1}}\boldsymbol{L}_{\boldsymbol{\omega}}) < 1 \tag{4.32}$$

where $\rho(\boldsymbol{C}_{\boldsymbol{\omega}}^{-\mathbf{1}}\boldsymbol{L}_{\boldsymbol{\omega}})$ is the spectral radius (the largest eigenvalues in magnitude) of the matrix $\boldsymbol{C}_{\boldsymbol{\omega}}^{-\mathbf{1}}\boldsymbol{L}_{\boldsymbol{\omega}}$. Since this coefficient matrix contains time increment Δt, relaxation parameter α_ω and Reynolds number Re, the stability condition (4.32) depends on the choice of these parameters.

In the next Section, the numerical stability analysis of RBF approximation of Navier-Stokes equations applied to the lid-driven cavity flow is going to be performed and the values of Δt, α_ω, Re will be tabulated for achieving stability.

4.2.1 Stability of the Solution of Lid-Driven Cavity Flow

We consider the unsteady, laminar flow of a viscous, incompressible fluid in a square cavity with a moving top lid. The problem configuration and the boundary conditions are shown in Figure 4.1.

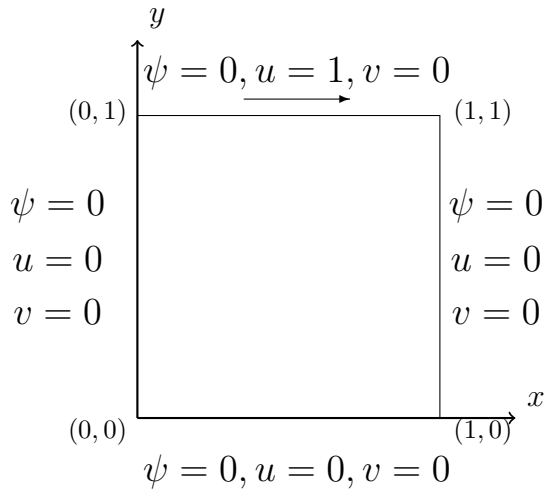

Figure 4.1: Problem 4.2.1: Lid-driven cavity and boundary conditions.

The time discretized system of equations (4.30)-(4.31) of RBF approximation to the Navier-Stokes equations in terms of stream function vector $\boldsymbol{\psi}$ and vorticity vector $\boldsymbol{\omega}$

were

$$\boldsymbol{\psi}^{m+1} = \boldsymbol{g_\psi}^m - \boldsymbol{K}\boldsymbol{\omega}^m \tag{4.33}$$

$$\boldsymbol{C_\omega}\boldsymbol{\omega}^{m+1} = \boldsymbol{g_\omega}^m - \boldsymbol{L_\omega}\boldsymbol{\omega}^m. \tag{4.34}$$

The iteration process starts with a initial value of vorticity $\boldsymbol{\omega}^0$. Then, the stream function equation (4.33) is solved by using m-th time level values of vorticity. After vorticity boundary conditions are obtained from the definition by using coordinate matrix $\boldsymbol{F}$, the vorticity equation (4.34) is solved at $(m+1)$-th time level. The iteration continues until the stopping criteria in terms of maximum error

$$||\boldsymbol{z}^{m+1} - \boldsymbol{z}^m||_\infty < \epsilon \tag{4.35}$$

is satisfied where $\boldsymbol{z}$ denotes either $\boldsymbol{\psi}$ or $\boldsymbol{\omega}$. Preassigned tolerance is taken $\epsilon = 10^{-6}$ to reach the steady-state solutions.

In the numerical computations, we use linear radial basis functions $\varphi = 1 + r$. The boundary is discretized by taking $N_b = 80, 96$ and 120 boundary points for the Reynolds numbers $100, 500$ and 1000 with corresponding time increments $\Delta t = 0.8, 0.5$ and 0.1, respectively. In order to obtain smooth numerical solutions more number of points are taken as Re increases. The numerical results are shown in Figure 4.2 in terms of streamlines and vorticity contours for fixed relaxation parameter $\alpha_\omega = 0.6$.

Figure 4.2 shows the effect of the increase in Reynolds number on the flow $(\psi,\ \omega)$. It is observed from the streamlines that for fixed $Re = 100$, the primary vortex of the flow moves towards the upper right corner due the movement of the upper wall and secondary small vortex appears at the right lower corner of the cavity. As Reynolds number increases, the primary vortex shifts through the center of the cavity with a decreasing magnitude. The secondary vortex in the lower right corner enlarges and another vortex occurs at the lower left corner. With a further increase in Reynolds number ($Re = 1000$) these secondary vortices grow in bottom corners. Vorticity contours are slightly symmetric with respect to $x = 0.5$ for $Re = 100$. However, they move away from the center towards the walls as Re increases and the center of the cavity is almost stagnant. This indicates that the vorticity gradients are very strong at the walls, especially $x = 1$ wall. The fluid rotates with a constant angular velocity. These numerical results are in well agreement with the ones in [47].

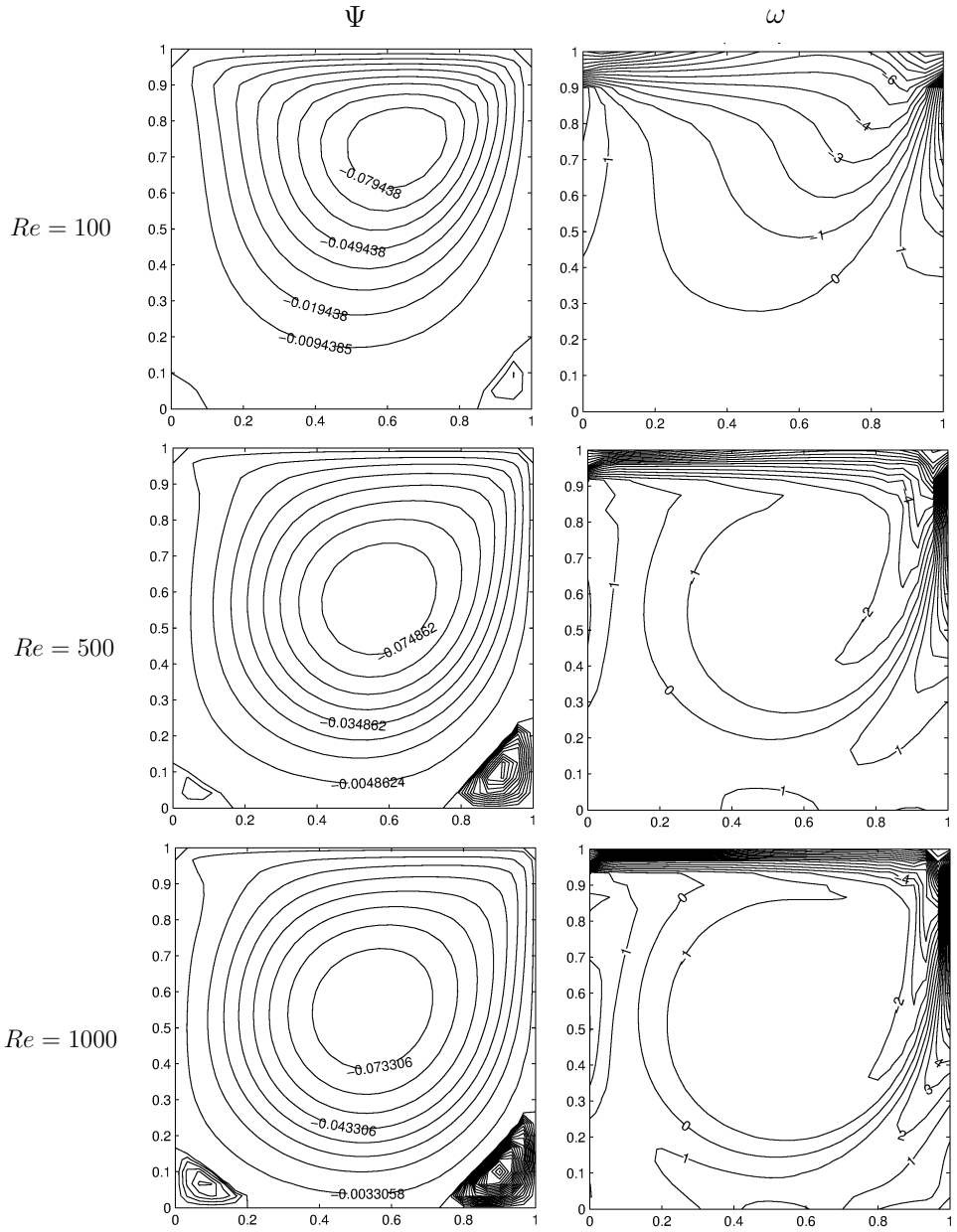

Figure 4.2: Problem 4.2.1: Flow behaviors for $Re = 100, 500, 1000$ using $\Delta t = 0.8, 0.5, 0.1$, respectively.

Now, we carry the stability analysis computationally for the explicit Euler method applied to the RBF discretized systems (4.33)-(4.34) of Navier-Stokes equations for the lid-driven cavity flow. The stability condition (4.32) ($\rho(\boldsymbol{C_\omega^{-1}L_\omega}) < 1$) is checked for several values of time increments Δt, relaxation parameters α_ω and Reynolds number Re. The maximum eigenvalues are presented in Tables 4.1-4.2 by using $N_b = 80$ boundary points.

In Table 4.1, the spectral radii of the coefficient matrix $\boldsymbol{C_\omega^{-1}L_\omega}$ of the vorticity equation (4.34) are obtained for different values of time increments and relaxation parameters when $Re = 100$. As the relaxation parameter decreases, the maximum eigenvalue also decreases but for the choice of $\alpha_\omega \leq 0.5$ the method becomes unstable. Since the smaller eigenvalue is obtained for the choice of $\alpha_\omega = 0.6$, we use this value for the rest of the computations. We also observe that although the time discretization scheme is explicit (Euler method), quite large time increment like $\Delta t = 0.8$ can be used to obtain stable numerical solution.

Table 4.2 shows the variation of the maximum eigenvalues with respect to time increment and relaxation parameter together with the number of iterations required for steady-state solution. An increase in the Reynolds number as $Re = 500,\ 1000$ increases the spectral radius of the coefficient matrix. As the time increment decreases, both the number of iterations and maximum eigenvalues increase. We deduce that the system (4.34) is stable for the choice of $\Delta t \leq 0.9$ with $\alpha_\omega = 0.6$.

Thus, the RBF approximation for the unsteady Navier-Stokes equations (4.33)-(4.34) is stable for appropriately taken time increment Δt, relaxation parameter α_ω for the required Reynolds number Re. In general, for $Re = 100, 500$ and 1000 with $N_b = 80$, $\alpha_\omega = 0.6$ is computationally found suitable for achieving stability by using quite large time increments with an explicit scheme.

$\rho(\boldsymbol{C_\omega^{-1}L_\omega})$				
α_ω	$\Delta t = 0.1$	$\Delta t = 0.3$	$\Delta t = 0.6$	$\Delta t = 0.8$
1	-0.97231106	-0.92129202	-0.85407002	-0.81445236
0.9	-0.97223418	-0.92066761	-0.85190893	-0.81094447
0.8	-0.97215687	-0.92003322	-0.84968288	-0.80730141
0.7	-0.97207913	-0.91938860	-0.84738887	-0.80351517
0.6	-0.97200096	-0.91873350	-0.84502376	-0.79957717
0.5	1	1	1	1
0.4	-	-	-	-

Table 4.1: Spectral radius ρ for $Re = 100$, $N_b = 80$, $\epsilon = 10^{-6}$.

	$Re = 500$		$Re = 1000$	
Δt	$\rho(\boldsymbol{C_\omega^{-1}L_\omega})$	Iteration Number	$\rho(\boldsymbol{C_\omega^{-1}L_\omega})$	Iteration Number
0.9	-0.95750884	101	-0.97990757	215
0.8	-0.96212279	104	-0.98211611	228
0.7	-0.96676302	98	-0.98433058	227
0.6	-0.97142971	124	-0.98655098	235
0.5	-0.97612320	154	-0.98877739	299
0.4	-0.98084367	194	-0.99100980	375
0.3	-0.98559134	257	-0.99324824	493
0.2	-0.99036645	377	-0.99549273	717
0.1	-0.99516925	715	-0.99774330	1342

Table 4.2: Spectral radius ρ for $\alpha_\omega = 0.6$, $N_b = 80$, $\epsilon = 10^{-6}$.

4.3 Stability Analysis of the Unsteady MHD Convection Flow

In this Section, radial basis function approximation is extended to the transient natural convection flow under a horizontally applied magnetic field. Then, the stability analysis is performed for the vorticity transport and the temperature equations.

The governing equations are Navier-Stokes equations including buoyancy and Lorentz forces and energy equation. Induced magnetic field, Joule heating and viscous dissipation are neglected. Thus, the two-dimensional unsteady MHD convection flow equations are given in terms of stream function, temperature, vorticity and pressure as (Chapter 1, equations (1.82)-(1.85))

$$\nabla^2\psi = -\omega \tag{4.36}$$

$$\nabla^2 T = PrRe(\frac{\partial T}{\partial t} + u\frac{\partial T}{\partial x} + v\frac{\partial T}{\partial y}) \tag{4.37}$$

$$\nabla^2\omega = Re(\frac{\partial \omega}{\partial t} + u\frac{\partial \omega}{\partial x} + v\frac{\partial \omega}{\partial y}) + M^2\frac{\partial v}{\partial x} - \frac{Gr}{Re}\frac{\partial T}{\partial x} \tag{4.38}$$

$$\nabla^2 p = -2Re(\frac{\partial v}{\partial x}\frac{\partial u}{\partial y} - \frac{\partial u}{\partial x}\frac{\partial v}{\partial y}) - M^2\frac{\partial v}{\partial y} + \frac{Gr}{Re}\frac{\partial T}{\partial y} \tag{4.39}$$

where the non-dimensional parameters are the Reynolds number $Re = LU_0/\nu$, Hartmann number $M = L\mu H_0\sqrt{\sigma/\rho\nu}$, Grashof number $Gr = g\beta(T_{hot} - T_{cold})L^3/\nu^2$ and the Prandtl number $Pr = \rho c_p\nu/\lambda$.

The RBF approximation (2.31) is applied to the unsteady MHD convection equations (4.36)-(4.39) by taking the right hand side functions as

$$f = -\omega \tag{4.40}$$

$$f = PrRe(\frac{\partial T}{\partial t} + u\frac{\partial T}{\partial x} + v\frac{\partial T}{\partial y}) \tag{4.41}$$

$$f = Re(\frac{\partial \omega}{\partial t} + u\frac{\partial \omega}{\partial x} + v\frac{\partial \omega}{\partial y}) + M^2\frac{\partial v}{\partial x} - \frac{Gr}{Re}\frac{\partial T}{\partial x} \tag{4.42}$$

$$f = -2Re(\frac{\partial v}{\partial x}\frac{\partial u}{\partial y} - \frac{\partial u}{\partial x}\frac{\partial v}{\partial y}) - M^2\frac{\partial v}{\partial y} + \frac{Gr}{Re}\frac{\partial T}{\partial y} \tag{4.43}$$

which results in matrix-vector equations with the help of the coordinate matrix $\boldsymbol{F}$ for the space derivatives of unknowns

$$\boldsymbol{\psi} = \boldsymbol{g_\psi} + \boldsymbol{K}(-\boldsymbol{\omega}) \tag{4.44}$$

$$\boldsymbol{T} = \boldsymbol{g_T} + PrRe\boldsymbol{K_T}(\frac{\partial \boldsymbol{T}}{\partial t} + [\boldsymbol{u}]_{\boldsymbol{d}}\frac{\partial \boldsymbol{F}}{\partial x}\boldsymbol{F^{-1}T} + [\boldsymbol{v}]_{\boldsymbol{d}}\frac{\partial \boldsymbol{F}}{\partial y}\boldsymbol{F^{-1}T}) \tag{4.45}$$

$$\begin{aligned}\boldsymbol{\omega} = \boldsymbol{g_\omega} &+ Re\boldsymbol{K_\omega}(\frac{\partial \boldsymbol{\omega}}{\partial t} + [\boldsymbol{u}]_{\boldsymbol{d}}\frac{\partial \boldsymbol{F}}{\partial x}\boldsymbol{F^{-1}\omega} + [\boldsymbol{v}]_{\boldsymbol{d}}\frac{\partial \boldsymbol{F}}{\partial y}\boldsymbol{F^{-1}\omega}) \\ &+ M^2\boldsymbol{K_\omega}\frac{\partial \boldsymbol{F}}{\partial x}\boldsymbol{F^{-1}v} - \frac{Gr}{Re}\boldsymbol{K_\omega}\frac{\partial \boldsymbol{F}}{\partial x}\boldsymbol{F^{-1}T}\end{aligned} \tag{4.46}$$

$$\begin{aligned}\boldsymbol{p} = \boldsymbol{g_p} &- 2Re\boldsymbol{K}((\frac{\partial \boldsymbol{F}}{\partial x}\boldsymbol{F^{-1}}[\boldsymbol{v}]_{\boldsymbol{d}})(\frac{\partial \boldsymbol{F}}{\partial y}\boldsymbol{F^{-1}}[\boldsymbol{u}]_{\boldsymbol{d}})) \\ &+ 2Re\boldsymbol{K}(\frac{\partial \boldsymbol{F}}{\partial x}\boldsymbol{F^{-1}}[\boldsymbol{u}]_{\boldsymbol{d}})(\frac{\partial \boldsymbol{F}}{\partial y}\boldsymbol{F^{-1}}[\boldsymbol{v}]_{\boldsymbol{d}}) - M^2\boldsymbol{K}\frac{\partial \boldsymbol{F}}{\partial y}\boldsymbol{F^{-1}v} \\ &+ \frac{Gr}{Re}\boldsymbol{K}\frac{\partial \boldsymbol{F}}{\partial y}\boldsymbol{F^{-1}T}\end{aligned} \tag{4.47}$$

where the matrices $\boldsymbol{K_T}$ and $\boldsymbol{K_\omega}$ are similarly obtained as the matrix $\boldsymbol{K}$ given in Section 2.1.2, page 36, equation (2.31), but it contains the boundary conditions of this problem. The vector $\boldsymbol{g_\xi}$, $\boldsymbol{\xi}$ denotes $\boldsymbol{\psi}$, $\boldsymbol{T}$, $\boldsymbol{\omega}$, $\boldsymbol{p}$ and the matrices $\boldsymbol{K}$ and $\boldsymbol{F}$ are defined in Section 2.1.2. Again, $[\boldsymbol{u}]_{\boldsymbol{d}}$ and $[\boldsymbol{v}]_{\boldsymbol{d}}$ are the diagonal matrices whose entries are computed as $\boldsymbol{u} = \frac{\partial \boldsymbol{F}}{\partial y}\boldsymbol{F^{-1}\psi}$ and $\boldsymbol{v} = -\frac{\partial \boldsymbol{F}}{\partial x}\boldsymbol{F^{-1}\psi}$, respectively.

The simplified form of the equations (4.45)-(4.47) are

$$\boldsymbol{S_T T} = \boldsymbol{g_T} + PrRe\boldsymbol{K_T}\frac{\partial \boldsymbol{T}}{\partial t} \tag{4.48}$$

$$\boldsymbol{S_\omega \omega} = \boldsymbol{g_\omega} + Re\boldsymbol{K_\omega}\frac{\partial \boldsymbol{\omega}}{\partial t} + \tilde{\boldsymbol{b}}_{\boldsymbol{\omega}} \tag{4.49}$$

$$\boldsymbol{p} = \tilde{\boldsymbol{b}}_{\boldsymbol{p}} \tag{4.50}$$

where

$$\begin{aligned}\boldsymbol{S_T} &= I - PrRe\boldsymbol{K_T}([\boldsymbol{u}]_{\boldsymbol{d}}\frac{\partial \boldsymbol{F}}{\partial x}\boldsymbol{F^{-1}} + [\boldsymbol{v}]_{\boldsymbol{d}}\frac{\partial \boldsymbol{F}}{\partial y}\boldsymbol{F^{-1}}), \\ \boldsymbol{S_\omega} &= I - Re\boldsymbol{K_\omega}([\boldsymbol{u}]_{\boldsymbol{d}}\frac{\partial \boldsymbol{F}}{\partial x}\boldsymbol{F^{-1}} + [\boldsymbol{v}]_{\boldsymbol{d}}\frac{\partial \boldsymbol{F}}{\partial y}\boldsymbol{F^{-1}}), \\ \tilde{\boldsymbol{b}}_{\boldsymbol{\omega}} &= M^2\boldsymbol{K_\omega}\frac{\partial \boldsymbol{F}}{\partial x}\boldsymbol{F^{-1}v} - \frac{Gr}{Re}\boldsymbol{K_\omega}\frac{\partial \boldsymbol{F}}{\partial x}\boldsymbol{F^{-1}T}\end{aligned}$$

and

$$\tilde{\boldsymbol{b}}_{\boldsymbol{p}} = \boldsymbol{g}_{\boldsymbol{p}} - 2Re\boldsymbol{K}((\frac{\partial \boldsymbol{F}}{\partial x}\boldsymbol{F}^{-1}[\boldsymbol{v}]_{\boldsymbol{d}})(\frac{\partial \boldsymbol{F}}{\partial y}\boldsymbol{F}^{-1}[\boldsymbol{u}]_{\boldsymbol{d}})) + 2Re\boldsymbol{K}(\frac{\partial \boldsymbol{F}}{\partial x}\boldsymbol{F}^{-1}[\boldsymbol{u}]_{\boldsymbol{d}})(\frac{\partial \boldsymbol{F}}{\partial y}\boldsymbol{F}^{-1}[\boldsymbol{v}]_{\boldsymbol{d}}) - M^2\boldsymbol{K}\frac{\partial \boldsymbol{F}}{\partial y}\boldsymbol{F}^{-1}\boldsymbol{v} + \frac{Gr}{Re}\boldsymbol{K}\frac{\partial \boldsymbol{F}}{\partial y}\boldsymbol{F}^{-1}\boldsymbol{T}.$$

The discretization of the time derivatives in the temperature and vorticity equations (4.48)-(4.49) using the Euler method and the relaxation parameters α_T and α_ω (Section 2.1.2) gives

$$\boldsymbol{C_T}\boldsymbol{T}^{m+1} = \boldsymbol{g_T}^{m} - \boldsymbol{L_T}\boldsymbol{T}^{m} \tag{4.51}$$

$$\boldsymbol{C_\omega}\boldsymbol{\omega}^{m+1} = \boldsymbol{g_\omega}^{m} - \boldsymbol{L_\omega}\boldsymbol{\omega}^{m} + \tilde{\boldsymbol{b}}_{\boldsymbol{\omega}}^{\,m+1} \tag{4.52}$$

where the matrices $\boldsymbol{C_T}$, $\boldsymbol{L_T}$, $\boldsymbol{C_\omega}$ and $\boldsymbol{L_\omega}$ are given by

$$\boldsymbol{C_T} = \alpha_T\boldsymbol{S_T} - \frac{PrRe}{\Delta t}\boldsymbol{K_T}, \qquad \boldsymbol{L_T} = (1-\alpha_T)\boldsymbol{S_T} + \frac{PrRe}{\Delta t}\boldsymbol{K_T} \tag{4.53}$$

$$\boldsymbol{C_\omega} = \alpha_\omega\boldsymbol{S_\omega} - \frac{Re}{\Delta t}\boldsymbol{K_\omega}, \qquad \boldsymbol{L_\omega} = (1-\alpha_\omega)\boldsymbol{S_\omega} + \frac{Re}{\Delta t}\boldsymbol{K_\omega}. \tag{4.54}$$

Thus, the RBF discretized system for unsteady MHD convection equations can be written as

$$\boldsymbol{\psi}^{m+1} = \boldsymbol{g_\psi}^{m} - \boldsymbol{K}\boldsymbol{\omega}^{m} \tag{4.55}$$

$$\boldsymbol{C_T}\boldsymbol{T}^{m+1} = \boldsymbol{g_T}^{m} - \boldsymbol{L_T}\boldsymbol{T}^{m} \tag{4.56}$$

$$\boldsymbol{C_\omega}\boldsymbol{\omega}^{m+1} = \boldsymbol{g_\omega}^{m} - \boldsymbol{L_\omega}\boldsymbol{\omega}^{m} + \tilde{\boldsymbol{b}}_{\boldsymbol{\omega}}^{\,m+1} \tag{4.57}$$

$$\boldsymbol{p}^{m+1} = \tilde{\boldsymbol{b}}_{\boldsymbol{p}}^{\,m+1}. \tag{4.58}$$

Here, $\boldsymbol{C_T^{-1}}\boldsymbol{g_T}^{m}$ and $\boldsymbol{C_\omega^{-1}}\boldsymbol{g_\omega}^{m}$, $\boldsymbol{C_\omega^{-1}}\tilde{\boldsymbol{b}}_{\boldsymbol{\omega}}^{\,m+1}$ are the known vectors in the temperature equation (4.56) and vorticity equation (4.57), respectively. Since these vectors do not contribute to the stability analysis, the stability characteristics of (4.56) and (4.57) are similar to the stability of general initial value problem.

Thus, the numerical stability conditions for RBF approximation to the MHD convection equations are [20, 44]

$$\rho(\boldsymbol{C_T^{-1}}\boldsymbol{L_T}) < 1 \tag{4.59}$$

$$\rho(\boldsymbol{C_\omega^{-1}}\boldsymbol{L_\omega}) < 1 \tag{4.60}$$

where $\rho(\boldsymbol{C_T^{-1}L_T})$ and $\rho(\boldsymbol{C_\omega^{-1}L_\omega})$ are the maximum eigenvalues of the matrices $\boldsymbol{C_T^{-1}L_T}$ and $\boldsymbol{C_\omega^{-1}L_\omega}$, respectively.

In order to show that RBF discretized system gives the stable solution, we are going to analyze the MHD convection flow in a square cavity in the next Section. The spectral radii of the coefficient matrices of the temperature and vorticity equations are given for different values of time increment Δt, Grashof number Gr and Hartmann number M.

4.3.1 Stability of the Solution of MHD Convection Flow in the Square Cavity

The convection flow in a square cavity under the impact of horizontally magnetic field is considered. The left wall is heated and the right wall is kept cooled, while the other walls are adiabatic (Figure 4.3).

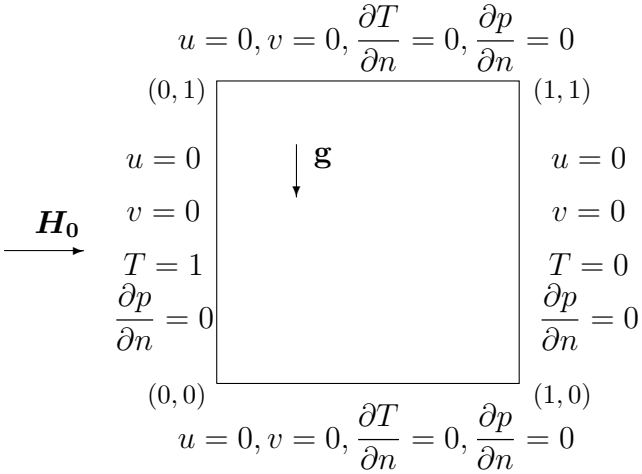

Figure 4.3: Problem 4.3.1: Square cavity and boundary conditions.

The discretized system of MHD convection equations (4.55)-(4.58)

$$\boldsymbol{\psi}^{m+1} = \boldsymbol{g_\psi}^m - \boldsymbol{K\omega}^m \tag{4.61}$$

$$\boldsymbol{C_T T}^{m+1} = \boldsymbol{g_T}^m - \boldsymbol{L_T T}^m \tag{4.62}$$

$$\boldsymbol{C_\omega \omega}^{m+1} = \boldsymbol{g_\omega}^m - \boldsymbol{L_\omega \omega}^m + \tilde{\boldsymbol{b}}_{\boldsymbol{\omega}}^{m+1} \tag{4.63}$$

$$\boldsymbol{p}^{m+1} = \tilde{\boldsymbol{b}}_{\boldsymbol{p}}^{m+1} \tag{4.64}$$

are solved iteratively. First, $\boldsymbol{\psi}^{m+1}$ is obtained from the stream function equation (4.61) with an initial value of vorticity $\boldsymbol{\omega}^0$. After the velocity components are com-

puted, the temperature equation (4.62) is solved with an initial temperature $\boldsymbol{T}^0$. The vorticity boundary conditions are obtained from the vorticity definition with the help of the coordinate matrix $\boldsymbol{F}$. Then, we solve vorticity equation (4.63). The iteration process is stopped when the preassigned tolerance ϵ is reached between two time levels for reaching steady-state. Then, the pressure equation (4.64) is solved with steady-state values of temperature and vorticity components.

The steady-state solutions are obtained by taking stopping criteria as 10^{-5} for fixed relaxation parameters of vorticity and temperature as $\alpha_\omega = \alpha_T = 0.6$. The boundary of the problem is discretized with 80 points. We use several values of Hartmann number as $M = 0,\ 30,\ 50$ and 100 with $\Delta t = 0.1,\ 0.1,\ 0.05$ and 0.01, respectively, for fixed $Re = 100$ and $Pr = 0.71$. The numerical results are presented in terms of streamlines, vorticity contours, isotherms and pressure contours.

In Figure 4.4, the effect of the Hartmann number is analyzed for fixed $Gr = 10^4$. It is observed that as Hartmann number increases, the main vortex of the flow is enlarged vertically and tends to be divided into two pieces with a decreasing magnitude. Increase in M causes the Hartmann and side layers near to the vertical and horizontal wall, respectively. With a further increase in M isotherms are distributed uniformly from the left hot wall to the right cold wall which indicates that magnetic field reduces the convection dominance. When external magnetic field is applied, pressure contours are divided into four symmetric vortices with respect to vertical and horizontal centerlines. These results are in well agreement with the ones obtained in [13]. Also, we have similar behaviors as in the case of steady MHD convection flow (Figure 3.46 in Chapter 3).

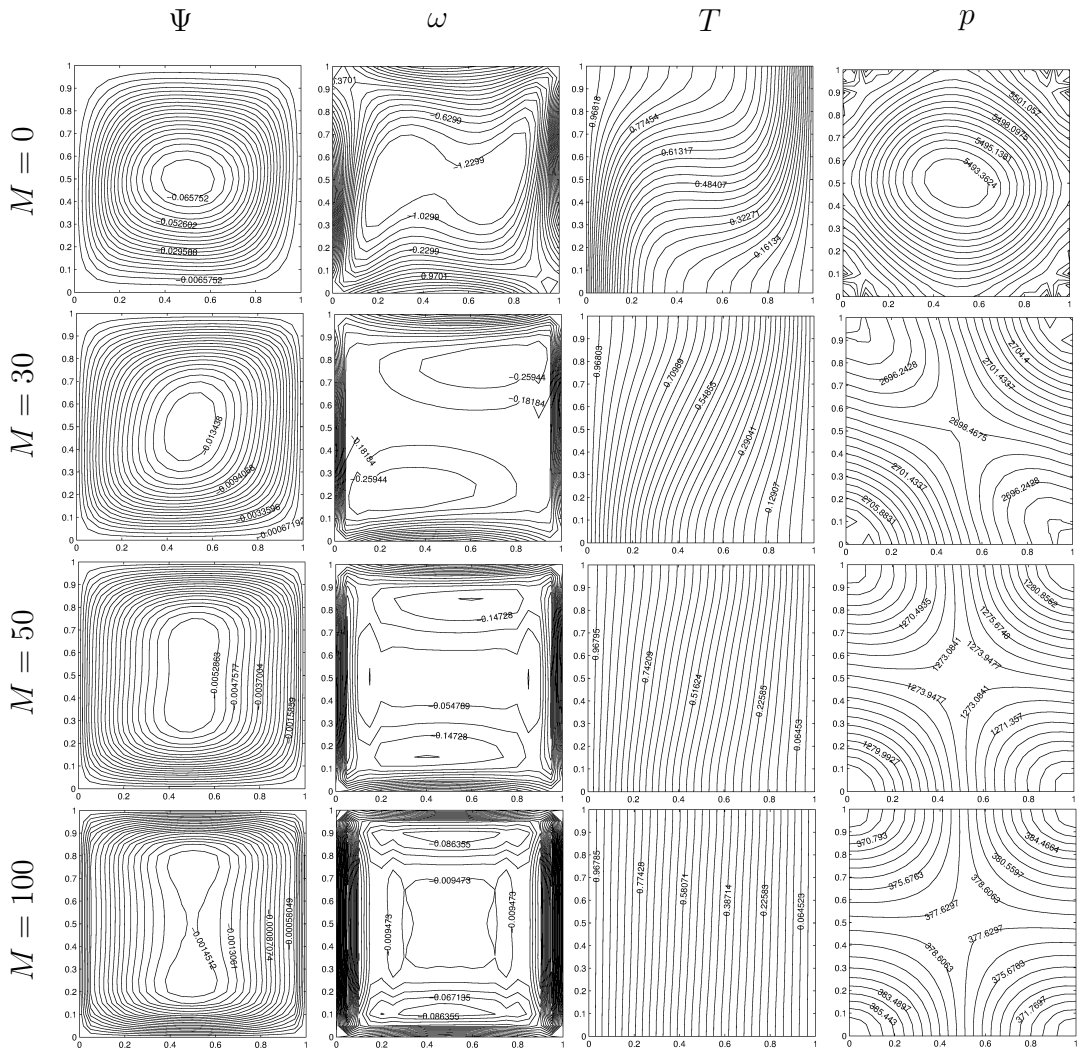

Figure 4.4: Problem 4.3.1: Streamlines, vorticity contours, isotherms and pressure contours for $Gr = 10^4$ and $M = 0, 30, 50, 100$ with $\Delta t = 0.1, 0.1, 0.05, 0.01$, respectively.

In order to show that the numerical results of MHD convection flow obtained from RBF discretized systems (4.61)-(4.64) are stable, computations are carried for a variation of Δt, Gr and M with fixed $Re = 100$ and $Pr = 0.71$. The spectral radius of the coefficient matrices $\boldsymbol{C_\omega^{-1}L_\omega}$ and $\boldsymbol{C_T^{-1}L_T}$ of the vorticity and temperature equations are given in Tables 4.3-4.5 for fixed $\alpha_\omega = \alpha_T = 0.6$.

Table 4.3 shows the effects of Grashof number Gr and the time increment Δt on the maximum eigenvalues of vorticity and temperature for fixed $M = 0$ and $\epsilon = 10^{-4}$. It is observed that, the maximum eigenvalues of vorticity and temperature discretized equations coefficient matrices decrease with an increase in either Δt or Gr. We obtain stable solutions for the choice of $\Delta t \leq 0.8$ with an increase in Gr. However, when Grashof number increases up to 10^5, we need to take small time increments such as $\Delta t \leq 0.3$ due to the convection dominance.

In Tables 4.4-4.5, the spectral radius of the coefficient matrices $\boldsymbol{C_\omega^{-1}L_\omega}$ and $\boldsymbol{C_T^{-1}L_T}$ are presented for several values of M and Δt for fixed $Gr = 10^4$ and $\epsilon = 10^{-5}$. As Hartmann number increases, the maximum eigenvalues of vorticity and temperature coefficient matrices increase, but these values do not exceed one. We can also deduce that when the magnetic field is absent ($M = 0$), the solution is stable for $\Delta t \leq 0.8$ (Table 4.3). Also, as M increases, small time increment is needed for the stable results.

Hence, with relaxation parameters $\alpha_\omega = \alpha_T = 0.6$ the suitable choice of time increment gives stable solutions for fixed Grashof number and Hartmann number. Although large time increment can be used, the increase in Gr and M need smaller Δt compared to small values of Gr and M. Thus, the stability of RBF discretized system of the MHD convection flow equations (4.61)-(4.64) is achieved by choosing suitably large time increment and relaxation parameters for each Gr and M values considered in MHD convection flow.

	$Gr = 10^3$		$Gr = 10^4$		$Gr = 10^5$	
Δt	$\rho(\boldsymbol{C_\omega^{-1}L_\omega})$	$\rho(\boldsymbol{C_T^{-1}L_T})$	$\rho(\boldsymbol{C_\omega^{-1}L_\omega})$	$\rho(\boldsymbol{C_T^{-1}L_T})$	$\rho(\boldsymbol{C_\omega^{-1}L_\omega})$	$\rho(\boldsymbol{C_T^{-1}L_T})$
0.8	-0.8554	-0.8950	-0.8535	-0.8648	-	-
0.7	-0.8721	-0.9074	-0.8704	-0.8804	-	-
0.6	-0.8891	-0.9200	-0.8877	-0.8965	-	-
0.5	-0.9066	-0.9328	-0.9053	-0.9128	-	-
0.4	-0.9244	-0.9458	-0.9234	-0.9295	-	-
0.3	-0.9427	-0.9590	-0.9419	-0.9466	-0.9316	-0.9215
0.2	-0.9613	-0.9724	-0.9608	-0.9640	-0.95374	-0.9468
0.1	-0.9804	-0.9861	-0.9802	-0.9818	-0.9765	-0.9730

Table 4.3: Spectral radius ρ for $\alpha_\omega = \alpha_T = 0.6$, $N_b = 80$, $Pr = 0.71$, $M = 0$ $\epsilon = 10^{-3}$.

	$M = 0$		$M = 30$	
Δt	$\rho(\boldsymbol{C_\omega^{-1}L_\omega})$	$\rho(\boldsymbol{C_T^{-1}L_T})$	$\rho(\boldsymbol{C_\omega^{-1}L_\omega})$	$\rho(\boldsymbol{C_T^{-1}L_T})$
0.3	-0.94188105	-0.94657340		
0.2	-0.96079836	-0.96399757	-0.96129412	-0.97188658
0.1	-0.98016592	-0.98180224	-0.98041970	-0.98582373
0.05	-0.99002360	-0.99085117	-0.99015200	-0.99288159
0.01	-0.99799512	-0.99816216	-0.99802104	-0.99857143

Table 4.4: Spectral radius ρ for $\alpha_\omega = \alpha_T = 0.6$, $N_b = 80$, $Pr = 0.71$, $Gr = 10^4$, $\epsilon = 10^{-5}$.

	$M = 50$		$M = 100$	
Δt	$\rho(\boldsymbol{C_\omega^{-1}L_\omega})$	$\rho(\boldsymbol{C_T^{-1}L_T})$	$\rho(\boldsymbol{C_\omega^{-1}L_\omega})$	$\rho(\boldsymbol{C_T^{-1}L_T})$
0.05	-0.99015788	-0.99311783	-	-
0.01	-0.99802223	-0.99861900	-0.99802296	-0.99863028

Table 4.5: Spectral radius ρ for $\alpha_\omega = \alpha_T = 0.6$, $N_b = 80$, $Pr = 0.71$, $Gr = 10^4$, $\epsilon = 10^{-5}$.

4.4 Stability Analysis of the Unsteady Full MHD Flow Equations

This Section extends the numerical stability of radial basis function approximation to the full MHD flow equations which results from the addition of the magnetic potential equation to the MHD equations since induced magnetic field is not neglected (large values of magnetic Reynolds number is taken).

We consider the two-dimensional, unsteady, laminar MHD flow of an incompressible, electrically conducting fluid including magnetic potential. The non-dimensional governing equations in terms of stream function ψ, vorticity ω and magnetic potential A are given in Chapter 1 (equations (1.111)-(1.113)) as

$$\nabla^2\psi = -\omega \tag{4.65}$$

$$\frac{1}{Re_m}\nabla^2 A = \frac{\partial A}{\partial t} + u\frac{\partial A}{\partial x} + v\frac{\partial A}{\partial y} \tag{4.66}$$

$$\begin{aligned}\frac{1}{Re}\nabla^2\omega = &\frac{\partial \omega}{\partial t} + u\frac{\partial \omega}{\partial x} + v\frac{\partial \omega}{\partial y} \\ &- \frac{M^2}{ReRe_m}\left[B_x\frac{\partial}{\partial x}\left(\frac{\partial B_y}{\partial x} - \frac{\partial B_x}{\partial y}\right) + B_y\frac{\partial}{\partial y}\left(\frac{\partial B_y}{\partial x} - \frac{\partial B_x}{\partial y}\right)\right]\end{aligned} \tag{4.67}$$

where $B_x = \dfrac{\partial A}{\partial y}$ and $B_y = -\dfrac{\partial A}{\partial x}$ are the induced magnetic field components. $u = \dfrac{\partial \psi}{\partial y}$ and $v = -\dfrac{\partial \psi}{\partial x}$ are the velocity components. Reynolds number $Re = LU_0/\nu$, magnetic Reynolds number $Re_m = LU_0\sigma\mu$ and Hartmann number $M = LB_0\sqrt{\sigma/\nu\rho}$ are the dimensionless parameters.

For the RBF approximation explained in Section 2.1.2, we take the right hand side functions of full MHD equations (4.65)-(4.67) as

$$f = -\omega \tag{4.68}$$

$$f = Re_m\left(\frac{\partial A}{\partial t} + u\frac{\partial A}{\partial x} + v\frac{\partial A}{\partial y}\right) \tag{4.69}$$

$$\begin{aligned}f = Re\Big(&\frac{\partial \omega}{\partial t} + u\frac{\partial \omega}{\partial x} + v\frac{\partial \omega}{\partial y}\Big) \\ &- \frac{M^2}{Re_m}\left[B_x\frac{\partial}{\partial x}\left(\frac{\partial B_y}{\partial x} - \frac{\partial B_x}{\partial y}\right) + B_y\frac{\partial}{\partial y}\left(\frac{\partial B_y}{\partial x} - \frac{\partial B_x}{\partial y}\right)\right].\end{aligned} \tag{4.70}$$

Using the coordinate matrix $\boldsymbol{F}$ for evaluating the space derivatives in non-homogeneous term f and applying RBF approximation to equations (4.65)-(4.67), we obtain the ma-

trix system of the full MHD equations in terms of vectors of stream function, velocity components, magnetic potential, induced magnetic field components and the vorticity as

$$\boldsymbol{\psi} = \boldsymbol{g_\psi} + \boldsymbol{K}(-\boldsymbol{\omega}) \tag{4.71}$$

$$\boldsymbol{u} = \frac{\partial \boldsymbol{F}}{\partial y}\boldsymbol{F^{-1}}\boldsymbol{\psi}, \qquad \boldsymbol{v} = -\frac{\partial \boldsymbol{F}}{\partial x}\boldsymbol{F^{-1}}\boldsymbol{\psi} \tag{4.72}$$

$$\boldsymbol{A} = \boldsymbol{g_A} + Re_m\boldsymbol{K}(\frac{\partial \boldsymbol{A}}{\partial t} + [\boldsymbol{u}]_{\boldsymbol{d}}\frac{\partial \boldsymbol{F}}{\partial x}\boldsymbol{F^{-1}}\boldsymbol{A} + [\boldsymbol{v}]_{\boldsymbol{d}}\frac{\partial \boldsymbol{F}}{\partial y}\boldsymbol{F^{-1}}\boldsymbol{A}) \tag{4.73}$$

$$\boldsymbol{B_x} = \frac{\partial \boldsymbol{F}}{\partial y}\boldsymbol{F^{-1}}\boldsymbol{A}, \qquad \boldsymbol{B_y} = -\frac{\partial \boldsymbol{F}}{\partial x}\boldsymbol{F^{-1}}\boldsymbol{A} \tag{4.74}$$

$$\begin{aligned}\boldsymbol{\omega} = \boldsymbol{g_\omega} &+ Re\boldsymbol{K}(\frac{\partial \boldsymbol{\omega}}{\partial t} + [\boldsymbol{u}]_{\boldsymbol{d}}\frac{\partial \boldsymbol{F}}{\partial x}\boldsymbol{F^{-1}}\boldsymbol{\omega} + [\boldsymbol{v}]_{\boldsymbol{d}}\frac{\partial \boldsymbol{F}}{\partial y}\boldsymbol{F^{-1}}\boldsymbol{\omega}) \\ &- \frac{M^2}{Re_m}\boldsymbol{K}([\boldsymbol{B_x}]_{\boldsymbol{d}}\frac{\partial \boldsymbol{F}}{\partial x}\boldsymbol{F^{-1}}\boldsymbol{d_{xy}} + [\boldsymbol{B_y}]_{\boldsymbol{d}}\frac{\partial \boldsymbol{F}}{\partial y}\boldsymbol{F^{-1}}\boldsymbol{d_{xy}})\end{aligned} \tag{4.75}$$

where the vector $\boldsymbol{d_{xy}}$ is defined as $\boldsymbol{d_{xy}} = \frac{\partial \boldsymbol{F}}{\partial x}\boldsymbol{F^{-1}}\boldsymbol{B_y} - \frac{\partial \boldsymbol{F}}{\partial y}\boldsymbol{F^{-1}}\boldsymbol{B_x}$. The diagonal matrices$[\boldsymbol{u}]_{\boldsymbol{d}}$, $[\boldsymbol{v}]_{\boldsymbol{d}}$, $[\boldsymbol{B_x}]_{\boldsymbol{d}}$ and $[\boldsymbol{B_y}]_{\boldsymbol{d}}$ are constructed with the diagonal elements $\boldsymbol{u}$, $\boldsymbol{v}$, $\boldsymbol{B_x}$ and $\boldsymbol{B_y}$, respectively. Matrices $\boldsymbol{K}$, $\boldsymbol{F}$ and the vectors $\boldsymbol{g_\psi}$, $\boldsymbol{g_A}$, $\boldsymbol{g_\omega}$ are similarly defined as in Section 2.1.2.

For the simplicity of notations , the equations (4.73)-(4.75) can be rewritten as

$$\boldsymbol{S_A}\boldsymbol{A} = \boldsymbol{g_A} + Re_m\boldsymbol{K}\frac{\partial \boldsymbol{A}}{\partial t} \tag{4.76}$$

$$\boldsymbol{S_\omega}\boldsymbol{\omega} = \boldsymbol{g_\omega} + Re\boldsymbol{K}\frac{\partial \boldsymbol{\omega}}{\partial t} + \tilde{\boldsymbol{b}}_{\boldsymbol{\omega}} \tag{4.77}$$

where the matrices $\boldsymbol{S_A}$, $\boldsymbol{S_\omega}$ and the vector $\tilde{\boldsymbol{b}}_{\boldsymbol{\omega}}$ are defined as

$$\begin{aligned}\boldsymbol{S_A} &= I - Re_m\boldsymbol{K}([\boldsymbol{u}]_{\boldsymbol{d}}\frac{\partial \boldsymbol{F}}{\partial x}\boldsymbol{F^{-1}} + [\boldsymbol{v}]_{\boldsymbol{d}}\frac{\partial \boldsymbol{F}}{\partial y}\boldsymbol{F^{-1}}), \\ \boldsymbol{S_\omega} &= I - Re\boldsymbol{K}([\boldsymbol{u}]_{\boldsymbol{d}}\frac{\partial \boldsymbol{F}}{\partial x}\boldsymbol{F^{-1}} + [\boldsymbol{v}]_{\boldsymbol{d}}\frac{\partial \boldsymbol{F}}{\partial y}\boldsymbol{F^{-1}}), \\ \tilde{\boldsymbol{b}}_{\boldsymbol{\omega}} &= -\frac{M^2}{Re_m}\boldsymbol{K}([\boldsymbol{B_x}]_{\boldsymbol{d}}\frac{\partial \boldsymbol{F}}{\partial x}\boldsymbol{F^{-1}}\boldsymbol{d_{xy}} + [\boldsymbol{B_y}]_{\boldsymbol{d}}\frac{\partial \boldsymbol{F}}{\partial y}\boldsymbol{F^{-1}}\boldsymbol{d_{xy}}).\end{aligned}$$

Using the explicit Euler method for the time derivatives in the equations (4.76)-(4.77) and relaxation parameters α_A and α_ω for magnetic potential and vorticity, respectively

explained in the Section 2.1.2, we obtain

$$\boldsymbol{C_A A}^{m+1} = \boldsymbol{g_A}^m - \boldsymbol{L_A A}^m \tag{4.78}$$

$$\boldsymbol{C_\omega \omega}^{m+1} = \boldsymbol{g_\omega}^m - \boldsymbol{L_\omega \omega}^m + \tilde{\boldsymbol{b}}_{\boldsymbol{\omega}}^{\,m+1} \tag{4.79}$$

where

$$\boldsymbol{C_A} = \alpha_A \boldsymbol{S_A} - \frac{Re_m}{\Delta t}\boldsymbol{K}, \qquad \boldsymbol{L_A} = (1-\alpha_A)\boldsymbol{S_A} + \frac{Re_m}{\Delta t}\boldsymbol{K}$$

$$\boldsymbol{C_\omega} = \alpha_\omega \boldsymbol{S_\omega} - \frac{Re}{\Delta t}\boldsymbol{K}, \qquad \boldsymbol{L_\omega} = (1-\alpha_\omega)\boldsymbol{S_\omega} + \frac{Re}{\Delta t}\boldsymbol{K}.$$

Thus, the final discretized system for the unsteady full MHD equations can be given as

$$\boldsymbol{\psi}^{m+1} = \boldsymbol{g_\psi}^m - \boldsymbol{K\omega}^m \tag{4.80}$$

$$\boldsymbol{u}^{m+1} = \frac{\partial \boldsymbol{F}}{\partial y}\boldsymbol{F^{-1}}\boldsymbol{\psi}^{m+1}, \qquad \boldsymbol{v}^{m+1} = -\frac{\partial \boldsymbol{F}}{\partial x}\boldsymbol{F^{-1}}\boldsymbol{\psi}^{m+1} \tag{4.81}$$

$$\boldsymbol{C_A A}^{m+1} = \boldsymbol{g_A}^m - \boldsymbol{L_A A}^m \tag{4.82}$$

$$\boldsymbol{B_x}^{m+1} = \frac{\partial \boldsymbol{F}}{\partial y}\boldsymbol{F^{-1}}\boldsymbol{A}^{m+1}, \qquad \boldsymbol{B_y}^{m+1} = -\frac{\partial \boldsymbol{F}}{\partial x}\boldsymbol{F^{-1}}\boldsymbol{A}^{m+1} \tag{4.83}$$

$$\boldsymbol{C_\omega \omega}^{m+1} = \boldsymbol{g_\omega}^m - \boldsymbol{L_\omega \omega}^m + \tilde{\boldsymbol{b}}_{\boldsymbol{\omega}}^{\,m+1}. \tag{4.84}$$

In the magnetic potential and vorticity transport equations (4.82)-(4.84), the vectors $\boldsymbol{g_A}^m$, $\boldsymbol{g_\omega}^m$ and $\tilde{\boldsymbol{b}}_{\boldsymbol{\omega}}^{\,m+1}$ are known and do not contribute to the stability analysis.

Thus, the stability conditions for the RBF discretized system of full MHD equations are [20, 44]

$$\rho(\boldsymbol{C_A^{-1}L_A}) < 1 \tag{4.85}$$

$$\rho(\boldsymbol{C_\omega^{-1}L_\omega}) < 1 \tag{4.86}$$

where $\rho(\boldsymbol{C_A^{-1}L_A})$ and $\rho(\boldsymbol{C_\omega^{-1}L_\omega})$ are the spectral radii of the matrices $\boldsymbol{C_A^{-1}L_A}$ and $\boldsymbol{C_\omega^{-1}L_\omega}$, respectively.

In the next Section, the stability conditions (4.85)-(4.86) will be checked for the MHD flow in a lid-driven cavity to obtain stable results.

4.4.1 Stability of the Solution of MHD Flow in a Lid-Driven Cavity

The unsteady, laminar flow of an incompressible, viscous, electrically conducting fluid in a square cavity with a moving top wall is considered. The external magnetic field is applied in the y-direction. The problem configuration is given in Figure 4.5.

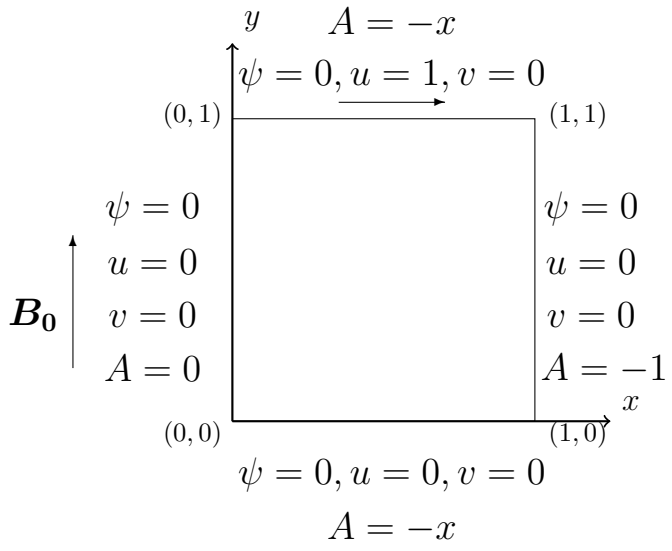

Figure 4.5: Problem 4.4.1: Lid-driven cavity and boundary conditions.

The RBF discretized system of full MHD equations (4.80)-(4.84) in terms of stream function $\boldsymbol{\psi}$, velocity components $(\boldsymbol{u}, \boldsymbol{v})$, magnetic potential $\boldsymbol{A}$, induced magnetic field components $(\boldsymbol{B_x}, \boldsymbol{B_y})$ and vorticity $\boldsymbol{\omega}$ vectors are given as

$$\boldsymbol{\psi}^{m+1} = \boldsymbol{g_\psi}^m - \boldsymbol{K}\boldsymbol{\omega}^m \tag{4.87}$$

$$\boldsymbol{u}^{m+1} = \frac{\partial \boldsymbol{F}}{\partial y}\boldsymbol{F^{-1}}\boldsymbol{\psi}^{m+1}, \qquad \boldsymbol{v}^{m+1} = -\frac{\partial \boldsymbol{F}}{\partial x}\boldsymbol{F^{-1}}\boldsymbol{\psi}^{m+1} \tag{4.88}$$

$$\boldsymbol{C_A}\boldsymbol{A}^{m+1} = \boldsymbol{g_A}^m - \boldsymbol{L_A}\boldsymbol{A}^m \tag{4.89}$$

$$\boldsymbol{B_x}^{m+1} = \frac{\partial \boldsymbol{F}}{\partial y}\boldsymbol{F^{-1}}\boldsymbol{A}^{m+1}, \qquad \boldsymbol{B_y}^{m+1} = -\frac{\partial \boldsymbol{F}}{\partial x}\boldsymbol{F^{-1}}\boldsymbol{A}^{m+1} \tag{4.90}$$

$$\boldsymbol{C_\omega}\boldsymbol{\omega}^{m+1} = \boldsymbol{g_\omega}^m - \boldsymbol{L_\omega}\boldsymbol{\omega}^m + \tilde{\boldsymbol{b}}_{\boldsymbol{\omega}}^{m+1}. \tag{4.91}$$

The iterative process starts with initial vorticity $\boldsymbol{\omega}^0$ and magnetic potential $\boldsymbol{A}^0$. The stream function equation (4.87) is solved. Then, the velocity components are obtained from the equation (4.88). After $\boldsymbol{g_A}^{m+1}$ is found by using the equation (4.89), the induced magnetic field components are computed from the equation (4.90). The

unknown vorticity boundary conditions are obtained from vorticity definition by using the coordinate matrix $\boldsymbol{F}$. With these boundary conditions vorticity equation (4.91) is solved. The iteration continues until the absolute error

$$||\boldsymbol{z}^{m+1} - \boldsymbol{z}^{m}||_{\infty} < \epsilon \tag{4.92}$$

is satisfied where $\boldsymbol{z}$ denotes $\boldsymbol{\psi}$, $\boldsymbol{A}$ or $\boldsymbol{\omega}$. $\epsilon = 10^{-4}$ is the preassigned tolerance to obtain steady-state solution.

The numerical results are obtained for several values of Reynolds number, magnetic Reynolds number and Hartmann number with fixed relaxation parameters $\alpha_A = \alpha_\omega = 0.6$. We use $N_b = 100$ boundary points for the variation of Re and Re_m, but more boundary points $N_b = 160$ are taken for increasing Hartmann number values $M = 50, 100$. We present the flow behavior and magnetic potential profile in Figures 4.6-4.8.

We first show in Figure 4.6 that the effect of the increase in Re on the flow and magnetic potential behaviors for fixed $M = 10$ and $Re_m = 100$. For $Re = 100$ the main vortex of the flow is close to the upper wall due to its movement. As Re increases, the main vortex moves through the center of the cavity with decreasing magnitude and the secondary vortex is formed in the right bottom corner. Increase in Re causes the circulation of the equivorticity lines. However, not much alteration occurs in magnetic potential lines.

In Figure 4.7, the variation in Re_m is presented for fixed $Re = 100$, $M = 10$. It is observed that increase in Re_m does not cause a significant change on the flow. Magnetic potential lines circulate inside the cavity since the convection terms become dominant in the magnetic potential equation as Re_m increases.

We analyze the influence of the magnetic field on the flow and magnetic potential behaviors for fixed $Re = Re_m = 100$ in Figure 4.8. We use $N_b = 100, 160, 160$ boundary points for $M = 10, 50, 100$ with $\Delta t = 0.2, 0.1, 0.05$, respectively. One can observe that increase in M causes the Hartmann layer formation near the moving top lid. As magnetic field intensity increases, vorticity contours squeeze through the top wall with the effect of the moving lid and the rest of the cavity is stagnant. As M increases, magnetic potential lines are distributed uniformly due to the decrease in

the magnitude of velocity in convection terms of magnetic equation.

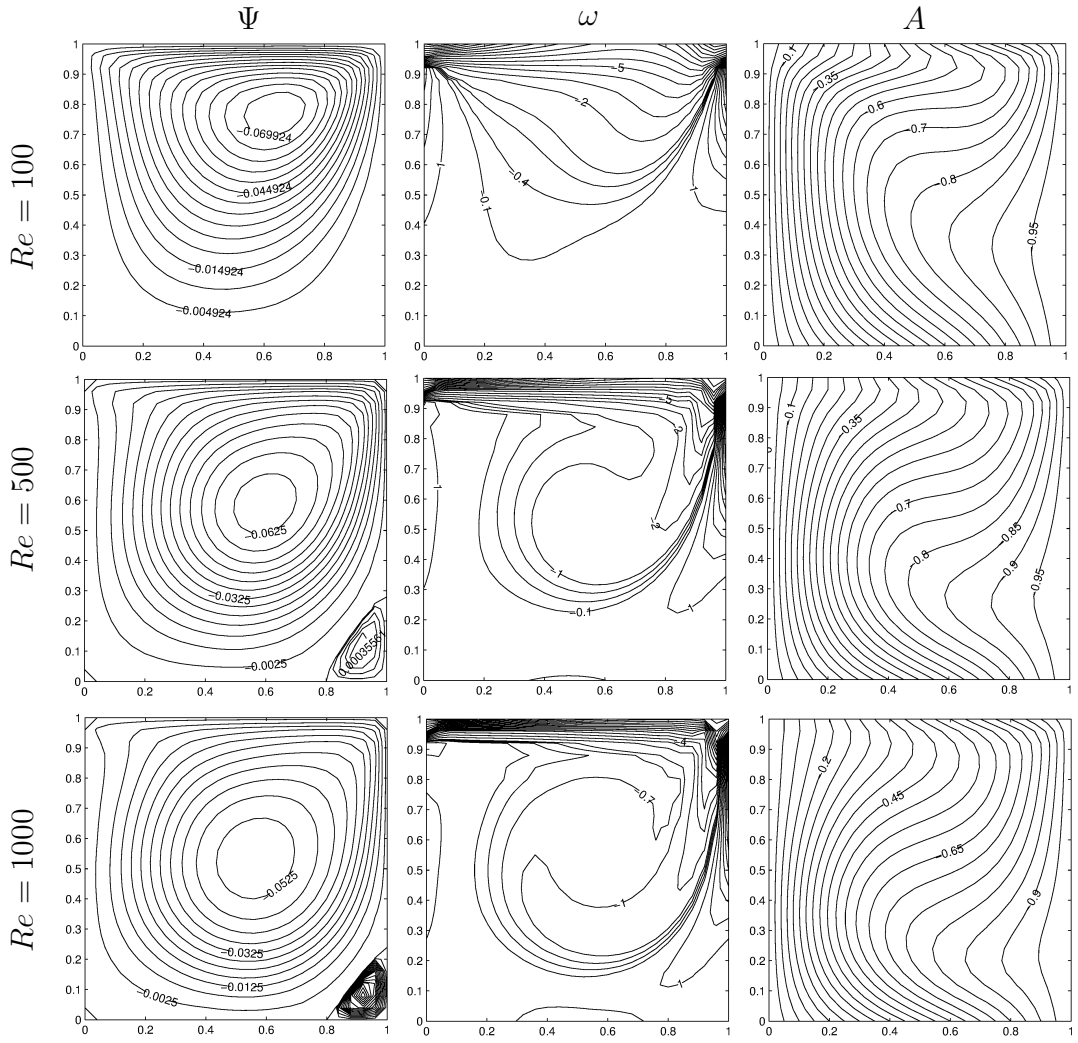

Figure 4.6: Problem 4.4.1: Streamlines, vorticity contours, magnetic potential lines for $Re = 100, 500, 1000$ using $\Delta t = 0.2$, $M = 10$, $Re_m = 100$.

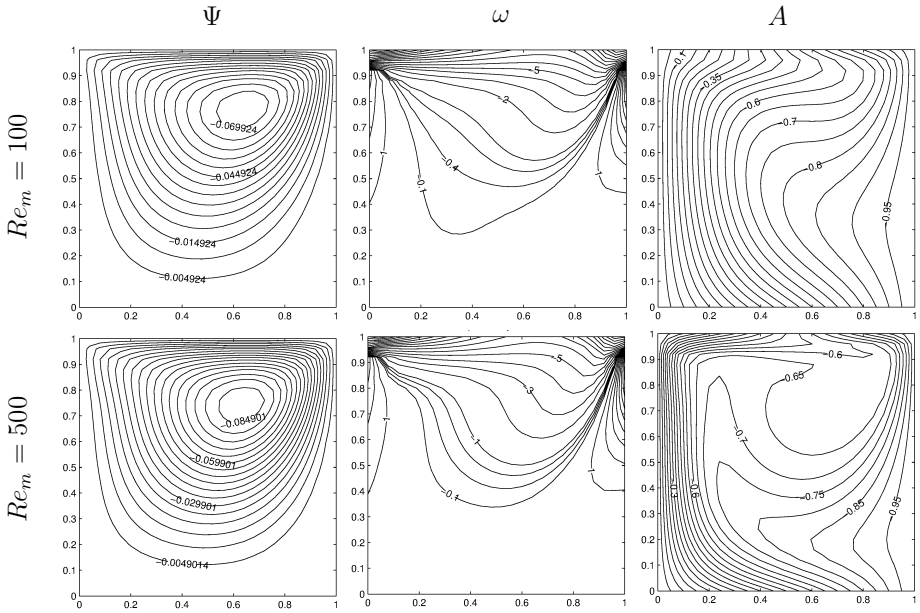

Figure 4.7: Problem 4.4.1: Streamlines, vorticity contours, magnetic potential lines for $Re_m = 100, 500$ using $\Delta t = 0.2$, $Re = 100$, $M = 10$.

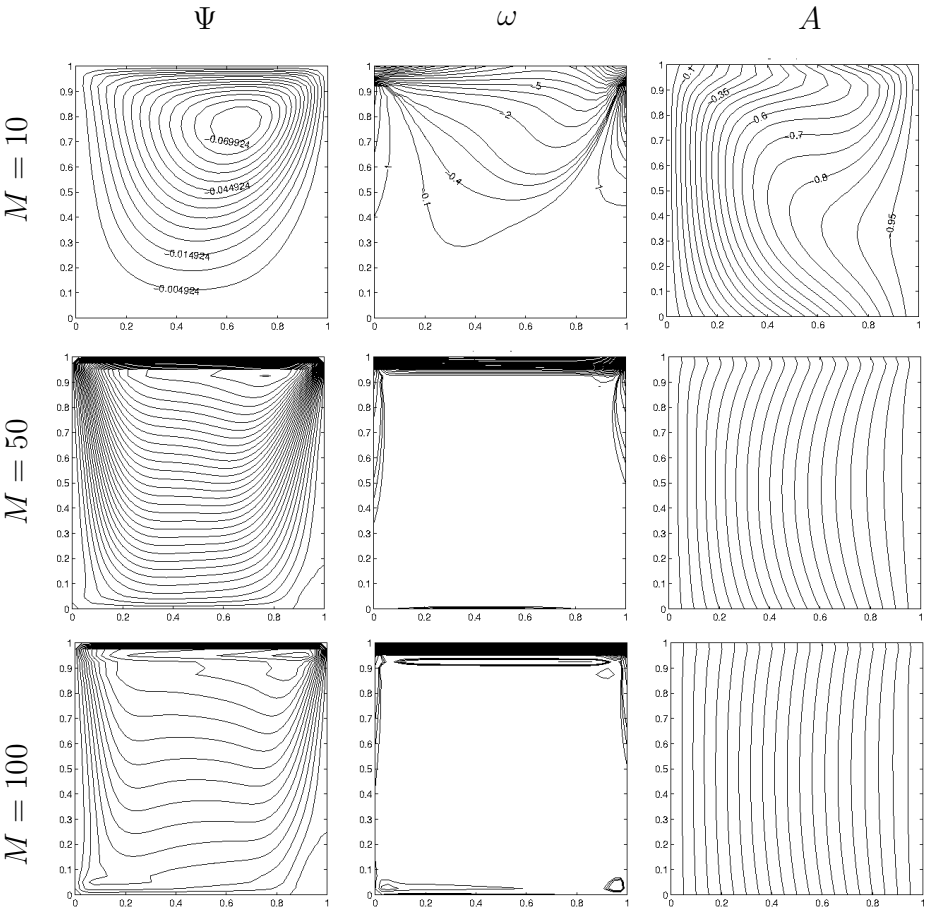

Figure 4.8: Problem 4.4.1: Streamlines, vorticity contours, magnetic potential lines for $M = 10, 50, 100$ using $\Delta t = 0.2, 0.1, 0.05$, respectively, $Re = Re_m = 100$.

Now, we perform the stability analysis of RBF approximation of full transient MHD equations (4.80)-(4.84). The maximum eigenvalues of coefficient matrices $\boldsymbol{C_A^{-1}L_A}$ and $\boldsymbol{C_\omega^{-1}L_\omega}$ are given in Tables 4.6-4.9 for several values of relaxation parameters α_A, α_ω, time increment Δt, Reynolds number Re, magnetic Reynolds number Re_m and Hartmann number M.

Table 4.6 presents the spectral radii for the variation in Re and Δt with fixed $\alpha_A = \alpha_\omega = 0.6$, $Re_m = 100$ and $M = 10$. We observe that when $Re = 100$ maximum eigenvalues of $\boldsymbol{C_A^{-1}L_A}$ equal to maximum eigenvalues of $\boldsymbol{C_\omega^{-1}L_\omega}$ since the coefficient matrices are the same for $Re_m = Re$ and $\alpha_A = \alpha_\omega$. Although we increase the Reynolds number, it is even possible to use larger time increment Δt as 0.7 to obtain stable results since maximum eigenvalues stay almost the same.

In Table 4.7, maximum eigenvalues are obtained for different values of Re_m and Δt with fixed $Re = 100$, $\alpha_A = \alpha_\omega = 0.6$. Increase in Re_m affects maximum eigenvalues of magnetic potential more than maximum eigenvalues of vorticity due to the dominance of convection terms of magnetic potential equation. Stable results are obtained for $\Delta t \leq 0.5$.

Tables 4.8-4.9 indicate the variation of spectral radius with respect to Hartmann number, time increment and relaxation parameters. When $M = 50$ stable solution is obtained for $\Delta t = 0.2$ and $\Delta t \leq 0.1$ with $0.8 \leq \alpha_A = \alpha_\omega \leq 0.9$ and $0.6 \leq \alpha_A = \alpha_\omega \leq 0.9$, respectively. As M increases up to 100, the stability conditions are satisfied for $\Delta t = 0.1$, $\Delta t = 0.09$ and $\Delta t \leq 0.05$ with $\alpha_A = \alpha_\omega = 0.9$, $0.8 \leq \alpha_A = \alpha_\omega \leq 0.9$ and $0.6 \leq \alpha_A = \alpha_\omega \leq 0.9$, respectively. This shows that increase in Hartmann number requires smaller time increment for the range of relaxation parameters, due to the square of Hartmann number in front of the reaction term of vorticity equation.

Thus, we can obtain stable solution of RBF discretized system of the full MHD equations (4.80)-(4.84) for some appropriately taken relaxation parameters α_A, α_ω, time increment Δt, Reynolds number Re, magnetic Reynolds number Re_m and Hartmann number M.

$Re = 100$			$Re = 500$		$Re = 1000$	
Δt	$\rho(\boldsymbol{C_A^{-1}L_A})$	$\rho(\boldsymbol{C_\omega^{-1}L_\omega})$	$\rho(\boldsymbol{C_A^{-1}L_A})$	$\rho(\boldsymbol{C_\omega^{-1}L_\omega})$	$\rho(\boldsymbol{C_A^{-1}L_A})$	$\rho(\boldsymbol{C_\omega^{-1}L_\omega})$
0.7	-	-	-0.8526	-0.96323	-0.8642	-0.9832
0.5	-0.8637	-0.8637	-0.8920	-0.9736	-0.9007	-0.9879
0.2	-0.9427	-0.9427	-0.9550	-0.9893	-0.9588	-0.9952
0.1	-0.9708	-0.9708	-0.9772	-0.9946	-0.9791	-0.9976

Table 4.6: Spectral radius ρ for $\alpha_\omega = \alpha_A = 0.6$, $N_b = 100$, $M = 10$, $Re_m = 100$, $\epsilon = 10^{-4}$.

$Re_m = 100$			$Re_m = 500$	
Δt	$\rho(\boldsymbol{C_A^{-1}L_A})$	$\rho(\boldsymbol{C_\omega^{-1}L_\omega})$	$\rho(\boldsymbol{C_A^{-1}L_A})$	$\rho(\boldsymbol{C_\omega^{-1}L_\omega})$
0.5	-0.86374857	-0.86374857	-0.96666555	-0.86538498
0.2	-0.94266304	-0.94266304	-0.98649340	-0.94338326
0.1	-0.97081716	-0.97081716	-0.99321397	-0.97118835

Table 4.7: Spectral radius ρ for $\alpha_\omega = \alpha_A = 0.6$, $N_b = 100$, $M = 10$, $Re = 100$ $\epsilon = 10^{-4}$.

$\Delta t = 0.2$		$\Delta t = 0.1$
$\alpha_A = \alpha_\omega$	$\rho(\boldsymbol{C_A^{-1}L_A}) = \rho(\boldsymbol{C_\omega^{-1}L_\omega})$	$\rho(\boldsymbol{C_A^{-1}L_A}) = \rho(\boldsymbol{C_\omega^{-1}L_\omega})$
0.9	-0.96066846	-0.97997568
0.8	-0.96052058	-0.97993550
0.7	-	-0.97989513
0.6	-	-0.97985766
0.5	-	-

Table 4.8: Spectral radius ρ for $N_b = 120$, $M = 50$, $Re = Re_m = 100$, $\epsilon = 10^{-4}$.

$\Delta t = 0.1$		$\Delta t = 0.09$	$\Delta t = 0.05$
$\alpha_A = \alpha_\omega$	$\rho(\boldsymbol{C_A^{-1}L_A}) = \rho(\boldsymbol{C_\omega^{-1}L_\omega})$	$\rho(\boldsymbol{C_A^{-1}L_A}) = \rho(\boldsymbol{C_\omega^{-1}L_\omega})$	$\rho(\boldsymbol{C_A^{-1}L_A}) = \rho(\boldsymbol{C_\omega^{-1}L_\omega})$
0.9	-0.98051159	-0.98242813	-0.99016804
0.8	-	-0.98239725	-0.99015837
0.7	-	-	-0.99014866
0.6	-	-	-0.99013959
0.5	-	-	-

Table 4.9: Spectral radius ρ for $N_b = 120$, $M = 100$, $Re = Re_m = 100$, $\epsilon = 10^{-4}$.

In this Chapter, we perform the numerical stability analysis of unsteady Navier-Stokes equations, transient MHD convection flow and transient full MHD problems. We do not find the region of absolute stability, but find the optimum values of the time increment and problem variables satisfying the stability condition computationally by looking at the spectral radii of the related coefficient matrices. We conclude that although the explicit Euler method is used for the time discretization in the RBF approximation, one can use quite large time increments in the computations for achieving stable numerical solutions.

CHAPTER 5

CONCLUSION

This thesis deals with the numerical solutions of two-dimensional, laminar, steady or unsteady flow of an incompressible, viscous, electrically conducting fluid in the presence of magnetic field. The hydrodynamic and magnetohydrodynamic equations are combined for the modeling of the MHD flow. The primary focus is on the application of the RBF approximation for solving MHD flow equations, although the DRBEM and the DIBEM implementations are also presented.

In the first part of the thesis, the effect of the magnetic field with different orientations on Stokes flow is analyzed. Three test problems are considered for different physical domains which are the lid-driven cavity, constricted square cavity with moving left wall and horizontal channel with backward-facing step. The uniform magnetic field, which is perpendicular to the moving wall, causes Stokes flow to extend the whole cavity, contrary to magnetic field in the same direction with the movement of the wall. In this case, creeping flow moves through the moving wall forming a boundary layer and secondary flow is developed near the opposite wall which is also observed when the cavity is constricted. Constriction of the cavity causes the magnitude of the flow to decrease regardless of the direction of the magnetic field. The increase in the intensity of the magnetic field in the pipe-axis direction generating the electric potential does not affect the Stokes flow behavior. However, the effect is observed on the MHD incompressible flow behavior due to the convective terms in the momentum equations.

The RBF solutions of the MHD convection Stokes and MHD convection incompressible flows with or without viscous dissipation are presented by taking $Re = 0.6$ and

$Re = 100$, respectively in the second part of the thesis. Viscous dissipation causes a significant change on isotherms forming a thermal layer near the cold wall in both cases. However, this effect on the Stokes flow can be observed for the small values of Grashof number ($Gr \geq 90$), contrary to MHD convection incompressible flow. In addition, the RBF approximation is applied to MHD convection flow in a constricted enclosure to examine the impacts of the constriction on the heat transfer. It is concluded that convection is suppressed when the constriction ratio of the cavity or the magnetic field intensity increases. However, it is dominated when Grashof number increases.

In the final part of the thesis, the RBF approximation is extended to solve the unsteady flow problems with the use of explicit Euler method for the time discretization. The stability analysis for RBF solutions of the transient Navier-Stokes, unsteady MHD convection and unsteady full MHD flow equations is also carried in terms of spectral radius of related coefficient matrices in the RBF discretized system. The optimal choices of the time increment, relaxation parameters and physical parameters are found for achieving stable solutions. It is observed that the maximum eigenvalue decreases as the relaxation parameter decreases, but the time increment increases. The numerical solutions are unstable when the relaxation parameter is less than or equal to 0.5. Although, the time derivative is discretized using explicit Euler method, one does not need to use small time increment for obtaining stable solutions.

The radial basis function approximation makes it possible to solve numerically MHD flow and MHD convection flow equations containing nonlinearities with an easy implementation and considerably small computational cost.

REFERENCES

[1] N. M. Al-Najem, K. M. Khanafer, and M. M. El-Refaee. Numerical study of laminar natural convection in tilted enclosure with transverse magnetic field. *International Journal of Numerical Methods for Heat and Fluid Flow*, 8:651–672, 1998.

[2] S. Alchaar, P. Vasseur, and E. Bilgen. The effect of a magnetic field on natural convection in a shallow cavity heated from below. *Chemical Engineering Communications*, 134:195–209, 1995.

[3] N. Alsoy-Akgün and M. Tezer-Sezgin. DRBEM and DQM solutions of natural convection flow in a cavity under a magnetic field. *Progress in Computational Fluid Dynamics, An International Journal*, 13(5):270, 2013.

[4] C. J. S. Alves and A. L. Silvestre. Density results using Stokeslets and a method of fundamental solutions for the Stokes equations. *Engineering Analysis with Boundary Elements*, 28:1245–1252, 2004.

[5] L. T. Benos, S. C. Kakarantzas, I. E. Sarris, A. P. Grecos, and N. S. Vlachos. Analytical and numerical study of MHD natural convection in a horizontal shallow cavity with heat generation. *International Journal of Heat and Mass Transfer*, 75:19–30, 2014.

[6] C. Bozkaya. *Boundary element method solution of initial and boundary value problems in fluid dynamics and magnetohydrodynamics*. Doctoral Thesis. METU, Ankara, 2008.

[7] N. Bozkaya and M. Tezer-Sezgin. The DRBEM solution of incompressible MHD flow equations. *International Journal for Numerical Methods in Fluids*, 67(10):1264–1282, 2011.

[8] M. D. Buhmann. *Radial basis functions: theory and implementations*, volume 12 of *Cambridge Monographs on Applied and Computational Mathematics*. Cambridge University Press, Cambridge, 2003.

[9] C. A. Bustamante, H. Power, Y. H. Sua, and W. F. Florez. A global meshless collocation particular solution method (integrated radial basis function) for two-dimensional Stokes flow problems. *Applied Mathematical Modelling*, 37(6):4538–4547, 2013.

[10] C. S. Chen, C. M. Fan, and P. H. Wen. The method of approximate particular solutions for solving certain partial differential equations. *Numerical Methods for Partial Differential Equations*, 28(2):506–522, 2012.

[11] C. W. Chen, D. L. Young, C. C. Tsai, and K. Murugesan. The method of fundamental solutions for inverse 2D Stokes problems. *Computational Mechanics*, 37(1):2–14, 2005.

[12] C. Y. Choi and E. Balaras. A dual reciprocity boundary element formulation using the fractional step method for the incompressible Navier-Stokes equations. *Engineering Analysis with Boundary Elements*, 33:741–749, 2009.

[13] M. J. Colaço, G. S. Dulikravich, and H. R. B. Orlande. Magnetohydrodynamic simulations using radial basis functions. *International Journal of Heat and Mass Transfer*, 52:5932–5939, 2009.

[14] P. A. Davidson. *An introduction to magnetohydrodynamics*. Cambridge Texts in Applied Mathematics. Cambridge University Press, Cambridge, 2001.

[15] T. Eldho and D.-L. Young. Solution of Stokes flow problem using dual reciprocity boundary element method. *Journal of the Chinese Institute of Engineers*, 24(2):141–150, 2001.

[16] C. A. J. Fletcher. *Computational techniques for fluid dynamics*. Springer Series in Computational Physics. Springer-Verlag, Berlin, second edition, 1991.

[17] N. L. Gajbhiye and V. Eswaran. Numerical simulation of MHD flow and heat transfer in a rectangular and smoothly constricted enclosure. *International Journal of Heat and Mass Transfer*, 83:441–449, 2015.

[18] B. Gebhart. Effects of viscous dissipation in natural convection. *Journal of Fluid Mechanics*, 14:225–232, 1962.

[19] U. Ghia, K. N. Ghia, and C. T. Shin. High-Re solutions for incompressible flow using the Navier-Stokes equations and a multigrid method. *Journal of Computational Physics*, 48:387–411, 1982.

[20] S. Gümgüm. *The dual reciprocity boundary element method solution of fluid flow problems*. Doctoral Thesis. METU, Ankara, 2010.

[21] M. Gürbüz and M. Tezer-Sezgin. MHD Stokes flow in lid-driven cavity and backward-facing step channel. *European Journal of Computational Mechanics*, 24:279–301, 2015.

[22] K. Hitesh. Radiative heat transfer with hydromagnetic flow and viscous dissipation over a stretching surface in the presence of variable heat flux. *Thermal Science*, 13(2):163–169, 2009.

[23] F. P. Incropera and D. P. DeWitt. *Introduction to Heat Transfer*. Wiley, 1996.

[24] M. K. Jain. *Numerical solution of differential equations*. A Halsted Press Book. John Wiley & Sons, Inc., New York, second edition, 1984.

[25] A. Javed, K. Djijdeli, and J. T. Xing. Shape adaptive RBF-FD implicit scheme for incompressible viscous Navier–Strokes equations. *Computers & Fluids*, 89:38–52, 2014.

[26] G. Juncu. The influence of viscous dissipation on the unsteady conjugate forced convection heat transfer from a fluid sphere. *International Journal of Heat and Mass Transfer*, 90:542–551, 2015.

[27] G. H. R. Kefayati, M. Gorji-Bandpy, H. Sajjadi, and D. D. Ganji. Lattice boltzmann simulation of MHD mixed convection in a lid-driven square cavity with linearly heated wall. *Scientia Iranica, Transactions B: Mechanical Engineering*, 19:1053–1065, 2012.

[28] C. N. Kim. A liquid metal magnetohydrodynamic duct flow with sudden contraction in a direction perpendicular to a magnetic field. *Computers & Fluids*, 108:156–167, 2015.

[29] P. M. Kishore, V. Rajesh, and S. V. Verma. Effects of heat transfer and viscous dissipation on MHD free convection flow past an exponentially accelerated vertical plate with variable temperature. *Journal of Naval Architecture and Marine Engineering*, 7(2):101–110, 2010.

[30] J. A. Kołodziej and J. K. Grabski. Application of the method of fundamental solutions and the radial basis functions for viscous laminar flow in wavy channel. *Engineering Analysis with Boundary Elements*, 57:58–65, 2015.

[31] W. Layton, H. Tran, and C. Trenchea. Numerical analysis of two partitioned methods for uncoupling evolutionary MHD flows. *Numerical Methods for Partial Differential Equations*, 30(4):1083–1102, 2014.

[32] D. C. Lo. High-resolution simulations of magnetohydrodynamic free convection in an enclosure with a transverse magnetic field using a velocity–vorticity formulation. *International Communications in Heat and Mass Transfer*, 37(5):514–523, 2010.

[33] C. F. Loeffler, A. L. Cruz, and A. Bulcão. Direct use of radial basis interpolation functions for modelling source terms with the boundary element method. *Engineering Analysis with Boundary Elements*, 50:97–108, 2015.

[34] C. F. Loeffler, W. J. Mansur, H. d. M. Barcelos, and A. Bulcão. Solving Helmholtz problems with the boundary element method using direct radial basis function interpolation. *Engineering Analysis with Boundary Elements*, 61:218–225, 2015.

[35] U. Müller and L. Bühler. *Magnetofluiddynamics in channels and containers*. Springer, New York, 2001.

[36] R. Nasrin and S. Parvin. Hydromagnetic effect on mixed convection in a lid-driven cavity with sinusoidal corrugated bottom surface. *International Communications in Heat and Mass Transfer*, 38(6):781–789, 2011.

[37] H. A. Navarro, L. Cabezas-Gómez, R. C. da Silva, and A. N. Montagnoli. A generalized alternating-direction implicit scheme for incompressible magneto-hydrodynamic viscous flows at low magnetic Reynolds number. *Applied Mathematics and Computation*, 189(2):1601–1613, 2007.

[38] R. Nyabuto, J. K. Sigey, J. A. Okelo, and J. M. Okwoyo. Magneto-hydrodynamics analysis of free convection flow between two horizontal parallel infinite plates subjected to constant heat flux. *The SIJ Transactions on Computer Networks and Communication Engineering*, 1:79–83, 2013.

[39] H. Ozoe. *Magnetic Convection*. Imperial College. Press, 2005.

[40] A. Pantokratoras. Effect of viscous dissipation in natural convection along a heated vertical plate. *Applied Mathematical Modelling*, 29(6):553–564, 2005.

[41] S. Parvin and N. Hossain. Finite element simulation of MHD combined convection through a triangular wavy channel. *International Communications in Heat and Mass Transfer*, 39(6):811–817, 2012.

[42] P. W. Patridge, C. A. Brebbia, and L. C. Wrobel. *The Dual Reciprocity Boundary Element Method*. Computational Mechanics Publications, Elsevier Science, 1992.

[43] A. Peratta and V. Popov. Numerical stability of the BEM for advection-diffusion problems. *Numerical Methods for Partial Differential Equations*, 20(5):675–702, 2004.

[44] P. S. Ramesh and M. H. Lean. Stability of the multiple reciprocity method for transient heat conduction. *Communications in Numerical Methods in Engineering*, 9:629–634, 1993.

[45] D. F. Rogers. *Laminar flow analysis*. Cambridge University Press, New York, 1992.

[46] N. Rudraiah, R. M. Barron, M. Venkatachalappa, and C. K. Subbaraya. Effect of a magnetic field on free convection in a rectangular enclosure. *International Journal of Engineering Science*, 33(8):1075–1084, 1995.

[47] M. Sahin and R. G. Owens. A novel fully implicit finite volume method applied to the lid-driven cavity problem-Part I: High Reynolds number flow calculations. *International Journal for Numerical Methods in Fluids*, 42:57–77, 2003.

[48] H. Sajjadi, M. Gorji-Bandpy, D. Ganji, and G. R. Kefayati. Lattice boltzmann simulation of MHD mixed convection in a two-sided lid-driven square cavity. *Heat Transfer-Asian Research*, 41(2):179–195, 2012.

[49] Y. V. S. S. Sanyasiraju and G. Chandhini. Local radial basis function based gridfree scheme for unsteady incompressible viscous flows. *Journal of Computational Physics*, 227(20):8922–8948, 2008.

[50] A. Sellier, S. H. Aydin, and M. Tezer-Sezgin. Free-space fundamental solution of a 2D steady slow viscous MHD flow. *CMES. Computer Modeling in Engineering & Sciences*, 102(5):393–406, 2014.

[51] S. Sharp. Stability analysis for boundary element methods for the diffusion equation. *Applied Mathematical Modelling*, 10(1):41–48, 1986.

[52] J. A. Shercliff. *A textbook of magnetohydrodyamics*. Pergamon Press, Oxford-New York-Paris, 1965.

[53] C. Shu, H. Ding, and N. Zhao. Numerical comparison of least square-based finite-difference (LSFD) and radial basis function-based finite-difference (RBFFD) methods. *Computers & Mathematics with Applications*, 51(8):1297–1310, 2006.

[54] Y.-S. Smyrlis and A. Karageorghis. Some aspects of the method of fundamental solutions for certain biharmonic problems. *CMES. Computer Modeling in Engineering & Sciences*, 4(5):535–550, 2003.

[55] S. Soleimani Kutanaei, N. Roshan, A. Vosoughi, S. Saghafi, A. Barari, and S. Soleimani. Numerical solution of Stokes flow in a circular cavity using mesh-free local RBF-DQ. *Engineering Analysis with Boundary Elements*, 36(5):633–638, 2012.

[56] M. Tezer-Sezgin and C. Bozkaya. *DRBEM Solution of MHD Flow and Electric Potential in a Rectangular Pipe with a Moving Lid, Numerical Mathematics and Advanced Applications, ENUMATH 2015*. Springer, 2016.

[57] D. J. Tritton. *Physical fluid dynamics*. Oxford Science Publications. The Clarendon Press, Oxford University Press, New York, second edition, 1988.

[58] C. C. Tsai, D. L. Young, and A. H.-D. Cheng. Meshless BEM for three-dimensional Stokes flows. *CMES. Computer Modeling in Engineering & Sciences*, 3(1):117–128, 2002.

[59] M. Vasudeviah and K. Balamurugan. On forced convective heat transfer for a Stokes flow in a wavy channel. *International Communications in Heat and Mass Transfer*, 28:289–297, 2001.

[60] K. Yapıcı and S. Obut. Laminar mixed-convection heat transfer in a lid-driven cavity with modified heated walls. *Heat Transfer Engineering*, 36:303–314, 2015.

[61] H. Yosinobu and T. Kakutani. Two-dimensional Stokes flow of an electrically conducting fluid in a uniform magnetic field. *Journal of the Physical Society of Japan*, 14:1433–1444, 1959.

[62] D. L. Young, C. W. Chen, C. M. Fan, K. Murugesan, and C. C. Tsai. The method of fundamental solutions for Stokes flow in a rectangular cavity with cylinders. *European Journal of Mechanics. B. Fluids*, 24(6):703–716, 2005.

[63] D. L. Young, S. C. Jane, C. Y. Lin, C. L. Chiu, and K. C. Chen. Solutions of 2D and 3D Stokes laws using multiquadratics method. *Engineering Analysis with Boundary Elements*, 28:1233–1243, 2004.

[64] D. L. Young, S. J. Jane, C. M. Fan, K. Murugesan, C. C. Tsai, and K. Murugesan. The method of fundamental solutions for 2D and 3D Stokes problems. *Journal of Computational Physics*, 211:1–8, 2006.

[65] D. L. Young, C. C. Tsai, T. I. Eldho, and A. H.-D. Cheng. Solution of Stokes flow using an iterative DRBEM based on compactly-supported, positive-definite radial basis function. *Computers & Mathematics with Applications*, 43(3-5):607–619, 2002.

[66] Z. Yun-Xin and T. Yong-Ji. Meshless schemes for unsteady Navier-Stokes equations in vorticity formulation using radial basis functions. *Journal of Computational and Applied Mathematics*, 192(2):328–338, 2006.

CURRICULUM VITAE

PERSONAL INFORMATION

Surname, Name: Gürbüz, Merve
Nationality: Turkish (TC)
Date and Place of Birth: 10.05.1989, Ankara
Marital Status: Single
E-mail: mervegurbuzm@gmail.com

EDUCATION

Degree	Institution	Year of Graduation
B.S.	METU, Mathematics	2012
High School	Çağrıbey Anatolian High School	2007

PROFESSIONAL EXPERIENCE

Year	Place	Enrollment
2010-2013	METU, Department of Mathematics	Student Assistant

FOREIGN LANGUAGES

English (fluent), German(elementary)

AWARDS

- 2012-2016, TÜBİTAK-National Ph.D. Fellowship Programme 2211

PUBLICATIONS

Publications in International Journals

1. M. Gürbüz, M. Tezer-Sezgin, MHD Stokes flow in lid-driven cavity and backward-facing step channel, European Journal of Computational Mechanics, 24:6, 2015, 279-301.

2. Merve Gürbüz, M. Tezer-Sezgin, MHD Stokes flow and heat transfer in a lid-driven square cavity under horizontal magnetic field, Mathematical Methods in Applied Sciences, DOI: 10.1002/mma.4321.

3. M. Tezer-Sezgin, Merve Gürbüz, MHD convection flow in a constricted channel, Analele Stiinifice ale Universitatii Ovidius Constanta. Seria Matematica, 2016 (submitted).

4. Merve Gürbüz, M. Tezer-Sezgin, RBF Solution of MHD Stokes flow and MHD flow in a constricted enclosure, Engineering Analysis with Boundary Elements, 2017 (submitted).

5. Merve Gürbüz, M. Tezer-Sezgin, Numerical solutions of MHD incompressible convection flow in channels, Mathematical Methods in Applied Sciences, 2017 (submitted).

International Conference Publications (Proceedings)

1. M. Gürbüz, M. Tezer-Sezgin, Two-dimensional Stokes flow of an electrically conducting fluid in a channel under uniform magnetic field, Proceeding of International Conference on Boundary Element and Meshless Techniques BETEQ 2015, 6-8 July, Valencia, Spain, pages: 126-131.

2. M. Gürbüz, M. Tezer-Sezgin, Lid-driven cavity and backward-facing step Stokes flow under an applied magnetic field, Proceeding of Tenth UK Conference On Boundary Integral Methods UKBIM 2015, 13-14 July, Brighton, UK, pages: 66-75.

3. M. Gürbüz, M. Tezer-Sezgin, Natural convection MHD Stokes flow in a square cavity, Proceedings of the 16th International Conference on Computational and Mathematical Methods in Science and Engineering CMMSE 2016, 4-9 July, Cadiz, Spain, pages: 615-623.

4. M. Gürbüz, M. Tezer-Sezgin, MHD Stokes flow in a smoothly constricted rectangular enclosure, Proceeding of International Conference on Boundary Element and Meshless Techniques BETEQ 2016, 11-13 July, Ankara, Turkey, pages: 73-78.

5. M. Gürbüz, M. Tezer-Sezgin, RBF solution of incompressible MHD convection flow in a pipe, Eleventh Workshop On Mathematical Modeling of Environmental and Life Sciences Problems MMELSP 2016, 12-16 October, Constanta, Romania, page: 16.

6. M. Tezer-Sezgin, M. Gürbüz, MHD Convection Flow in a Constricted Channel, Eleventh Workshop On Mathematical Modeling of Environmental and Life Sciences Problems MMELSP 2016, 12-16 October, Constanta, Romania, page: 28.

7. M. Gürbüz, M. Tezer-Sezgin, Numerical stability of RBF solution for unsteady full MHD flow equations, International Workshop on Mathematical Methods in Engineering MME 2017, 27-29 April, Ankara, Turkey, page : 77.

POSTER PRESENTATIONS

- M. Gürbüz, M. Tezer-Sezgin, RBF solution of convective heat transfer MHD flow, 3rd Workshop of Association for Turkish Women in Maths, 27-29 May, 2016, İzmir, Turkey.

PROJECTS

- M. Gürbüz, M. Tezer-Sezgin, Radial basis function approximation of the solution of MHD flow and electric potential, BAP-1, Department of Mathematics, Middle East Technical University, January 1 - December 31, 2015. Project No: BAP-01-01-2015-006.